Salinity stratification and lateral variability in the Northern Indian Ocean: from calm diurnal cycles to cyclone-induced recovery: a dissertation in Marine Science and Technology - Marine and Atmospheric System Modeling and Analysis.

Kerhalkar, Siddhant

University of Massachusetts Dartmouth
School for Marine Science and Technology

Salinity Stratification and Lateral Variability in the Northern Indian Ocean: From Calm Diurnal Cycles to Cyclone-Induced Recovery

A Dissertation in
Marine Science and Technology -
Marine and Atmospheric System Modeling and Analysis
by
Siddhant Kerhalkar

Submitted in Partial Fulfillment of the
Requirements for the Degree of
Doctor of Philosophy

August 2025

We approve the dissertation of Siddhant Kerhalkar

Date of Signature

Amit Tandon
Commonwealth Professor, Department of Estuarine and Ocean Sciences
Dissertation Advisor

Miles A Sundermeyer
Professor, Department of Estuarine and Ocean Sciences
Dissertation Committee

Steven Lohrenz
Professor, Department of Estuarine and Ocean Sciences
Dissertation Committee

J. Thomas Farrar
Senior Scientist, Physical Oceanography Department
Woods Hole Oceanographic Institution, Woods Hole, MA
Dissertation Committee

Kenneth Hughes
Senior Lecturer, School of Science
University of Waikato, Hamilton, New Zealand
Dissertation Committee

Mark Altabet
Graduate Program Director, Marine Science and Technology
Chairperson, Department of Estuarine and Ocean Sciences

Kevin Stokesbury
Dean, School for Marine Science and Technology

Tesfay Meressi
Associate Provost for Graduate Studies

Abstract

Salinity Stratification and Lateral Variability in the Northern Indian Ocean: From Calm Diurnal Cycles to Cyclone-Induced Recovery

by Siddhant Kerhalkar

Monsoons over the Indian subcontinent deliver copious seasonal rainfall from June to November, yet their inherent Monsoon Intra-seasonal Oscillations (MISOs) remain poorly predicted. Errors in MISO predictions significantly affects regional and global weather forecasts. Improving MISO predictability requires a deeper understanding of ocean-atmosphere coupling and improved representation of upper-ocean stratification within the Northern Indian Ocean (NIO), particularly at mesoscale and submesoscale length scales. This dissertation investigates upper-ocean variability at these scales under two key meteorological regimes preceding MISO onset: calm, clear-sky conditions and tropical cyclone events.

Chapters 2 and 3 of this dissertation examine the spatial inhomogeneity in sea surface temperature (SST) evolution over diurnal and intra-seasonal timescales, respectively. Both chapters focus on how unique freshwater-driven salinity stratification contributes to this variability, utilizing remote sensing, in-situ observations, and 1-D modeling.

Chapter 2 reveals that while satellites show diurnal SST amplitude differences of O(1°C) over 100 km, in-situ observations capture finer-scale and more extreme variability. The upper ocean's response to diurnal heating is inhomogeneous over mesoscale and smaller lengths (< 100 km), particularly on days with Diurnal Warm Layer (DWL) presence compared to non-DWL days. Observations and complementary 1-D model simulations demonstrate that lateral differences in salinity stratification can account for up to 0.2°C differences in diurnal SST magnitudes for shallow mixed layer scenarios (< 8 m). Salinity stratification also modifies vertical DWL evolution at scales comparable to initial mixed layer depth.

Chapter 3 extends this analysis to intra-seasonal timescales, demonstrating a nuanced

role for salinity stratification in modulating spatial variability in SST evolution. Depending on the surface forcing and water clarity, enhanced salinity stratification can either increase or decrease surface warming, thereby driving spatial differences in SST of O(0.5°C) over 14-21 days. Higher daily mean net heat flux and turbid water conditions lead to stronger warming and density enhancement in salinity fronts. Conversely, warming is suppressed in cases of lower heat flux, leading to partial density compensation, where temperature and salinity changes offset each other's effects on density and thus reduce the gradient. An analytical threshold daily mean heat flux (Q_{cross}) is derived to predict when stratification leads to stronger warming. This threshold typically falls between 103-130 $\mathrm{W\,m^{-2}}$ in tropical open-ocean contexts, varying with initial and forcing conditions. These findings highlight a crucial interplay between salinity stratification, surface fluxes, and bio-optical feedbacks in shaping intraseasonal SST evolution and its spatial variability.

Chapter 4 presents rare in-situ observations of the upper ocean following Cyclone Biparjoy in the NIO. The post-cyclone wake, nearly 30 km wide, exhibited asymmetric buoyancy gradients and vertical structures of temperature, salinity, and velocity at its edges. This asymmetry reflects the influence of submesoscale processes like Ekman Buoyancy Fluxes and Mixed Layer Eddies, with downfront (upfront) orientation relative to southwesterly monsoon winds at the edges of the wake. These unique observations highlight how interactions between monsoon winds and underlying three-dimensional submesoscale processes, in conjunction with surface heating, accelerate the recovery of a slow-moving cyclone wake.

Collectively, the findings from this dissertation highlight the dynamic nature of upper-ocean variability under contrasting meteorological conditions and offer physical insights that can guide improvements in MISO forecasting.

Acknowledgements

My time at School for Marine Science and Technology (SMAST) in New Bedford over the past six years has shown me just how true the saying is: "*It takes a village to raise a child*". I have been incredibly fortunate to receive the unwavering support, encouragement, and kindness of so many individuals, both near and far, throughout this journey. To each of you, I extend my deepest gratitude.

First and foremost, I am profoundly grateful to my advisor, Professor Amit Tandon, for guiding me through this long journey and helping me grow as both a scientist and a person. I know I was not always the easiest to advise (just ask my parents), but I benefited immensely from our many discussions about science, career, and life over years (especially during our fieldwork in Arabian Sea). Beyond the science, I am grateful to you and Roochi ma'am for your warm hospitality over the years, which made New Bedford feel a little more like home.

I consider myself incredibly fortunate to have a fantastic Ph.D. committee comprising Dr. J. Thomas Farrar, Dr. Kenneth Hughes, Professor Steven Lohrenz, and Professor Miles Sundermeyer, whose collective guidance was instrumental in shaping both my research and me as a scientist. They sparked my curiosity, offered thoughtful guidance on science and its communication, and pushed me to maintain high standards and refine my work. Their unwavering encouragement during challenging committee meetings also meant a great deal to me.

I extend my sincere thanks to all the professors at SMAST and University of Massachusetts Dartmouth (UMass Dartmouth) whose courses I had the opportunity to take. A special mention goes to Professor Mark Altabet, who gave me the opportunity to join a field campaign during the peak COVID-19 pandemic to study nitrogen loss in the Oxygen Minimum Zones of the Tropical Pacific under his leadership—an experience that was completely different from my physical oceanography work in the Indian Ocean. I am especially thankful

to Dr. Jonathan Lilly for his outstanding LiSYS and Time Series courses, which were both insightful and inspiring.

I am also grateful that through various Office of Naval Research projects like MISO-BoB and EKAMSAT-ASTraL, which supported my Ph.D., I had the opportunity to exchange ideas and receive guidance from incredibly talented and generous group of scientists. I am especially thankful to my co-authors on various papers: Andrew Lucas, Verena Hormann, Luca Centurioni, Tamara Schlosser, Leah Johnson, Ankitha Kannad, Alex Kinsella and Craig Lee, for their time and feedback on my work. I am especially indebted to Jen MacKinnon and Janet Sprintall. Their thoughtful feedback and early discussions on ideas significantly improved the quality and direction of this work. I truly value every bit of their guidance, which was instrumental in bringing this dissertation to completion.

I would like to acknowledge the academic and administrative support provided by SMAST and UMass Dartmouth, especially from Mike Marino, Cindy Costa, Sue Silva, Arlene Wilkinson, Chris Fox, Gail Lyonnais, Sydney Carreiro, Callie Rumbut, Susan Burke Pedreira, Vicki Vital, Meghan Houghton and Daniel Pirbudagov. Your kind help ensured that I could focus my time and energy on my studies and research rather than getting bogged down in logistics or searching for answers on my own. I also would like to thank the Associate Provost's office, UMass Dartmouth for their support through the Distinguished Doctoral Fellowship

I am truly grateful for the unwavering support, invaluable help, and camaraderie of all my labmates in Tandon Laboratory at UMass Dartmouth. I especially want to thank Cauê Lazaneo, Shikha Singh, Filipe Pereira, Iury Simões-Sousa, Suraj Singh, and Ramana Patibandla for their help in navigating research, the Ph.D. journey, and for countless idea exchanges during their time in the lab. Your collaborative spirit, sharp scientific instincts, and creative approaches pushed me to grow. Christian Buckingham, thank you for your kindness and steady support, and for always being available to talk about Ph.D. struggles

and ideas over dinners at Moby Dick or Rose Alley. I learned a great deal from you, especially about curved fronts and symmetric instabilities. Patrick Pasteris, thank you for sharing insights from your fascinating engineering work and home projects. Parth Sastry and Debarshi Sarkar—beyond science—thank you for our many entertaining conversations about football (the original kind), Formula 1, and controversial opinions, creating a constant hankering for Chinese takeouts after work, or Dunkin' prior to work: it has been a fun experience seeing you both grow in the lab. Debarshi, you were also a great bunkmate during fieldwork, always keeping us entertained with your quirky habits—and our conference trips were always a blast. Finally, I am grateful to my undergraduate mentees—Nick Monroe, Vicky Balabanova, and Ersen'S Joseph—who helped me strive to become a better mentor.

I am also profoundly thankful to the captains, crews, chief scientists, and science teams of the SR1911 and RR2306 cruises aboard R/V Sally Ride and R/V Roger Revelle respectively. The data central to this dissertation would not exist without their immense effort and dedication. I am equally grateful for the friendships and connections forged during these cruises—and during SR2011 and TN432 aboard R/V Sally Ride and R/V Thomas G. Thompson—which greatly enriched my experience.

My time at SMAST was truly enriched by the friendships formed across the two buildings. I especially thank Alanna and Elizabeth for all the fun moments during my time here—from navigating COVID challenges and virtually reviving the IMS symposium, to sharing Ph.D. struggles, celebrating each other's milestones, and commiserating about life. I will always cherish those memories. I am also grateful for the friendships that came through knowing you both, including your partners, Liam and Craig, whose humor and memes offered much-needed support. Danilo and Bailey, I have always appreciated your honesty, transparency and your refreshingly unfiltered attitude. Ágata, thank you for being my local guardian during my early years and for sharing the ups and downs of grad school—I will always treasure the

memories we made, and I hope to see you and Iury again soon. Nicky and Valentina, thank you for the fun adventures, restaurant outings and tolerating my dad-jokes, especially during COVID when you were my closest companions. Cata and Titi, thank you for the lively house parties (including teaching me to dance to Danza Kuduro), and Le, for our enjoyable swim sessions.

My gratitude also extends to Luca for our 'therapy talks' at SMAST, and to Andie for our ice-cream hangs. I am thankful for my time playing with the wonderful SMAST FC team (Ágata, Sesha, Mianna, Lia, Keith, Max, Drake, Evan, David, Adam, Parth, Debarshi, Juan), who tolerated my goalkeeping quirks and made every moment on and off the pitch unforgettable. André, thanks for the fun tennis sessions. I am also deeply grateful to Steph, Kev, Ozzie, and the entire Wamsutta gang (Parth, Debarshi, Drake, and Kam) for countless dinners and memorable hangs. Max and Mianna—thank you for the incredible tailgating sessions before we cheered our hearts out for the mighty New England Revs: *"Oh when the Revs go marching in!"*. Some of the best times, indeed!

Finally, this dissertation—and the entire journey—would not have been possible without the unwavering love and steadfast support of my family back home. A heartfelt thank you to my Aai and Baba for your boundless love, blessings, and for always giving me the strength to persevere. This dissertation is dedicated to you both, and I hope I have made you proud. I am also deeply grateful to my extended family—my mamas and mamis, kakas and kakus—for their constant encouragement and support. And to my wonderful cousins, Neerja, Varun, and Sahil—thank you for all the fun conversations, especially during the tough days of COVID, which helped keep me sane and grounded. Not to forget that it was your idea that the best dissertation defense is a good dissertation offense. I cannot wait to celebrate this milestone with all of you the next time I am home.

Contents

List of Figures

List of Tables

नवमासधृतं गर्भं भास्करस्य गभस्तिभिः।
पीत्वा रसं समुद्राणां द्यौः प्रसूते रसायनम्॥

Nurtured for nine months by the rays of the Sun, having imbibed the essence of the oceans, the sky gives birth to the elixir — rainfall.

– Vālmīki, *Rāmāyaṇa 4.28.3*

Chapter 1 Introduction

1.1 Indian Summer Monsoons

The Indian Summer Monsoon is a seasonal weather phenomenon that affects the land surrounding the Northern Indian Ocean (NIO), particularly the Indian subcontinent. Commonly referred to as the monsoons, it delivers majority of the annual rainfall between June and November. The seasonal rains are essential for agricultural output and water supply in economies that depend heavily on farming. In India alone, agriculture employs more than 50% of the workforce and contributes over 20% to the national GDP, making the monsoon an essential driver of economic stability and food security (Gadgil and Gadgil, 2006). However, even a modest 10 % deviation from the mean seasonal rainfall (which is approximately 88 cm) can result in droughts or floods in different regions of the country. The economic consequences as a result of such events are substantial: a 10% variation in seasonal rainfall can lead to a 2% fluctuation in India's Gross Domestic Product and a 6% change in Food Grain Production (Gadgil, 2003).

Beyond economic implications, the monsoon season also holds significant public health implications, creating conditions highly conducive to the spread of diseases like malaria and potentially triggering epidemics (National Academies of Sciences, Engineering, and Medicine, 2016). Furthermore, the extreme events associated with the monsoons (floods and droughts) result in an average of 22 fatalities per event as well as severe damages to infrastructure, highlighting the high societal cost of monsoon variability in regions home to more than one-third of the global population (Gadgil, 2003; Ray et al., 2021).

Although the impacts of monsoons appear to be rooted locally, such disturbances can set off cascading effects on food security and diseases regionally and globally. Additionally, several studies report that the monsoons are dynamically linked to larger-scale climate drivers. These include the Madden Julian Oscillation (MJO), an eastward-moving disturbance of

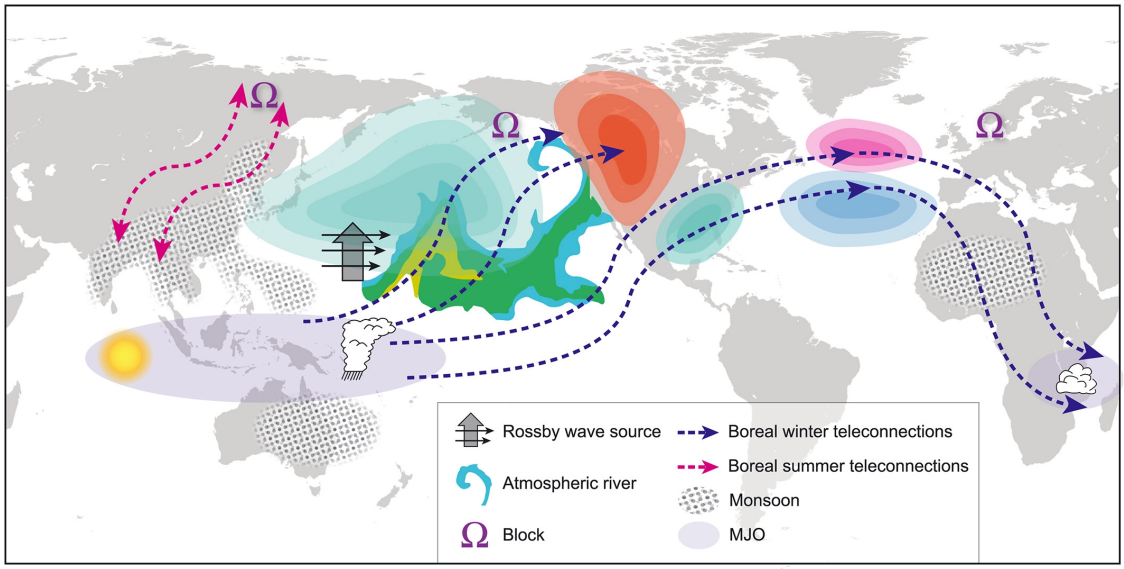

Figure 1.1: Schematic representation of the connections and influences between various tropical and extratropical phenomenon inferred from observational and numerical studies. The convective activity of the tropics associated with Madden Julian Oscillation (MJO), indicated by the gray shading with the cloud symbol, creates a Rossby wave source, consisting of strong divergent flow (heavy arrow) oriented up the gradient of vorticity (light arrows). The resulting Rossby waves affect the probability of occurrence of the dominant modes of variability in midlatitudes, including the North Atlantic Oscillation (lue and magenta shading) and the Pacific North-America patterns (light green and orange shading). The frequency of blocking (indicated by $\mathbf{\Omega}$) and atmospheric rivers (dark green and the yellow shading in the Pacific Ocean) are strongly affected by the MJO convectively driven heat source. The global monsoon systems (indicated by the dotted pattern) also interact with midlatiudes, in particular the Indian Monsoon system. Under certain conditions these circulation anomalies of the midlatitudes can feed back onto the subsequent evolution of the convective activity of the tropics (i.e., new MJO phases and breaks in the Indian summer monsoon precipitation), whereas at other times midlatitude nascent energy fluxes, without any relationship to a tropical forcing, can impinge into the tropics, forcing tropical circulations and organized convection. These potentially two-way interactions are indicated by the blue dotted lines and arrows (for boreal winter) and the magenta dotted lines and arrows (for boreal summer). Adapted from Stan et al. (2017)

clouds, rainfall, and winds over the tropical Indian and Pacific Oceans, and the El Niño–Southern Oscillation (ENSO), a global climate phenomenon driven by variations in winds and sea surface temperatures over the tropical Pacific (Figure 1.1; Zhang et al. 2001; Lau and Waliser 2007; Chattopadhyay et al. 2016). Given that the monsoon and MJO forecasts are typically prone to errors, these inaccuracies propagate across the tropics and affect weather forecasts in these regions within 10 to 20 days (Lin et al., 2009). Furthermore, monsoons and MJO interact with extratropical systems, further amplifying their influence beyond the tropics (Stan et al., 2017). For these reasons, improving our understanding and prediction of the monsoons are important not only for South Asia but also for global weather and climate forecasting.

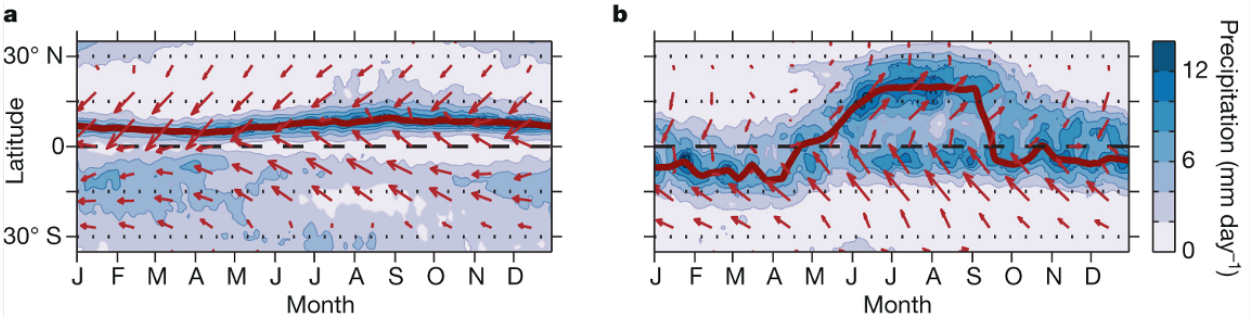

Figure 1.2: Mean precipitation (color scale) and surface winds (vectors) as a function of time of year, zonally averaged over (a) the Pacific sector (160°E–100°W) and (b) the South Asian monsoon sector (65°E–95°E). The Intertropical Convergence Zone (ITCZ), identified by the precipitation maximum, is marked by red lines. Adapted from Schneider et al. (2014)

Monsoons were historically understood as a large-scale sea breeze, where the warming of land drew moist ocean air inland and led to convective rainfall (Halley, 1686). Recent studies identify the primary driver as the northward migration of the Intertropical Convergence Zone (ITCZ), a feature especially pronounced over the Indian subcontinent (Figure 1.2, Gadgil 2003, 2018; Schneider et al. 2014). The topography in the Tibetan Plateau (Northern part of

the Indian subcontinent) acts as a thermal insulator, blocking the cold and dry air from the north and thus trapping warm, moist air over the Indian subcontinent (Nie et al., 2010). In addition to large-scale atmospheric drivers, the monsoon is also influenced by synoptic-scale low-pressure systems originating over the warm NIO, which propagate inland and trigger rainfall (Gadgil, 2003).

Although monsoons are typically considered seasonal, they exhibit strong intra-seasonal variability that exists irrespective of the overall seasonal outlook (Figure 1.3). The Monsoon Intra-Seasonal Oscillations (MISO) are analogous to the MJOs as they propagate with 30–60 day and 10–20 day modes (Goswami et al., 2016). Unlike the MJO, MISOs include a northward propagating component of the east–west rain band. The 30–60 day mode typically propagates northward from the equator into the Indian subcontinent at a speed of about 1 $\mathrm{m\,s^{-1}}$, while the 10–20 day mode propagates westward at a faster speed of 5 $\mathrm{m\,s^{-1}}$ (Goswami et al., 2016).

Recent studies reveal that MISOs are primarily driven by barotropic instabilities arising from the meridional gradients in zonal winds, interacting with warm sea surface temperature (SST) anomalies. The horizontal eddy momentum fluxes associated with this instability are thought to support the northward propagation of MISO (Zhou et al., 2017; Phillips et al., 2021). Specifically, these eddy fluxes advect moisture into regions ahead of the main convective envelope, effectively preconditioning the atmosphere and enabling convective anomalies to migrate northward. As MISOs propagate, they strongly influence surface flux anomalies and modify the nature of air-sea interaction (Sobel et al., 2008). They are typically characterized by two distinct phases: the active phase and the break phase (Bhat, 2002; Goswami et al., 2016). During the break phase, weak winds and clear skies prevail over the NIO, allowing for strong diurnal SST cycles. In contrast, the active phase is marked by persistent

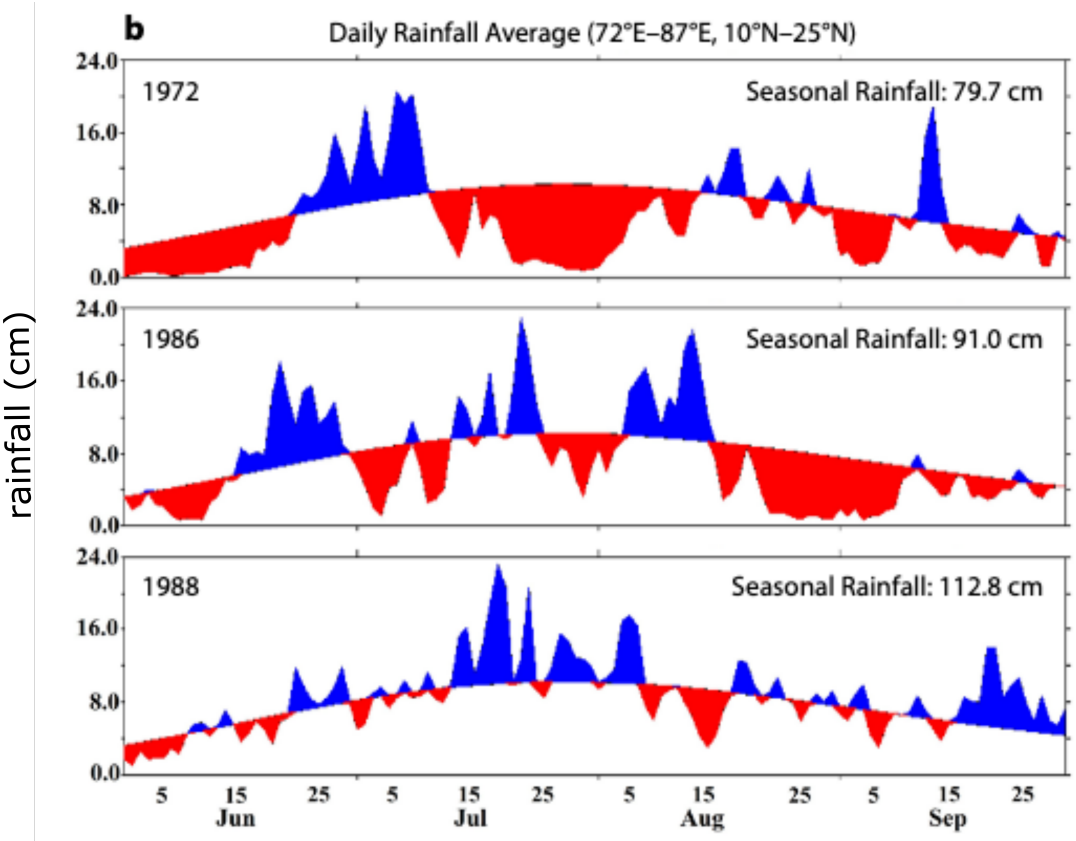

Figure 1.3: Daily rainfall anomalies (relative to climatology) from June 1 to September 30 for 1972 (top), 1986 (middle) and 1988 (bottom). The years 1972 and 1986 were drought years while 1988 was a flood year. Blue color indicates an Active phase while red color indicates a Break phase. Adapted from Goswami et al. (2016).

high winds, increased precipitation and overcast skies (Figure 1.3), which suppress diurnal SST variability (Bhat, 2002; Sengupta and Ravichandran, 2001).

1.2 Modeling challenges of MISO

Given the strong ocean-atmosphere coupling involved in MISO propagation as well as the role of ocean processes over length scales smaller than 100 km to drive larger-scale atmospheric variability (Seo et al., 2023), models that actively couple the ocean and atmosphere (instead of using SST as a prescribed boundary condition) demonstrate improved forecasting range

of intra-seasonal oscillations like MJO and MISO (e.g., DeMott et al., 2015). Studies have shown that one of the major challenges in forecasting MISOs lies in accurately simulating upper-ocean physics and air-sea interaction over the northern Indian Ocean (Phillips et al., 2021). Incorporating high-frequency surface fluxes as well as finer spatial and vertical resolution helps capture the atmospheric-ocean variability and coupling more realistically (Bernie et al., 2005; Ramu et al., 2016). However, improved forecasts of intra-seasonal oscillations like MISO also rely heavily on resolving the physical representation of surface fluxes, ocean mixing, and radiative properties at scales smaller than 100 km, given their direct impact on the SST (Lucas et al., 2014; Beal et al., 2020).

1.3 Uniqueness of the Northern Indian Ocean

The dynamics of the NIO are shaped by salinity stratification that make this region fundamentally different from other tropical basins. These characteristics introduce unique ocean-atmosphere interaction feedbacks that cannot be fully resolved by simply increasing model spatial resolution (Phillips et al., 2021).

Freshwater discharge from monsoon rainfall and major rivers (such as the Ganga-Brahmaputra and Irrawaddy river systems) leads to peak freshwater input in the northern Bay of Bengal (eastern basin of the NIO, Figure 1.4) between June and September (e.g., Sengupta et al., 2006; Sree Lekha et al., 2018; Jarugula et al., 2024). This influx results in strong surface salinity stratification, which suppresses vertical mixing by wind and enhances upper-ocean stability (Sengupta et al., 2016). Mesoscale eddies (with horizontal scales of 10–100 km and Rossby numbers of order 0.1, typically in geostrophic balance) play a key role in redistributing this freshwater southward and laterally across the Bay (Figure 1.5). This redistribution leads to the formation of sharp salinity fronts on O(10km) scales (Rao and Sivakumar, 2003; Sengupta et al., 2006; Mahadevan et al., 2016; Sengupta et al., 2016; Wijesekera et al., 2016; Sree Lekha et al., 2018, 2020). This mesoscale-structured stratification further supports

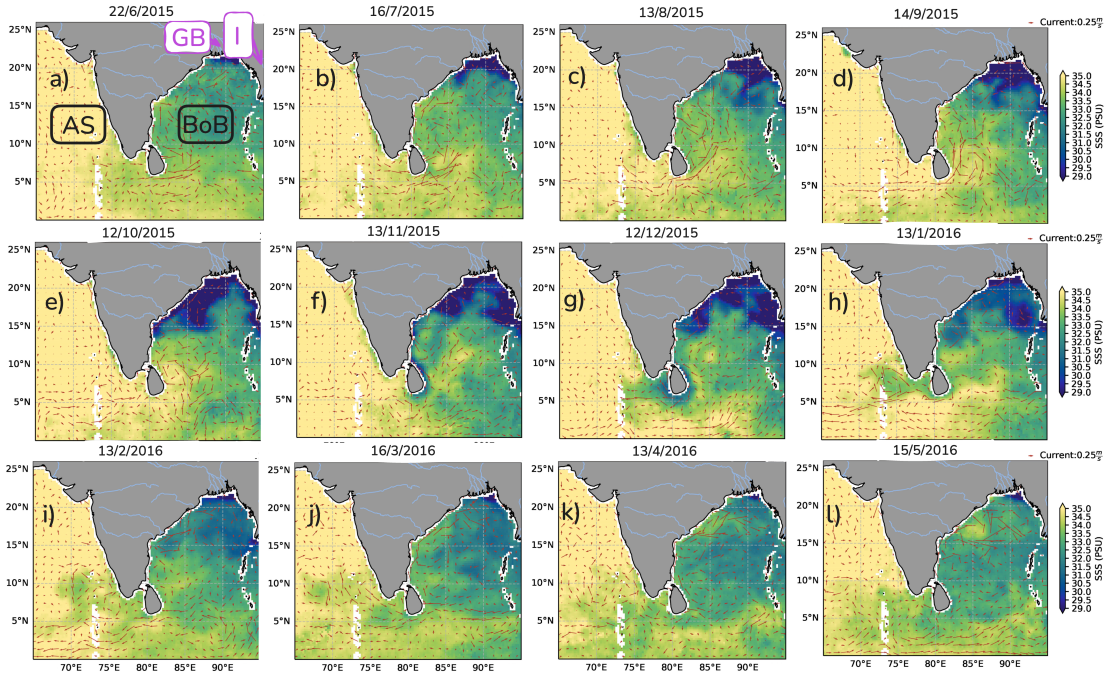

Figure 1.4: (a)-(l) Surface Salinity images from SMAP (Entekhabi et al., 2014) with arrows indicating geostrophic currents for different months in the year 2015-16. GB, I, BoB and AS in panel-(a) indicates the river basins Ganga-Brahmaputra, Irrawady as well as ocean basins, Bay of Bengal and Arabian Sea.

submesoscale processes (length scales of O(0.1-10 km), Rossby and Richardson number of O(1) and typically not in geostrophic balance) that give rise to phenomena such as frontal sharpening, instabilities, and frontal slumping, all of which modulates air-sea interactions (Ramachandran et al., 2018; Jaeger and Mahadevan, 2018; Ramachandran and Tandon, 2020).

Freshwater redistribution is additionally influenced by seasonally reversing boundary currents such as the East India Coastal Current (EICC), which flows along the eastern coast of India. The EICC flows northward during February to September and southward during October to January as a result of strong monsoon wind forcing (e.g., Pargaonkar et al., 2025). The EICC together with coastally trapped Kelvin waves, transports fresh, turbid wa-

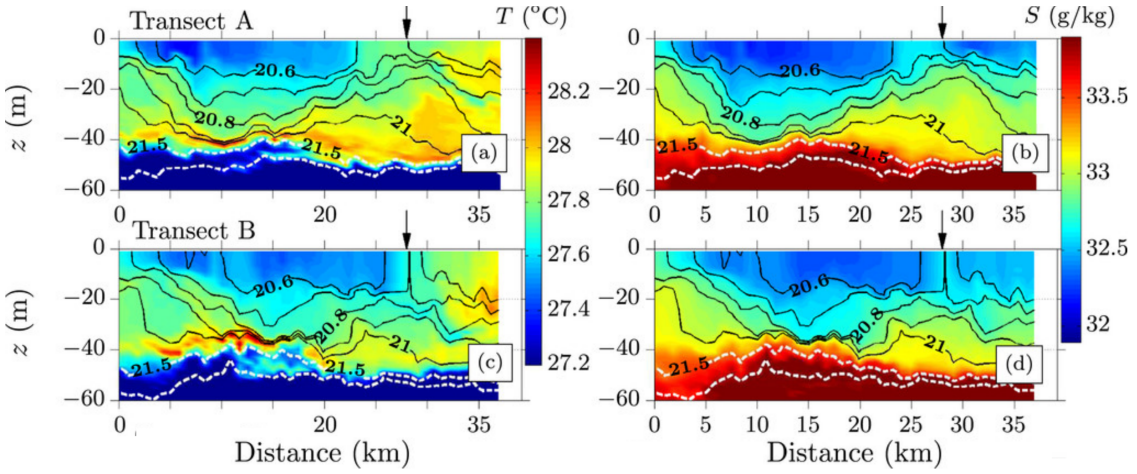

Figure 1.5: Sections of temperature and salinity plotted as a function of the distance traveled by the ship in the North Bay of Bengal. The contours indicate isopycnals, with the solid and dashed lines separated by 0.05 and 0.5 kg m^{-3} respectively. Adapted from Ramachandran et al. (2018).

ters from the northern BoB to its southern reaches—extending as far south as 5 ° N within a few months (Sengupta et al., 2006; Rao et al., 2010; Jarugula et al., 2024). Part of this freshwater is also exported westward to the Arabian Sea (western basin of the NIO) via the EICC and westward-propagating Rossby waves (Figure 1.4), particularly during December through February (Rao and Sivakumar, 2003; Vinayachandran et al., 2007; Vinayachandran and Nanjundiah, 2009; Hormann et al., 2019; Rainville et al., 2022). This exchange alters the vertical stratification in the Arabian Sea, and both basins in the NIO frequently exhibit salinity-stratified mixed layers (also referred to as barrier layers). Such salinity gradients and stratification are often unresolved even in regional models (Vinayachandran and Nanjundiah, 2009).

The presence of these shallow, salinity-stratified mixed layers in the NIO coincides with the spring intermonsoon season, characterized by clear skies, weak winds, and high daily net surface heat fluxes (on the order of 100 W m^{-2}, Weller et al. 2002, 2019). With minimal

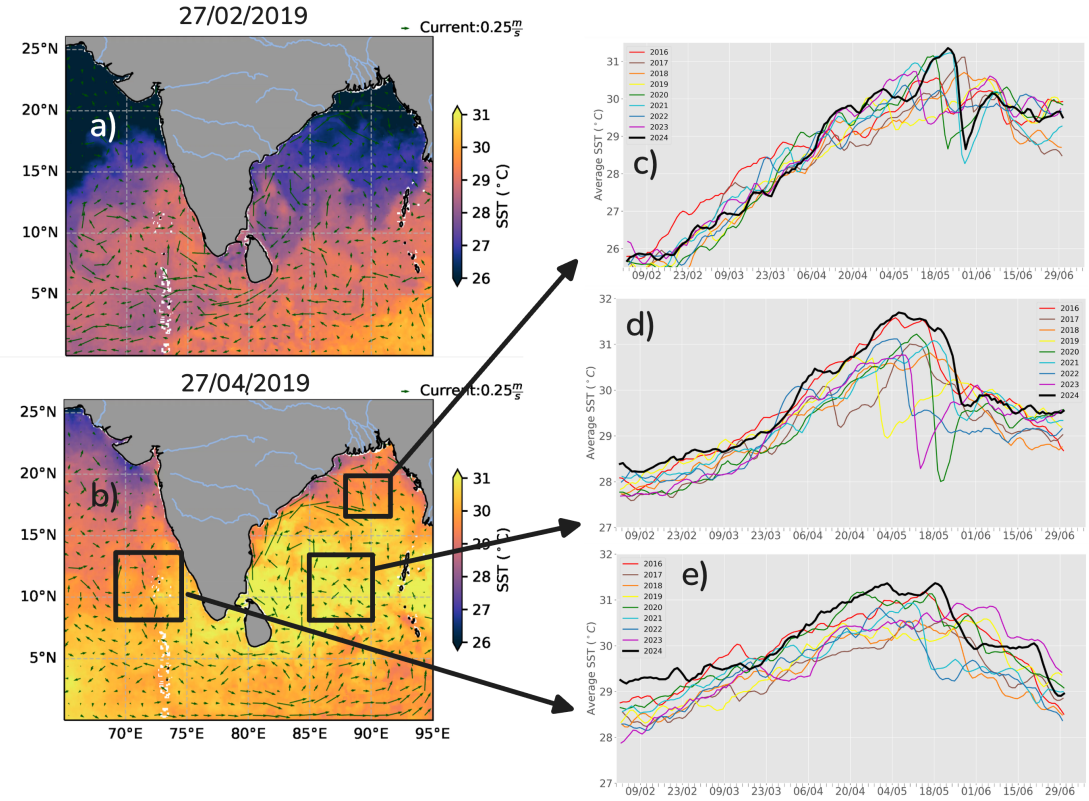

Figure 1.6: SST from OISST (Reynolds et al., 2007) in the Northern Indian Ocean for (a) 27 February 2019 and (b) 27 April 2019. (c)-(e) panels indicate the spatial mean time-series of SST in the spring intermonsoon season within the box highlighted for different years between 2016 and 2024.

lateral advection and low eddy kinetic energy, the upper-ocean heat budget becomes largely one-dimensional (Weller et al., 2002; Thangaprakash et al., 2016; Sun et al., 2022). Such conditions allow for increased diurnal SST amplitude and possible formation of Diurnal Warm Layers (DWLs; Thompson et al. 2019; Hughes et al. 2020a). They also contribute to a seasonal rise in SST of 3–4°C (Figure 1.6). The resulting warm surface layer, often called the Mini Warm Pool, acts as a critical thermal reservoir. This reservior of heat along with the daily occuring DWLs and larger-scale atmospheric convergence can trigger atmospheric

convection on diurnal and intraseasonal timescales, influencing MISOs (Rao et al., 2015; de Szoeke et al., 2021; Pradhan et al., 2022).

The Mini Warm Pool also creates favorable conditions for pre-monsoon tropical cyclone formation in the NIO, as vertical wind shear is typically low enough to permit convective systems to intensify into cyclones (Kikuchi and Wang, 2010; Phillips et al., 2021). Although only around 21% of NIO cyclones develop during the spring intermonsoon season (March–May), they are disproportionately intense, with nearly 88% of these cyclones escalating to severe stages (Bhardwaj et al., 2019) and impacting the Indian subcontinent (345 averaged mortalities per cyclone event, Ray et al. 2021). The mini-warm pool's presence further favors the rapid intensification of these cyclones (Prakash et al., 2022). In some years, such cyclones play a crucial role in advancing the progress of monsoons as part of the monsoon onset vortex (Krishnamurti et al., 1981). These cyclones typically generate a cold wake in the upper ocean after its passage (e.g., Price, 1981; Cornillon et al., 1987; Kerhalkar et al., 2025). Understanding the recovery of such cyclone wakes is particularly important as it influences upper-ocean thermal structure and the subsequent evolution of MISO (Krishnamurti et al., 1981; Evan and Camargo, 2011; Krishnamurti et al., 2007).

1.4 Structure of the dissertation

Despite the recognized importance of the salinity-stratified NIO in modulating MISOs, significant knowledge gaps remain regarding the role of mesoscale and submesoscale air-sea interaction processes that precondition the ocean prior to MISO onset and evolution. This dissertation addresses some of these gaps.

Chapter 2 systematically investigates how spatial variability in salinity stratification, across mesoscale and submesoscale lengths, influences the spatial patterns of diurnal SST variability. While previous studies have examined isolated cases, a comprehensive analysis using large datasets is still lacking. To address this gap, this chapter utilizes in-situ ob-

servations from surface drifters, moored buoys, and air-sea flux profilers, comparing them with satellite-based microwave SSTs, which often lack adequate spatial resolution. This investigation also distinguishes the spatial gradients in SST between days characterized by the presence or absence of Diurnal Warm Layers (DWLs). While DWLs can extend over spatial scales of O(1000km) (Bellenger and Duvel, 2009), little is known about the spatial gradients in SST that exist within the DWLs and hence is addressed in this chapter. Furthermore, Chapter 2 also explores how differences in salinity stratification influence the vertical evolution of DWL, using both observations and one-dimensional ocean modeling.

Building upon the insights from Chapter 2, Chapter 3 aims to understand the role of salinity stratification in governing intra-seasonal changes in SST evolution (excluding the diurnal components) and their spatial variability. This is crucial for understanding the spatial variability in SST within the Mini Warm Pool region over submesoscale and mesoscale lengths. Assessing such variability through in-situ observations is challenging, especially in the data-sparse NIO (Beal et al., 2020; Phillips et al., 2021). Therefore, this chapter employs a one-dimensional modeling approach to overcome these observational limitations. Previous studies (e.g., Sengupta et al., 2002; Echols and Riser, 2020; Yuan et al., 2020) have shown that salinity stratification can either enhance surface warming by trapping heat in shallower depths, or reduce warming due to more efficient nighttime cooling over those same shallow depths. Chapter 3 systematically addresses this apparent conundrum. Results from Chapter 2 and 3 collectively highlight how salinity fronts can evolve into SST fronts over diurnal to intraseasonal timescales (which could influence the atmospheric dynamics and further evolution of MISOs).

Finally, given the frequent occurrence of pre-monsoon tropical cyclones in the region prior to MISO onset, understanding the mechanisms behind cold wake recovery is crucial. While the formation of cyclone-induced cold wakes is well-studied, their recovery phase remains

poorly understood due to a lack of direct observations. Chapter 4 addresses this gap by presenting rare ship-based measurements of a cyclone wake. The results aim to reveal the role of various submesoscale processes in addition to diurnal heating to play an important role in wake recovery.

Chapter 5 aims to synthesize the findings from Chapters 2, 3, and 4, which are relatively standalone studies. This synthesis ties them to the overarching theme of this dissertation: improving the predictability of intraseasonal oscillations like monsoons, by enhancing the representation of small-scale ocean processes.

Chapter 2 Modulation of Diurnal SST and Diurnal Warm Layer Variability by Salinity-Driven Stratification in the Bay of Bengal

Abstract

Diurnal cycles of Sea Surface Temperature (SST) are important for ocean–atmosphere coupling. However, observations of their lateral variability, especially in freshwater-dominated regions and during presence of Diurnal Warm Layers (DWLs), remain limited. This chapter investigates the spatial differences in the diurnal SST amplitude (during DWL and non-DWL days) and subsurface DWL evolution in the Bay of Bengal using remote sensing, in-situ observations, and 1-D modeling. While satellite data reveal O(1°C) differences in diurnal SST amplitude over 100 km, in-situ observations uncover finer-scale and more extreme variability, especially during DWL events. We observe that lateral differences in diurnal SST amplitude over mesoscale and smaller lengths (< 100 km) are larger during DWL days (median: 0.2°C, extreme: 1.4°C) when compared to non-DWL days (median: 0.1°C, extreme: 0.2°C). Observations from drifters and complementary 1-D model simulations reveal that lateral differences in salinity-driven stratification leads to diurnal SST amplitude differences of about 0.2°C for shallow mixed layer scenarios (< 8 m). While stratification differences explain the median variability in diurnal SST amplitude, extreme differences in diurnal SST require additional contributions from spatial variations in surface forcing and optical properties. Observations also reveal that lateral differences in salinity stratification modify the DWL response, leading to O(10 m) differences in DWL depth, making it the same order as typical MLD scales in the Bay. These results highlight the critical role of small-scale differences in salinity-driven stratification (set by rainfall and mesoscale flow fields in the Bay) in causing diurnal SST and DWL response differences.

Significance Statement

The daily cycle of Sea Surface Temperature (SST) plays a key role in ocean–atmosphere heat and moisture exchange. This effect is particularly enhanced during the presence of Diurnal Warm Layers, which are anomalously warm upper-ocean layers formed during low wind speeds. This chapter explores how daily SST warming varies over distances less than 100 km, especially during the DWL presence. Using satellite and in-situ data from the Bay of Bengal, we find that warming can differ by up to 1°C across around 100 km. These differences arise partly from salinity-driven stratification, but variations in surface forcing and water optics also play a role. Understanding these patterns is important because they affect the ocean and atmosphere interaction, influencing atmospheric convection and weather.

2.1 Introduction

Sea Surface Temperature (SST) is an important parameter that connects atmosphere and ocean dynamics through air-sea fluxes. The diurnal cycle of SST is driven by the diurnal variability of incoming shortwave radiation (SWR, Kondo et al. 1979; Imberger 1985; Price et al. 1986; Lotliker et al. 2016). Part of the incoming SWR warms the top few meters and leads to the formation of a stratified diurnal warm layer (DWL) in the presence of light-to-moderate wind speeds (Imberger, 1985; Fairall et al., 1996a; Stuart-Menteth et al., 2005; Soloviev and Lukas, 2006). DWLs typically have vertical scales of O(10 m) and spatial scales of up to O(1000 km) (Soloviev and Lukas, 1997; Prytherch et al., 2013; Bellenger and Duvel, 2009). The stratification within the DWL traps momentum and heat within it, causing temperature anomalies of O(0.1 °C to 1 °C) and near-surface velocity anomalies of 0.1-0.3 $\mathrm{m\,s^{-1}}$ as compared to the bulk of the mixed layer (Price et al., 1986; Sutherland et al., 2016; Shcherbina et al., 2019; Hughes et al., 2021). The momentum trapping within the DWL leads to high vertical shear, which is destabilizing in nature and competes with the stabilizing heat-driven stratification (Price et al., 1986; Sutherland et al., 2016; Hughes

et al., 2020a, 2021). This shear starts dominating in the afternoon once the incoming SWR reduces, causing the DWL to deepen (e.g., Hughes et al., 2021). The DWL is mixed away during the night-time convective mixing (e.g., Hughes et al., 2020a).

DWLs impact air-sea interaction over various time-scales. In the equatorial Indian Ocean, the presence of DWLs induces a deviation in the diurnal cycle of atmospheric convection. This deviation is evident through a secondary peak in convection during the afternoon, which occurs alongside the typical primary maximum in the convection in the early morning (Bellenger et al., 2010; de Szoeke et al., 2021). The inclusion of DWLs in bulk flux calculations results in an instantaneous difference of up to 50 $\mathrm{W\,m^{-2}}$ in the air-sea fluxes compared to non-DWL-resolving calculations (Clayson and Bogdanoff, 2013). The inclusion of the DWL effects in coupled atmosphere-ocean models improves the representation of deep convection and enhances the predictability of the seasonal phenomena like the Madden-Julian Oscillation (MJO) and monsoons (Seo et al., 2014; Pradhan et al., 2022; Song et al., 2024).

Traditionally, DWLs have been conceptualized as one-dimensional features dependent on SWR, wind speeds and the optical properties of water (Price et al., 1986; Webster et al., 1996; Stuart-Menteth et al., 2005; Merchant et al., 2008; Thompson et al., 2019). However in regions like the Bay of Bengal, freshwater fluxes from rainfall and rivers significantly modify the background stratification. Mesoscale eddies redistribute this freshwater throughout the Bay, influencing both the vertical stratification and creating salinity fronts over O(10 km), referred to as mesoscale-structured stratification (Sengupta and Ravichandran, 2001; Shenoi et al., 2002; Rao and Sivakumar, 2003; Sengupta et al., 2006; Mahadevan et al., 2016; Sengupta et al., 2016; Wijesekera et al., 2016; Sree Lekha et al., 2018, 2020). Anecdotal observations suggest that such mesoscale-structured stratification may influence diurnal cycles of SST and DWL evolution, trapping heat to a shallower depth (e.g., Shroyer et al., 2016). Since DWLs respond to surface forcing and background stratification, lateral vari-

ability in these factors over mesoscale and smaller length scales (observed in other ocean basins, e.g. Nuijens et al. 2024; Song et al. 2022; Sengupta et al. 2016) may lead to spatial differences in DWL evolution and influence atmospheric boundary layer dynamics through air-sea coupling.

Despite multiple satellite-based studies detecting lateral gradients in diurnal SST amplitudes (Merchant et al., 2008; Gentemann et al., 2008; Marullo et al., 2016), the influence of lateral variability in background stratification on diurnal SST amplitude and DWLs remains largely unexplored at mesoscale and smaller lengths. Investigating these differences using satellite observations is challenging due to cloud cover, satellite pass times, and the lack of vertical structure information. Furthermore, microwave remote sensing products currently cannot resolve features at length scales finer than about 50 km (though gridded at 25 km, Wentz et al. 2014b; Entekhabi et al. 2014).

The primary objective of this chapter is to quantify lateral differences in diurnal SST amplitudes during DWL events. It also assesses the role of salinity-driven stratification in shaping these differences and the subsurface structure of DWLs across mesoscale and smaller scales in the Bay of Bengal. We pose the following questions:

- Given that surface forcing and background stratification vary over O(100 km), how do in-situ differences in diurnal SST respond across O(1–100 km) during DWL events?

- How do variations in salinity-driven stratification modulate lateral differences in diurnal cycles of SST and the subsurface evolution of DWLs?

To address these questions, we utilize in-situ observations from the ASIRI (Air–Sea Interactions in the Northern Indian Ocean, Wijesekera et al. 2016) and MISO-BoB (Monsoon Intra-seasonal Oscillations in the Bay of Bengal, Shroyer et al. 2021) field campaigns conducted in 2015 and 2019 respectively. We also employ a one-dimensional turbulence model

to examine the effects of salinity stratification on variability in diurnal SST amplitudes and DWL evolution. In Section 2.2, we describe the remote sensing and observational datasets, methods and models used in this chapter. Next, we describe the comparison of lateral variability in diurnal SST amplitudes from remote sensing and surface drifters as well as mooring triad network (Section 2.3). Then we describe the in-situ differences in diurnal cycles and investigate the role of salinity stratification (Section 2.4, 2.5). We additionally show an example of how differences in salinity stratification over O(30 km) length creates differences in the vertical evolution of Diurnal Warm Layers (Section 2.6). The broader implications of this research are discussed in Section 2.7, with a summary of chapter's findings in Section 2.8.

2.2 Data and methods

2.2.1 Data sources

ASIRI field campaign in 2015

Forty-six surface drifters (Figure A.1, see Appendix A.1.1 for their technical details) drogued at 15 m depth were deployed in the Northern Bay as a part of ASIRI (Wijesekera et al., 2016; Hormann et al., 2016). Deployed in ten groups of four to five drifters each, they were released along the periphery of a mesoscale cyclonic eddy and in proximity to a pronounced salinity front (see Figure-1a,b in Essink et al. 2019). This arrangement resulted in drifter pair separations ranging from 0.5 to 30 km. The drifters measured the surface temperature at 0.2 m depth and salinity at 0.5 m depth (with an accuracy of 0.05°C and 0.003 g/kg respectively). The drifters sampled every 5 minutes during the field campaign (23 August–21 September 2015), and every 30 minutes thereafter. More details on deployment and the quality control can be found in Hormann et al. (2016) and Essink et al. (2019). This chapter uses drifter data from September to November 2015, covering the Fall Intermonsoon and Northeast Monsoon seasons (based on season classifications in Weller et al. 2019).

A triad mooring network in the northern Bay of Bengal collected simultaneous atmo-

spheric and oceanographic data during 2015, spanning all the seasons (Weller et al., 2019). This network consisted of two long-term operational sites maintained by the India's National Institute of Ocean Technology (NIOT, BD08 at 18.2°N, 89.7°E and BD09 at 17.9°N, 89.7°E, Appendix A.1.2) and a third mooring deployed by the Woods Hole Oceanographic Institution (WHOI) for the ASIRI campaign at 18.0°N, 89.5°E (Appendix A.1.3). The three moorings were approximately 30 km apart (see Figure 2.1b here and Figure 2a in Simoes-Sousa et al. 2022). Further details on mooring instrumentation can be found in Appendix A.1.2- A.1.3 of this dissertation (Figures A.2, A.3 and Table A.1).

MISO-BoB field campaign in 2019

Thirty surface drifters were deployed about 300 km off the Indian coast in the western side of the Bay of Bengal during the MISO-BoB field campaign (06 July to 04 August 2019, which span the Summer Monsoon period, Local time = UTC + 5.5 hours). Initially spaced 20 km apart, these drifters were similar to those used in 2015 (Figure A.1, Appendix A.1.1) but lacked surface salinity sensors (Figure A.5). The drifters mostly followed a mesoscale anticyclonic eddy (indicated by letter A in Figure A.5) and measured surface temperature and sea level pressure (SLP) every 15 minutes.

Additionally, three Drogued-Buoy Air Sea Interaction Systems (D-BASIS*; referred to as D1, D2 and D3), were deployed to simultaneously measure the air-sea fluxes and upper-ocean structure (Figure A.4, A.5). Each D-BASIS profiler consists of a WHOI surface buoy (similar to the 2015 mooring discussed above) equipped with meteorological sensors (Appendix A.1.3). Meteorological data were recorded at 1-minute intervals and averaged to 15-minute resolution to match that of the surface drifters. Bulk air-sea fluxes from these measurements are calculated using the COARE 3.6 algorithm (Fairall et al., 1996b, 2003). Due to a damaged radiometer on D3, SWR data from nearby D2 (initially deployed 40 km

*named in honor of the esteemed Indian oceanographer, Prof. Debasis Sengupta

away and coming as close as 20 km, Figure A.5b) was used to calculate the air-sea fluxes for D3.

Each D-BASIS profiler also carries a Scripps Institution of Oceanography (SIO) Wirewalker (Figure A.4, Appendix A.1.4 of this dissertation, Pinkel et al. 2011; Zheng et al. 2022). This wave-powered profiler continuously sampled the upper 100 m of the ocean. The Wirewalker profiler measured subsurface temperature, salinity, velocity, thermal microstructure, bio-optical properties and underwater spectral irradiance at a vertical resolution of 0.25 m. The measurements taken during the smooth upward motion of the profiler are used here. Hence, the effective time resolution between profiles was nearly 10 minutes. The D-BASIS had drag elements attached to the line at 200 m depth as to ensure that it drifted at a typical speed of 0.2-0.3 $\mathrm{m\,s^{-1}}$ with currents, thereby maintaining one-dimensional sampling most of the time (see Appendix A.1.4 and Appendix A.4 for details). For the analysis using drifters and D-BASIS profilers from this field campaign, we restrict the data to the period between 07 and 28 July 2019.

Spatial variability in the central Bay was assessed using a rapid profiling shipboard system FastCTD (e.g., MacKinnon et al., 2021). It profiles the temperature and salinity in the upper 200 m while the ship moves at 2-5 knots. The vertical resolution of the FastCTD dataset was 1 m and each profile took 1.5 minutes to complete, giving a typical horizontal resolution of 210 m.

2.2.2 Remote sensing

We use daily SST data from the Advanced Microwave Scanning Radiometer 2 (AMSR-2; https://www.remss.com/missions/amsr/) aboard the AQUA satellite. This satellite operates in a sun-synchronous orbit with a 1:30 AM/PM equator crossing time. The daily version of AMSR-2 provides SST measurements at an effective resolution of 46 km (despite being gridded on a 25 km scale, Wentz et al. 2014b). Daytime and nighttime satellite passes

from September to November 2015 and from July to August 2019 are used to infer the diurnal SST amplitude.

In order to distinguish the role of rainfall-induced stratification and mesoscale-structured stratification, we use data from IMERG (Integrated Multi-satellitE Retrievals for Global precipitation measurement, https://gpm.nasa.gov/data/imerg, Huffman et al. 2015) for 17 and 18 July 2019. This dataset has a time resolution of 30 minutes and a spatial resolution of 10 km.

2.2.3 Models

The General Ocean Turbulence Model (GOTM) provides a one-dimensional ocean model framework that includes various vertical mixing schemes (Burchard et al., 1999). GOTM also provides flexibility to choose the stability functions, wave breaking and internal wave parameterizations. GOTM with the $k-\epsilon$ mixing scheme (which involves a subgrid-scale kinetic energy (k) and the subgrid dissipation (ϵ) parameterization, with both variables evolved using separate prognostic transport equations) has been used in previous studies to accurately model the diurnal variability in SSTs, thermal stratification, salinity and Turbulent Kinetic Energy (TKE) dissipation rate (Pimentel et al., 2008; Johnson et al., 2023; Burchard and Bolding, 2001; Drushka et al., 2016; Burchard et al., 2002; Schmitt et al., 2024). We use the two-equation $k-\epsilon$ turbulence closure scheme with the dynamic dissipation rate length scale along with the Canuto A version of the stability function (Canuto et al., 2001). With the exception of the omitted internal wave breaking parameterization, all other settings align with GOTM's default options (see Burchard et al. 1999. Each GOTM simulation is performed for a 24-hour period and is initialized at sunrise. The vertical and temporal resolution for GOTM runs are 0.05 m and 1 minute respectively. The prescribed surface forcing conditions and optical properties of water vary across cases and are detailed in Sections 2.5 and 2.6.

2.2.4 Methods

Quantifying the diurnal SST amplitudes

Diurnal SST amplitude from remote sensing is estimated as the difference in SSTs between daytime and nighttime passes. The drifter measurements are synchronized with the satellite pass times to enable direct comparison between remote sensing and in-situ drifters.

For the in-situ analysis, we quantify the diurnal SST amplitude by using the concept of foundational temperature (T_f, Donlon et al. 2007; Prytherch et al. 2013). T_f is defined as the temperature just before sunrise for each day (6 am to 6 am the next day) and for each drifter/D-BASIS profiler/Mooring. Linear interpolation between the T_f points is performed to create a continuous T_f trend. This trend would account for heating/cooling for time scales larger than diurnal. The diurnal SST amplitude is then calculated as the peak difference between the SST and T_f over midday hours (e.g., 12:00–15:00 local time).

Classification of DWL conducive days based on observations

Identifying DWLs typically requires well-resolved vertical profiles of temperature, stratification, and shear (e.g., Thompson et al., 2019), such as those provided by the D-BASIS profilers (see Appendix A.2). However, detailed vertical profiles are lacking in both platforms: surface drifters provide measurements only at the surface, and the triad mooring network offers limited vertical resolution, with sensors spaced 4–10 m apart. To address this limitation, we follow Thompson et al. (2019) and use a threshold-based classification scheme to identify DWL-conducive (DWL-C) days at the triad moorings. Specifically, DWL-C days are classified as those with mean wind speeds below 6 $\mathrm{m\,s^{-1}}$ (measured at 3 m height) and peak shortwave radiation (SWR) exceeding 750 $\mathrm{W\,m^{-2}}$. Conversely, other days not meeting these criteria are classified as DWL-NC (not conducive to DWL formation).

These thresholds are based on both our D-BASIS observations (Appendix A.2) and limits

established in prior studies (Thompson et al., 2019), and are consistent with conditions favorable for DWL formation in past work (Prytherch et al., 2013; Hughes et al., 2020a,b, 2021). For drifters, which do not measure wind or surface fluxes directly, we assign DWL-C or DWL-NC classifications based on the periods identified at the Triad moorings and D-BASIS (as long as drifters are within a 1000 km radius of the Triad mooring/D-BASIS). This assumption is supported by the broad spatial extent of DWLs (e.g., Bellenger and Duvel, 2009).

Metric for DWL deepening depth

We use the depth of the maximum temperature gradient ($z_{T_{zmax}}$) to determine the depth of the DWL from the observations in D-BASIS profilers and GOTM simulations (Hughes et al., 2020b). This method is used because the temperature is well-resolved vertically in these datasets, thereby allowing its vertical gradient (T_z) to be treated as a continuous quantity. This parameter cannot be tracked in the 2015 triad mooring network due to its vertically discrete temperature measurements.

2.3 Comparison of remote sensing and drifters in capturing lateral variability in diurnal SST amplitude

In-situ observations from moorings and drifters are often unavailable over mesoscale length scales (O(100 km)) in the Bay, highlighting the value of remote sensing for capturing lateral differences in diurnal SST. To assess the accuracy of AMSR-2 in resolving these patterns, we compare the AMSR-2 diurnal SST magnitudes with drifters and the triad mooring network during September–November 2015 (after spatially interpolating the satellite data to the drifter/mooring locations).

Overlaying in-situ diurnal SST magnitude variations onto AMSR-2 maps for a specific day (in this case, 26 September 2015) reveals a general agreement (Figure 2.1a). However, a closer examination of the in-situ data (within the boxes in Figure 2.1a) reveals contrasts in diurnal

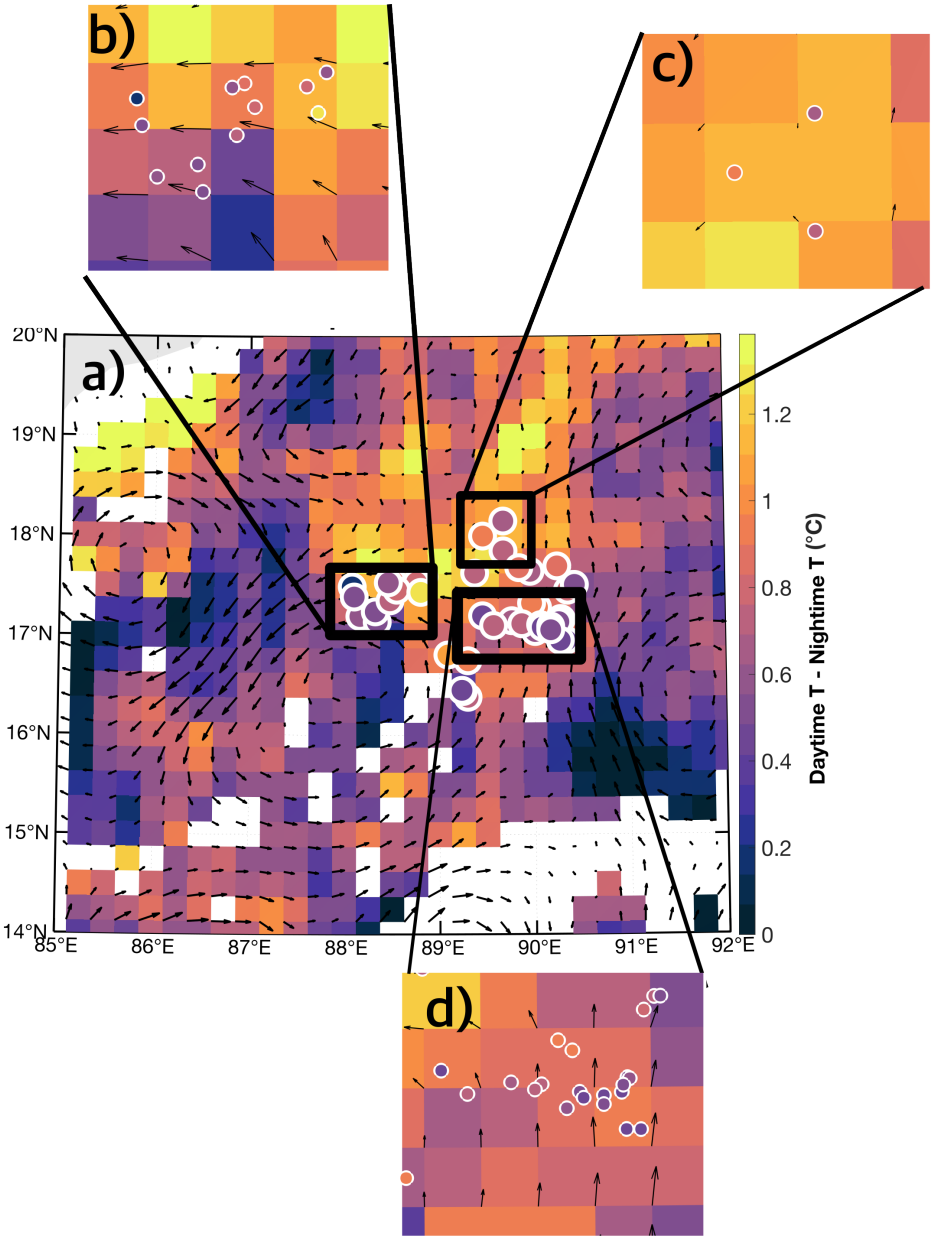

Figure 2.1: (a) Difference between daytime and nighttime temperatures on 26 September 2015 from AMSR-2, with colored circles denoting the same quantity from in-situ drifters and the triad mooring network. (b), (c), (d) Zoomed views of regions within the boxes in (a). Black arrows indicate the geostrophic currents on 26 September 2015, while the white points in (a) indicate missing data.

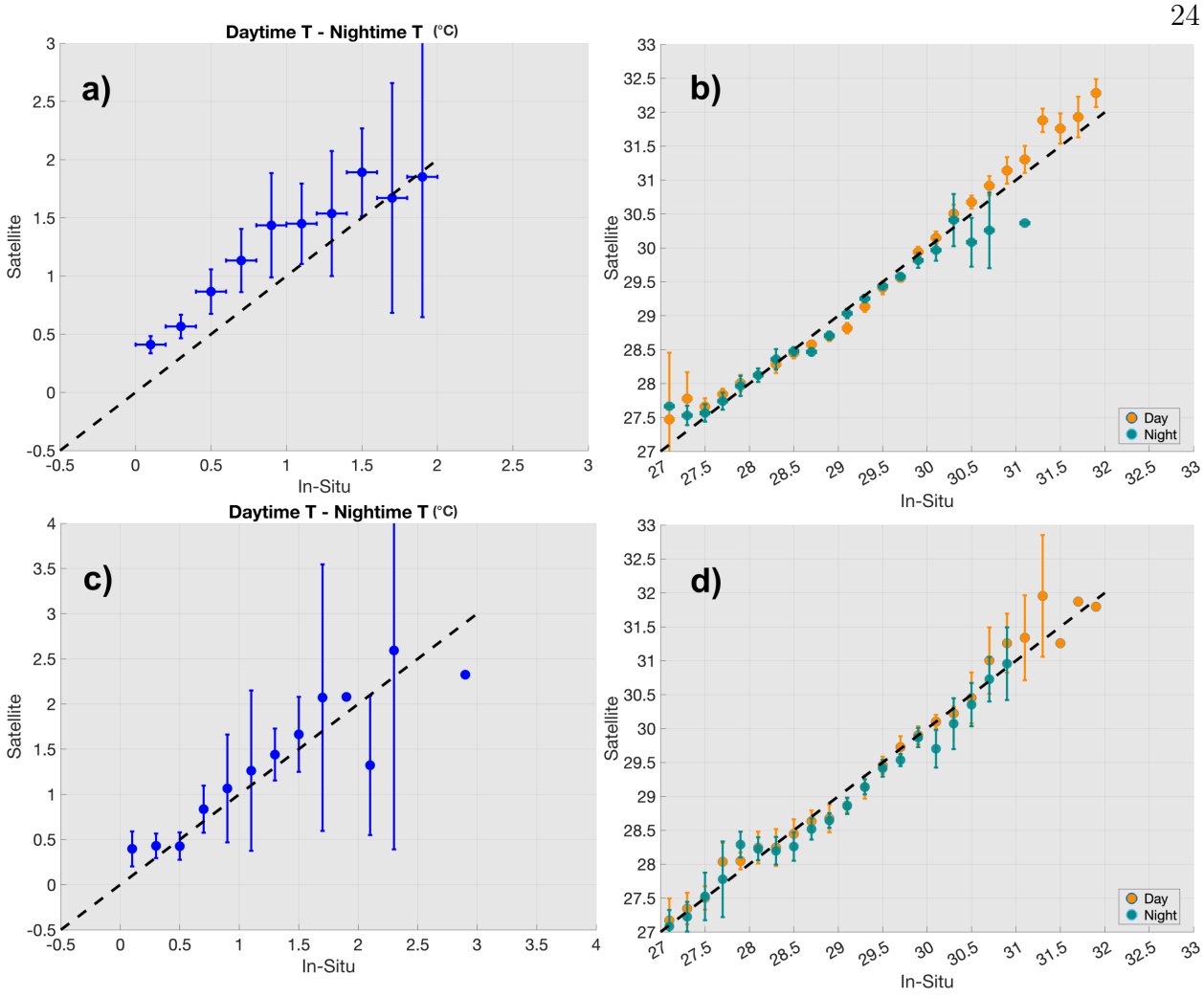

Figure 2.2: (a) Detailed comparison of differences in daytime and nighttime temperature from in-situ drifters and corresponding remote sensing measurements from 01 September to 30 November 2015 and 06 July to 04 August 2019. (b) Comparison of daytime (orange) and nighttime (green) temperatures over the same period as (a). The dashed lines in (a) and (b) indicate the line of equality. The vertical error bars indicate three standard deviations of the satellite measurements within the bin while the horizontal error bars indicate the accuracy of in-situ estimates. (c) and (d) are the same as (a) and (b) except for in-situ triad mooring network between 01 January and 31 December 2015. NOTE: Horizontal error bars (errors in in-situ observations) are not visible in panels (b)–(d) because they are smaller than the marker size.

SST magnitudes at grid scales smaller than AMSR-2's spatial resolution, showing differences as high as 0.4 °C (Figure 2.1b,c,d). This demonstrates significant lateral differences in diurnal SST magnitudes over mesoscale and smaller length scales (50 km or less).

To extend our comparison, we analyzed SST and diurnal SST magnitudes from AMSR-2, contrasting them with in-situ observations from drifters and the triad mooring network. We observe that satellite-derived diurnal SST magnitudes are consistently higher than in-situ values by approximately 0.2–0.3°C. These discrepancies increase up to 0.5°C for drifter observations on days with strong diurnal warming (greater than 1.5°C, Figure 2.2a,c). These larger in-situ magnitudes are also associated with greater uncertainty in the satellite estimates. A binned scatter plot of daytime and nighttime temperatures from the two sources shows that many differences are linked to offsets in absolute daytime and nighttime values, particularly for in-situ daytime temperatures below 27.5 °C and nighttime temperatures above 30 °C (Figure 2.2b,d). Potential sources of such discrepancies include the difference in measurement depth (where the drifters measures the bulk temperature while AMSR-2 measures the skin temperature of the ocean) as well as presence of lateral differences in diurnal cycles of SST over mesoscale and smaller length scales. Preliminary tests using skin-layer models like POSH (Profiles of Surface Heating, Gentemann et al. 2009) and F96 (Fairall et al., 1996a) indicate that depth-related differences account for only O(0.05 °C) of the observed offsets, reinforcing the role of lateral SST differences at smaller spatial scales that cannot be resolved by coarse-resolution remote sensing. Building on these findings, we next analyze the in-situ diurnal SST magnitudes from the 2015 and 2019 field campaigns, classifying them into DWL-C and DWL-NC days.

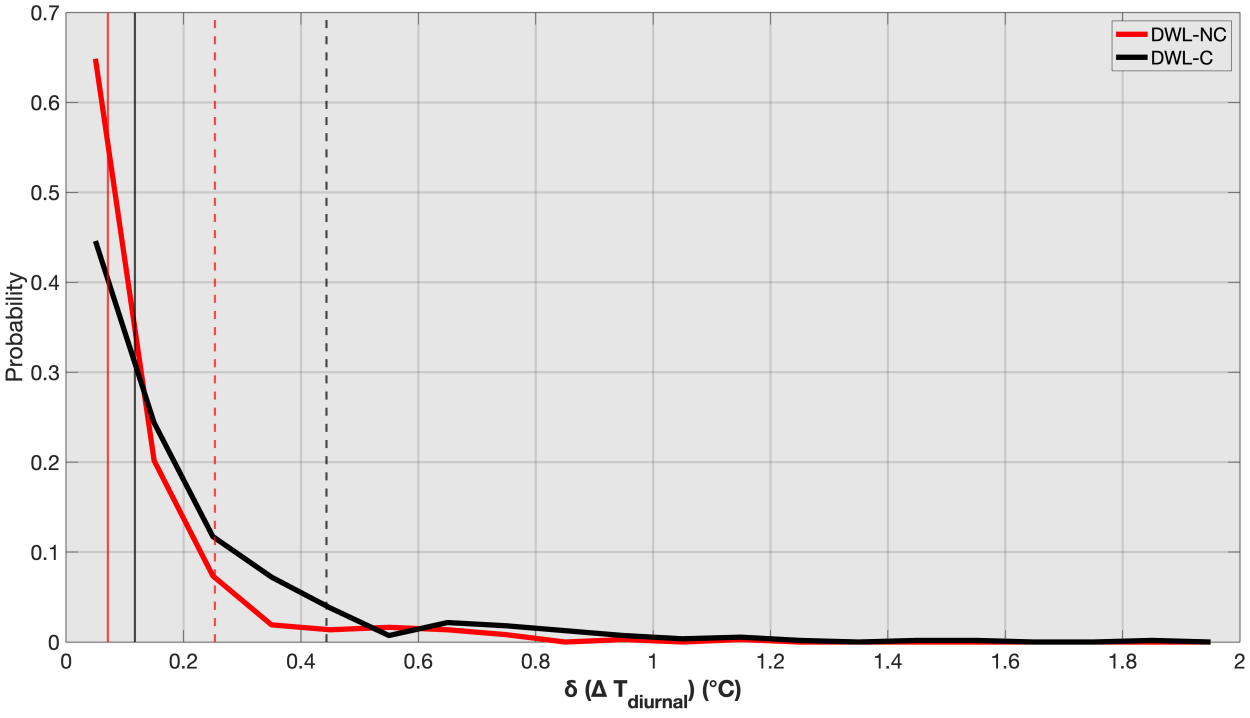

Figure 2.3: Probability Distribution Function (PDFs) of spatial differences in diurnal SST magnitudes from the triad mooring network for DWL-NC days (red line) and expected DWL-C days (black line). The corresponding vertical solid lines indicate the median values while the dashed lines indicate the 90th percentile values for the DWL-NC and DWL-C days.

2.4 In-situ observations of diurnal SSTs and their lateral differences in presence and absence of DWLs

Using the previously defined thresholds, we identify 188 DWL-C days in the triad mooring network during 2015. While the probability distributions of lateral differences in diurnal SSTs for DWL-C and DWL-NC days from the triad mooring network are broadly similar (Figure 2.3), the lateral differences below 0.1°C are less likely to occur on DWL-C days (45%) than on DWL-NC days (65%). The median lateral difference is 0.11°C for DWL-C days, compared to 0.07°C for DWL-NC days. Notably, the 90th percentile values for differences in

diurnal SST magnitudes for DWL-C and DWL-NC days are 0.48°C and 0.28°C respectively. This indicates that spatial inhomogeneity in diurnal SST is more pronounced during DWL-C days. However, this result is based on a limited dataset (nearly 1000 data points) with a fixed spatial separation (30 km), despite its year-round coverage.

We conduct similar analysis using larger set of observations from drifters in 2015 and 2019 (approximately 11000 and 1200 data points respectively) that spanned different seasons to investigate mesoscale and sub-mesoscale variability. These observations are binned by lateral differences in diurnal SST magnitudes and drifter separation (Figure 2.4). During DWL-NC days, the lateral differences in diurnal SSTs remain relatively uniform (0.05°C median and 0.1°C 90^{th} percentile values) across 0 to 100 km separation in both years (Figure 2.4). In contrast, DWL-C days exhibit stronger lateral variability in diurnal SST magnitudes. Median differences are approximately 0.2 °C and increase with separation (Figure 2.4). The 90^{th} percentile values during DWL-C days also show greater variability. In 2019, differences of around 0.4°C over 20 km and about 0.8°C over 50–100 km are observed (Figure 2.4b). The differences of about 0.8°C over 20 km and up to 1.4°C over 100 km are observed in 2015 (Figure 2.4a). This points to enhanced spatial inhomogeneity in diurnal SSTs during DWL events.

To test the hypothesis that lateral differences in salinity stratification influences diurnal SST variability, we use salinity differences between drifter pairs (with separation distances under 100 km) as a proxy for stratification differences and analyze their relationship with diurnal SST differences. We observe salinity differences up to $2\,\mathrm{g\,kg^{-1}}$ between drifter pairs, typical for the Bay of Bengal's Fall Intermonsoon given heavy rainfall and river runoff (e.g., Sree Lekha et al., 2018). Despite these large salinity differences, the median and 90^{th} percentile diurnal SST differences increase only by about 0.1–0.2°C with increasing salinity stratification, regardless of DWL presence (Figure 2.5). This result aligns with anecdo-

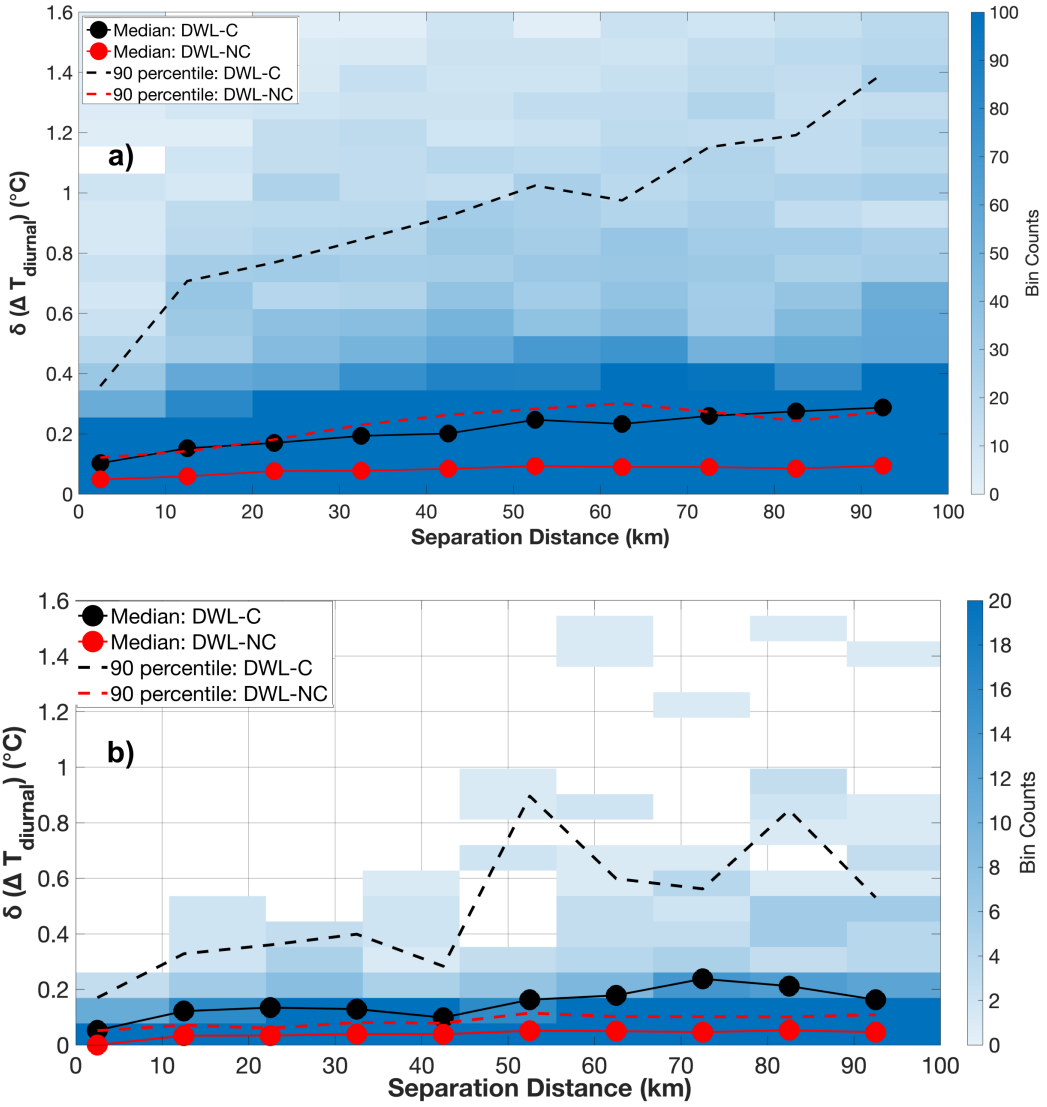

Figure 2.4: Binned scatter plot of spatial differences in diurnal SST magnitudes between drifter pairs versus their separation distances for (a) 01 September to 30 November 2015 (11,186 observations) and (b) 06 July to 04 August 2019 (1,207 observations). Color indicates the number of observations per bin (every 10 km and 0.1°C). Solid lines with circle markers show the median values in each separation-distance bin, separated into DWL-C days (black) and DWL-NC days (red). Dashed lines indicate the 90$^{\text{th}}$ percentile values in each bin.

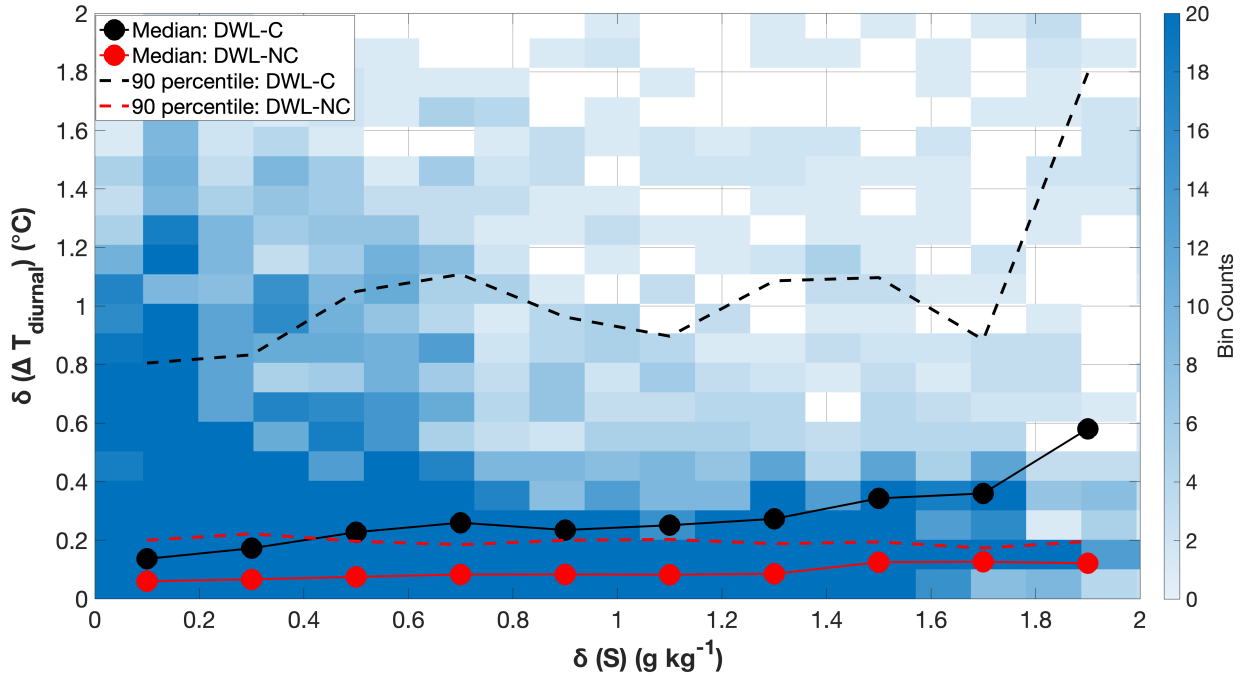

Figure 2.5: Binned scatter plot of spatial differences in diurnal SST magnitude in drifter pairs separated by less than 100 km against the in-situ surface salinity differences (as a proxy for differences in vertical salinity stratification) for 01 September to 30 November 2015. Color indicates the number of observations per bin (every 0.1 g kg^{-1} and 0.1°C). The solid line with circle markers indicate the median values in each bin of salinity difference, segregated into DWL-C days (black) and DWL-NC days (red). The dashed lines indicate the 90$^{\text{th}}$ percentile values in each bin.

tal values from Shroyer et al. (2016), though it is lower than estimates from other studies (Soloviev and Lukas, 1997; Moulin et al., 2021).

Our observations indicate that lateral differences in salinity stratification account for the magnitude of median diurnal SST differences (black solid lines in Figure 2.4). However, the contribution of salinity stratification in diurnal SSTs fall short of accounting for the observed extreme values in diurnal SST differences (black dotted lines in Figure 2.4). This suggests contributions from other factors (e.g., heat flux variability, wind, ocean optical properties), which are not measured by drifter observations.

However, these unmeasured variables by drifter may also introduce uncertainty in the binned relationships shown in Figure 2.5. In order to isolate the role of salinity stratification on diurnal SSTs, we next use the one-dimensional GOTM model to systematically assess its impact on diurnal SST response differences.

2.5 Exploring the influence of salinity stratification on diurnal SST variability

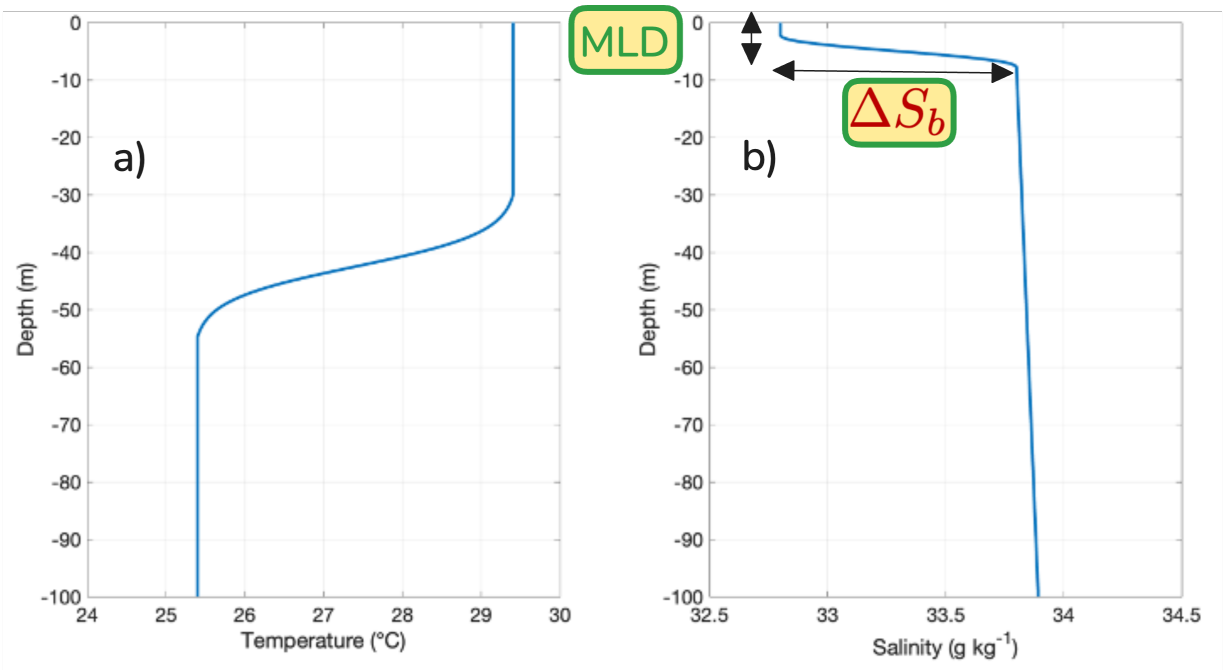

Figure 2.6: Initial vertical profiles of (a) temperature and (b) salinity for GOTM parameter space exploration. The stratification in the initial profiles is controlled using the Mixed layer depth (MLD) and the change in salinity at the base of mixed layer (Δ S_b).

GOTM simulations are initialized with temperature and salinity profiles based on D-BASIS observations (Figure 2.6, discussed more in Section 2.6) to explore the influence of salinity stratification on diurnal SSTs. Salinity control of the upper ocean stratification is achieved through the initial MLD at sunrise and the initial salinity change at the base of the

MLD ($\triangle S_b$) illustrated in Figure 2.6b. GOTM simulations are forced with diurnally varying solar radiation peaking at 1000 $\mathrm{W\,m^{-2}}$ (based on Renner et al. 2019), with constant cooling components of the heat flux (i.e., longwave radiation, latent heat flux, and sensible heat flux, which typically cool the Indian ocean) and wind speeds over a 24-hour run. We explore the parameter space by varying the initial MLD (2-15 m), $\triangle S_b$ (0-1 $\mathrm{g\,kg^{-1}}$), net heat flux (0, 33 and 123 $\mathrm{W\,m^{-2}}$, achieved by adjusting the cooling components) and wind speeds (3-6 $\mathrm{m\,s^{-1}}$). We also vary the optical properties by using theoretical Jerlov-I absorption profile (Paulson and Simpson, 1977) and an observed absorption profile derived from D-BASIS irradiance measurements (Schlosser et al., 2022).

For a representative case (net heat flux of 123 $\mathrm{W\,m^{-2}}$, Jerlov-I water type, 6 $\mathrm{m\,s^{-1}}$ winds), we observe little variation in diurnal SST for deeper initial MLD and weaker $\triangle S_b$ (Figure 2.7a). However, the sensitivity of diurnal SST magnitude to $\triangle S_b$ is relatively stronger for shallow MLDs between 2 and 4 m, with differences of O(0.1°C). We fix the initial MLD to 4 m (where stratification-driven variability is strongest) to assess how changing net heat flux and wind speed affect diurnal SST's dependence on stratification. As expected, diurnal SST varies with heat fluxes and wind speeds (0.57 °C to 1.2 °C). However, the lateral differences in diurnal SST due to the salinity stratification variations are within a range of 0.07 °C to 0.15 °C (Figure 2.7b).Varying optical properties has a relatively minor effect on this sensitivity (Figure 2.7c).

Our modeling results suggest that lateral variations in salinity stratification can explain the median diurnal SST differences observed by drifters during DWL days, assuming minimal lateral variations in winds and heat fluxes over these scales (given that MLDs shallower than 10 m are a common feature in the Bay, e.g., Weller et al. 2019). However, the larger differences in diurnal SST in Figure 2.4 likely reflect combined effects of spatial variability in stratification, optical properties, wind speed, net heat flux, and cloud cover, all of which

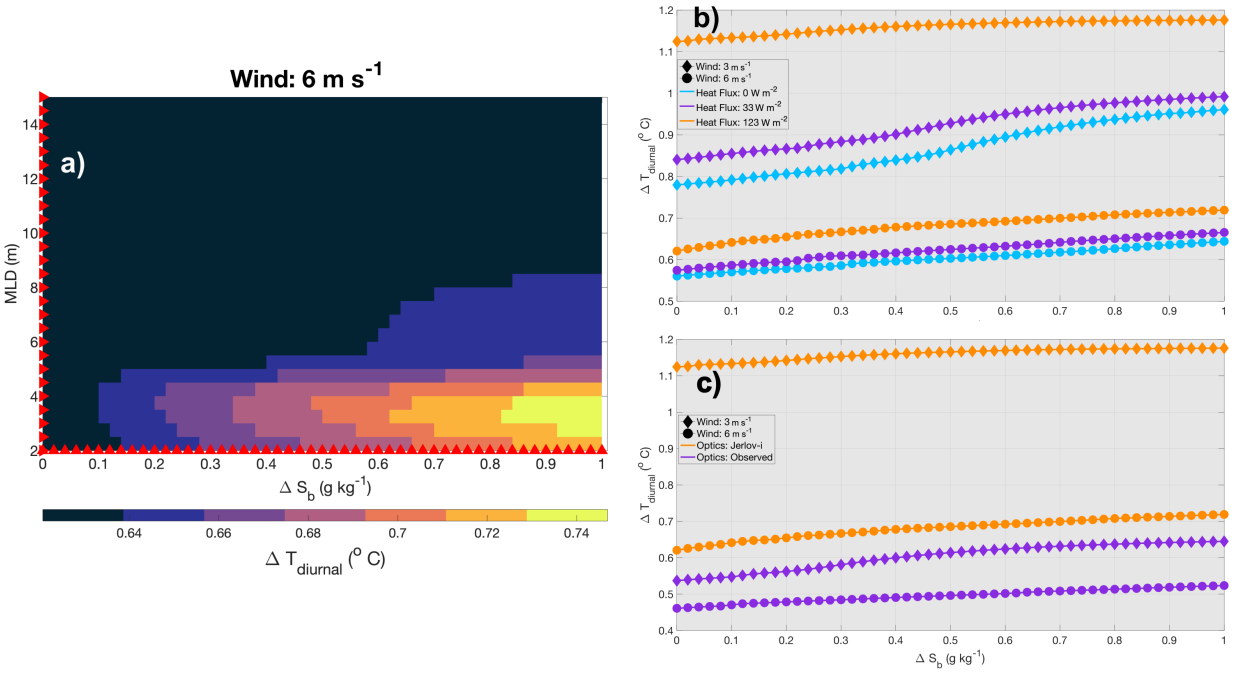

Figure 2.7: (a) Diurnal SST magnitude from GOTM as a function of change in salinity at the base of mixed layer ($\triangle S_b$, in x-axis) and initial MLD (y-axis) for a diurnally varying clear sky day with wind speed of 6 m s^{-1} and mean heat flux of 123 W m^{-2} (based on a single day of simulation). (b) Diurnal SST magnitude as a function of initial change in salinity at the base of mixed layer of 4 m ($\triangle S_b$) for different wind speeds (diamond and circle markers for 3 m s^{-1} and 6 m s^{-1} scenarios respectively) and daily mean heat fluxes. (c) is same as (b) but for varying wind speed and optical properties. The mean heat flux in this case is 123 W m^{-2}.

can vary on mesoscale and smaller length scales. The next section uses a D-BASIS example to illustrate how lateral stratification differences can shape subsurface DWL evolution.

2.6 Impact of differences in salinity-driven stratification on the vertical evolution of DWLs

The subsurface temperature profiles at D2 and D3 illustrate the DWL formation in the morning and their subsequent mixing by late afternoon during 18-22 July 2019 (Figure 2.8b,e). The DWL presence correlates with elevated daytime stratification (N^2) and shear (S), with

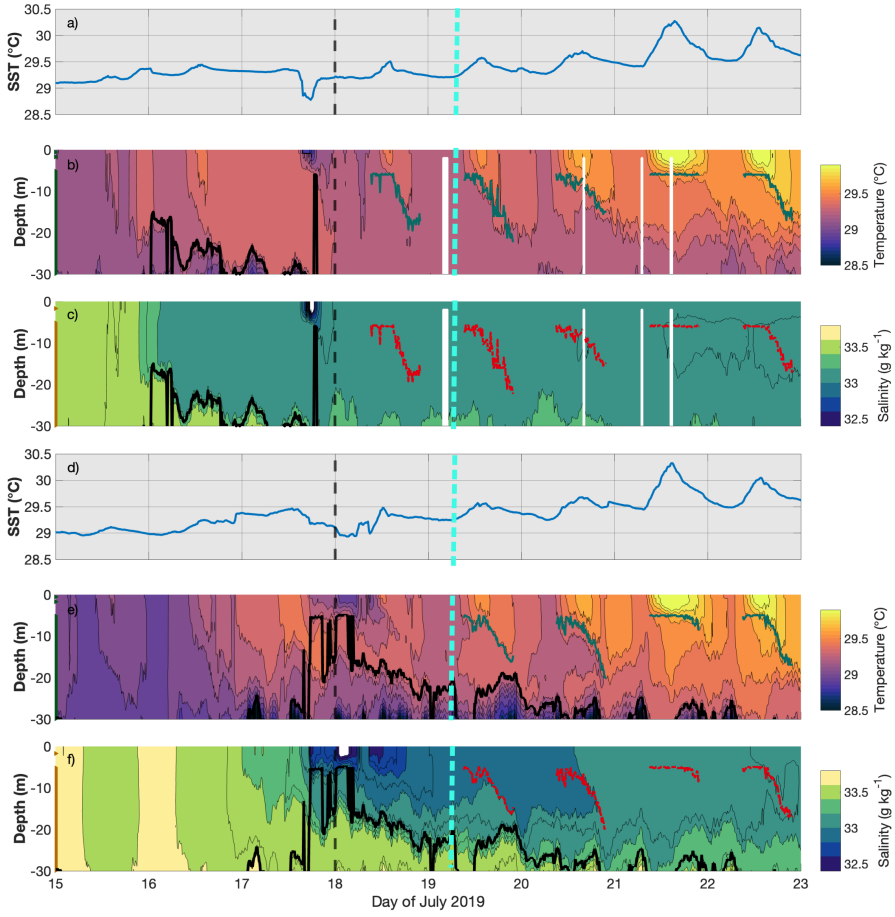

Figure 2.8: (a) Observed SST for D2, (b) observed temperature and (c) salinity at D2 from 15-22 July 2019. The measurements from the surface buoy are included in panel (b) and (c) as they were measured at 0.55 m and 1.7 meter depth. The green lines in panel (b) as well as the red lines in panel (c) indicate the DWL depth. The thick black lines in panels (b) and (c) indicate the seasonal pycnocline depth (where N^2 is greater than 5×10^{-4} s^{-2}). The markers at the left end of the panels (b) and (c) indicate the depths where the measurements were taken (continuous set of markers reflect the high resolution data density of the wirewalker below 5 m). The panels (d), (e), (f) are similar to panels (a), (b), (c) respectively for D3. The black dashed vertical lines in panels (a)–(f) indicate the beginning of the DWL period during the 2019 field campaign (see Appendix A.2), while the cyan dashed line marks the model initialization time in Figure 2.9. All time series are shown in local time (IST).

N^2 up to two orders of magnitude and S up to one order of magnitude higher than on non-DWL days (Figure A.8b,d,e).

Despite their proximity (20-40 km, Figure A.5b) and similar surface forcing (wind speeds and heat fluxes, Figure A.6), D2 and D3 exhibit notable differences in DWL evolution (Figure 2.8b,e). A primary example is the vertical evolution of DWLs on 19 July 2019, which significantly differs due to variations in pre-existing salinity stratification between the two sites (Figure 2.8c,f). The average stratification over the top 15 m at sunrise (pre-DWL) is two orders of magnitude higher at D3 (1.23×10^{-4} s^{-2}) compared to D2 (2.12×10^{-6} s^{-2}, Figure 2.9a). Correspondingly, the MLD at sunrise (using the $0.125\,\mathrm{kg\,m^{-3}}$ density criterion) differs by about 20 m between D3 and D2 (15 m and 35 m respectively). The contrast in pre-existing stratification before the DWL evolution at D2 and D3 (Figure 2.8) arises from a combination of mesoscale-structured stratification as well as the cold pool event (Appendix A.3).

Despite notable differences in pre-existing stratification, D2 and D3 exhibit similar diurnal SST magnitudes of 0.34 °C. This outcome is consistent with our parameter space exploration (Section 2.5), which indicates that the MLDs at D2 and D3 are beyond the range where stratification strongly influences diurnal SST cycles. However, the stronger pre-existing stratification at D3 causes DWL depths to be shallower by about 8 m compared to D2 (Figure 2.9b). This suggests that pre-existing background stratification below the DWL primarily limits its vertical evolution through shear-driven mixing, thereby trapping the DWL to a shallower depth (see Appendix A.4 for further details on the validity of the 1-D DWL evolution in the enhanced stratification case, and Appendix A.5 for additional discussion on the impact of enhanced stratification on the TKE budget).

Idealized one-dimensional GOTM simulations, using initial profiles and surface forcing from D2 and D3, along with optical properties based on irradiance measurements from the

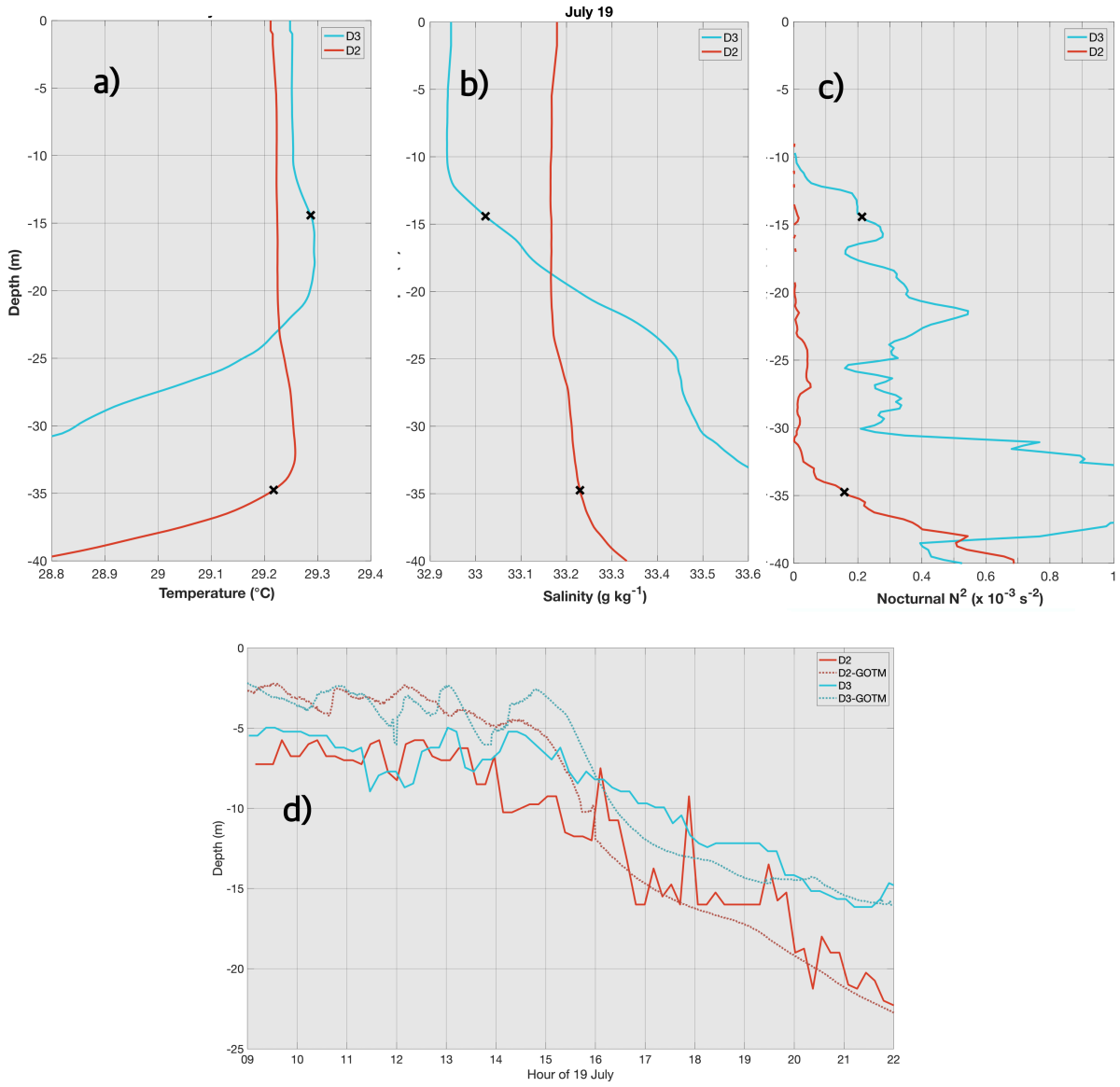

Figure 2.9: (a) Temperature, (b) salinity, (c) stratification profiles observed at D2 (red) and D3 (blue) just before sunrise on 19 July (cyan line in Figure 2.8). The two "x" marks indicate the respective MLDs based on the $0.125\,\mathrm{kg\,m^{-3}}$ criteria (Monterey and Levitus, 1997). (d) Solid lines indicate the observed DWL depths at D2 and D3, while the dashed lines indicate the DWL depths from the corresponding GOTM simulations on 19 July 2019. Time series are shown in local time (IST).

D-BASIS (Schlosser et al., 2022), successfully estimate the final DWL depth (Figure 2.9b). However, the finer details of DWL evolution cannot be compared. In the morning, the simulated DWLs are often shallower than the 5 m observational limit for the temperature gradient observations (used to track the DWL evolution). Although the DWL deepens in the afternoon, the coarser vertical resolution (0.25 m) of observations limits direct comparison with the model's finer vertical structure.

Beyond pre-existing stratification differences, another example of varied DWL evolution between D2 and D3 stems from the advection of a rain lens (see Appendix A.3 of this paper; also Drushka et al. 2016). The DWL at D2 deepens steadily in a typical one-dimensional evolution to 20 m on 18 July 2019. The DWL at D3 in contrast remains confined above 5m due to stratification from the advected rain lens (see Appendix A.3), and a subsurface warm layer develops (Figure 2.8d,e).

These observations collectively highlight how spatial variability in background stratification, rainfall and the advection of the resulting lens can lead to lateral differences in DWL evolution. Such differences cause lateral variability in upper ocean heat content and vertical mixing, consequently leading to lateral disparities in subsequent DWL evolution, air-sea feedback, and interfacial fluxes.

2.7 Discussion

The results presented here show ubiquitous lateral differences in diurnal SST magnitude of average magnitude 0.1-0.2°C over scales as small as O(10 km). Our results also indicate that lateral diurnal SST differences are slightly larger on DWL conducive days than on non-conducive days. While solar insolation, wind speeds, and optical properties of water are known drivers of diurnal SST and DWL differences (e.g., Webster et al., 1996; Ohlmann, 2003; Pimentel et al., 2019), our results show that variations in background salinity stratification (unique to regions like the Bay of Bengal) also play a key role. This result is consistent with

anecdotal examples in Shroyer et al. (2016). Although other studies report more drastic differences due to shallow freshwater lenses (e.g., Soloviev and Lukas, 1997; Moulin et al., 2021), our idealized one-dimensional GOTM simulations produce diurnal SST differences similar to those observed in the Bay of Bengal. These differences emerge only when the initial MLD (prior to DWL formation at sunrise) is shallow. However, such models may underestimate these values as Johnson et al. (2023) showed that one-dimensional turbulence closure models overestimate vertical entrainment at the base of the mixed layer on DWL days compared to Large Eddy Simulations (LES). To better constrain the role of salinity stratification in diurnal cycles of SST, longer-term co-located measurements of meteorological variables, diurnal cycles of SST, and ocean boundary layers, as well as analyses of high temporal and vertical resolution mooring records are needed.

D-BASIS observations from the 2019 field campaign reveal significant variations in background stratification over approximately 30 km. These variations play a key role in driving lateral differences in sub-surface evolution of DWLs, which affect vertical heat distribution and can trigger submesoscale processes (Bogdanoff, 2017). In addition to background stratification, lateral advection processes can cause lateral differences in DWLs (e.g. 18 July 2019 case). The advection could be caused by lateral slumping of fronts due to submesoscale processes, differential advection or the profiler moving into a watermass of different stratification. Previous work has shown the existence of strong diurnal variations in the velocity shear near fronts (Dauhajre and McWilliams, 2018; Johnson et al., 2020b) which further impact the stratification (Johnson et al., 2020a) and potentially influence the DWL evolution. Isolating these types of stratification changes using D-BASIS is difficult due to the inherent space-time aliasing.

DWLs are shown to be a regular feature in this region, with 188 DWL-C days recorded in 2015 (from the mooring records). Some of the DWL-C days discussed here were also during

the months of June to September (36 times in the year 2015), signaling their occurrence even when the monsoon season is prevalent in the Bay.

Modulation of air-sea fluxes and atmospheric convection by DWLs has traditionally been studied using a one-dimensional framework (e.g., Bellenger et al., 2010; de Szoeke et al., 2021; Clayson and Bogdanoff, 2013). However, SST fronts influence atmospheric convection variability and create secondary circulations within the Marine Atmospheric Boundary layer (MABL, e.g., Sullivan et al. 2020, 2021; Skyllingstad et al. 2007). Our observations of horizontal variability in DWLs further motivates the recent systematic modeling studies extending beyond laterally homogeneous coupled LES studies of Sullivan et al. (2025), incorporating multi-scale coupling between laterally variable DWLs and overlying MABL dynamics.

2.8 Conclusions

Remote sensing combined with in-situ observations reveals significant lateral differences in the diurnal SST amplitudes across a diverse range of sub-basin length scales in the Bay of Bengal. Using the day-night passes of the satellite AMSR-2, we observe differences of O(1°C) in the diurnal SST amplitude over mesoscale length scales of O(100 km) or larger. However, remote sensing poorly resolves the lateral differences in diurnal SSTs when compared to a dense network of surface drifters and a mooring triad. The underestimation in lateral diurnal SST differences is especially pronounced in extreme cases where in-situ values reveal differences as high as 2°C. Using the meteorological conditions from the mooring triad network to identify the conducive days for Diurnal Warm Layers (DWLs), we find that the lateral differences in diurnal SST amplitudes are larger on DWL conducive days (0.12°C median, 0.48°C 90^{th} percentile) when compared to the non-conducive DWL days (0.07°C median, 0.27°C 90^{th} percentile). Data from a dense network of surface drifters deployed during the 2015 and 2019 field campaigns show similar trends over length scales of 1–100

km. On DWL days, median lateral diurnal SST differences range from 0.05 °C to 0.2 °C, with 90^{th} percentile values ranging from 0.2 °C to 1.4 °C. These ranges are smaller for non-DWL days, with the median differences ranging from 0.05 °C to 0.1 °C and 90^{th} percentile values between 0.1 °C to 0.2 °C. Drifters equipped with surface salinity sensors further reveal that increasing lateral differences in surface salinity (a proxy for stratification differences) led to increasing lateral differences in diurnal SSTs by about 0.2°C, regardless of DWL presence.

We use idealized one-dimensional modeling to explore how diurnal SST amplitude varies with initial MLD and salinity stratification, under different wind speeds, optical properties, and heat fluxes. Our simulations confirm that the impact of salinity stratification on the diurnal SST amplitude is about 0.07 °C to 0.15 °C, but only for very shallow MLDs (less than 8 m). This indicates that lateral variability in salinity-driven stratification (especially with shallow MLDs in the Bay) can substantially modulate diurnal warming.

Deployment of two D-BASIS profilers across several consecutive days in the Bay reveals the presence of lateral variability in the subsurface evolution of DWLs over a separation of roughly 30 km. As expected, lateral advection modifies the DWL behavior and creates lateral differences in the penetration of the DWLs by 5-10 m. Additionally, lateral disparities in pre-existing stratification over O(30 km) drove significant sub-surface DWL variability. For instance, D3 exhibited a shallower DWL depth compared to D2 due to enhanced stratification driven by mesoscale-structured stratification differences on 19 July (before the formation of DWLs). These DWL differences affect the vertical distribution of heat within the upper ocean.

In summary, this chapter quantifies lateral differences in diurnal SSTs over submesoscale and smaller mesoscale lengths, and highlights the role of differences in salinity stratification in driving these differences. Our results from this chapter show that variations in salinity stratification alone cannot account for the extreme differences in diurnal SST amplitudes at

these scales. These extreme differences in diurnal SSTs could stem from small-scale coastal plumes causing optical property variations (McKie et al. 2024; Pimentel et al. 2019), or variations in wind speeds (Song et al., 2022) and heat fluxes (e.g., due to patchy clouds or differences in cooling components; Nuijens et al. 2024; Song et al. 2022). This chapter highlights the presence of small-scale lateral DWL variations that occur in regions with strong salinity gradients. Such salinity gradients are often unresolved in regional models (Vinayachandran and Nanjundiah, 2009), potentially leading to an underestimation of diurnal SST and DWL gradients in these model simulations.

Data availability statement

The NIOT mooring data are available at: http://do.incois.gov.in/. The WHOI mooring data from 2015 can be accessed at: http://uop.whoi.edu/projects/Bengal/QCData.html. The D-BASIS data, FastCTD data from 2019, and Surface Drifter data from 2015 and 2019 are available upon request from the lead author (Siddhant Kerhalkar) or his advisor (Amit Tandon). AMSR-2 satellite data were obtained from www.remss.com, and rainfall estimates from IMERG were obtained from https://gpm.nasa.gov/data/imerg. The geostrophic currents are derived from AVISO (https://www.aviso.altimetry.fr/), a remotely sensed altimetry product. Simulations were performed using version 6.0 of the General Ocean Turbulence Model (GOTM), available at https://gotm.net/portfolio/.

Acknowledgments

Portions of this chapter are under review by the *Journal of Physical Oceanography* coauthored by Siddhant Kerhalkar, Amit Tandon, J.Thomas Farrar, Jennifer A MacKinnon, Tamara L Schlosser, Leah Johnson, Andrew J Lucas, Verena Hormann and Luca R Centurioni The authors would like to thank US Office of Naval Research for their support to the ASIRI as well as MISO-BoB Department Research Initiative. S.Kerhalkar and A.Tandon were supported by N00014-17-1-2355, N00014-18-1-2799, N00014-19-1-2410 and

N00014-23-1-2054, J.T.Farrar by N00014-17-1-2880, T.L.Schlosser and A.J.Lucas by N00014-17-1-2391, L.Johnson by N00014-17-1-2393, V.Hormann and L.R.Centurioni by N00014-19-1-2691, N00014-13-1-0477, N00014-15-1-2286. A.Tandon was additionally supported by N00014-23-1-2473. The authors would also like to thank the Captain, crew and the science party of R/V Sally Ride during MISO-BoB Leg-2 for their help in data collection. S.K would like to thank the Associate Provost's office, University of Massachusetts Dartmouth for their support through the Distinguished Doctoral Fellowship. S.K is thankful to Emily Shroyer, Kenneth Hughes, Jonathan Nash, Eric D'Asaro, Christian Buckingham, Steven Lohrenz and Miles Sundermeyer for their stimulating discussions on various aspects of this work. The authors would like to express their sincere gratitude to the two anonymous reviewers and the editor of *Journal of Physical Oceanography*, Dr. Gregory Foltz for their constructive suggestions, which greatly enhanced the quality and clarity of this chapter.

Chapter 3 Impacts of Salinity Stratification on Sub-Seasonal SST Warming in the Northern Indian Ocean

Abstract

The Northern Indian Ocean (NIO) experiences strong upper ocean warming during the spring intermonsoon season, with nearly 90% of the days showing net heat gain. However, observations reveal spatially heterogeneous Sea Surface Temperature (SST) trends in these regions over intra-seasonal timescales (15-45 days) and mesoscale and smaller length scales (< 100 km), coinciding with significant lateral variability in winds and salinity stratification. This chapter investigates the role of salinity-driven mixed layers in driving these gradients in foundational SST warming using 1-D modeling. Simulation results using realistic surface forcing show that lateral differences in stratification result in spatial differences in warming of foundational SST by about 0.2-0.5°C over 14-21 days, specifically for shallow mixed layers. However, the influence of stratification on foundational SST warming is nuanced and varies across the NIO, leading to either enhanced or reduced warming. Idealized simulations show that this contrast depends on net heat flux and water optical properties, with stratified cases warming more under high fluxes and turbid conditions. To generalize, we derive an analytical expression for the crossover heat flux (Q_{cross}), the threshold at which stratified and unstratified cases warm equally. Q_{cross} depends on shortwave radiation, mixed layer depth, and optical properties. For representative clear-sky conditions, Q_{cross} ranges from 103 to 136 $\mathrm{W\,m^{-2}}$. These findings underscore the role of salinity-driven stratification and bio-optical feedbacks in shaping SST gradients, with likely implications for subseasonal to seasonal monsoon forecasting.

Key points

- Spatial variability of O(1°C) is observed during the spring intermonsoon warming in the Northern Indian Ocean.
- Salinity stratification can enhance or suppress surface warming by up to 0.5°C, depending on heat fluxes and water optics.
- The threshold for daily mean heat flux value where salinity stratification begins to amplify surface warming is quantified (Q_{cross}).

Plain language summmary

The Northern Indian Ocean (NIO) undergoes intense surface warming during the spring intermonsoon season, prior to Monsoons. Observations reveal that the warming trend in the surface temperatures is spatially uneven over intra-seasonal timescales (15-45 days) and shorter length scales (< 100 km). This variability coincides with significant lateral differences in wind speeds and salinity stratification. This chapter reveals that for shallow mixed layers, salinity stratification significantly influences the surface warming differences. Interestingly, the impact of salinity stratification on surface warming are found to be varying in the NIO, leading to either enhanced or reduced warming. Idealized simulation results provide evidence that this difference is due to the sensitivity of surface warming nature to net heat flux and water optics. Under higher heat flux and more murkier conditions, stratified cases warm more. We also derive a theoretical flux value at which stratified and unstratified scenarios result in the same SST warming rate. This threshold ranges from 103 to 136 $\mathrm{W\,m^{-2}}$ under typical clear-sky conditions and tropical open-ocean waters, depending on water clarity and mixed layer depth. These results highlight the importance of salinity-driven stratification and bio-optical feedbacks in modulating regional SST evolution, factors that can influence tropical cyclone intensity and monsoon predictability.

3.1 Introduction

A precursor to the onset of Monsoons and their associated high wind speeds and rainfall is the presence of warm waters in the Northern Indian Ocean (NIO) during the spring intermonsoon season (Vinayachandran and Shetye, 1991; Rao and Sivakumar, 1999). Conditions in the NIO during this period are characterized by clear skies with net surface heat fluxes of O(100 $\mathrm{W\,m^{-2}}$) and wind speeds below 6 $\mathrm{m\,s^{-1}}$ (Weller et al., 1998, 2019). Such conditions increase the foundational sea surface temperature (SST), denoted as $\boldsymbol{T}_f$ hereafter and defined as the component of SST that varies on timescales longer than the diurnal cycle (Donlon et al., 2007; Prytherch et al., 2013), by approximately 3–4°C (Weller et al., 1998, 2019). The conditions during the spring intermonsoon season also lead to high diurnal SST amplitudes and possible Diurnal Warm Layer (DWL) formation (Stuart-Menteth et al., 2003; Clayson and Weitlich, 2007; Shenoi et al., 2009; Thompson et al., 2019). The heat budget during this period is largely one-dimensional, driven by surface heat fluxes and characterized by negligible lateral heat advection and low eddy kinetic energy (Weller et al., 2002; Thangaprakash et al., 2016; Sun et al., 2022). These persistent warm waters (the Mini Warm Pool) as well as the DWL presence serve as a source for atmospheric convection over diurnal and intra-seasonal timescales (Rao et al., 2015; de Szoeke et al., 2021). These air-sea interactions influence pre-Monsoon tropical cyclones as well as the onset and evolution of the Monsoon (Rao and Sivakumar, 1999; Balaguru et al., 2012; Sijikumar and Rajeev, 2012; Pradhan et al., 2022).

The NIO is also uniquely influenced by the seasonal discharge of river water from the Bay of Bengal (East Basin in the NIO), with peak discharge in August and September (Sengupta et al., 2006; Jarugula et al., 2024). Mesoscale eddies, Ekman currents and the East India Coastal Current redistribute this riverwater throughout the Bay of Bengal, extending its influence to the Southern Bay (Rao and Sivakumar, 2003; Sengupta et al., 2006, 2016; Sree Lekha et al., 2018; Chaudhuri et al., 2021; Jarugula et al., 2024). This freshwater mod-

ifies the vertical stratification by forming salinity-stratified mixed layers (or barrier layers) and creating salinity fronts over O(10 km) (Sengupta and Ravichandran, 2001; Shenoi et al., 2002; Rao and Sivakumar, 2003; Sengupta et al., 2006; Mahadevan et al., 2016; Sengupta et al., 2016; Wijesekera et al., 2016; Sree Lekha et al., 2018; Hormann et al., 2019; Sree Lekha et al., 2020). The East India coastal current, along with coastally trapped Kelvin waves and downwelling Rossby waves, facilitate the freshwater exchange between the Bay of Bengal and the Arabian Sea (west basin in the NIO, Rao and Sivakumar 2003; Vinayachandran and Nanjundiah 2009; Rao et al. 2010; Hormann et al. 2019). This exchange alters the vertical stratification in the Arabian Sea as well (Sprintall and Tomczak, 1992; Echols and Riser, 2020).

The presence of such shallow salinity-stratified mixed layers enhances diurnal SST amplitudes in the NIO region (Shroyer et al., 2016; Kerhalkar et al., In Review). These layers significantly modulate the upper ocean heat budget by inhibiting vertical mixing of cooler subsurface waters, allowing heat to accumulate near the surface and promoting $\boldsymbol{T_f}$ warming (e.g., Yuan et al., 2020). However, these layers also lead to an increased escape of penetrative heat fluxes to deeper waters (due to penetrative shortwave radiation) by a factor of 3 (Sengupta et al., 2008). This effectively reduces the heat retained within the mixed layer, thereby limiting the $\boldsymbol{T_f}$ warming or even cause $\boldsymbol{T_f}$ cooling (Vinayachandran et al., 2007; Sengupta et al., 2008; Echols and Riser, 2020). Due to these competing effects, there remains a lack of consensus on the role of salinity-stratified mixed layers in $\boldsymbol{T_f}$ evolution during the spring intermonsoon, with limited observational studies suggesting their influence on $\boldsymbol{T_f}$ evolution may be minimal (Echols and Riser, 2020).

Given this ambiguity regarding the role of salinity stratification in $\boldsymbol{T_f}$ evolution, and recognizing the influence of SST fronts over mesoscale and smaller lengths on local and large-scale air-sea interactions (e.g., Skyllingstad et al., 2007; Seo et al., 2023), quantifying

the spatial differences in SST within the NIO mini-warm pool is essential. In addition, the role of salinity fronts in causing spatial inhomogeneities in T_f needs to be assessed. These two aspects remains largely unexplored due to lack of concurrent, high-vertical resolution in-situ observations at mesoscale and smaller length scales (< 100 km) in this data-sparse region (Beal et al., 2020; Phillips et al., 2021). This gap in understanding also has implications for the evolution of initial salinity fronts, which could either experience density enhancement or develop density compensation across the front, depending on how salinity stratification impacts the evolution of T_f.

To address this gap, we use a combination of remote sensing, 1-D ocean modeling and surface forcing derived from two in-situ moorings in the NIO (one each in the Northern Bay and South-Eastern Arabian Sea) to answer the following questions:

- What are the typical differences in the warming trends of T_f across mesoscale and smaller gradients during the existence of the mini-warm pool?
- How does salinity stratification differences contribute in causing lateral differences in T_f evolution?
- Does the presence of salinity stratification suppress or accelerate the T_f warming? How does this depend on surface forcing conditions like optical properties of water, wind speeds, and heat fluxes?

We first describe the remote sensing, observational datasets and 1-D model used in this chapter (Section 3.2). Next, we describe the extent of lateral variability in SST trends and surface salinity from remote sensing (as a proxy for differences in salinity stratification) in the NIO (Section 3.3). The role of salinity stratification in causing the differences in T_f warming in the Northern Bay of Bengal (NBoB) and South-Eastern Arabian Sea (SEAS) is considered next, using 1-D model forced with realistic surface forcing from in-situ moorings (Section 3.4).

We then use 1-D model with idealized forcing conditions to isolate the differences in action of salinity stratification on T_f warming trends (Section 3.5). Finally, we develop an analytical expression to explain the role of salinity stratification in the evolution of T_f (Section 3.6). The broader implications of this research are discussed in Section 3.7, with a summary of findings in Section 3.8.

3.2 Data and methods

3.2.1 In-situ sources

In this chapter, we use SST, surface meteorological variables and derived bulk fluxes using COARE algorithm (Fairall et al., 1996b, 2003) from AD08 and ASIRI moorings. The AD08 mooring in the SEAS (located at 11.7°N and 68°E, Blue star in Figure 3.1a) is one of the long-term operational sites maintained by the India's National Institute of Ocean Technology (NIOT, Joseph et al. 2022). We derive bulk fluxes using COARE 3.6 with hourly observations at the AD08 mooring. Our analysis uses the data from February to May 2018, corresponding to the spring intermonsoon season (Weller et al., 1998).

The ASIRI mooring was deployed by the Woods Hole Oceanographic Institution (WHOI) for the ASIRI (Air–Sea Interactions in the Northern Indian Ocean, Wijesekera et al. 2016) field campaign in the NBoB (located at 18.0°N, 89.5°E, Green star in Figure 3.1a) between December 2014 and January 2016. COARE 3.0 algorithm is used to derive bulk fluxes from the 1-minute time resolution observations at this site. We use data from February to May 2015, also representing the spring intermonsoon season (Weller et al., 2016). Further details on the instrumentation and measurements at the AD08 and ASIRI moorings can be found in Joseph et al. (2022), Weller et al. (2016) and Weller et al. (2019).

To assess the typical mixed layer depths (MLDs) around the AD08 and ASIRI moorings in the SEAS and NBoB, respectively, we use ARGO float profiles (Roemmich et al., 2009).

Profiles are selected within a 3° × 2° box centered around AD08 and the ASIRI moorings. The analysis is restricted to the spring intermonsoon season for years 2003 to 2024.

3.2.2 Remote sensing

To examine the spatial variations in T_f and its changes, we utilize NOAA 0.09° Daily Optimum Interpolation Sea Surface Temperature (OISST, Reynolds et al. 2007). This is a level-3 blended product combining microwave and infrared data, at a spatial resolution of nearly 9 km. For understanding the spatial differences in the sea surface salinity (SSS), we use Soil Moisture Active Passive mission (SMAP) data. Although gridded at a 25 km scale, its effective spatial resolution is 47 km (Brown et al., 2013). Daily wind data is obtained from the Advanced Microwave Scanning Radiometer 2 (AMSR-2) aboard the AQUA satellite. Daily wind measurements from AMSR-2 are available at an effective resolution of 46 km, despite being gridded to a 25 km scale as well (Wentz et al., 2014b). Our analysis spans the period from 01 March to 30 April 2018 as to overlap with availability of observations at the AD08 mooring.

3.2.3 Models

The General Ocean Turbulence Model (GOTM) is a one-dimensional ocean model framework that includes various vertical mixing schemes (Burchard et al., 1999). GOTM also provides options for selecting stability functions, as well as parameterizations for wave breaking and internal waves. The k–ϵ turbulence closure scheme within GOTM parameterizes subgrid-scale turbulent kinetic energy (k) and its dissipation rate (ϵ), with both variables evolved using separate prognostic transport equations. This scheme has been employed in previous studies to model the upper ocean (e.g., Johnson et al., 2023; Burchard et al., 2002; Drushka et al., 2016). In this chapter, we use the k–ϵ mixing scheme along with the dynamic dissipation rate length scale and the Canuto A version of the stability function (Canuto et al.,

2001). We adopted GOTM's default settings, omitting only the internal wave breaking parameterization (Burchard et al., 1999).

We conduct two suites of simulations: one forced with realistic surface fluxes from mooring observations (Section 3.4) and another using idealized surface forcing (Section 3.5). All simulations are initialized near sunrise (0:00 UTC) and are run with vertical and temporal resolution of 0.05 m and 1 minute respectively. Additional details on the initial and forcing conditions for these simulations are provided in Sections 3.4 and 3.5.

3.3 Observed spatial variability in T_f, SSS, winds and MLDs during spring intermonsoon season

Satellite SST measurements from the 2018 spring intermonsoon season show the NIO warming to above 29°C by the end of April (Figure 3.1a), creating conditions favorable for atmospheric convection (e.g., Gadgil, 2003). The corresponding increase in the foundational temperature (ΔT_f) over the months of March and April ranges from 1 to 4°C (equivalent to 0.5–2°C per month), with higher ΔT_f values in NBoB compared to the SEAS (Figure 3.1b,c). This regional difference within the NIO is likely driven by differences in net surface heat fluxes, which are higher by O(50 $\mathrm{W\,m^{-2}}$) in the NBoB than in the SEAS (Figure 3.2). This occurs despite largely clear skies and similar shortwave radiation (SWR) in both regions. Over 90% of the days during this period exhibit positive net heat fluxes, supporting the overall warming trend.

Beyond basin-wide differences, satellite SST also reveals O(1°C) spatial variability in $\Delta\, T_f$ over mesoscale and smaller lengths (< 100 km) within both NBoB and SEAS (Figure 3.1b,c). While such variability suggests partial influence of spatial variability in the net heat fluxes over mesoscale and smaller lengths, direct satellite observations of net heat fluxes is not possible. However, wind speeds in both regions during this period show spatial variability of O(2 $\mathrm{m\,s^{-1}}$) over mesoscale and smaller lengths (Figure 3.3a,c), with nearly similar spatially

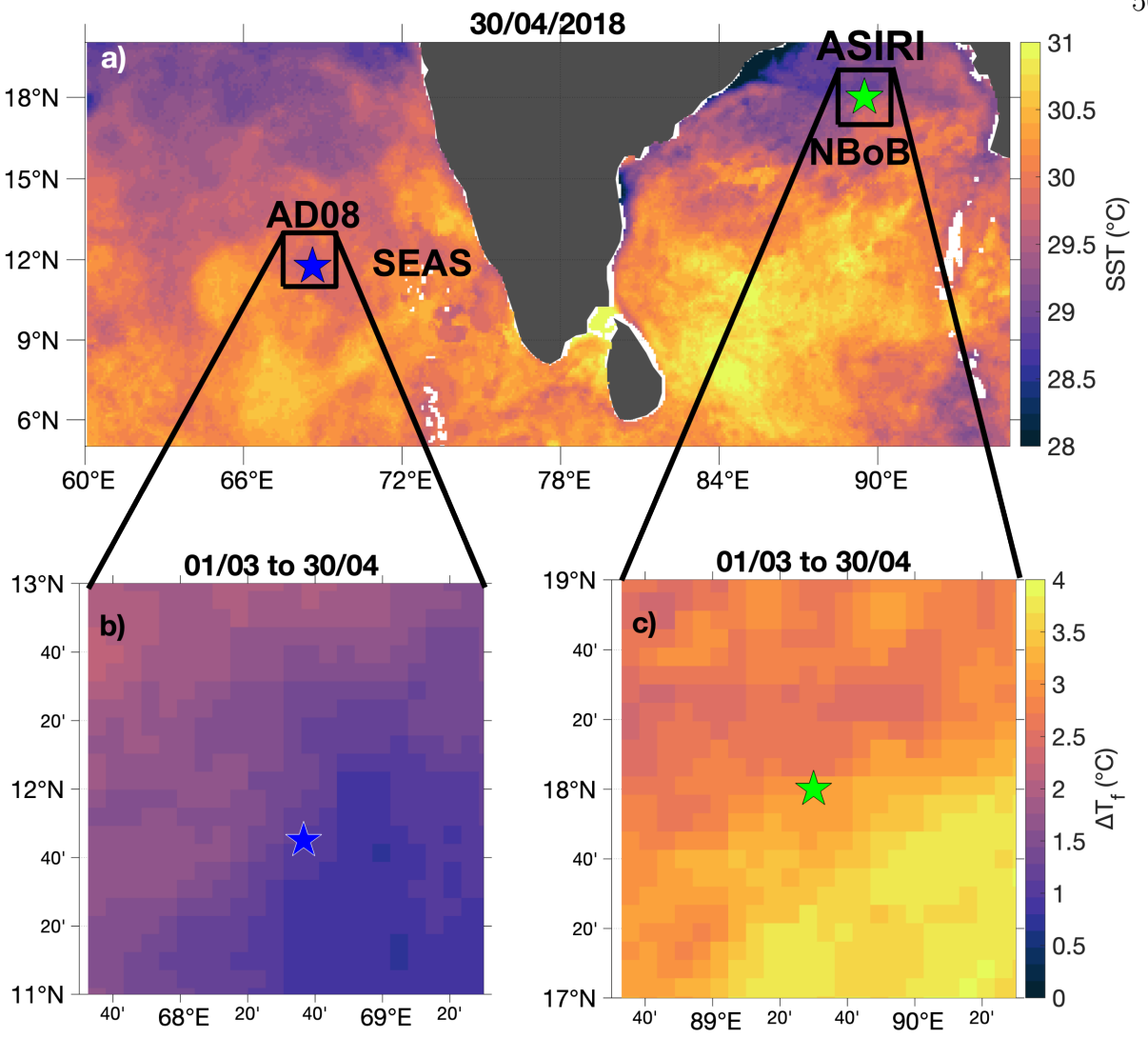

Figure 3.1: (a) SST of the Northern Indian Ocean on 30 April 2018 from OISST. The blue and green stars indicate the AD08 mooring in SEAS and ASIRI Mooring in NBoB respectively. (b) and (c) Change in T_f from 01 March to 30 April 2018 within the boxes in vicinity of the moorings as indicated in (a).

averaged wind speeds in both the regions (except between 15-30 April, where the NBoB has stronger winds by about 2 $\mathrm{m\,s^{-1}}$). These spatial differences in winds suggests a potential contribution to unresolved small-scale variability in surface heat fluxes.

Past studies indicate that salinity stratification significantly modifies SST and the up-

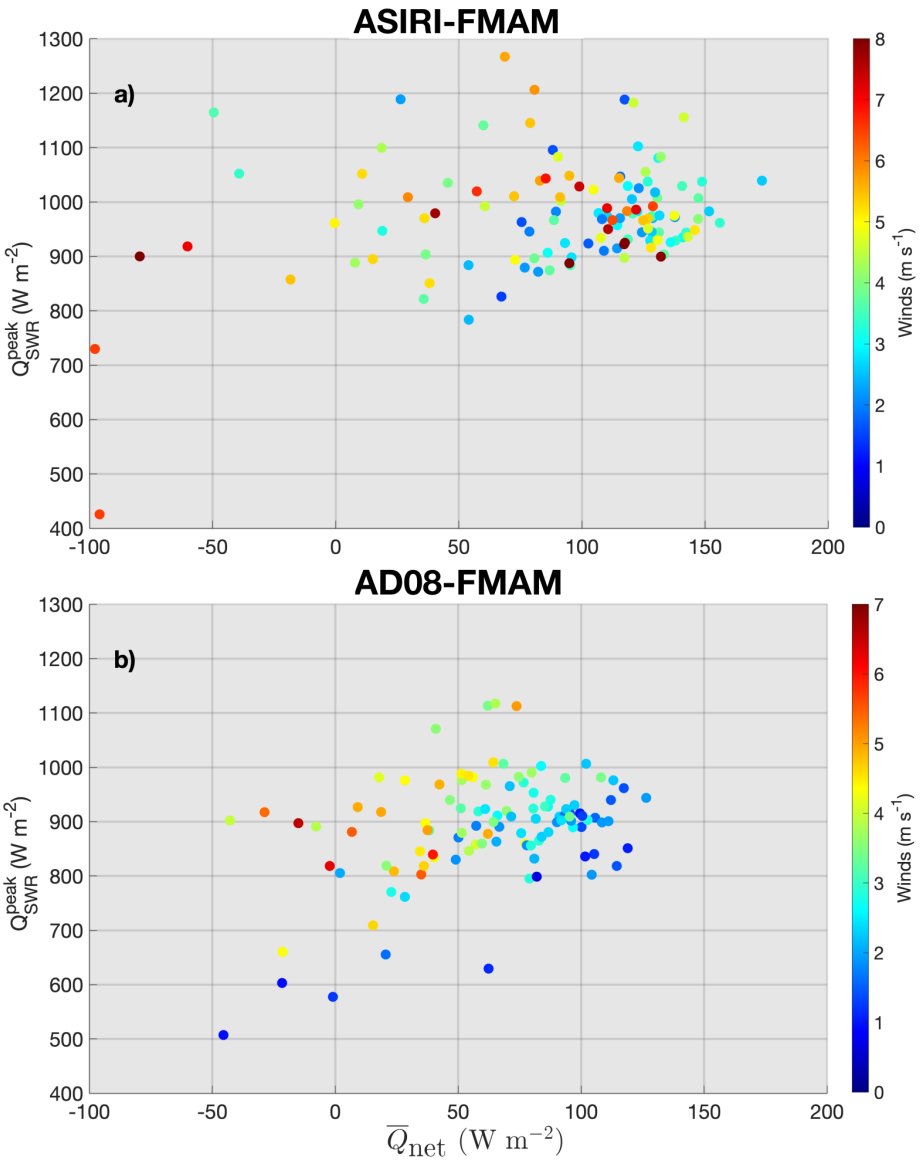

Figure 3.2: (a) Scatter plot of daily peak shortwave radiation (Q^{peak}_{SWR}, y-axis) vs. daily mean net heat flux ($\overline{Q_{net}}$, x-axis) from the ASIRI mooring in the NBoB during February-May 2015, with colors indicating the daily mean wind speed. (b) is the same as (a) but for AD08 mooring in the SEAS during February-May 2018.

per ocean heat budget as well (Sengupta et al., 2008; Yuan et al., 2020). Satellite SSS measurements reveal enhanced spatial variability of O(2 g kg^{-1}) over mesoscale and smaller

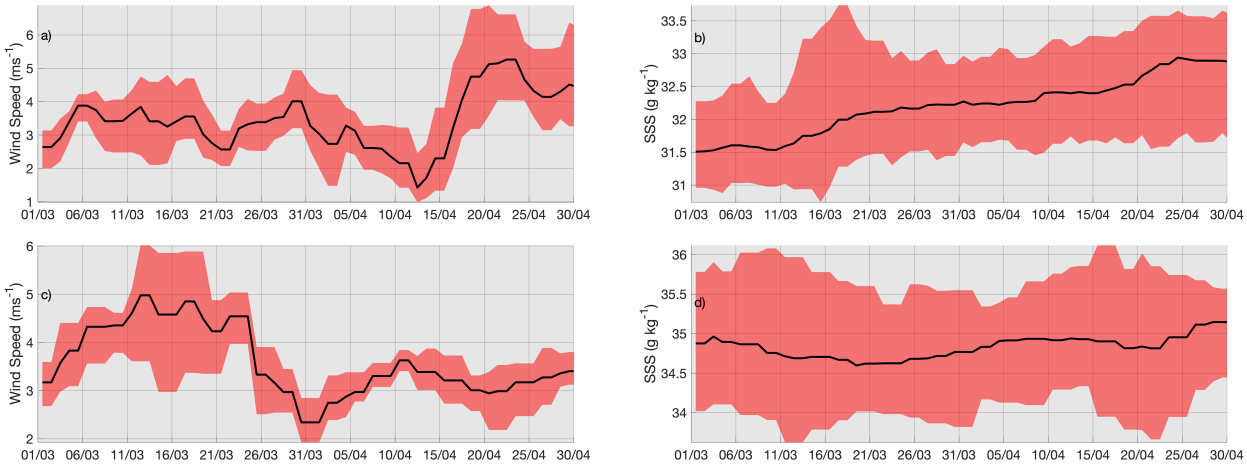

Figure 3.3: (a) Time series of the mean wind speed (black line) over the box in the NBoB (Figure 3.1c), with the range of values shown in red shade between 01 March and 30 April 2018. (b) Same as (a) but for SSS over the box in Figure 3.1c. (c) and (d) are the same as (a) and (b) over the box in SEAS (Figure 3.1b).

lengths in both NBoB and SEAS regions, with NBoB being consistently fresher than SEAS (Figure 3.3b,d). Because salinity variations at these length scales are typically much weaker below the surface, surface salinity gradients can serve as a proxy for lateral differences in salinity-driven stratification. Additionally, long-term ARGO float analysis highlights that MLDs are found to be varying between 5-30 m in NBoB and SEAS during the spring inter-monsoon season (Figure 3.4).

While spatial gradients in ΔT_f are clearly observed to be as high as 2°C, quantifying the causes of these observed spatial ΔT_f differences solely through observations is challenging. Therefore, we employ an idealized one-dimensional (1-D) modeling approach to explore how lateral differences in salinity stratification might drive lateral variations in ΔT_f.

3.4 1-D modeling experiments using observed surface forcing in NIO

GOTM simulations are forced with high-resolution surface fluxes and wind speeds from the ASIRI and AD08 moorings to understand the role of salinity stratification in causing lateral

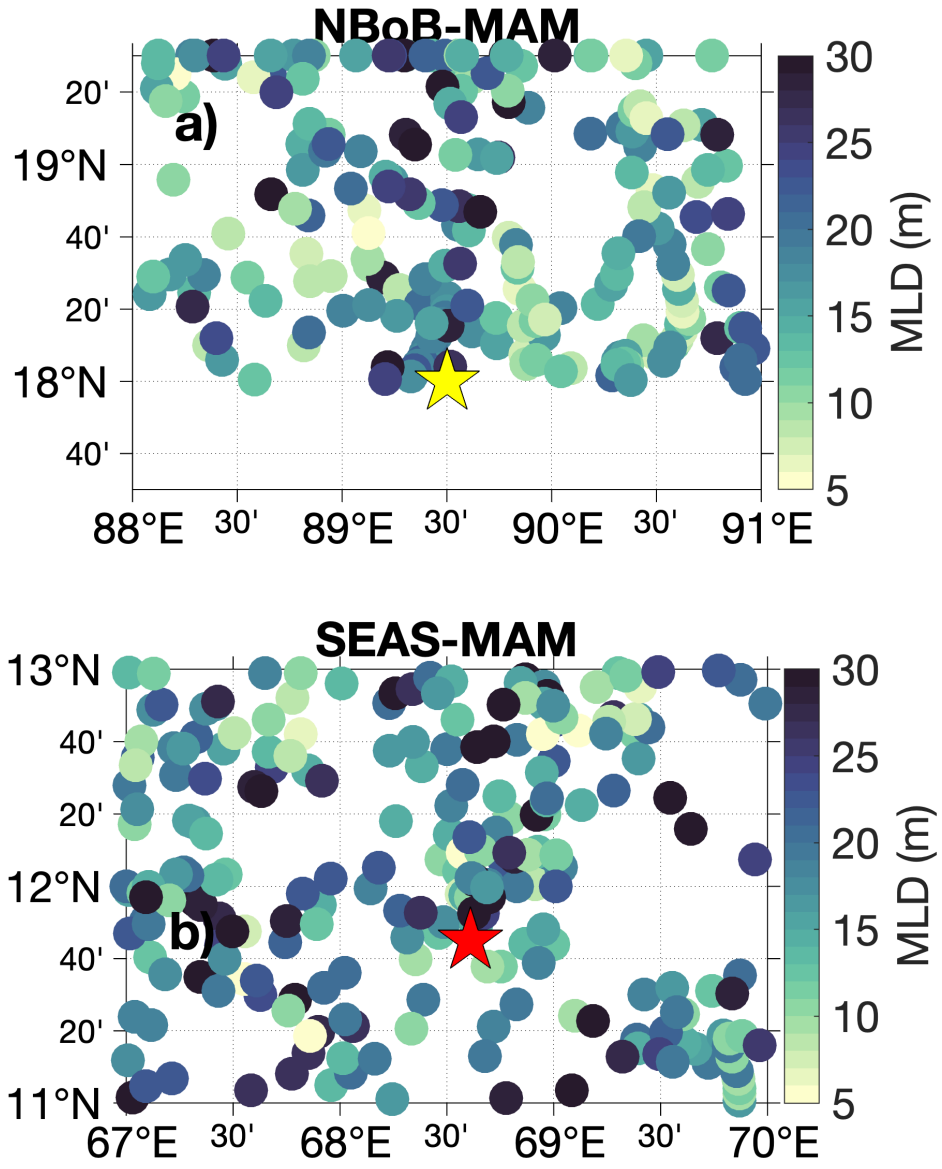

Figure 3.4: (a) MLDs inferred from ARGO floats in a 3° × 2° centered around the ASIRI mooring (in yellow star) in the NBoB for months of March, April and May between 2003 and 2024. (b) is the same as (a) but for a similar region around the AD08 mooring (in red star) in the SEAS.

variations in ΔT_f. Simulations are initialized with idealized temperature and salinity profiles inspired by past observations from these regions. The upper layer's temperature and salinity

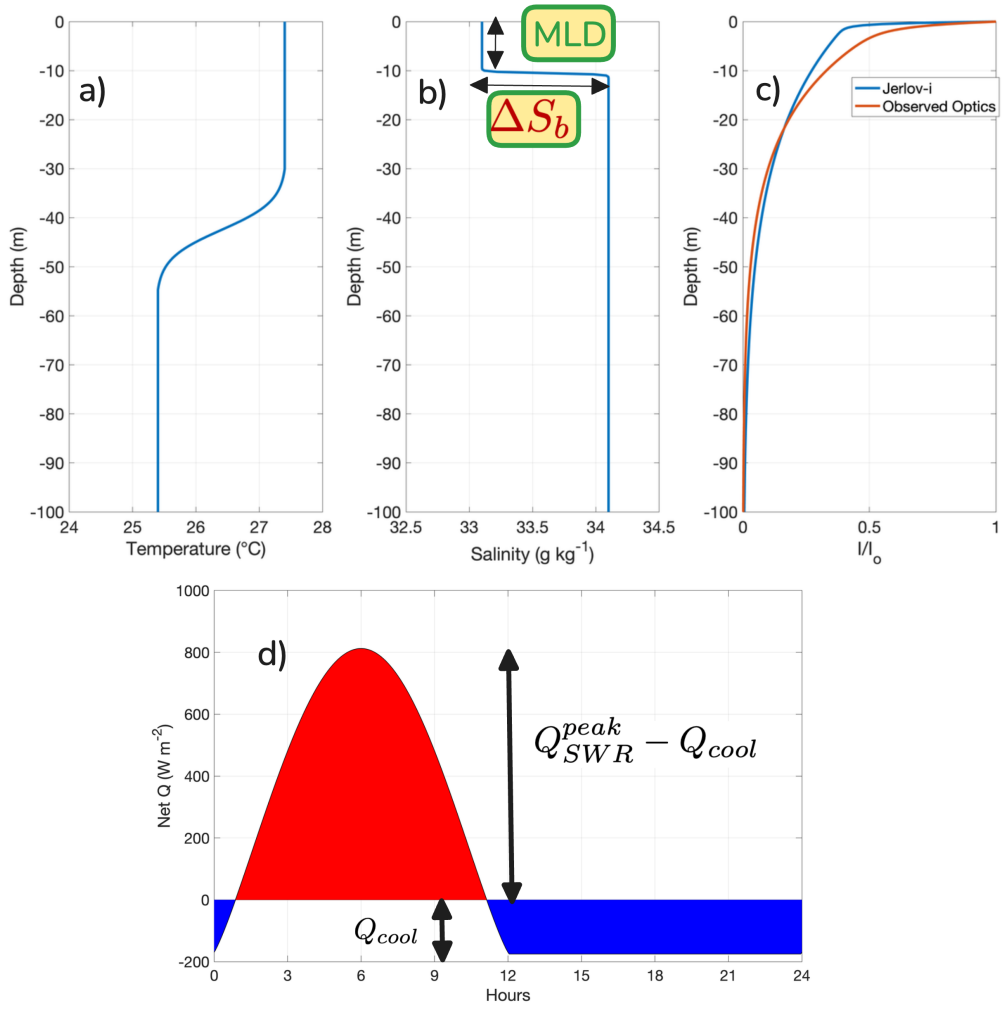

Figure 3.5: Initial vertical profiles of (a) temperature, (b) salinity and (c) ratio of downward irradiance (I) to incident irradiance at the surface (I_o), for the GOTM parameter space exploration. The temperature and salinity in the upper layer is set using the initial SST and SSS respectively. Stratification in the initial profiles is controlled using the MLD and the initial change in salinity at the base of mixed layer (ΔS_b). (d) A typical diurnally varying idealized forcing flux is shown as a function of time in UTC for Indian Ocean, with a constant cooling component of flux (i.e., sum of net longwave radiation, latent heat flux, and sensible heat flux, which typically cool the Indian Ocean, Q_{cool}) and diurnally varying SWR that peaks during the day (Q_{SWR}^{peak})

are set using the initial SST and SSS observed at the respective moorings (Figure 3.5a,b). Upper ocean stratification is controlled by the initial MLD at sunrise and the initial salinity change at the base of the MLD (ΔS_b). Additionally, a 2°C change in temperature over 10 m is assumed at a depth of 40 m to emulate a typical thermocline. We model the penetration of solar radiation using a double exponential decay with attenuation coefficients appropriate for Jerlov-I water type (Figure 3.5c, Paulson and Simpson 1977).

During a 21-day period between 08 March and 01 April 2015 in the NBoB, consistent wind speeds below 6 $\mathrm{m\,s^{-1}}$ favor DWL formation (Thompson et al., 2019; Kerhalkar et al., In Review). This causes the SSTs to exhibit a diurnal cycle (Figure 3.6a). The observed ΔT_f during this 21-day period is 2.2°C (Figure 3.6a). A simulation assuming no salinity stratification in the initial profile yields a ΔT_f of 2.1°C, with consistent upper ocean warming (down to 25 m depth) and presence of DWLs (Figure 3.6a,b). In contrast, using salinity-stratified initial conditions (initial MLD=6 m and ΔS_b=1 $\mathrm{g\,kg^{-1}}$) increases the ΔT_f by 0.4°C (to 2.5°C, Figure 3.6a). Presence of enhanced stratification traps the DWLs and the associated heat distribution to shallower depths (Figure 3.6c). Comparison of resulting temperature profiles reveal that the non-salinity-stratified scenario warms more for the first part of the period (till 17 March) at the surface (Figure 3.6d). In contrast, the salinity-stratified case warms more below its initial MLD when compared to the non-salinity-stratified case during this period (both cases warm in an absolute sense but differ in relative heating). This is a combined effect of surface cooling concentrated within a shallow MLD (leading to more cooling) and penetrative heat fluxes warming the sub-surface without the typical cooling at the end of the day (which happens in the non-salinity-stratified case; e.g., Sengupta et al. 2002). Conversely, the surface in salinity-stratified scenario warms more for the second part of the period (from 20 March) by trapping heat to a shallower depth (Figure 3.6d). As a result, the sub-surface is warmer for the non-salinity-stratified case when compared to the salinity-

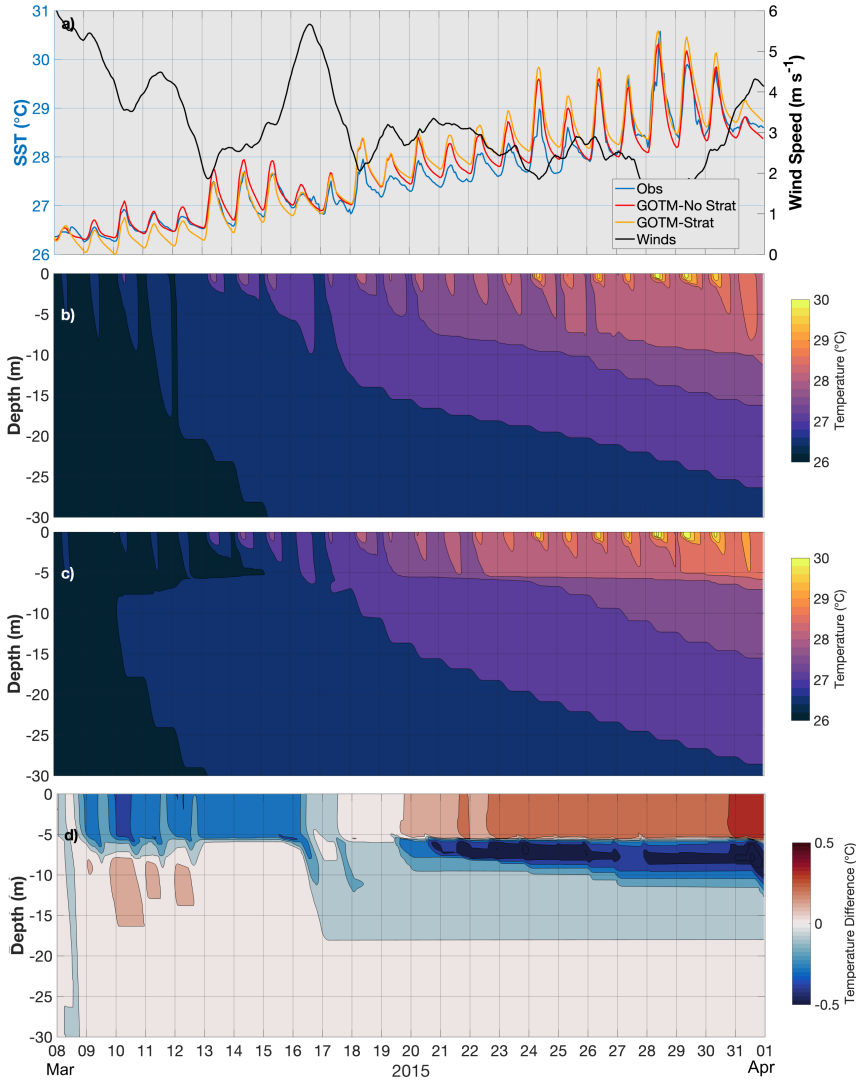

Figure 3.6: (a) Observed SST from ASIRI mooring in NBoB (in blue), modeled SST assuming no salinity stratification (in red) as well as modeled SST assuming an initial MLD=6 m and ΔS_b=1 g kg^{-1} (in yellow) between 08 March and 01 April 2015. 24-hour smoothed wind speed at the ASIRI mooring is shown in black line with its axes limits on the right. (b) Modeled temperature profiles assuming no salinity stratification (ΔS_b=0) between 08 March and 01 April 2015. (c) is the same as (b) but assuming an initial MLD= 6 m and ΔS_b=1 g kg^{-1}. (d) Difference in temperature between (c) and (b). Red color indicates that the salinity-stratified case in (c) is warmer than non-salinity-stratified case in (b).

stratified case during this period. Similar results from other periods in April and May 2015 in NBoB reveal that the surface in case of salinity-stratified scenarios demonstrates periods of both enhanced and reduced warming when compared to non-salinity-stratified scenarios (Figure 3.7, 3.8).

Observations from the AD08 mooring in the SEAS during a 15-day period (from 26 April to 10 May 2018) also show consistently low wind speeds, similar to the NBoB case discussed earlier. Here, the observed ΔT_f is 0.64°C (Figure 3.9a). The non-salinity stratified scenario (similar to above) reveals a 0.65 °C ΔT_f, but the salinity-stratified scenario results in a lower ΔT_f of 0.45°C (Figure 3.9a). Although DWLs are also present in these cases (Figure 3.9b,c), the surface of non-salinity stratified scenario is consistently warmer in the case of SEAS (Figure 3.9d). Thus SEAS and NBoB show contrasting results.

To comprehensively understand the role of salinity stratification on ΔT_f, we conduct multiple GOTM simulations with varying initial MLD (2-15 m) and ΔS_b (0-1 $\mathrm{g\,kg^{-1}}$), using the same surface forcing as discussed previously. These experiments reaffirm our earlier findings: in the SEAS scenario, enhanced stratification leads to a reduction in ΔT_f (Figure 3.10a). This effect is more pronounced for higher ΔS_b (> 0.8 $\mathrm{g\,kg^{-1}}$) and shallower initial MLDs (< 8 m), with differences of about 0.2°C in ΔT_f as a result. Conversely in the NBoB scenario, enhanced stratification results in a higher ΔT_f (Figure 3.10b). Similar to the SEAS scenario, this effect in the NBoB is more pronounced over shallow initial MLDs (< 6 m) and enhanced ΔS_b (> 0.7 $\mathrm{g\,kg^{-1}}$), resulting in differences of about 0.5°C in ΔT_f. Crucially, our detailed exploration of the NBoB scenario across its two distinct periods (discussed above) reveals contrasting results, with stratified scenarios leading to lower and higher ΔT_f values for the respective periods (Figure 3.11).

Overall, our 1-D simulations using observed surface forcing from the NBoB and SEAS demonstrate that salinity stratification can contribute up to 0.5°C of spatial variability in

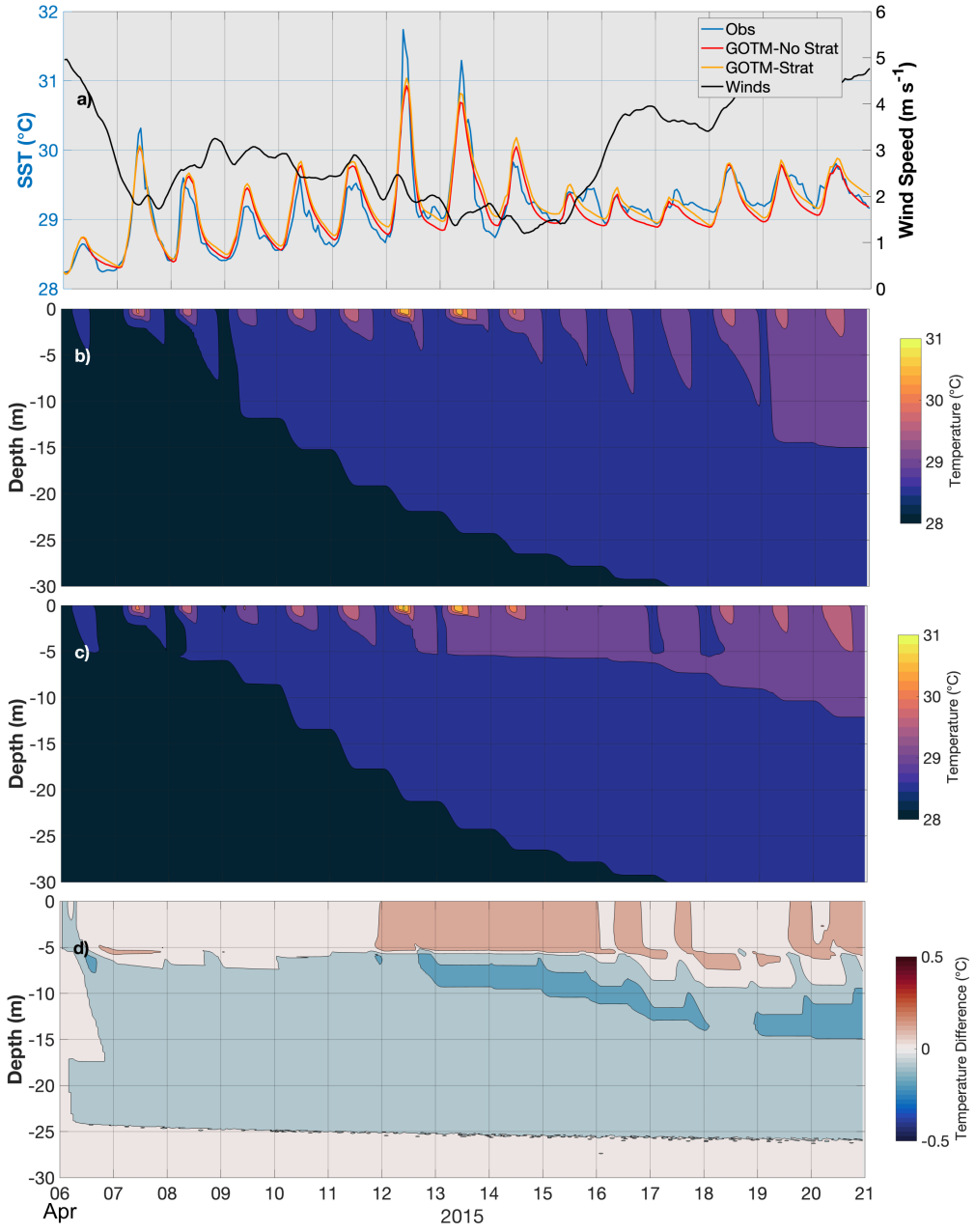

Figure 3.7: Same as Figure 3.6 except for 06-21 April 2015.

ΔT_f. This exercise suggests that the observed spatial gradients in ΔT_f are partly driven by salinity stratification, with additional influence from variability in optical properties and

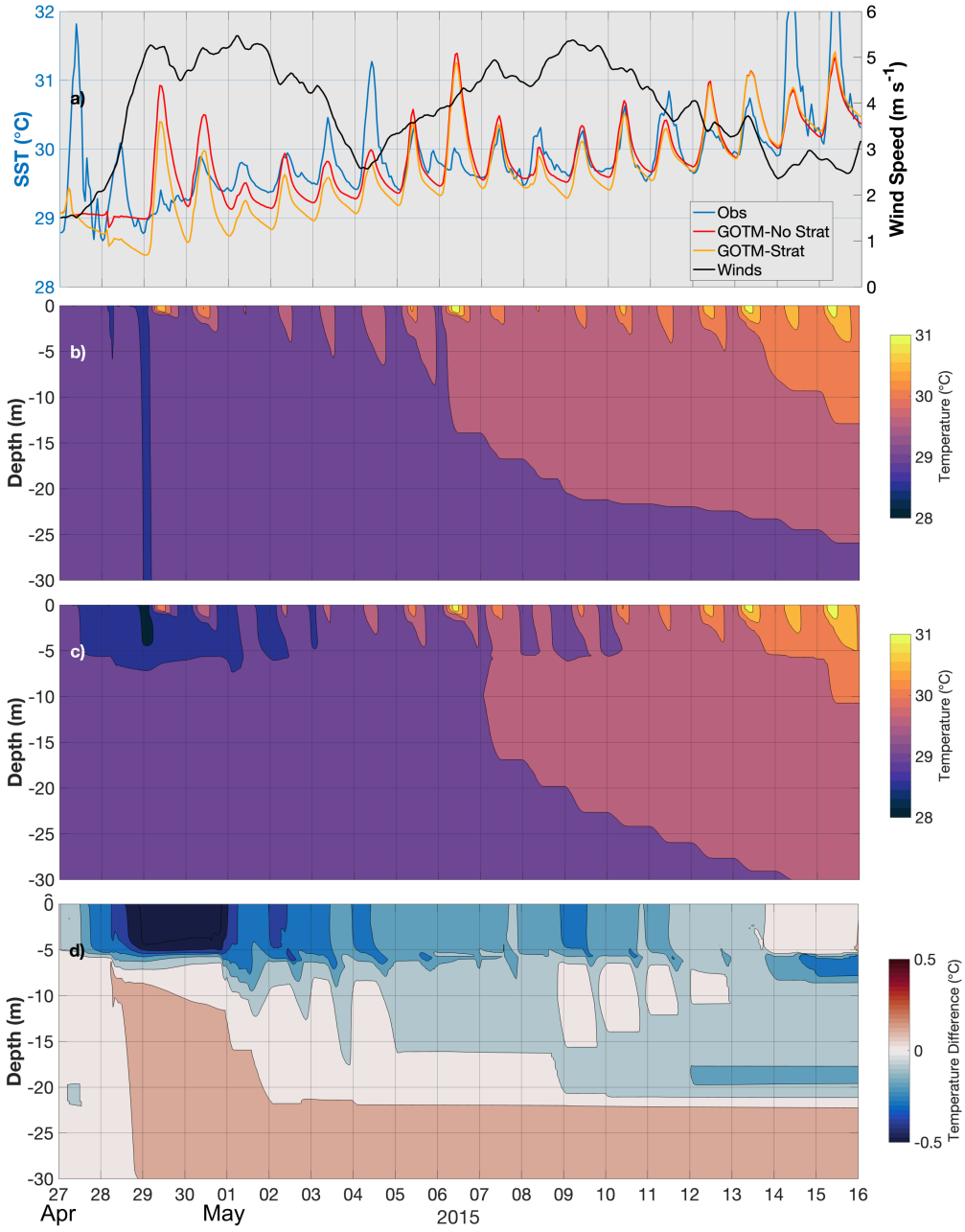

Figure 3.8: Same as Figure 3.6 except for 27 April to 16 May 2015.

surface heat fluxes. These results imply that salinity stratification has contrasting impacts

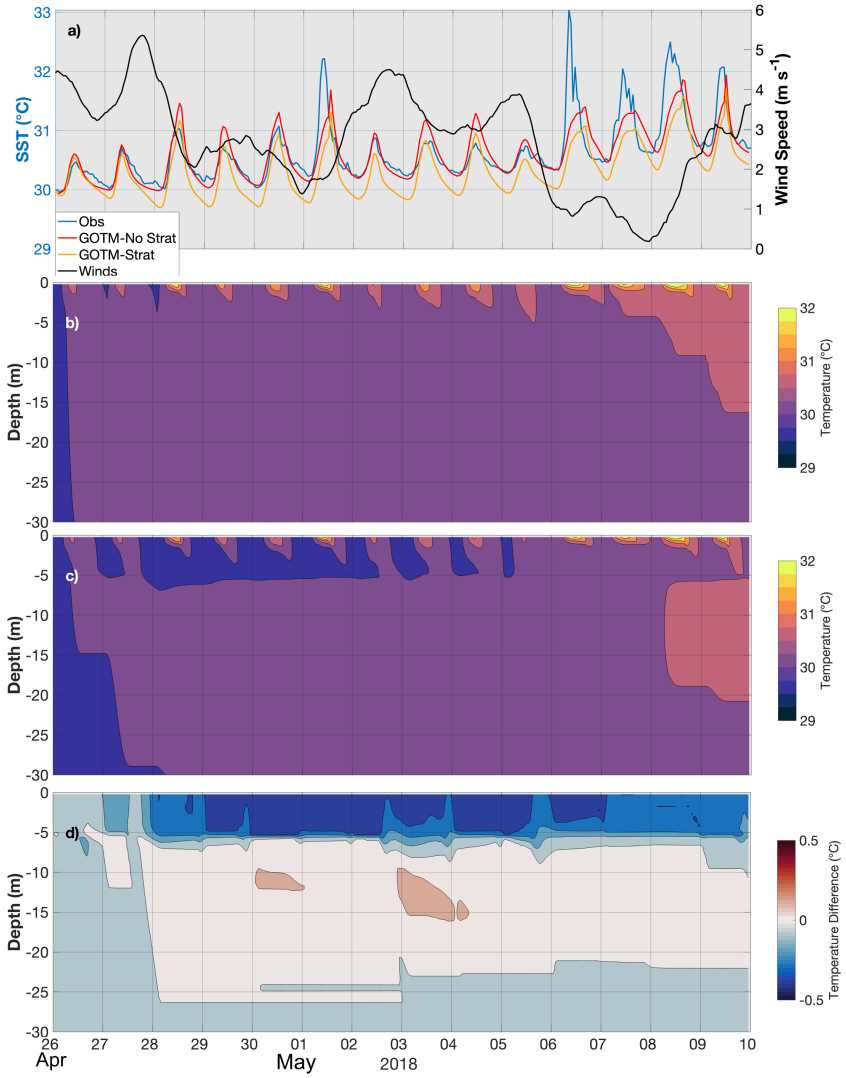

Figure 3.9: (a) Observed SST from AD08 mooring in SEAS (in blue), modeled SST assuming no salinity stratification (in red) as well as modeled SST assuming an initial MLD of 6 m and ΔS_b of 1 g kg^{-1} (in yellow) between 26 April and 10 May 2018. 24-hour smoothed Wind speed at the AD08 mooring is shown in black line with its axes limits on the right. (b) Modeled temperature profiles assuming no salinity stratification between 26 April and 10 May 2018. (c) is the same as (b) but assuming an initial MLD of 6 m and ΔS_b of 1 g kg^{-1}. (d) Difference in temperature between (c) and (b). Red color indicates that the salinity-stratified case in (c) is warmer than non-salinity-stratified case in (b).

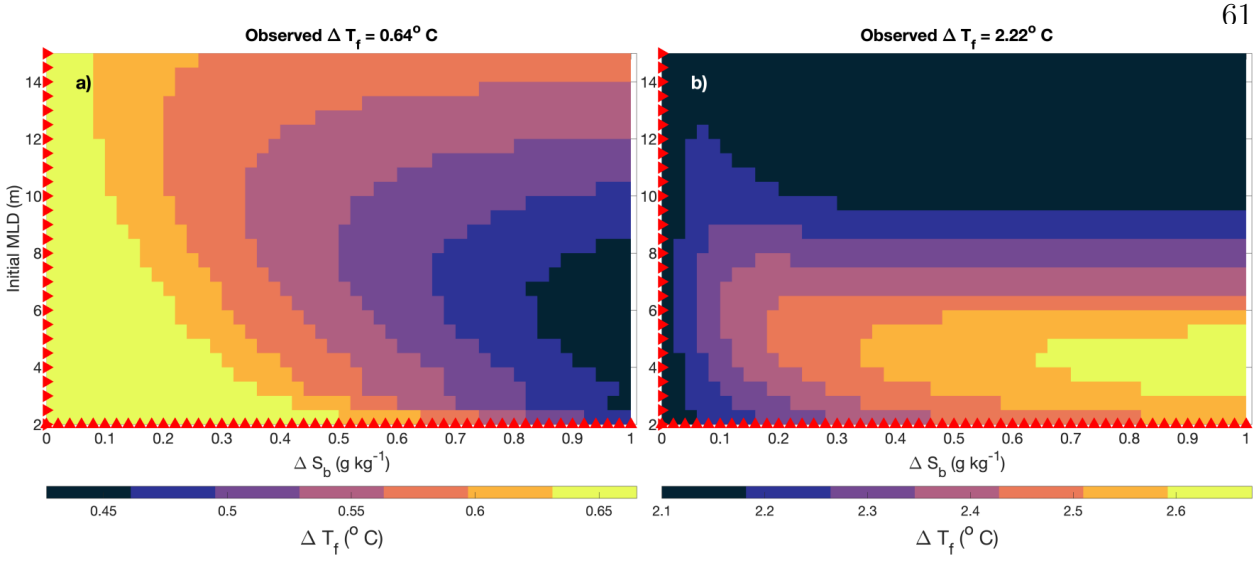

Figure 3.10: (a) Modeled ΔT_f between 08 March and 01 April 2015 as a function of ΔS_b (x-axis) and initial MLD (y-axis), forced with observed air-sea fluxes and wind speeds at ASIRI mooring in NBoB. The observed value of ΔT_f during the same period is indicated in the sub-title. (b) is the same as (a) but for AD08 mooring in SEAS between 26 April and 10 May 2018. The red markers at axes indicate the different parameters for which the simulations are performed.

on ΔT_f: in presence of surface warming, a salinity front could experience either enhanced or compensated density gradients. We resolve this conundrum in the next section.

3.5 1-D modeling experiments using idealized surface forcing

We adapt the heat budget framework from Rudnick and Weller (1993) to estimate ΔT_f, neglecting lateral advection and entrainment terms:

$$\Delta T_f = \frac{\int (F(H).Q_{SWR} - Q_{cool})dt}{\rho c_p H} \tag{3.1}$$

Here, $F(H)$ represents the fraction of SWR trapped within an effective MLD of H (dependent on the optical properties of water). Q_{SWR} and Q_{cool} represent the shortwave and cooling components of heat flux (i.e., sum of net longwave radiation, latent heat flux, and sensible

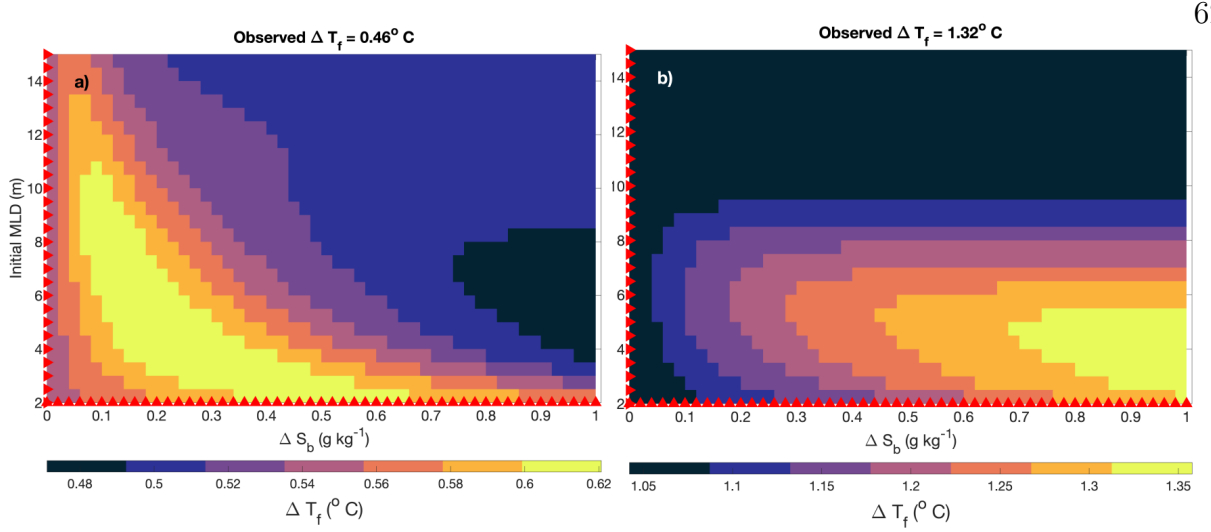

Figure 3.11: (a) Modeled ΔT_f between 08 March and 17 March 2015 as a function of ΔS_b (x-axis) and initial MLD (y-axis), forced with observed air-sea fluxes and wind speeds at ASIRI mooring in NBoB. The observed value of ΔT_f during the same period is indicated in the sub-title. (b) is the same as (a) but for the period between 20 March and 01 April 2015.

heat flux, which typically cool the Indian Ocean) respectively. ρ, c_p indicate the density and specific heat capacity of water (assumed as 3991 $\mathrm{J\,kg^{-1}\,K^{-1}}$). Building on equation 3.1, we conduct four distinct cases of parameter space explorations by adjusting the idealized surface forcing based on the parameters mentioned in Table 3.1. In each parameter space exploration case, GOTM simulations are forced for 30-day runs with diurnally varying solar radiation peaking at Q_{SWR}^{peak} (based on Renner et al. 2019) and constant cooling components of the heat flux (Q_{cool}, Figure 3.5d). This results in a daily mean net heat flux value of $\overline{Q_{net}}$ as mentioned in Table 3.1. Jerlov-I optical profile is used for all the cases, except case-4, which utilizes an optical profile observed in the NBoB during a 2019 field campaign (Figure 3.5c, pers comm: Tamara Schlosser, see Kerhalkar et al. In Review). We vary the initial MLD (2-15 m), ΔS_b (0-1 $\mathrm{g\,kg^{-1}}$) and wind speeds (3-6 $\mathrm{m\,s^{-1}}$) to explore the parameter space.

Case-1 shows that salinity-stratified scenarios result in a lower ΔT_f compared to non-

Table 3.1: Summary of forcing parameters and optical profiles for idealized cases.

Cases	Q_{SWR}^{peak} ($\mathrm{W\,m^{-2}}$)	Q_{cool} ($\mathrm{W\,m^{-2}}$)	$\overline{Q_{net}}$ ($\mathrm{W\,m^{-2}}$)	**Optics**
Case-1	1000	175	123	Jerlov-I
Case-2	1000	148	150	Jerlov-I
Case-3	1095	175	150	Jerlov-I
Case-4	1000	148	150	Observed

stratified cases by approximately 0.35°C (Figure 3.12a). This response is consistent with the SEAS case (Figure 3.10a), where enhanced stratification suppresses surface warming. The impact of salinity stratification is maximum at an initial MLD of 8 m with effects extending down to 14m. In contrast, results from case-2 (where the $\overline{Q_{net}}$ is increased from case-1 by reducing Q_{cool}) reveal that ΔT_f increases as the ΔS_b increases (Figure 3.12b) by about 0.6°C. The impact of ΔS_b is similar to the NBoB case (Figure 3.10b), thereby highlighting the role of $\overline{Q_{net}}$ in causing such contrasting effects of ΔS_b on ΔT_f. As for case-1, the effects of ΔS_b is maximum over a depth of 5-8 m, with effects extending down to 15 m.

Case-3 of the parameter space exploration further justifies the role of $\overline{Q_{net}}$. This case utilizes the Q_{cool} from case-1 with $\overline{Q_{net}}$ of case-2 (achieved by increasing Q_{SWR}). Results mirror those of case-2 in trend, though absolute ΔT_f values differ (Figure 3.12c). This difference arises due to the influence of optical properties of water, where the increase in Q_{SWR} absorbed within the depth H is smaller than the increase in Q_{cool} between cases-2 and 3 (see equation 3.1). The depth-dependent impact of ΔS_b on ΔT_f here is consistent with case-2 as well.

We conduct an additional parameter space exploration (case-4) where the water's optical properties are modified to allow deeper penetration of SWR (Figure 3.5c) while keeping all other surface forcing conditions similar to case-2. Comparison of results from case-4 and

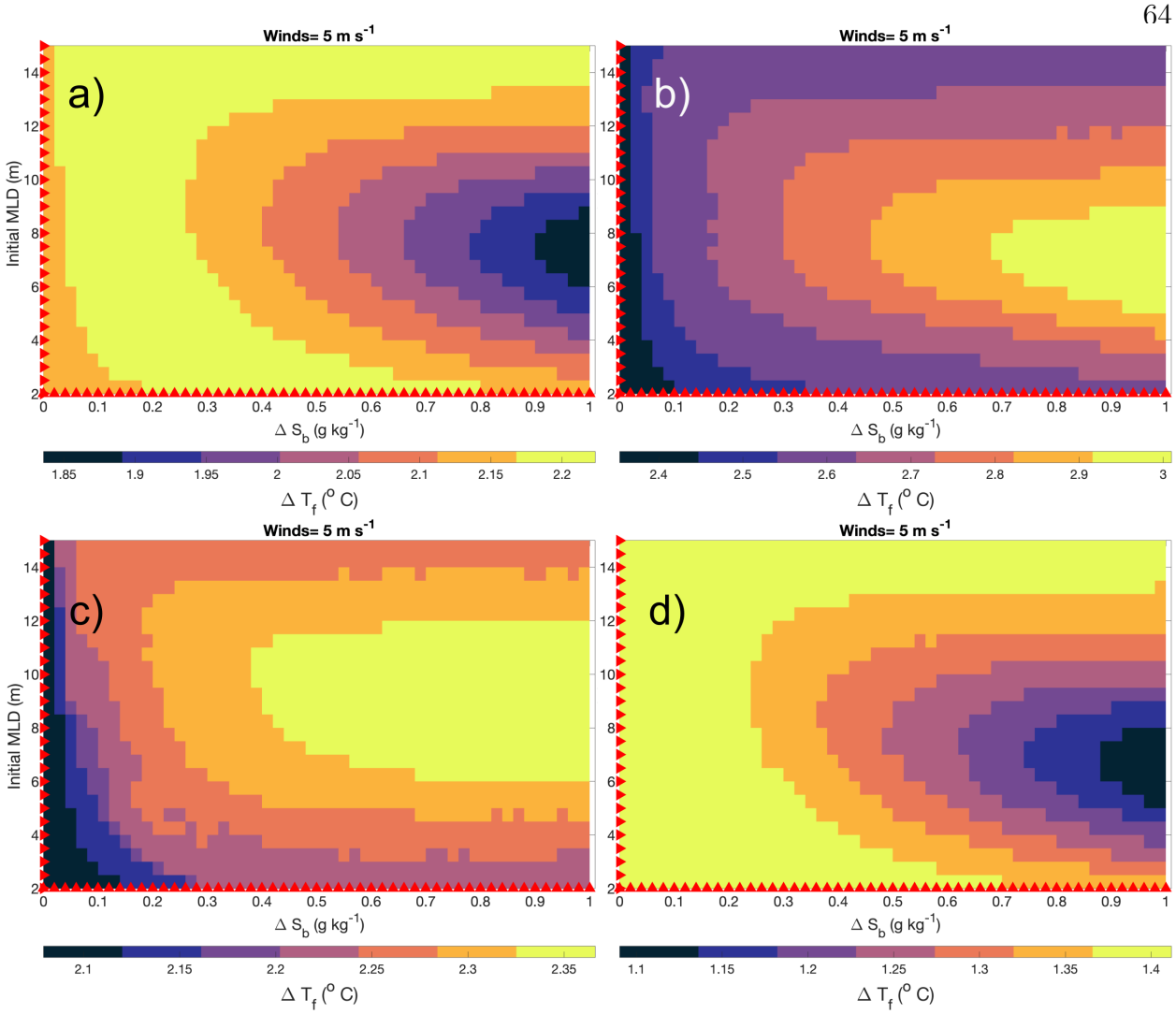

Figure 3.12: (a) ΔT_f over a 30-day period as a function of ΔS_b (x-axis) and initial MLD (y-axis) for a diurnally varying clear sky day with wind speed of 5 $\mathrm{m\,s^{-1}}$ for case-1. (b)-(d) is same as (a) for cases-2, 3, 4 respectively (Table 3.1). The red markers at axes indicate the different parameters for which the simulations are performed.

case-2 reveal that merely altering the optical properties leads to contrasting impacts of ΔS_b on ΔT_f. In case-4, salinity-stratified case warms less than non-salinity-stratified case by about 0.3°C (Figure 3.12d). This occurs because deeper penetration of SWR reduces the

F(H). Q_{SWR} term (equation 3.1). These idealized cases highlight the importance of surface heat fluxes and water's optical properties in driving the contrasting effects of ΔS_b on ΔT_f.

Next, we investigate the impact of varying wind speeds on our simulations. In non-salinity-stratified scenarios wind drives unrestricted vertical mixing. On the other hand, mixing is suppressed and wind mainly controls the entrainment across the stratified layer in salinity-stratified cases (e.g., Dewey and Moum, 1990). For simplicity, we intentionally exclude the effect of changing wind speeds on Q_{cool} in these idealized cases, although this is considered later and the results are qualitatively similar.

For idealized scenarios where ΔT_f increases with increasing ΔS_b (such as case-2), the influence of salinity stratification is more pronounced at higher wind speeds than at lower wind speeds (Figure 3.13). This occurs because higher wind speeds enhance entrainment across the stratified interface in salinity-stratified cases, while in non-salinity-stratified scenarios they promote deeper vertical mixing throughout the water column, thereby intensifying the ΔT_f contrast. Conversely, at lower wind speeds, vertical mixing in both salinity-stratified and non-salinity-stratified cases occurs over similar depth scales (since the wind-driven trapping depth scale for 3 $\mathrm{m\,s^{-1}}$ wind forcing and clear-sky conditions is nearly 5 m, see equation 16 in Price et al. 1986), resulting in small contrast in ΔT_f values.

However, for idealized scenarios where ΔT_f decreases with increasing ΔS_b (case-1 and 4), the impact of salinity stratification is more significant at lower wind speeds (Figure 3.13). This is because the warming within the MLD is muted in salinity-stratified cases under low wind speeds as a result of reduced entrainment and enhanced cooling component of heat fluxes. At higher wind speeds, this impact is diminished and occasionally ambiguous. For instance, with increasing ΔS_b values, ΔT_f may initially increase before decreasing. This complex behavior is attributed to higher entrainment rates, which bring warmer water from depths below the salinity-stratified MLD.

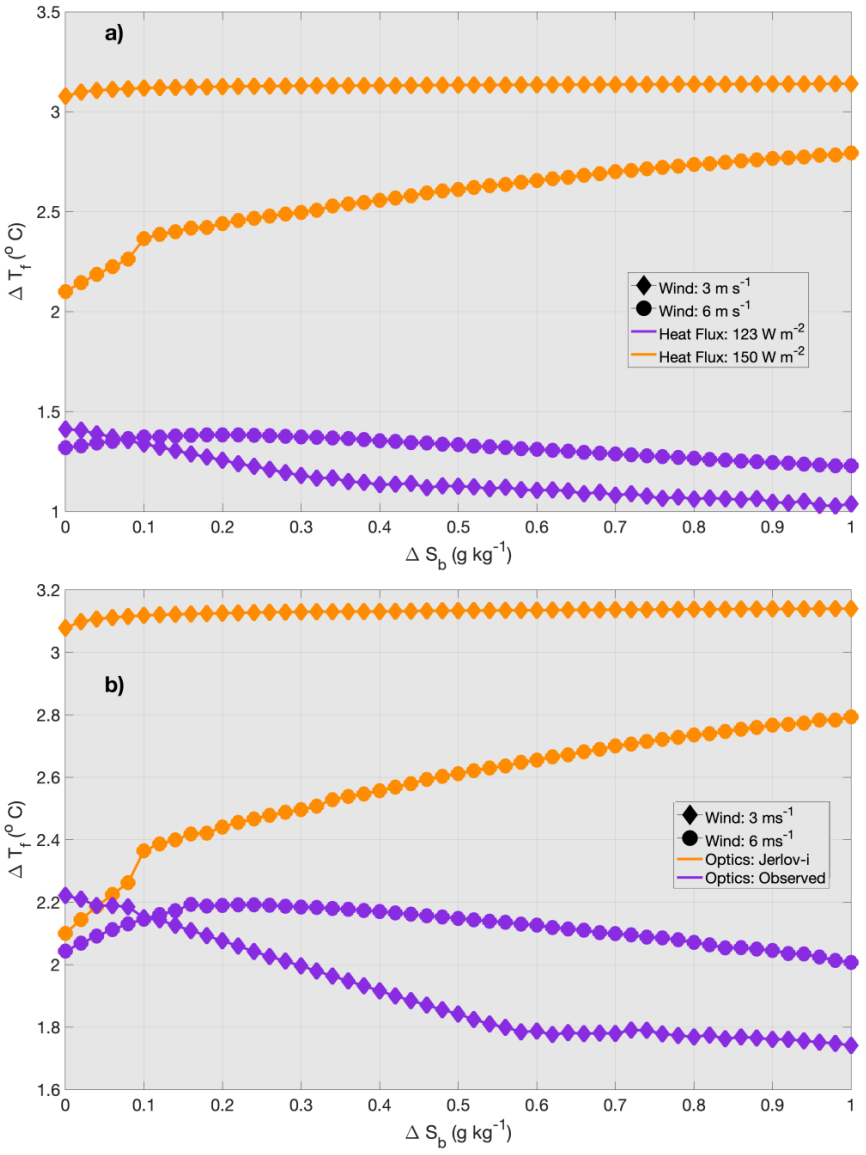

Figure 3.13: (a) ΔT_f over a 30-day period as a function of ΔS_b (x-axis) for an initial MLD=8 m for a diurnally varying clear sky day with daily $\overline{Q_{net}}$ of 123 (purple, Case-1) and 150 W m^{-2} (orange, Case-2), different wind speed scenarios (diamond and circle markers for 3 m s^{-1} and 6 m s^{-1} winds respectively). (b) is the same as (a) but for a daily $\overline{Q_{net}}$ of 150 W m^{-2} and different optical profiles (Jerlov-I in orange and observed optical profile in purple respectively, Case-2 and 4).

3.6 Crossover heat flux: Quantifying the ΔT_f vs ΔS_b regime shift

As previously discussed, the dependence of ΔT_f on ΔS_b is sensitive to both the $\overline{Q_{net}}$ and the optical properties of water. To mathematically identify the $\overline{Q_{net}}$ value at which this qualitative shift occurs, we derive the crossover heat flux (Q_{cross}), defined as the $\overline{Q_{net}}$ value where the ΔT_f is equal for the non-salinity stratified and the salinity-stratified scenarios. When $\overline{Q_{net}}$ exceeds Q_{cross}, the salinity-stratified scenario exhibits higher ΔT_f. Conversely, when $\overline{Q_{net}}$ does not exceed Q_{cross}, the salinity-stratified scenario exhibits lower ΔT_f. The derivation of Q_{cross} utilizes the simple 1-D heat budget equation described in equation 3.1.

$$\Delta T_f^{str} - \Delta T_f^{unstr} = \frac{F(H_{str}).\overline{Q_{SWR}} - \overline{Q_{cool}}}{\rho c_p H_{str}} - \frac{F(H_{unstr}).\overline{Q_{SWR}} - \overline{Q_{cool}}}{\rho c_p H_{unstr}} \tag{3.2}$$

The integral in equation 3.1 is replaced by daily mean (overbar) quantities for SWR (Q_{SWR}) and cooling heat fluxes (Q_{cool}). We assume that the heat flux quantities are identical in both the non-salinity-stratified (labeled "unstr") and salinity-stratified scenarios (labeled "str"). The H_{str} and H_{unstr} represent the effective depths controlled by the shallow salinity-stratification and deeper temperature-stratification/wind mixing respectively. Equating equation 3.2 to zero as to get $\Delta T_f^{str} = \Delta T_f^{unstr}$, yields a daily mean cooling heat flux expression as:

$$\overline{Q_{cool}} = \left[\frac{F(H_{str}).H_{unstr} - F(H_{unstr}).H_{str}}{H_{unstr} - H_{str}}\right]\overline{Q_{SWR}} \tag{3.3}$$

Using the expression for $\overline{Q_{cool}}$ in equation 3.3, we derive an expression for Q_{cross} as $\overline{Q_{SWR}} - \overline{Q_{cool}}$ (or the $\overline{Q_{net}}$ value where $\Delta T_f^{str} = \Delta T_f^{unstr}$), where H^* as the ratio between H_{unstr} and H_{str}:

$$Q_{cross} = \left[\frac{H^*[1 - F(H_{str})] - [1 - F(H_{unstr})]}{H^* - 1}\right]\overline{Q_{SWR}} \tag{3.4}$$

We use equation 3.4 for a representative case in this chapter (H_{str}= 5 m and H_{unstr}= 40 m)

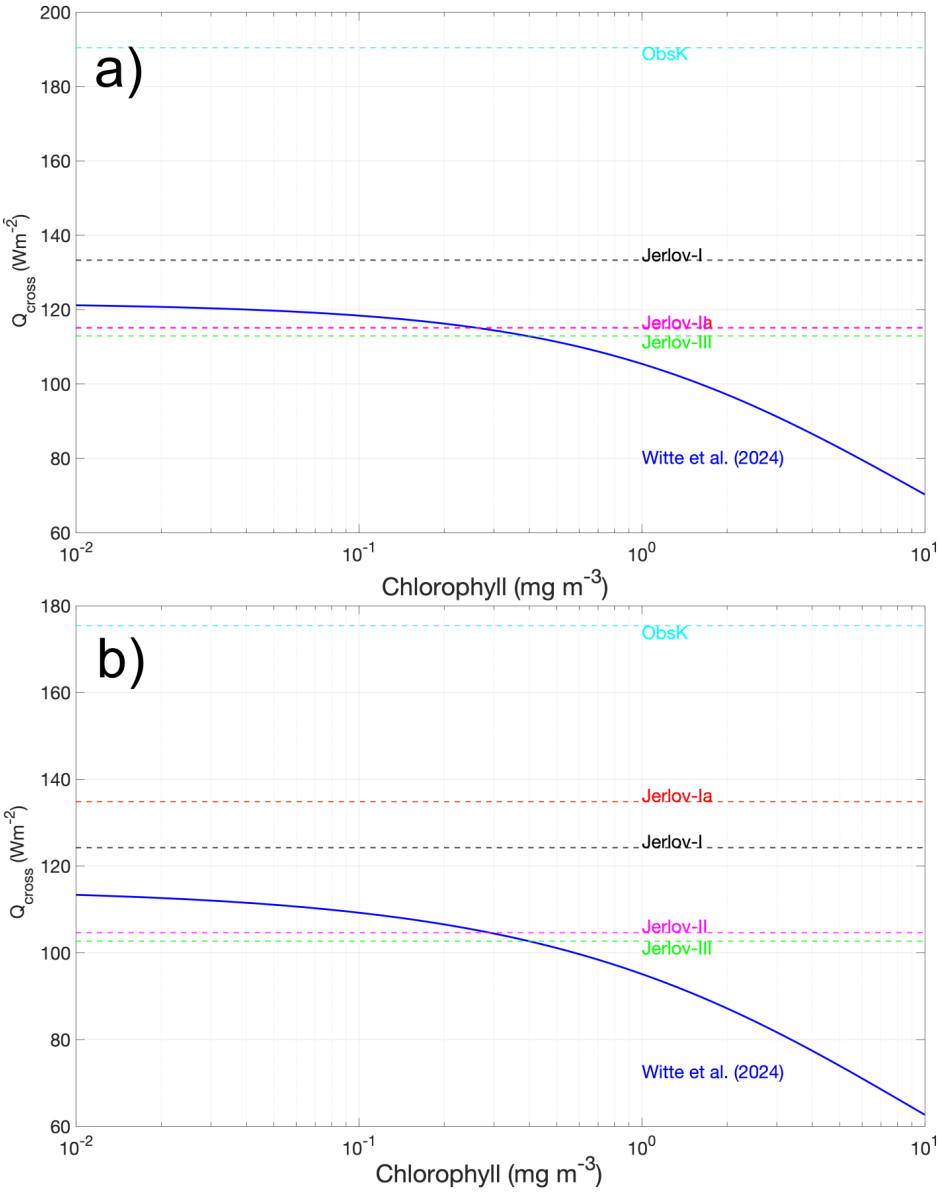

Figure 3.14: (a) Q_{cross} (in blue) as a function of Chlorophyll (log-scale in x-axis) based on optical profiles from Witte et al. (2024) for H_{str}=5 m and H_{unstr}= 40 m. Colored horizontal lines represent Q_{cross} corresponding to different Jerlov water types (as described in Paulson and Simpson 1977), and to an observed optical profile in the Bay of Bengal (light blue, Schlosser et al. 2022). Black, red, magenta, and green lines indicate Jerlov types I, Ia, II, and III, respectively. (b) is same as (a) for the special case where H_{unstr} is much larger than H_{str} (equation 3.5).

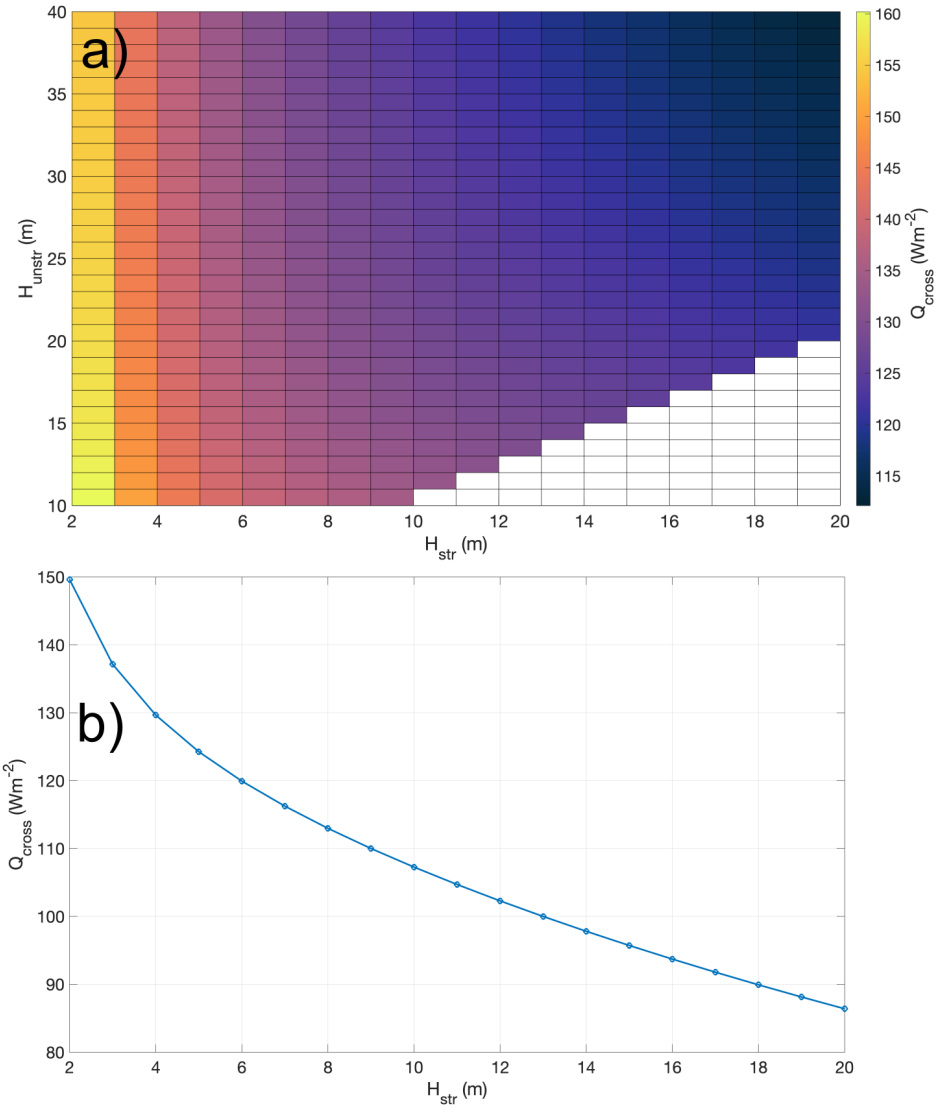

Figure 3.15: (a) Q_{cross} as a function of H_{str} (x-axis) and H_{unstr} (y-axis) for Jerlov-I water type for a typical clear sky day in April (based on equation 3.4). (b) Q_{cross} as a function of H_{str} for Jerlov-I water type in the special case where H_{unstr} is much larger than H_{str} (equation 3.5).

to estimate Q_{cross} using both theoretical optical profiles (Paulson and Simpson, 1977) and observed optical profiles from the NBoB (Schlosser et al., 2022; Kerhalkar et al., In Review).

We also incorporate chlorophyll-dependent optical profile parameterizations based on Witte et al. (2024) to examine the influence of chlorophyll on Q_{cross}.

Our results show that for a typical clear sky day in April, Q_{cross} values derived using theoretical optical profiles range between 115 to 135 $\mathrm{W\,m^{-2}}$ (Figure 3.14a). Q_{cross} values for Jerlov-I water type is calculated to be around 135 $\mathrm{W\,m^{-2}}$, compared to about 190 $\mathrm{W\,m^{-2}}$ when derived for the NBoB observed optical profiles. This higher Q_{cross} value aligns with the NBoB observations of waters clearer than Jerlov-I at times (pers comm: Tamara Schlosser). Enhanced water clarity promotes deeper SWR penetration, which accounts for the higher derived Q_{cross}. Q_{cross} for chlorophyll-dependent optical profiles reveals a monotonic decrease with a nonlinear decay as chlorophyll increases, with values ranging from 75 to 120 $\mathrm{W\,m^{-2}}$ (Figure 3.14a). For optical profiles corresponding to murkier waters (i.e., higher chlorophyll concentrations), Q_{cross} values are lower due to increased absorption of SWR within the MLD. Varying the values of H_{str} and H_{unstr} for Jerlov-I water type reveals Q_{cross} values ranging from 110 to 160 $\mathrm{W\,m^{-2}}$ (Figure 3.15a). Highest Q_{cross} values occur for shallower H_{str}. Conversely, Q_{cross} reaches its minimum when both H_{str} and H_{unstr} are deep.

A special limiting case occurs assuming that $H_{unstr} \gg H_{str}$. This represents a well-mixed scenario with an effectively infinitely deep mixed layer and pycnocline, when equation 3.4 simplifies to:

$$Q_{cross} = [1 - F(H_{str})]\,\overline{Q_{SWR}} \quad . \tag{3.5}$$

The Q_{cross} values estimated using the simplified case of an infinitely deep unstratified mixed layer ($H_{unstr} \gg H_{str}$; Equation 3.5) closely align with those from the full formulation discussed earlier (Figures 3.14b and 3.15b; Equation 3.4).

To verify the validity of the Q_{cross} formulation in Equation 3.4, we conducted a suite of 1-D simulations with varying stratified mixed layer depths (H_{str}), daily mean net heat flux ($\overline{Q_{net}}$), and wind speeds. The results show that Q_{cross} estimates from the simulations closely

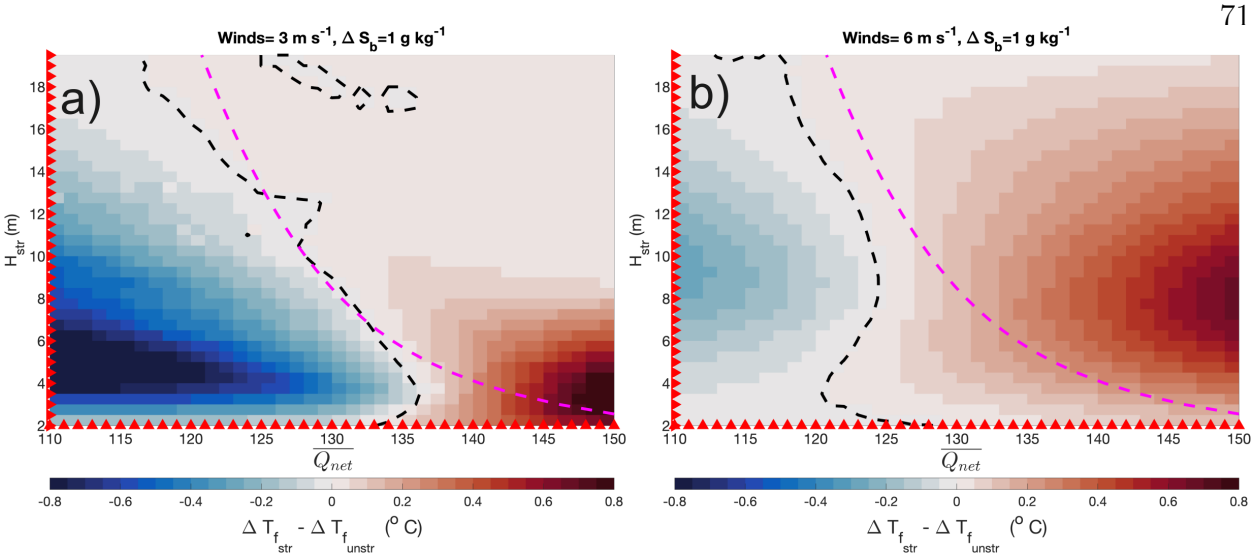

Figure 3.16: (a) Difference in ΔT_f over a 30-day period between a salinity-stratified scenario (varying H_{str}, $\Delta S_b = 1\ \mathrm{g\,kg^{-1}}$) and an unstratified (or deeper-stratified) scenario ($H_{unstr} = 20$ m, $\Delta S_b = 1\ \mathrm{g\,kg^{-1}}$) as a function of daily mean net heat flux ($\overline{Q_{net}}$, x-axis) and H_{str} (y-axis) for Jerlov-I water type and wind speed of $3\ \mathrm{m\,s^{-1}}$. The black dashed line indicates the contour where the difference in ΔT_f is zero (i.e., Q_{cross} from GOTM simulations), while the magenta dashed line indicates Q_{cross} from Equation 3.4. Red markers on the axes denote the parameter values used in the simulations. (b) Same as (a), except with wind speed of $6\ \mathrm{m\,s^{-1}}$.

match the theoretical values from Equation 3.4 under low-wind conditions (Figure 3.16a). For $6\ \mathrm{m\,s^{-1}}$ wind speeds, however, the model-derived Q_{cross} deviates from the theoretical formulation by about 5–10 $\mathrm{W\,m^{-2}}$ (Figure 3.16b), highlighting the weaker influence of entrainment on the Q_{cross} formulation in Equation 3.4. Importantly, the overall trend of Q_{cross} from model simulations is consistent with the theoretical estimates. These results are not strongly dependent on the turbulence closure scheme, as similar behavior is obtained in 1-D GOTM simulations using the Mellor–Yamada scheme (Figure 3.17; Mellor and Yamada 1982).

The theoretical framework developed in this section not only highlights the unique roles of the initial upper ocean structure, water's optical properties, and surface heat fluxes in

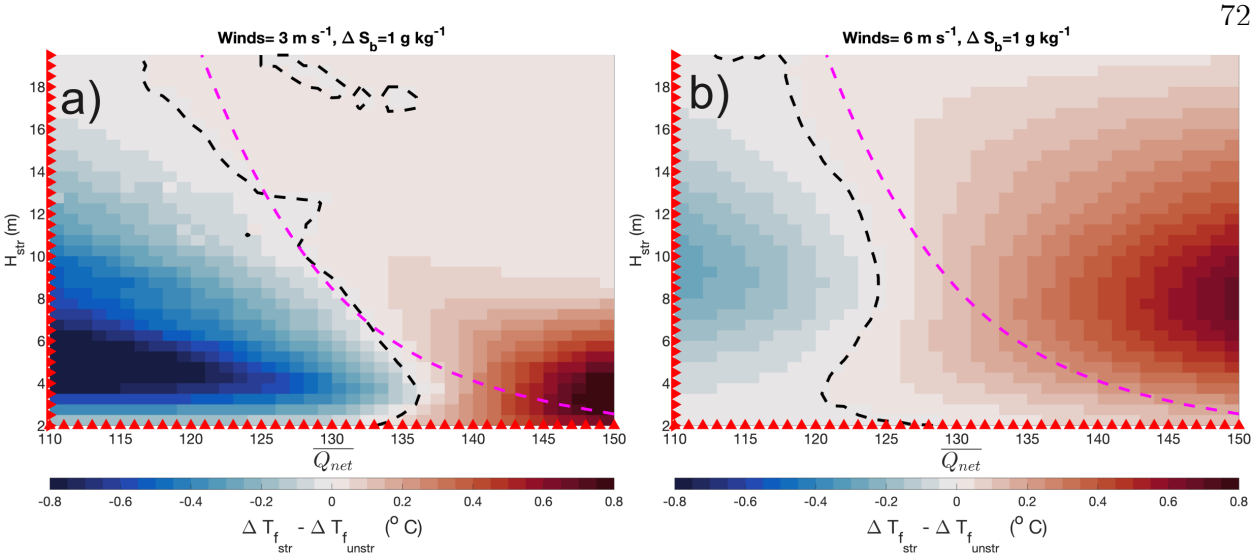

Figure 3.17: Same as Figure 3.16 except for GOTM is run with Mellor-Yamada turbulence closure scheme (Mellor and Yamada, 1982).

characterizing SST evolution and its spatial variability, but also provides crucial quantitative insights into the often ambiguous influence of salinity stratification on this evolution.

3.7 Discussion

The results presented here highlight significant differences of O(1°C) in foundational SST warming (ΔT_f) across intra-seasonal timescales and over mesoscale and smaller lengths in the Northern Indian Ocean. These variations reflect spatial differences in surface heat fluxes, wind speed, salinity stratification, and water optical properties, all of which are observed to vary across these scales (e.g., Song et al., 2022; Nuijens et al., 2024; Shroyer et al., 2016; Kerhalkar et al., In Review; McKie et al., 2024; Pimentel et al., 2019). Idealized 1-D simulations forced with surface heat fluxes from in-situ moorings reveal that O(0.5°C) of the ΔT_f differences are attributable to the role of salinity stratification. Both stratified and unstratified scenarios warm in an absolute sense but differ in relative heating. These simulations further show that when daily mean net heat flux ($\overline{Q_{net}}$) exceeds a critical threshold

(Q_{cross}), the stratified conditions lead to stronger warming compared to unstratified cases. The opposite is true for daily mean net heat fluxes below Q_{cross}. This response contrasts with the influence of salinity stratification on diurnal SST amplitudes, which consistently increase by about 0.07 °C to 0.15 °C under stratified conditions regardless of the heat flux regime (Kerhalkar et al., In Review). The ΔT_f differences described above also suggest a possible feedback on the surface heat fluxes (particularly the cooling component of heat fluxes) driven by salinity stratification, which is not accounted for in the above simulations. To explore this, we use 1-D GOTM in a one-way coupled configuration such that the model is forced with observed meteorological conditions. The model computes the fluxes internally based on the COARE algorithm (Fairall et al., 1996b) using the model-derived SSTs. Results from these coupled simulations confirm that the influence of salinity stratification on ΔT_f differences persists (Figure 3.18) and reveal that the resulting impact on surface heat fluxes are O(10 W m^{-2}) (Figure 3.19).

While the physical mechanisms discussed here are robust, the magnitude of ΔT_f over intra-seasonal timescales is sensitive to vertical entrainment (e.g., Seager et al., 1988). Recent studies have shown that entrainment beneath the mixed layer and hence the SST is sensitive to the choice of the 1-D model/turbulence closure scheme (Johnson et al., 2023). Because entrainment could potentially modify the mixed layer depth, Q_{cross} may be sensitive to the chosen mixing scheme and the temporal evolution of the mixed layer (which is not captured as stratification in the GOTM does not change much during the simulation period).

Our discussions of Q_{cross} in this chapter are currently limited to clear sky conditions. However, the application of the derived formulation (equation 3.4 and 3.5) indicates that the values of Q_{cross} in the North Indian Ocean can range between 50-150 W m^{-2} depending on the time of the year, cloud cover conditions in the region for Bay of Bengal and Arabian Sea (Figure 3.20) for a H_{str} and H_{unstr} of 5 and 40 m respectively and Jerlov-I water type

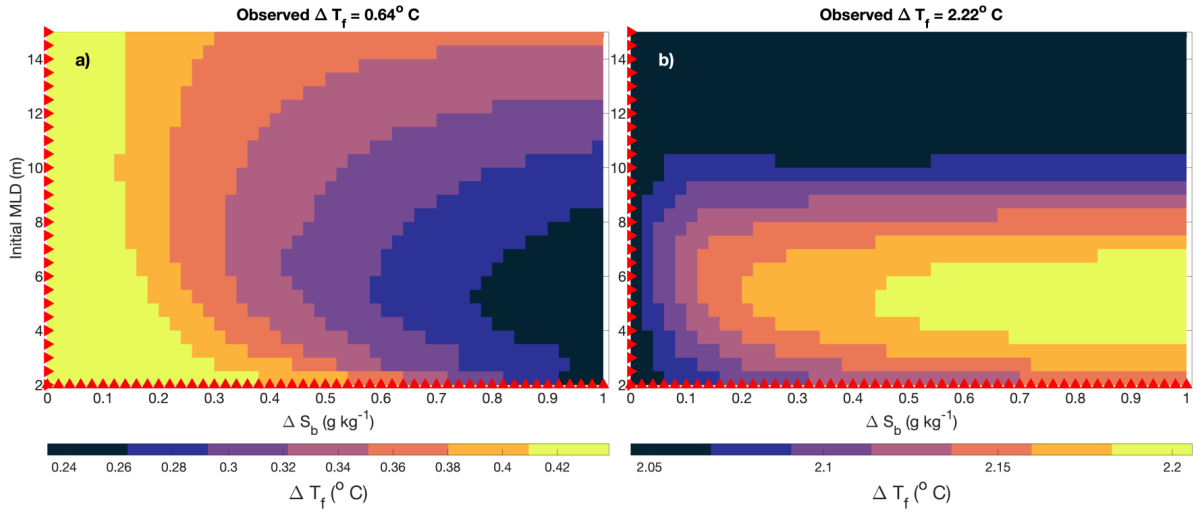

Figure 3.18: Same as Figure 3.10, but for the case where GOTM is used in a one-way coupled configuration (GOTM is forced with observed meteorological conditions and computes the fluxes internally using the COARE algorithm (Fairall et al., 1996b) based on model-derived SSTs.)

(Paulson and Simpson, 1977). Comparison of Q_{cross} with observed daily mean net heat flux ($\overline{Q_{net}}$) at AD08 and ASIRI moorings shows that the latter exceeds Q_{cross} 11.6% of the time in SEAS (AD08) and 21.4% at the ASIRI mooring in NBoB over the observation period (Figure 3.20). During February–May (mini–warm pool formation), these probabilities are 10.8% at SEAS (AD08) and 38% at NBoB (ASIRI). Allowing for a 5 W m^{-2} uncertainty in Q_{cross} due to vertical entrainment (see Section 3.6) increases the exceedance frequencies to 15.7% and 26% for SEAS and NBoB respectively (period average), and to 15.8% and 48% during the mini–warm pool months in SEAS and NBoB respectively (Figure 3.20). Using fluxes from the MERRA-2 reanalysis for 2015 (Global Modeling and Assimilation Office (GMAO), 2015) in the Northern Indian Ocean, we find that the probabilities of $\overline{Q_{net}}$ exceeding Q_{cross} (Figure 3.21) are similar to those reported from in-situ observations, with clear spatial variability in the probabilities.

Building on the earlier discussion of Q_{cross}, these results imply that in regions with promi-

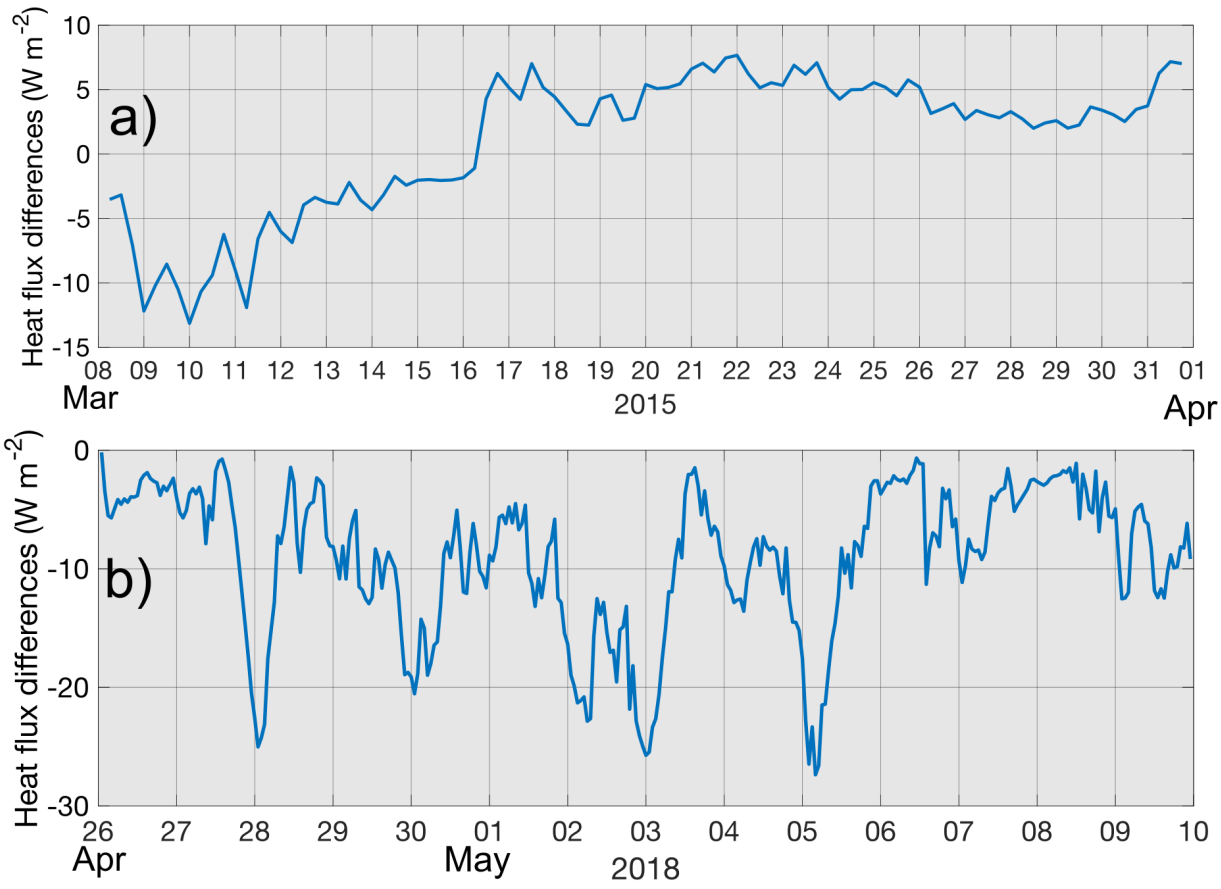

Figure 3.19: Difference in air-sea heat flux between the stratified (initial MLD= 6 m and ΔS_b= 1 g kg^{-1}) and unstratified scenarios (no salinity stratification) for GOTM runs in one-way coupled configuration (see Figure 3.18 caption) for (a) ASIRI mooring in NBoB and (b) AD08 mooring in SEAS. Positive values indicate that the net heat flux is higher in unstratified scenario than in stratified scenario.

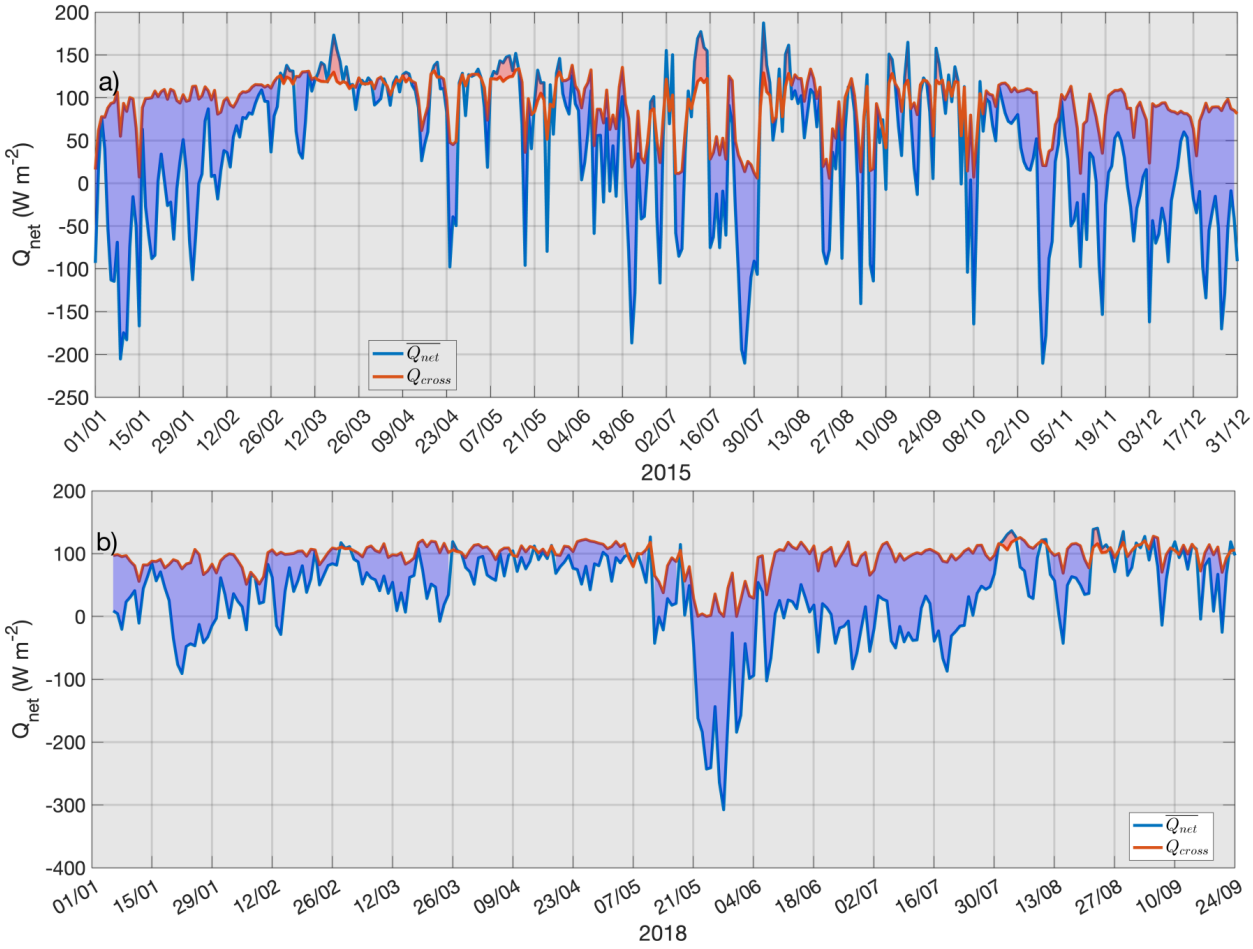

Figure 3.20: (a) Daily Q_{cross} values (in red) based on the Shortwave radiation data from the ASIRI mooring in the NBoB region for the year 2015, assuming H_{str}=5 m and H_{unstr}=40 m. Daily mean net heat flux ($\overline{Q_{net}}$) observed at the ASIRI mooring during the same duration is indicated by blue line. The red shaded areas indicate times when $\overline{Q_{net}} > Q_{cross}$, while the blue shaded areas are times when $\overline{Q_{net}} < Q_{cross}$. (b) is the same as (a) for AD08 mooring in the SEAS region between January and September 2018.

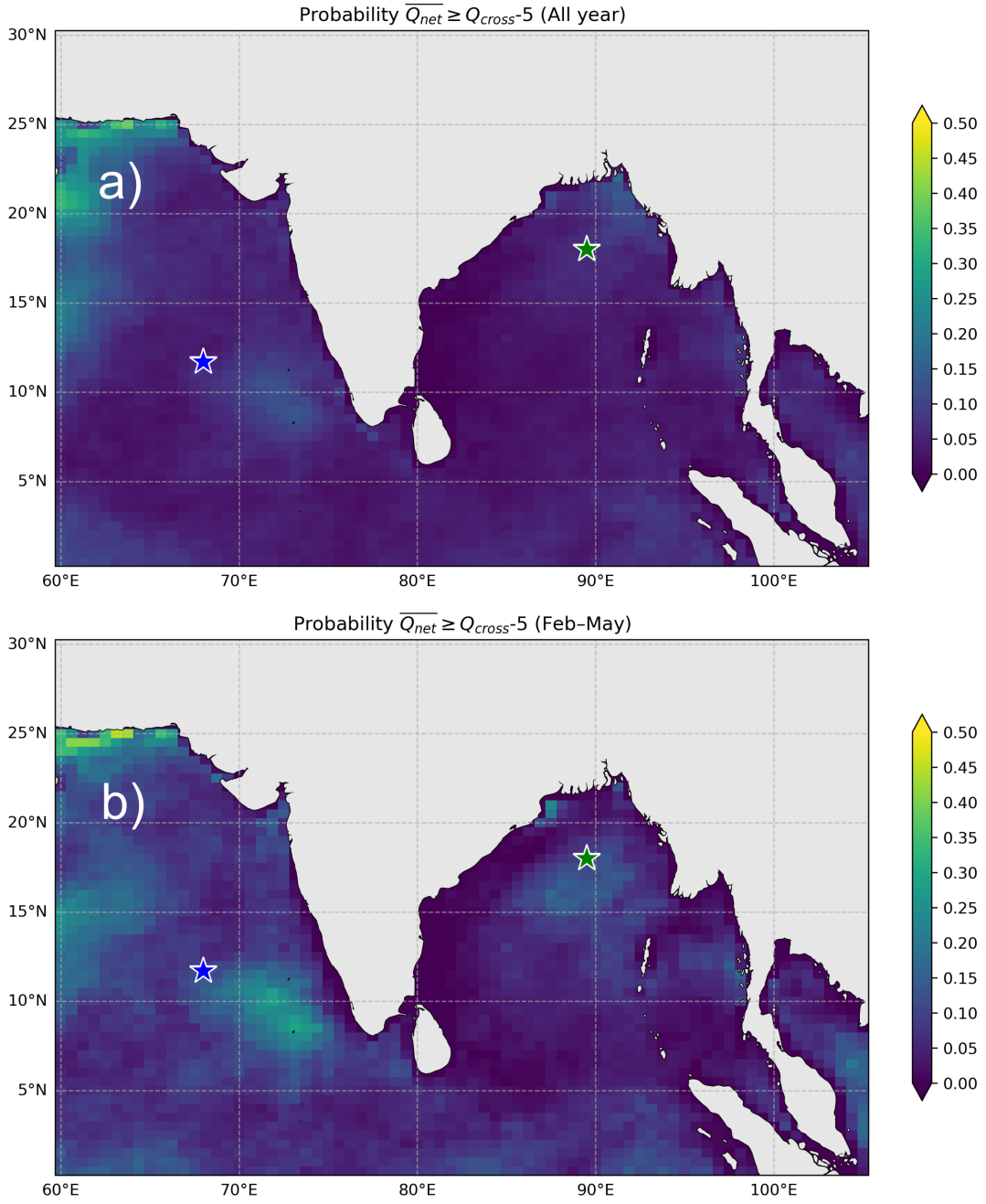

Figure 3.21: (a) Probability of daily mean net heat flux ($\overline{Q_{net}}$) from MERRA-2 (Global Modeling and Assimilation Office (GMAO), 2015) exceeding daily Q_{cross} values-5 (to account for deviations due to vertical entrainment), assuming shortwave radiation from MERRA-2, with H_{str} = 5 m and H_{unstr} = 40 m, for the year 2015. Blue and green star indicate the AD08 mooring in SEAS and the ASIRI mooring in the NBoB, respectively. (b) Same as (a), but for February–May (mini warm pool formation period).

nent salinity fronts, differential ΔT_f across the front is expected. This could either enhance the density across the front or cause density compensation depending on the value of surface heat fluxes. However, these dynamics are likely to be influenced by unresolved processes such as mesoscale advection and submesoscale frontal activity, which are not represented in our 1-D framework (e.g., Buckley et al., 2020; Jaeger and Mahadevan, 2018; Kerhalkar et al., 2025).

Given the tight coupling between marine atmospheric boundary layer (MABL) and the ocean boundary layer (e.g., Seo et al., 2023; Sullivan et al., 2020, 2021), SST fronts can influence atmospheric convection, generate secondary circulations, and modulate other MABL characteristics on intraseasonal timescales (Skyllingstad et al., 2007). The resulting MABL adjustments subsequently modulate SST variability and upper ocean thermal structure. The SST variability and the upper ocean thermal strucuture during the pre-monsoon heating periods examined in this chapter are crucial for driving key air-sea interaction processes, such as tropical cyclone development (Vinayachandran et al., 2007). They also affect monsoon forecasts across sub-seasonal to seasonal timescales (Krishnamurti et al., 2007). To improve our understanding of these phenomena, it is important to study such interactions between the ocean and atmospheric boundary layers more closely.

3.8 Conclusion

The northern Indian Ocean experiences strong upper ocean heating during the spring intermonsoon season that precedes the monsoon (Figure 3.1). Over 90% of the days during this period show a net heat gain by the ocean (Figure 3.2). However, remote sensing observations reveal that this heating is spatially heterogeneous, with intra-seasonal (15–60 day) differences in T_f warming rates of O(1°C) across mesoscale and smaller lengths (< 100 km). These variations are accompanied by lateral differences in surface wind speeds and salinity of O(2 $\mathrm{m\,s^{-1}}$) and O(2 $\mathrm{g\,kg^{-1}}$) respectively (Figure 3.3). Argo float profiles further indicate

variability in mixed layer depths of O(25 m) across the region. All of the above mentioned factors can contribute to the spatial variability in the surface heating rates as well as air-sea heat flux values on intra-seasonal timescales.

To evaluate the role of salinity stratification in modulating these gradients, we conducted a suite of 1-D simulations. Simulations forced with realistic surface fluxes from mooring records in the northern Indian Ocean, reveal 0.2-0.5°C differences in ΔT_f change over 14-21 days due to salinity stratification differences (Figure 3.6-3.10). This variability is evident only for cases with shallow initial mixed layers (< 14 m). Interestingly, the role of salinity stratification on the ΔT_f is contrasting; for the Arabian Sea scenario, the stratified case warms comparatively less than the unstratified case (Figure 3.6, 3.10a), whereas for the Bay of Bengal, the stratified case have higher or lower warming rates than the unstratified case at times (Figure 3.6, 3.10b, 3.7- 3.11). To further investigate this contrast, we conduct idealized simulations with constant wind speeds, diurnally varying shortwave radiation (for a clear-sky day scenario), constant cooling components of heat fluxes and optical properties of water (Figure 3.5d, Table 3.1). Our results demonstrate that relative warming in stratified case when compared to unstratified case is sensitive to the net surface heat flux and optical properties of water. Under higher daily mean net heat flux and more turbid scenarios, the stratified cases warm comparatively more than the unstratified case (Figure 3.12, 3.13). This suggests that in regions with strong salinity fronts, elevated heat fluxes and turbidity can enhance density contrasts across the front, which is more pronounced under higher wind speeds. In contrast, the initial salinity front may become partially density-compensated due to comparitively reduced warming in the stratified case than unstratified during lower daily mean net heat flux or clearer water conditions. This particular effect is pronounced under lower wind speeds.

Finally, we derive an analytical expression for crossover heat flux (Q_{cross}), defined as the

heat flux at which stratified and unstratified scenarios have an equal ΔT_f. When the daily mean net heat flux values exceeds Q_{cross}, presence of salinity stratification causes comparatively more surface warming than in unstratified cases. Q_{cross} is found to be a function of water's optical properties, inital mixed layer depth for stratified and unstratified cases and the daily mean shortwave radiation. For a representative case of mixed layer depths of 5 m and 40 meter for stratified and unstratified cases respectively under clear sky conditions with peak shortwave radiation of 1000 $\mathrm{W\,m^{-2}}$, Q_{cross} vary between 110 $\mathrm{W\,m^{-2}}$ (for Jerlov-III water type) and 135 $\mathrm{W\,m^{-2}}$ (for Jerlov-I water type, Figure 3.14a, 3.15a). Assuming an infinitely deep mixed layer for the unstratfied case, the above Q_{cross} values change to 103 $\mathrm{W\,m^{-2}}$ and 125 $\mathrm{W\,m^{-2}}$ respectively (Figure 3.14b, 3.15b). The theoretical formulation of Q_{cross} is supported by 1-D model simulations, showing close agreement under low-wind conditions and consistent overall trends across turbulence closure schemes (Figures 3.16, 3.17). Additionally, the crossover flux values have a strong dependency on the optical absorption properties. The range of Q_{cross} values and the observed daily mean net heat fluxes helps to clarify the role of salinity stratification on different outcomes of surface warming observed in our simulation results, underscoring the unique role of bio-physical coupling in upper ocean heating. The differences in SST evolution and upper ocean heat distribution due to the role of salinity stratification and optical properties highlighted in this chapter could have potential impacts on tropical cyclone and monsoon forecasts.

Data availability statement

The NIOT mooring data are available at: http://do.incois.gov.in/. The WHOI mooring data from 2015 can be accessed at http://uop.whoi.edu/projects/Bengal/QCData.html. SMAP and OISST satellite data were obtained from www.remss.com. ARGO data were obtained using ARGOPy python library (Maze and Balem, 2020). Simulations were per-

formed using version 6.0 of the General Ocean Turbulence Model (GOTM), available at https://gotm.net/portfolio/.

Acknowledgements

Portions of this chapter are being prepared for submission to the *Journal of Geophysical Research-Oceans* authored by Siddhant Kerhalkar, Amit Tandon and Jennifer MacKinnon. The authors would like to thank US Office of Naval Research for their support to the ASIRI, MISO-BoB and EKAMSAT Department Research Initiative. S.Kerhalkar and A.Tandon were supported by N00014-17-1-2355, N00014-18-1-2799, N00014-19-1-2410 and N00014-23-1-2054. A.Tandon was additionally supported by N00014-23-1-2473. S.K would like to thank the Associate Provost's office, University of Massachusetts Dartmouth for their support through the Distinguished Doctoral Fellowship. S.K is additionally thankful to Tom Farrar, Alex Kinsella, Tamara Schlosser, Leah Johnson, Kenneth Hughes, Steven Lohrenz and Miles Sundermeyer for their stimulating discussions on various aspects of this work.

Chapter 4 Monsoon-Frontal Interactions Drive Cyclone Biparjoy's Wake Recovery in the Arabian Sea

Abstract

Cyclone-generated cold wakes enhance productivity and impact local air-sea interaction, paths and intensities of subsequent storms in the region. However, in-situ observations of recovery across such wakes are rare. A cold wake in the Arabian Sea was surveyed using multiple shipboard instruments approximately 10 days after the passage of Cyclone Biparjoy in 2023. The wake, nearly 30 km wide, had a stronger (weaker) buoyancy gradient at its eastern (western) edge and assumed a downfront (upfront) orientation relative to the southwesterly monsoon winds. This resulted in notable asymmetry in the vertical structure of temperature, salinity and velocity at the edges of the wake, indicating the importance of Ekman Buoyancy Fluxes and Mixed Layer Eddies. While the wake recovery following a cyclone is often attributed to one-dimensional diurnal heating and cooling, these observations underscore the role of interactions between monsoon winds and underlying three-dimensional submesoscale processes for a slow-moving cyclone wake recovery.

Key points

- Slow moving cyclone Biparjoy in the Arabian Sea triggers the formation of a cold, salty and productive wake, causing a 4°C drop in SSTs.
- In-situ observations reveal the asymmetric recovery of the cold wake, with differences in mixed layer depth and buoyancy gradients at edges.

Published in *Geophysical Research Letters* as Kerhalkar et al. (2025) – https://doi.org/10.1029/2024GL112413

Authors: Siddhant Kerhalkar, Ankitha Kannad, Alex Kinsella, Amit Tandon, Janet Sprintall, Craig M. Lee

- Winds interacting with the wake leads to Ekman Buoyancy Fluxes at sub-mesoscale length scales, emphasizing their role in wake's recovery.

Plain language summary

Tropical cyclones are known to create a cold trail of water mixed upward from deeper depths, but observations of recovery of the wake back to pre-cyclone conditions are rare. These wakes play a crucial role in modulating availability of nutrients in the ocean, impact local atmosphere-ocean interaction and future passage of storms in the region. This chapter describes the structure of the wake after slow-moving Cyclone Biparjoy traverses the Arabian Sea in 2023 and highlights processes associated with the wake recovery. Our observations reveal that the wake is asymmetrical in its density and velocity structure. This is a result of the interaction between southwest monsoon winds and the density differences at the edges of the wake. Alongside the daily cycle of heating and cooling, these interactions foster small-scale three-dimensional processes, that are found to be crucial for the cold wake recovery back toward typical pre-cyclone conditions.

4.1 Introduction

Tropical cyclones, known for their high wind speeds, create a cold (and sometimes salty) wake due to increased upwelling and vertical mixing, causing sea surface temperatures (SSTs) within the wake to drop by 2-4°C (Stramma et al., 1986). However, this wake forms asymmetrically relative to the cyclone track, usually to the right of the cyclone eye in the Northern Hemisphere, due to wind stress anomalies generated by cyclone passage (Price, 1981; Cornillon et al., 1987; Sanabia and Jayne, 2020). While the cold wake's formation as a result of upwelling and enhanced turbulent mixing is well understood (D'Asaro, 2003; Emanuel, 2003; D'Asaro et al., 2007; Yablonsky and Ginis, 2009; Vincent et al., 2012), its recovery back to pre-cyclone conditions has received less attention. Understanding the evolution of the cold wake and its recovery is critical as it can significantly impact ocean heat transport, and the

predictability of the path and intensity of subsequent storm systems that traverse the region (Emanuel, 2001; Pasquero and Emanuel, 2008; Karnauskas et al., 2021; Gutiérrez Brizuela et al., 2023). Significantly, cyclonic disturbances are often considered as the signature of the onset of Asian Monsoons, and hence, the cyclone wake conditions can impact the subsequent sub-seasonal predictions of monsoons (Krishnamurti et al., 1981; Evan and Camargo, 2011; Krishnamurti et al., 2007).

Early hypotheses suggested atmospheric surface forcing causes a wake recovery over 10 days or more (based on SST criterion defined in Price et al. 2008), but subsequent observational studies demonstrated that background advection also played a major role in the recovery of the cold wake (Mrvaljevic et al., 2013; Johnston et al., 2020). Numerical modeling results indicate that baroclinic instabilities at the edges of the cold wake lead to the formation of submesoscale mixed-layer eddies (Fox-Kemper et al., 2008; Smith et al., 2019; Yi et al., 2024). These small-scale eddies cause the initially vertical isopycnals at fronts to slump and become nearly horizontal, creating a more stable state and thus contributing to the wake's recovery adiabatically (Figure C.1 d-f, Haney et al. 2012; Mei and Pasquero 2012). In addition, winds blowing parallel to the fronts at the wake's edges can create asymmetric recovery patterns through Ekman Buoyancy Fluxes (EBFs). Specifically, winds that oppose the surface thermal wind shear (upfront winds) can drive cross-front density advection via Ekman flow, resulting in stable wind-driven buoyancy fluxes. The sheared Ekman flow displaces the front and causes initially vertical buoyancy gradients to become more horizontal (and thus restratifying in nature), facilitating wake recovery adiabatically (Figure C.1 a-c). Conversely, winds blowing in the direction of the surface thermal wind shear (downfront winds) lead to unstable conditions, enhancing mixing and deepening the mixed layer (thereby destratifying in nature), while also supporting frontogenesis and causing these fronts to remain relatively stationary (Thomas and Lee, 2005). EBFs also interact

with the restratifying effects of mixed-layer eddies and surface forcing, thereby accelerating the closure of cold wakes and driving complex recovery dynamics (Haney et al., 2012; Mahadevan et al., 2010).

Nonetheless, in-situ observations of lateral submesoscale processes affecting the recovery of the cold wake are lacking. For example, autonomous profilers such as Argo are typically not fast enough to capture the spatio-temporal evolution of the wake, even in highly networked field campaigns (e.g., D'Asaro et al., 2007; Johnston et al., 2021). While this challenge could be addressed with ship-based sampling, heightened surface waves associated with tropical cyclones along with other logistical obstacles render ship usage unfeasible unless the sampling strategy is critically timed, typically a few days after cyclone passage.

In this chapter, rare ship-based in-situ observations conducted in the Arabian Sea during the "Enhancing Knowledge of the Arabian Sea Marine Environment through Science and Advanced Training (EKAMSAT)" program, which sample the wake of slow-moving Cyclone Biparjoy in June 2023 are utilized. The goal of this chapter is to document the horizontal and vertical variability in the cyclone wake and its vicinity. This chapter first provides an overview of the instruments and satellite products used (Section 4.2). Following this, the cold wake recovery is discussed using unique observations, which also demonstrate the presence of submesoscale processes (Section 4.3). The findings of this chapter and their broader implications are discussed in Section 4.4.

4.2 Data and methods

A combination of measurements collected by a ship-mounted flow-through thermosalinograph (TSG) and an Underway CTD (uCTD) profiler was employed to investigate the temperature and salinity structures within the cold wake resulting from Tropical Cyclone Biparjoy in the Arabian Sea between 17-20 June 2023. The TSG provides measurements at 4 m depth based on R/V Revelle's seawater intake, while the uCTD collected profiles over the top 250

m with a vertical resolution of 4 m and a temporal resolution of 10 minutes (an approximate horizontal resolution of 1.7 km). Meteorological conditions were measured from sensors housed on the ship's bow mast. The velocity structure within the cold wake was measured using the Hydrographic Doppler Sonar System (HDSS, Pinkel 2012) over the top 550 m at a vertical resolution of 4.5 m. The mixed layer depth (MLD) is inferred from the uCTD measurements based on a 0.125 $\mathrm{kg\,m^{-3}}$ density difference from surface values (Monterey and Levitus, 1997), while the isothermal layer depth (ILD) is defined based on a 0.5°C temperature difference with respect to the surface values (Levitus, 1983). The barrier layer thickness (BLT) is the difference between the ILD and the MLD.

We also utilize various level-3 remote sensing products such as the 3-Day product from Advanced Microwave Scanning Radiometer-2 (AMSR-2, Wentz et al. 2014a) and NOAA 0.25° Daily Optimum Interpolation Sea Surface Temperature (OISST, Reynolds et al. 2007), a level-3 blended product combining microwave and infrared data, at a spatial resolution of nearly 25 km to examine the SSTs. Additionally, we assess the SST from level-2 versions of Moderate-resolution Imaging Spectroradiometer (MODIS) Aqua (NASA Goddard Space Flight Center, 2018) as well as Visible Infrared Imaging Radiometer Suite (VIIRS) on NOAA-20 and NPP platforms, with a spatial resolution of 750 m (Cao et al., 2013). We also use Advanced Very High Resolution Radiometer (AVHRR) SST data to obtain high-resolution nighttime images from the NOAA-18 and NOAA-19 platforms (Casey et al., 2010).

4.3 Results

4.3.1 Remote sensing of the cyclone wake recovery

Cyclone Biparjoy, a slow-moving cyclone with translation speeds of 1-2 $\mathrm{m\,s^{-1}}$ (Figure C.2a), formed over the southern Arabian Sea on 5 June 2023. It reached its peak intensity as a category-3 cyclone and moved northward before making landfall over Gujarat, India on 15 June (IMD, 2023). The cyclone's passage resulted in the formation of the cold wake

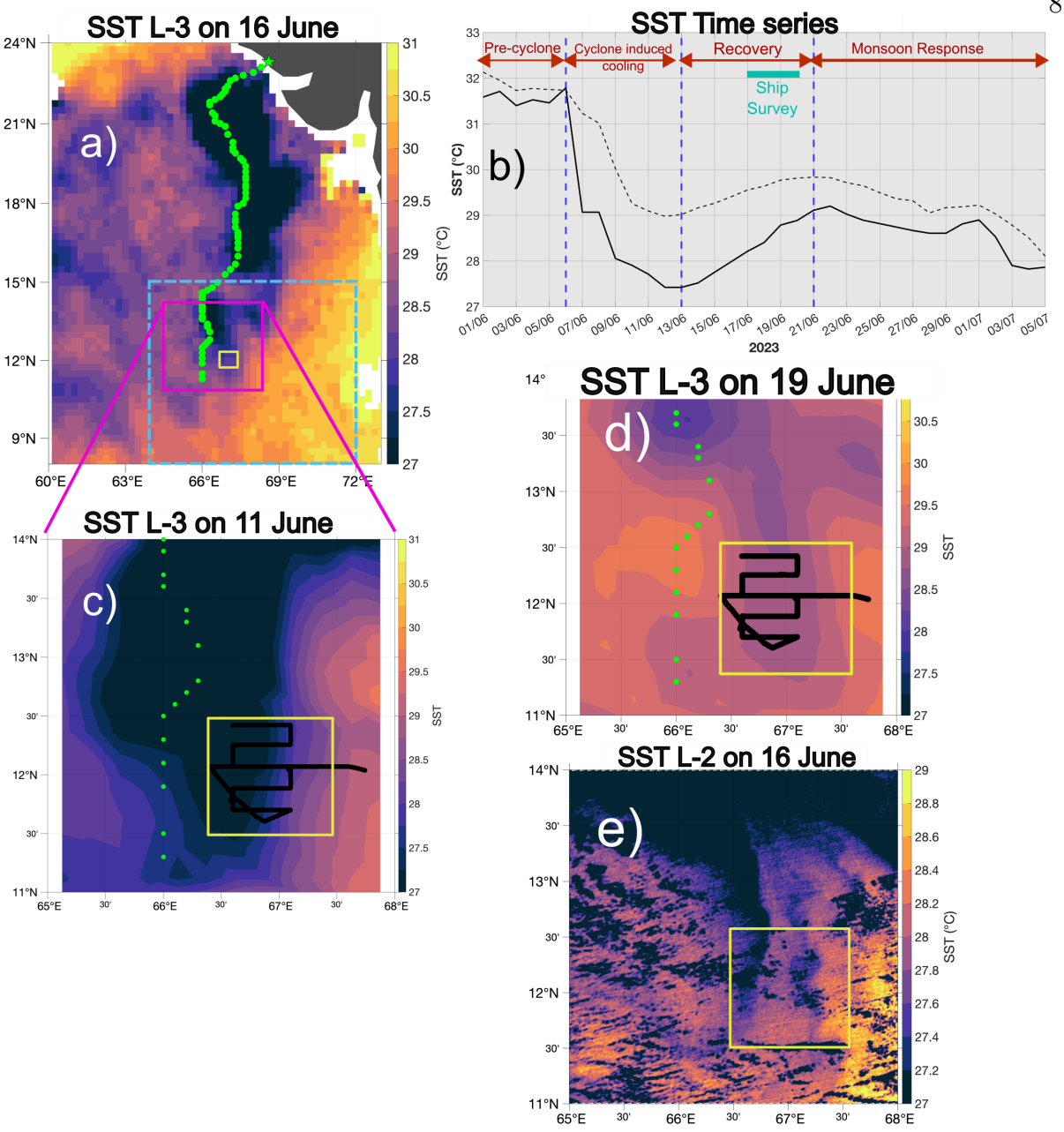

Figure 4.1: (a) SST from AMSR-2 on 16 June 2023. The green dots indicate the path of the cyclone Biparjoy (as obtained from IMD 2023). (b) Time series of mean SSTs from AMSR-2 between 1 June and 5 July 2023. The ship surveyed the wake 17-20 June and is indicated by cyan marker. Solid line indicates the mean SST over the smaller area around the ship operations in panel (a) (yellow solid box) while the dashed line indicates the same over the larger area in panel (a) (dashed blue box). (c) SST from AMSR-2 over the solid magenta box on 11 June 2023. (d) same as panel (c) but for 19 June 2023. Ship tracks are indicated by black lines in panels (c)-(d). e) MODIS Aqua L-2 product on 16 June 2023 over the same solid magenta box in (a). The black areas away from the cold wake in panel (e) are flagged as clouds or ice contamination. Yellow solid box in panels (c)-(e) indicate the area around the ship operations.

predominantly to the right of the track (Figure 4.1a), with a 4°C drop in SST over seven days (Figure 4.1b) at the ship's operational area (yellow box in Figure 4.1a).

The cyclone wake begins to recover on 13 June, which is identified by a rise in SST of 1.7°C over eight days (Figure 4.1b). With wind speeds and peak shortwave radiation in the wake area around 8 $\mathrm{m\,s^{-1}}$ and 940 $\mathrm{W\,m^{-2}}$ respectively (Figure C.3), the theoretical recovery period for the wake, if driven only by surface forcing, is estimated to be 18-29 days (see Appendix C.1, Price 1981; Haney et al. 2012). However, the rise in SST (or the surface recovery of the wake) ceases after 8 days instead (13-21 June, Figure 4.1b), reaching a steady state, although it fails to return to pre-cyclone values (Figure 4.1b). A large region of the southeastern Arabian Sea (marked by dashed blue line in Figure 4.1a) exhibits a similar lack of recovery to the pre-cyclone SST. The large-scale forcing by the monsoons over the Arabian Sea prevents the SST from recovering to pre-cyclone values (e.g., Weller et al., 2002). Additionally, the presence of small-scale lateral processes due to the cyclone wake, such as mixed layer eddies as well as EBFs, can contribute to the ambiguities in the recovery timescale (e.g., Haney et al., 2012).

A comparison of satellite maps of SST between 11 June and 19 June reveals a thinning and warming trend of the wake (Figure 4.1c,d, Figure C.4c-f). The western edge of the wake moves eastward under the influence of Ekman flow while the eastern edge remains nearly stationary (Figure 4.1c,d). This differential motion hints at the presence of EBFs around the wake. Additionally, the high resolution infrared L-2 images of SST highlights the complex structure of the wake, with a region of warm water surrounding two cold water zones, each around 27.4°C (Figure 4.1e, see Appendix C.2 for more detailed description). The edges of the wake also reveal its meandering nature, a detail that is often missed by coarser-resolution satellite products (Figure 4.1e). Given the meandering nature of the wake, which suggests the presence of lateral processes, and the observed wake recovery rate from

satellite SSTs exceeding theoretical estimates based on surface forcing, we next analyze in-situ subsurface measurements. These measurements help explore the wake's structure and further emphasize the role of lateral processes in explaining the discrepancy between observed and surface-forcing-based recovery rates.

4.3.2 In-situ survey of the wake

An in-situ survey from the ship's TSG and the uCTD system were conducted 10 days after the cyclone's passage to examine the structure of the generated wake (Figure C.3, C.5). The winds during this period were generally south-westerly (consistent with the direction of winds during the monsoon season, Figure C.3a). In the near-surface layer, the edges of the wake are characterized by colder waters (a difference of 0.72°C) compared to those in the vicinity of the wake (Figure 4.2a). However, the core of the wake is slightly warmer than its edges. The core is also saltier (a 0.45 $\mathrm{g\,kg^{-1}}$ difference) and denser (a 0.39 $\mathrm{kg\,m^{-3}}$ difference) than the surrounding waters. Due to this complex structure, the formation of the wake leads to the development of density fronts at its edges (despite the slight density compensation, see detailed secondary discussion in Appendix C.2). Subsequent observations during this survey also reveal the small-scale meridional variability of the wake, highlighting its meandering nature (Figure 4.2a,b). Additionally, the unique wake structure (with the warm wake core and cold edges) mentioned earlier is not observed during the repeat section (see Appendix C.2 and discussed further in this section).

The three-dimensional view of the sections reveals significant differences in the mixed layer structure throughout the wake and its vicinity (Figure 4.2c,d). Given the south-westerly winds and their orientation with respect to the wake-associated fronts, the presence of EBFs and mixed layer eddies is anticipated. These can potentially influence the upper ocean structure within the wake and its vicinity by causing an asymmetric recovery (Haney et al., 2012). To explore the vertical structure further, we next focus on the zonal section between

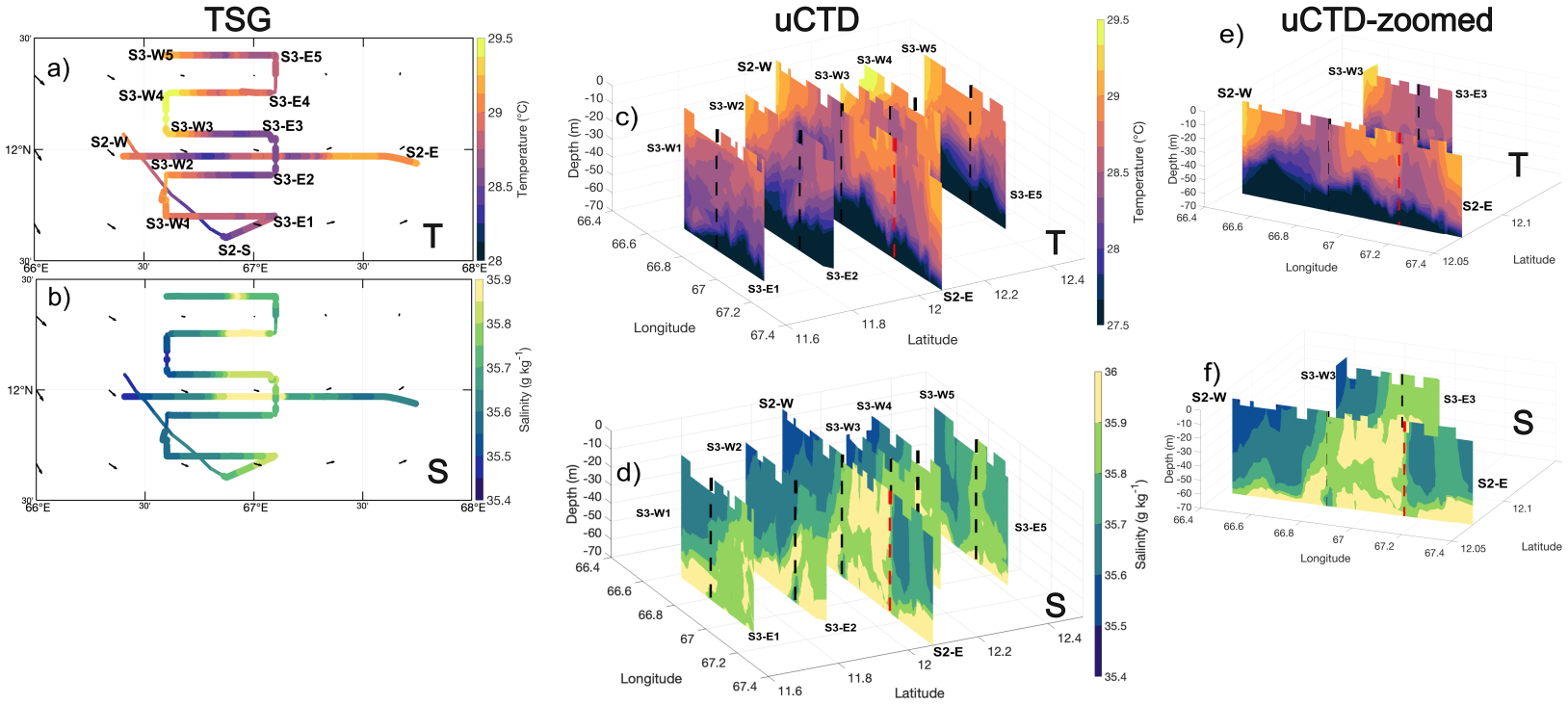

Figure 4.2: (a) Temperature and (b) salinity from the ship's TSG during the wake survey. (c) Temperature and (d) salinity from the uCTD during the wake survey. (e) and (f) are the same as (c) and (d) zooming into section S2-E to S2-W and section S3-E3 to S3-W3, respectively. The arrows in panels (a) and (b) are ocean surface currents from OSCAR (Dohan, 2021). Black dashed lines in panels (c)-(f) indicate the shift in meridional velocity over the mixed layer, marking the westward edge of the wake (see Figure 4.3 for more details). The red dashed line in panels (c)-(f) during the section S2-W to S2-E indicates the eastward edge of the wake. Panels (a), (c), (d), (e) and (f) feature various survey waypoints described in Table C.2. NOTE: The section S3-E3 to S3-W3 is on the same latitude as section S2-E to S2-W. For ease of visualization, the section S3-E3 to S3-W3 has been offset northward by 0.1° in panels (c)-(f), while the section S2-W to S2-E has been offset southward by 0.1° in panels (a) and (b).

the S2-E and S2-W waypoints. This section is the longest and captures both the eastward and westward edges of the wake (other sections only capture the westward edge, Figure 4.2).

Section between S2-E and S2-W

Sharp contrasts in velocity and salinity define the western and eastern edges of the cyclone wake, both of which are characterized by outcropping isopycnals of higher surface density (Figure 4.3). As mentioned earlier, the core of the wake is associated with warm and salty waters, while colder waters are found at the edges of the wake, which are surrounded by warmer and fresher waters. Within the wake itself, a MLD of 32 m and a BLT of 12 m are observed (Figure 4.3a,b). The wake is associated with weak eastward and northward flow (Figure 4.3c,d). The velocities in the vicinity of the wake contrast sharply with those within the wake (as further discussed below, Figure 4.3c,d).

The S2-E to S2-W section reveals an asymmetric nature associated with the wake recovery. To the west of the wake, isopycnals slope downwards to the west. The MLD is slightly shallower (by about 4 m) compared to within the wake itself (Figure 4.3a,b). This region is characterized by weak eastward flow (around 0.1 $\mathrm{m\,s^{-1}}$) and stronger southward velocities (0.3 $\mathrm{m\,s^{-1}}$). This flow contrasts sharply to the flow within the wake, producing strong horizontal shear at the front (Figure 4.3c,d).

Isopycnals east of the wake are sloping down to the east, with steeper slopes than those observed on the western edge. This region is also characterized by smaller scale features of O(1 km) around 67.2 ° E (Figure 4.2a,b). The MLD in the eastern edge is deeper (by 9 m), while the BLT is thicker (by 8 m) when compared to within the wake. Compared to the western edge of the wake, the eastern edge has a deeper mixed layer (by about 12 m) and a BLT that is nearly twice as thick. The flow in the eastern edge of the wake is weakly westward and northward. Upon eliminating the effects of the background flow

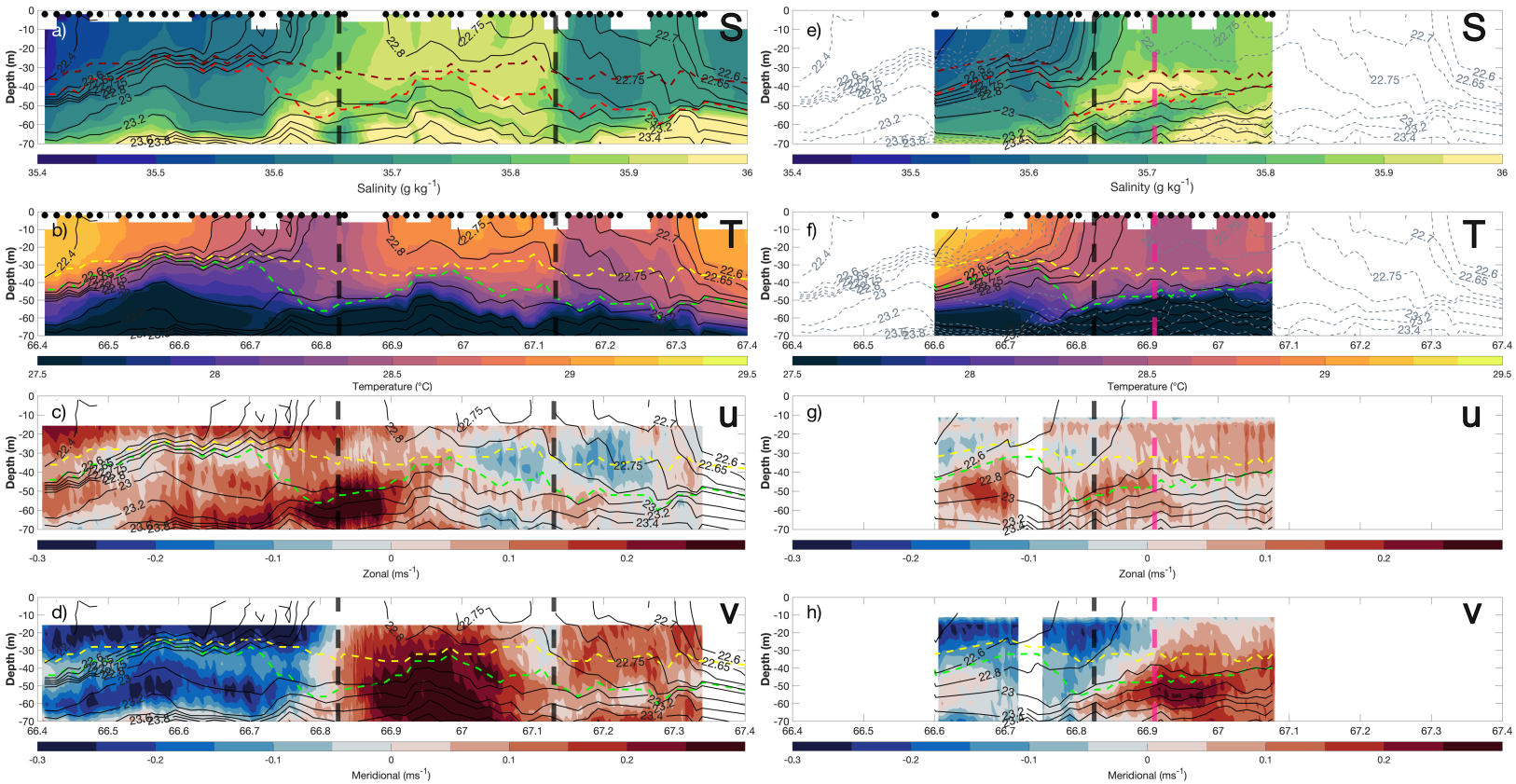

Figure 4.3: Vertical sections of (a) salinity, (b) temperature, (c) zonal velocity and (d) meridional velocity between S2-E and S2-W. The black dots in panels (a)-(b) are the individual uCTD profiles. Black contours in each panel indicate the isopycnals. The yellow (dark red in panel (a) line in panels (b)-(d) indicate the MLD while the green (red in panel (a) line indicate the ILD. Vertical black dashed lines indicate section dividers based on change in meridional velocity. Panels (e)-(h) are the same as (a)-(d) except the vertical section is between S3-W3 and S3-E3 (which is a shorter repeat section). The gray lines in panels (e) and (f) indicate the isopycnals from the original section (panels (a) and (b), respectively). The black dashed line in these panels is the westward edge of the wake in the original section (panels (a)-(d)) while the red dashed line is the westward edge of the wake in the S3-W3 and S3-E3 repeat section.

(by subtracting the mean velocities below the mixed layer depth along the whole section), evidence of weak convergence is observed in this area (Figure C.6).

Understanding the buoyancy gradients in the wake is crucial as they serve as reservoirs of potential and kinetic energy, which can catalyze instabilities and impact upper-ocean mixing and stratification (Haine and Marshall, 1998; Ferrari and Wunsch, 2009). The buoyancy gradients change signs along section S2-E to S2-W since the denser (i.e. less buoyant) waters within the wake are surrounded by lighter (or more buoyant) waters (Figure 4.4a). Asymmetry is observed in the surface buoyancy gradients as well, where the peak magnitude of the buoyancy gradient at the eastern edge of the wake ($2.5\times10^{-7}\ s^{-2}$) is 1.67 times higher than that on the western edge of the wake ($1.5\times10^{-7}\ s^{-2}$, Figure 4.4a). The buoyancy gradients associated with the cyclone wakes are of the same order of magnitude as within submesoscale meanders generated in the Gulf Stream (Shcherbina et al., 2015).

Estimates of buoyancy gradients (from uCTD) and south-westerly wind stresses (from ship-based meteorological measurements, Figure 4.4b) are used to calculate the Ekman buoyancy flux (EBF $= \frac{\tau_y}{\rho_o f}\frac{\partial b}{\partial x}$, where ρ_o is the reference density, f is the coriolis frequency, τ_y is the meridional wind stress while $\frac{\partial b}{\partial x}$ is the horizontal buoyancy gradient in the zonal direction). The temperature variation part of EBF is converted into equivalent Ekman heat fluxes (EHF $= \frac{\rho_o c_p (EBF_t)}{\alpha g}$, where $EBF_t = \frac{\tau_y}{\rho_o f}\alpha g\frac{\partial T}{\partial x}$. c_p is the specific heat of water, α is the thermal expansion coefficient and g is the acceleration due to the gravity). EHF values are found to be of O(500 W m^{-2}) at both edges of the wake (Figure 4.4b), significantly exceeding the observed surface heat fluxes, which have a daily average of approximately 150 W m^{-2} (Figure C.3b). Such elevated EHF values are capable of triggering submesoscale processes like frontal slumping and steepening (D'Asaro et al., 2011; Brannigan et al., 2015). This is further confirmed by calculating the Rossby number and Richardson number throughout the section, where these numbers are O(1) near the edges of the wake (Thomas et al., 2008).

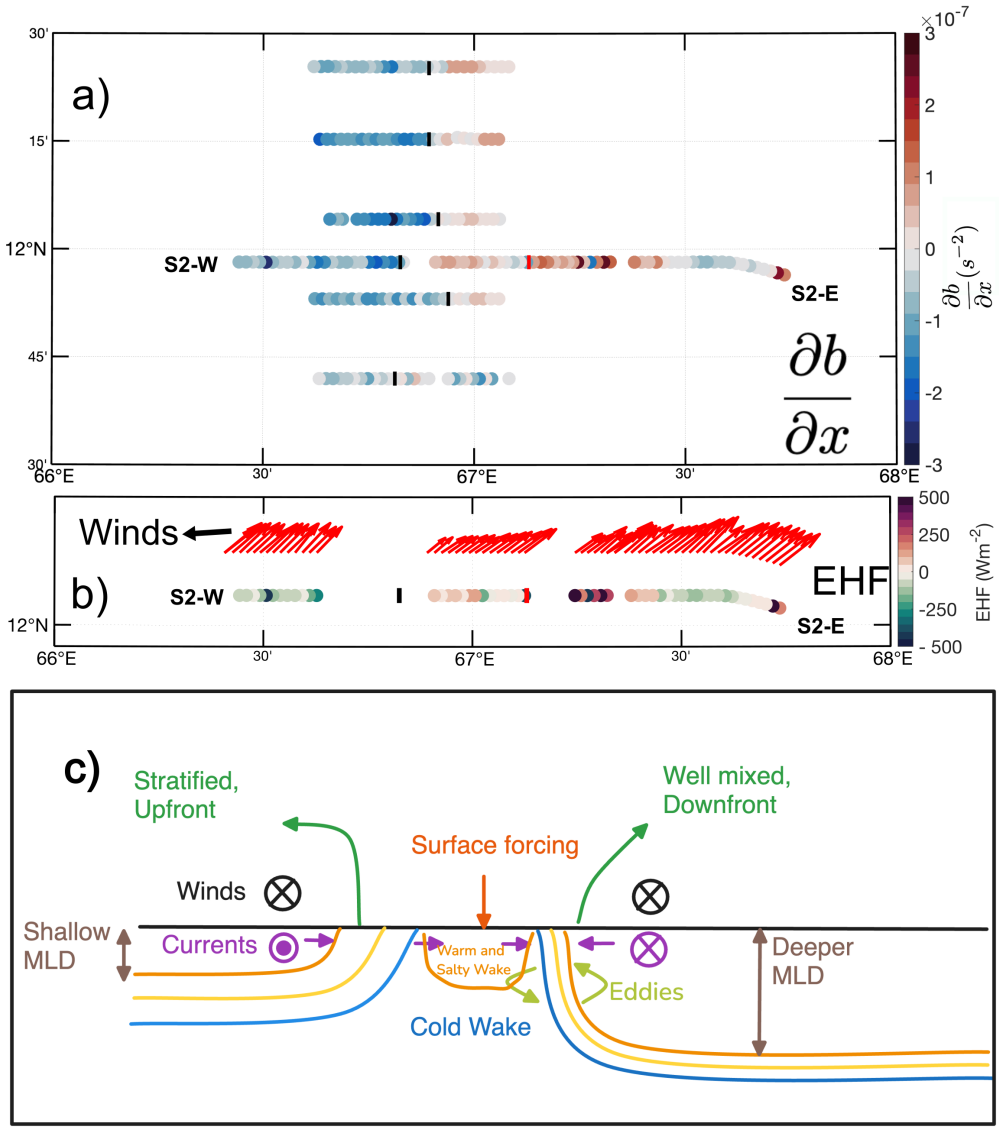

Figure 4.4: (a) Surface buoyancy gradients from the ship's survey in the wake and its vicinity. NOTE: The section S2-E to S2-W is offset by 0.1 ° to the south as to avoid overlap between repeating sections. (b) Ekman heat flux (EHF) in the section S2-W to S2-E. The red arrows indicate concurrent wind directions. Black line marker and Red line marker in panels (a)-(b) indicate the westward edge and eastward edge of the wake respectively. (c) Schematic explaining the forcing conditions and the asymmetric response of the cold wake in section S2-W to S2-E (adapted from Haney et al. 2012)

With respect to the orientation of the winds (Figure 4.4b) and the density gradients (Figure 4.3a-d, 4.4a), the western edge of the wake is forced by upfront wind component, while the eastern edge of the wake the winds have a significant downfront component. This explains the asymmetry observed in the vertical structure of the wake, where the west side (forced by upfront winds) is undergoing restratification (and hence shallower MLDs), while the east side (forced by downfront winds) has a stronger buoyancy gradient as a result of destratification (Figure 4.4c). This is consistent with the sign of the EHFs, which are stabilizing at the western edge of the wake and are destabilizing at the eastern edge. Despite the destabilizing effect from the EBFs at the eastern edge of the wake, the isopycnals are not fully vertical but slope down to the east, indicating ongoing restratification. Previous studies have shown that a front can undergo restratification even with a destratifying downfront configuration in the presence of mixed layer eddies (e.g., Mahadevan et al., 2010). Thus, the restratification at the eastern edge, despite its downfront configuration, provides indirect evidence of the presence of mixed layer eddies. Inferences about active restratification arise from the fact that the fronts in this case are yet to fully geostrophically adjust (a front is considered fully geostrophically adjusted when $N^2 = (\frac{\partial b}{\partial x})^2/f^2$, where N^2 is the vertical stratification, Tandon and Garrett 1994).

Using the theoretical scalings derived in Haney et al. (2012), we estimate that the separate recovery time scales associated with the surface forcing (T_{sf}), EBFs (T_{ebf}) and mixed layer eddies (T_{eddy}) are 29.6 ± 7, 25.4 ± 6 and 38.4 ± 8 days respectively (see Appendix C.1 for details of the scaling analysis). Thus, while EBFs alone lead to a slightly faster recovery rate, the combination of surface forcing and EBFs yields an estimated recovery timescale of 9 ± 2 days, while the combination of all of the above processes (including mixed layer eddies) results in an estimated recovery timescale of 7 ± 1 days (Appendix C.1). This timescale closely aligns with the observed SST recovery (Figure 4.1b), however high-resolution numerical

simulations are needed to further validate the recovery timescales quoted here. Nonetheless, this scaling analysis highlights that role of lateral processes like EBFs and mixed layer eddies in causing a faster recovery of the wake, underscoring the important role of wind-front coupling in such cases. Given the enhanced shear at the base of the mixed layer within the wake (Figure 4.3c,d), double-diffusive processes are not a significant contributor to the wake recovery (e.g., Kunze, 1990).

Section between S3-E3 and S3-W3: Repeat section

As mentioned previously, the zonal sections of the in-situ survey highlights slight meridional variations within the wake, thereby revealing the meandering nature of the wake (Figure 4.2, 4.4a). The repeat section between S3-E3 and S3-W3 (referred to as the repeat section hereafter) was conducted along the same latitude as the section S2-E to S2-W (discussed above, original section hereafter, Figure 4.2, Table C.2) nearly 28 hours later, and hence provided an opportunity to understand the evolution of the wake.

The repeat section is shorter and hence does not capture the eastward edge of the wake unlike the original section described above (Figure 4.2, 4.3e-h). However, the vertical structure of the repeat section is similar to the original section described above. The main difference is that the westward edge of the wake is displaced by 10 km to the east (Figure 4.3e-h) during the repeat section survey. This is also consistent with the disappearance of the unique wake structure (characterized by a warm core and cold edges) during the repeat section, as observed in both in-situ (Figure 4.2a,b) and satellite observations (Figure C.7c). This displacement could be due to several factors, including Ekman transport due to the south-westerly monsoon winds, advection by the background flow and/or near-inertial currents. While Ekman transport and advection are plausible causes, the near-inertial currents are less likely since Cyclone Biparjoy was initially a slow-moving cyclone (with translation speed of 1-2 $\mathrm{m\,s^{-1}}$, Figure C.2a), resulting in a smaller near-inertial response (Figure C.2c,

Price 1981). Near-inertial currents calculated using the slab model (Pollard and Millard, 1970) forced by MERRA-2 reanalysis product (Global Modeling and Assimilation Office (GMAO), 2015) were roughly 0.05 $\mathrm{m\,s^{-1}}$, which is about one-sixth of the observed currents in this section (Figure 4.3d,h).

4.4 Summary and discussion

Cyclone Biparjoy created a cold wake over the Arabian Sea in June 2023. SST began recovering post-cyclone, reaching steady state in 8 days, far more rapidly than the 18-29 days predicted by one-dimensional models forced by winds and surface fluxes (Price et al., 2008; Haney et al., 2012). The scaling of recovery timescales from Haney et al. (2012) using the observed parameters reveals that the Ekman Buoyancy Flux (EBF), surface forcing and mixed layer eddies have similar recovery timescales when acting in isolation (25.4 ± 6, 29.6 ± 7 and 38.4 ± 8 days respectively). However, an estimated recovery timescale of 7 days due to the combination of these processes closely matches the recovery timescale observed from satellite SSTs, highlighting the role of submesoscale processes in speeding up the recovery of the wake (Figure 4.1b).

In-situ observations across the wake reveal its asymmetrical structure during the recovery as a result of the presence of EBF. The asymmetry is caused due to the imposition of southwesterly winds on the wake, which leads to upfront forcing on the wake's western edge, leading to shallower MLDs and hence restratifying. In contrast, the wake's eastern edge is forced by downfront winds, with deeper MLD and a presumably destratifying nature. However, observations of sloped isopycnals at the eastern edge of the wake indicate a weak stratification, providing indirect evidence of the presence of mixed layer eddies (Fox-Kemper et al., 2008; Mahadevan et al., 2010). The EBF (O(500 $\mathrm{W\,m^{-2}}$)) as well as Rossby and Richardson numbers (both O(1)) associated with the cyclone wake were found to be sufficient to drive submesoscale processes at the edges of the wake as a result of the density gradients

and their interaction with the winds. Given that Cyclone Biparjoy was a slow-moving storm, the near-inertial currents were small. Additionally, in-situ observations across the wake also reveal its unique structure characterized by a warmer and saltier core with colder edges, surrounded by warmer and fresher waters. Such small scale differences within the wake structure are challenging to observe with coarser satellite measurements.

Results from this chapter present the first in-situ observations of a post-cyclone wake recovery in the Arabian Sea. Our observations emphasize the significance of the interaction between monsoon winds and the underlying three-dimensional submesoscale fronts in shaping the wake of a slow-moving cyclone through Ekman buoyancy fluxes. This contrasts with faster-moving cyclones, where near-inertial currents primarily dominate the wake evolution (Price, 1981). Understanding this recovery and the associated processes is vital, as it can influence ocean heat transport, nutrient availability (Babin et al. 2004), coral health (Dobbelaere et al., 2024), and the predictability of future cyclones and sub-seasonal weather patterns.

Data Availability Statement

Data from the instruments are embargoed under agreement between the U.S. and India until 2029 as one step in fostering the international collaboration. This time frame is intended to allow for students and postdoctoral researchers supported under the project to have sufficient time to publish observation-based results. After the embargo period, data may be requested from either the author (Siddhant Kerhalkar) or his advisor (Prof. Amit Tandon). The satellite data for AMSR-2 as well as OISST were obtained from `www.remss.com` , while the level-2 products of MODIS-Aqua and VIIRS were obtained from `https://oceancolor.gsfc.nasa.gov/cgi/browse.pl?sen=amod` . AVHRR SST data were obtained from `https://search.earthdata.nasa.gov/search` while OSCAR currents were obtained from `https:`

//podaac.jpl.nasa.gov/dataset/OSCAR_L4_OC_INTERIM_V2.0 . MERRA-2 data were obtained from https://disc.gsfc.nasa.gov/data-sets/M2T1NXLND_5.12.4/summary .

Acknowledgments

The authors gratefully acknowledge the support of the US Office of Naval Research for the EKAMSAT-ASTraL Department Research Initiative. S. Kerhalkar and A. Tandon received support from N00014-23-1-2054, A. Kannad and J. Sprintall from N00014-23-1-2091, A. Kinsella from N00014-23-1-2471, and C.M. Lee from N00014-23-1-2085. A. Tandon also acknowledges support from N00014-23-1-2473. The authors extend their gratitude to the Captain, crew, and science party of R/V Roger Revelle during the EKAMSAT pilot field campaign for their invaluable assistance with data collection. S. K. acknowledges the support of the Associate Provost's office, University of Massachusetts Dartmouth, through the Distinguished Doctoral Fellowship. Special thanks to Joaquim Goes, Charles Kovach, and Sherwin Ladner for their assistance in obtaining L-2 satellite images. The authors also thank Elizabeth J. Thompson, Ludovic Bariteau, Byron Blomquist, Chris Fairall and Sergio Pezoa (from NOAA PSL as a part of NOAA Global Ocean Monitoring and Observations program) as well as Joe (Harindra) Fernando, Jay Orson Hyde and Griffin Modjeski (from University of Notre Dame as a part of EKAMSAT-ASTraL) for their role in QC'ing the surface meteorological measurements presented here. Thanks to Eric D'Asaro for insightful discussions. The authors also thank the editor of *Geophysical Research Letters*, Dr. Kris Karnauskas, and the two anonymous reviewers for their constructive feedback during the peer review of the manuscript version of this chapter, which helped improve its clarity and impact.

Chapter 5 Dissertation Conclusions

Given the societal and economic relevance of monsoons in India, accurate prediction remains a critical priority. Northern Indian Ocean (NIO) plays an unprecedented role in shaping monsoon variability, as summarized in Chapter 1. This dissertation focuses on understanding air-sea interaction processes at mesoscale and submesoscale lengths. In particular, the strong influence of salinity on upper ocean stratification in this region as well as the presence of lateral salinity fronts motivates an in-depth investigation into how these factors modulate SST evolution and its spatial variability over mesoscale and submesoscale lengths. This investigation is performed over diurnal (Chapter 2) and intra-seasonal timescales (Chapter 3) using dense network of in-situ observations, remote sensing and 1-D modeling.

A synthesis of satellite-based and in-situ datasets reveals pronounced lateral differences in diurnal SST amplitudes across a range of spatial scales in the Bay of Bengal. Notably, these differences are more pronounced on days favorable for Diurnal Warm Layer (DWL) formation than on days when such conditions are not conducive. In-situ observations and 1-D modeling results suggest that variations in salinity stratification can account for up to 0.15 °C in spatial differences in diurnal SST magnitudes. Presence of enhanced salinity stratification causes an increase in diurnal SST magnitudes, particularly when the initial mixed layer depths are shallower.

Results from Chapter 2 also highlight that while lateral gradients in salinity stratification explain the bulk of median variability in diurnal SST magnitudes, extreme values of lateral differences in diurnal SSTs are likely influenced by additional factors. These include small-scale coastal plumes causing optical property variations (McKie et al. 2024; Pimentel et al. 2019), or variations in wind speeds (Song et al., 2022) and heat fluxes (e.g., due to patchy clouds or differences in cooling components; Nuijens et al. 2024; Song et al. 2022). Further insight into variability in sub-surface evolution of DWLs comes from the deployment of two

D-BASIS profilers for several days over a separation of roughly 30 km. Results highlight that advection and lateral disparities in pre-existing stratification drive significant variability in sub-surface DWL evolution, affecting the heat and turbulent kinetic energy budget over a diurnal timescale.

Chapter 3 investigates how salinity-driven stratification contributes to lateral differences in SST evolution on intraseasonal timescales. The chapter focuses on the spring intermonsoon season, a period marked by the formation of the mini-warm pool in the Northern Indian Ocean. During this time, both the southeastern Arabian Sea and northern Bay of Bengal exhibit pronounced salinity stratification, along with strong mesoscale variability in salinity and wind speed. Argo float observations indicate mixed layer depth variations of up to 25m across the region. Complementary satellite observations show that surface warming is spatially heterogeneous over mesoscale and smaller length scales during this season. Results from 1-D simulations with observed mooring surface fluxes indicate that differences in salinity stratification can lead to 0.2–0.5°C difference in SST change over an intra-seasonal period, particularly when the initial mixed layer depth is shallow (< 14m). Unlike the relatively straightforward enhancement of diurnal SSTs under stronger stratification, the effect on longer timescales is more nuanced. In the Arabian Sea, simulations consistently show that stratified cases warm less than their unstratified counterparts. In contrast, results from the Bay of Bengal exhibit mixed response, with stratified cases having higher or lower warming rates than the unstratified cases depending on the net surface heat flux and optical properties of water. Simulations with idealized surface forcing reveal that under stronger heating and more turbid conditions, stratified cases trap more heat and exhibit enhanced warming. Under weaker forcing or in clearer water scenarios, the stratified case may warm less, reducing density contrasts and partially compensating existing salinity fronts. These effects are further modulated by wind speed.

To generalize these outcomes, Chapter 3 introduces an analytical expression for the crossover heat flux (Q_{cross}), the threshold above which stratified scenarios produce more surface warming than unstratified cases. Q_{cross} depends on initial mixed layer depths of stratified and unstratified scnearios, shortwave radiation, and optical properties. For a representative case of mixed layer depths of 5 m and 40 meter for stratified and unstratified cases respectively under clear sky conditions with peak shortwave radiation of 1000 $W\,m^{-2}$, Q_{cross} varies between 110 and 135 $W\,m^{-2}$. Incorporating observed optical profiles based on chlorophyll from Witte et al. (2024), the crossover flux shows strong sensitivity to bio-optical conditions. Findings from Chapter 3 help clarify the role of salinity stratification on different outcomes of surface warming observed in the simulation results, underscoring the unique role of bio-physical coupling in upper ocean heating.

Preceding the onset of the monsoon, warmer surface waters during the spring intermonsoon season leads to an increased likelihood of cyclone formation. Chapter 4 investigates the oceanic response of one such event in the South-East Arabian Sea region. Cyclone Biparjoy generated a cold wake in June 2023, cooling the SST by 4°C. Satellite observations show that SSTs recovered within 8 days, significantly faster than the 18–29 days predicted by one-dimensional models driven solely by winds and surface heat fluxes (Price et al., 2008; Haney et al., 2012). Using the recovery timescale framework of Haney et al. (2012), the effects of Ekman Buoyancy Flux (EBF), surface fluxes, and mixed layer eddies individually have similar recovery timescales, yielding recovery timescales of 25.4 ± 6, 29.6 ± 7 and 38.4 ± 8 days respectively. When the combined effects of these processes are considered, the estimated recovery time reduces to approximately 7 days, closely aligning with the recovery timescale observed from satellite SSTs and underscoring the role of submesoscale processes in speeding up the recovery of the wake. In-situ observations across the wake further reveal its asymmetrical structure during the recovery as a result of the presence of EBF. The

asymmetry is caused due to the imposition of southwesterly winds on the wake. The western edge experienced upfront winds, resulting in shallow mixed layers and rapid restratification, while the eastern side underwent downfront forcing, associated with deeper mixed layers and enhanced mixing. However, sloped isopycnals at the eastern edge of the wake indicate a weak restratifying effect, hinting at the influence of mixed layer eddies (Fox-Kemper et al., 2008; Mahadevan et al., 2010). The EBF (O(500 $\mathrm{W\,m^{-2}}$)) as well as Rossby and Richardson numbers (both O(1)) associated with the cyclone wake were found to be sufficient to drive submesoscale processes at the edges of the wake as a result of the density gradients and their interaction with the winds. The wake also exhibited a distinct thermal and haline signature, with a warmer, saltier core flanked by colder edges and surrounded by fresher surface waters—fine-scale features that remain unresolved in coarse satellite datasets. The relatively slow translation speed of Cyclone Biparjoy limited the generation of near-inertial currents. These results underscore the importance of three-dimensional submesoscale processes, driven by wind–front interactions through Ekman buoyancy fluxes, in shaping cyclone wake recovery. Understanding these mechanisms is critical, as they affect heat redistribution, biogeochemical fluxes (Babin et al., 2004), coral reef health (Dobbelaere et al., 2024), and the predictability of subsequent storms and sub-seasonal atmospheric variability, including MISOs.

Overall, this dissertation examines the ocean's response to two extremes of weather categories: clear days with calm wind conditions as well as surface heating and tropical cyclone conditions. The findings help elucidate how salinity stratification contributes to spatial inhomogeneities in surface heating across mesoscale and smaller length scales, on both diurnal and intraseasonal timescales. This is particularly important in the context of the mini-warm pool in the Northern Indian Ocean, which is often assumed to be spatially homogeneous. Additionally, the dissertation highlights how submesoscale air-sea interaction processes can

accelerate the recovery of post-cyclone cold wakes. Collectively, these insights enhance our understanding of upper-ocean processes in the Northern Indian Ocean and offer pathways for improving the predictability of MISOs.

Appendix A Additional Material for Chapter 2

A.1 Additional details on the in-situ instruments

A.1.1 Surface Drifters

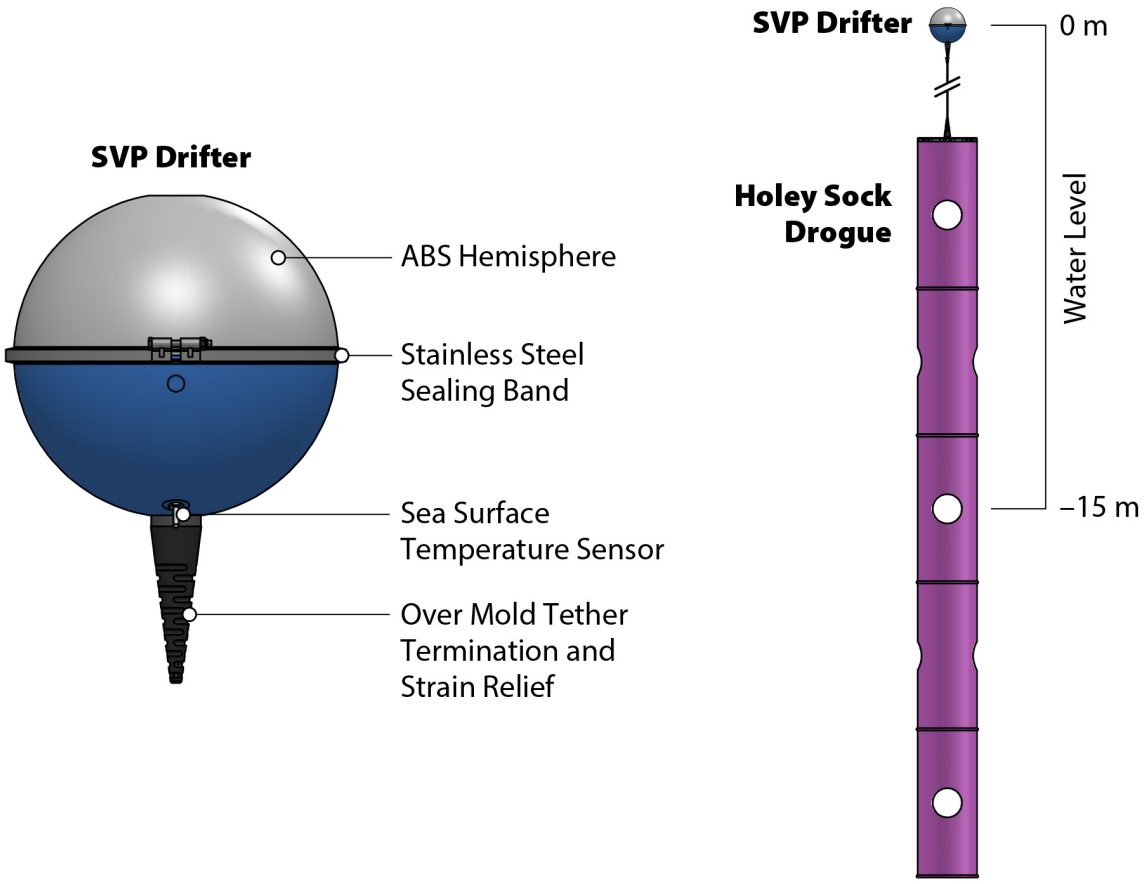

Figure A.1: Schematic of the SVP drifter designed and produced by the Lagrangian Drifter Laboratory at the Scripps Institution of Oceanography (adapted from Centurioni 2017).

The drifters used are part of the Surface Velocity Program (SVP), a component of the Global Drifter Program (Niiler et al., 1995; Centurioni et al., 2017). This instrument is

designed to map the near-surface circulation of the global ocean and collect data on SST and sea level pressure. Each SVP drifter consists of a buoy and a "holey-sock" drogue positioned at a depth of 15 meters to track currents (Figure A.1).

For the 2015 ASIRI and 2019 MISO-BoB field campaigns, all drifters were equipped with a thermistor 0.2 m below the surface to measure temperature. Additionally, 36 of the drifters deployed in 2015 ASIRI field campaign included an extra conductivity sensor at a depth of about 0.5 m to gather salinity data.

A.1.2 NIOT Moorings

The Ocean Moored buoy network for Northern Indian Ocean (OMNI) program addresses the long-standing need to understand the observed variability of upper-ocean thermohaline and current structures, which has an important bearing on the evolution of seasonal monsoons and cyclones (Venkatesan et al., 2013, 2018, 2021). Maintained by the National Institute of Ocean Technology (NIOT), India, the buoys consist of polyurethane foam-filled, fiber-reinforced plastic hulls moored to the seabed using a dead weight in an inverse catenary configuration.

NIOT buoys measure essential ocean variables and transmit this information in real-time through satellites using the Global Telecommunication System (GTS) format of the World Meteorological Organization. The data acquisition system is connected to various sensors that collect meteorological and oceanographic data. Specifically, the NIOT moorings observe wind speed and direction, air temperature, relative humidity, rainfall, incoming shortwave and longwave radiation, and sea-level pressure at approximately 3 m height (Figure A.2). They also measure ocean velocity profiles down to 100 m, and temperature and conductivity at multiple depths: 1 m, 5 m, 10 m, 15 m, 20 m, 30 m, 50 m, 75 m, 100 m, 200 m, and 500 m. Additionally, selected mooring sites are equipped with extra sensors, such as motion reference units for wave measurement and sensors for measuring biogeochemical parameters

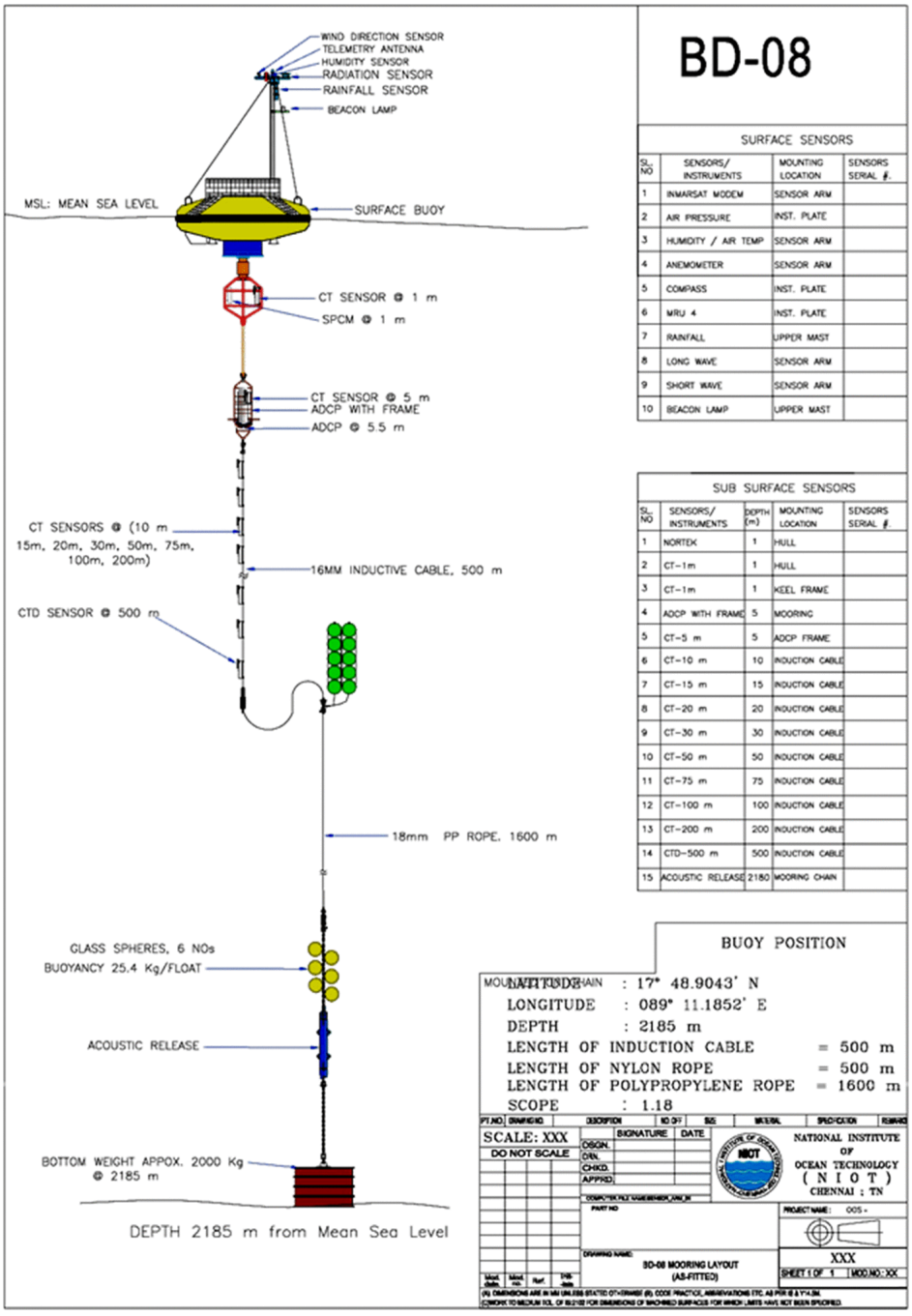

Figure A.2: NIOT OMNI mooring system along with sensor fitments (adapted from Ranganathan et al. 2024).

and ambient noise. More details on the instrument configuration can be found in Venkatesan et al. (2013) and Joseph et al. (2022).

A.1.3 WHOI Mooring

Table A.1: Instrument details for WHOI Mooring (ASIMET)

Measurement	**Make/Model**	**Specifications**
Air Temperature / Humidity	Rotronic HC2A-S	Accuracy: ± 0.8%RH, ±0.1 K at 10-30°C
Barometric Pressure	Vaisala PTB 210	Accuracy: 500-1100hPa; Non Linearity ±0.15 hPa; Total Accuracy (20°C) ±0.20 hPa
Precipitation	RM Young 50203 unheated	Threshold: 1 mm; Accuracy ± 1mm
Wind	RM Young 05106 Wind Monitor	ACCURACY: Wind Speed: ± 0.3 $m\,s^{-1}$ or 1% of reading; Wind Direction: ±3°
Compass	RM Young 32500	Resolution: 0.5 °; Accuracy: ± 2° (rms)
Short Wave Radiation	Kipp and Zonen SMP21 Pyranometer	Secondary Standard; Response Time (63%) <0.7 s, (95%) <2 s; Zero offsets (a) thermal radiation: <7 $W\,m^{-2}$ (b) temperature change: <2$W\,m^{-2}$
Long Wave Radiation	Kipp and Zonen SGR4 Pyrgeometer	Response Time (63%) 6s, (95%) 18s; Zero offsets temperature change: <2 $W\,m^{-2}$; Nonlinearity <1%; Temperature response <1%
Sea Temperature	Seabird Electronics 37SM	Accuracy: (T) ± 0.002°C (C) ±0.0003 $S\,m^{-1}$; Stability (T) 0.0002 °C (C) 0.0003 $S\,m^{-1}$; Resolution (T) 0.0001 °C (C) 0.00001 $S\,m^{-1}$
Sea Temperature	Seabird Electronics 56	Accuracy: ± 0.002°C; Stability 0.0002°C; Resolution 0.0001°C
multi-parameter	Campbell ClimaVUE50	Air Temperature: resolution 0.1°C, accuracy ±0.6 °C; Relative Humidity: resolution 0.1, accuracy ±3%RH; Wind Speed: resolution 0.01 $m\,s^{-1}$, accuracy 3%; Wind Direction: resolution 1 °, accuracy ±5°; Solar Radiation: resolution 1 $W\,m^{-2}$, accuracy ±5%; Precipitation: resolution 0.017mm, accuracy ±5%; Tilt: resolution 0.1 °, accuracy ±1 °; Lighting Average Distance: variable accuracy and resolution

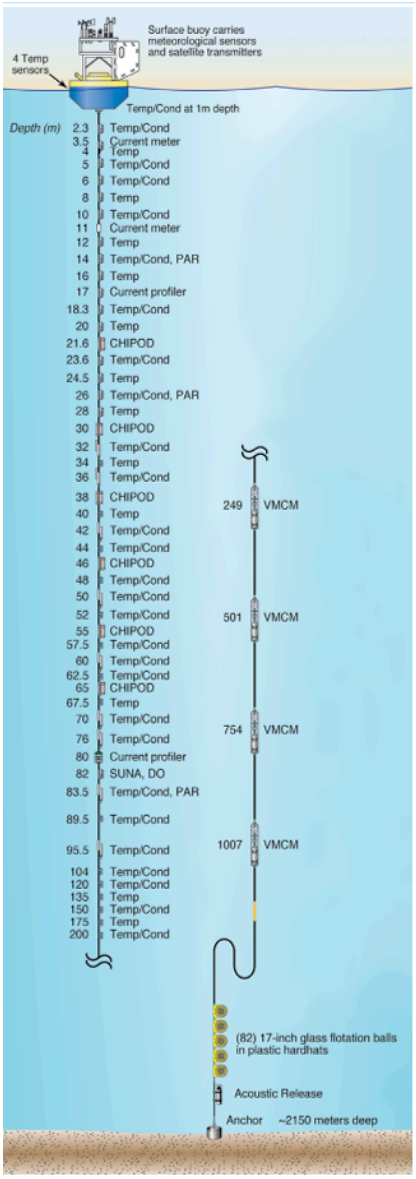

Figure A.3: Schematic drawing of the Woods Hole Oceanographic Institution (WHOI) surface mooring deployed at 18°N, 89.5°E. The placements are indicated for sensors that measure temperature (Temp), temperature and conductivity (Temp/Cond), turbulence (CHIPOD), velocity (current meter, current profiler, and Vector Measuring Current Meter, or VMCM), dissolved oxygen (DO), photosynthetically available radiation (PAR), and nutrients (SUNA). Adapted from Weller et al. (2016)

The WHOI surface mooring deployed at 18°N, 89.5°E, used a 3 m diameter buoy equipped with a suite of meteorological and oceanographic instruments. The buoy's tower held two ASIMET (Air-Sea Interaction METeorology) systems and a Vaisala WXT 520 for redundancy, collectively measuring wind speed and direction, air temperature and humidity, sea temperature and salinity, incoming shortwave and longwave radiation, barometric pressure, and precipitation (Figure A.3, Weller et al. 2016). These meteorological sensors were positioned approximately 3 m above the sea surface, while the ocean salinity and temperature sensors were located at 1 m depth on the buoy's bridle. The mooring line also contained various oceanographic instruments, including those that measured temperature, as well as sensors for both temperature and electrical conductivity to compute salinity and seawater density (Figure A.3). Additionally, horizontal water velocity was measured by some instruments that measured sound velocity at a single depth (current meters), and by current profilers that used upward-looking sonars to provide a vertical profile of ocean currents (Acoustic Current Doppler Profilers, ADCPs). Finally, the collected data was used with version 3.0 of the COARE flux algorithm (Fairall et al., 1996b, 2003) to calculate wind stress, latent heat flux, and sensible heat flux.

A.1.4 D-BASIS

Drogued-Buoy Air Sea Interaction System (D-BASIS) was deployed to simultaneously measure air-sea fluxes and the upper-ocean structure (Figure A.4). Each D-BASIS profiler consisted of a WHOI surface buoy equipped with meteorological sensors and a Scripps Institution of Oceanography (SIO) Wirewalker. Details of the WHOI surface mooring are the same as those discussed in the preceding section, while the Wirewalker details are covered in Section 2.2. There were also additional sensors located below the Wirewalker on the mooring line, which are discussed in Table A.2.

To ensure the D-BASIS profiler remained nearly stationary, the profiler included several

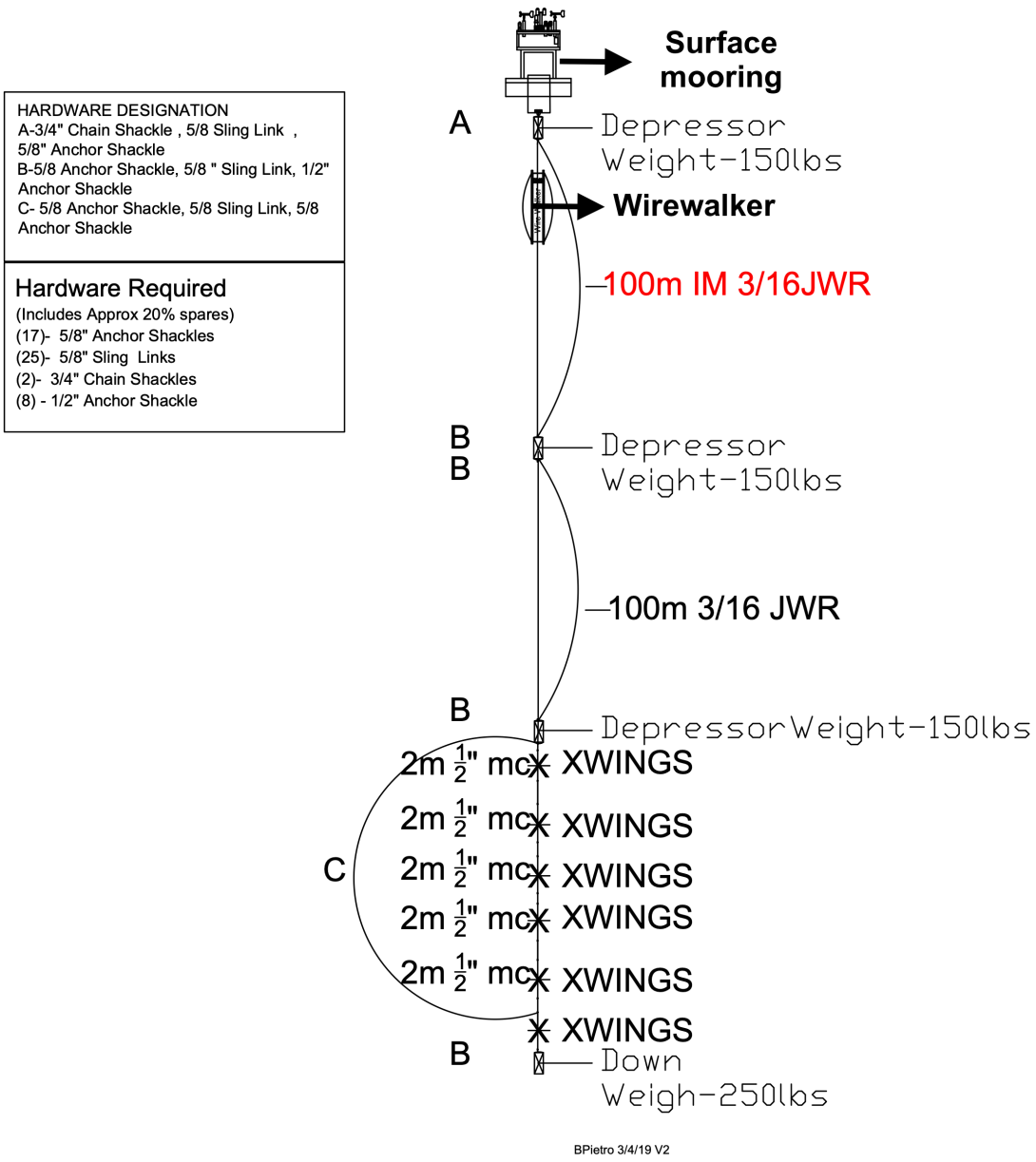

Figure A.4: Schematic drawing of the D-BASIS.

"X-wing" drag elements suspended deep in the water column. The X-wings were constructed from 3'x3' plastic sheets fastened to 2 m shots of mooring chain with aluminum angle stock.

Table A.2: Subsurface instrument details for D-BASIS

Measurement	**Make/Model**	**Serial Number**	**Depth**	**Notes**
Multi-parameter	SIO MOD WW	D3	3-100m	profiles currents
currents	TRDI 75 kHz Workhorse ADCP	15368	100m	pinging when deployed
temperature	RBR Solo T	72133	100m	attached to ADCP cage
temperature	RBR Solo T	100154	101m	high frequency sampling
temperature	RBR Solo T	100157	110m	high frequency sampling
temperature	RBR Solo T	100158	120m	high frequency sampling
temperature	RBR Solo T	100162	130m	high frequency sampling
temperature	RBR Solo T	101193	140m	high frequency sampling
temperature	RBR Solo T	101194	150m	high frequency sampling
temperature	RBR Solo T	101195	160m	high frequency sampling
temperature	RBR Solo T	101196	170m	high frequency sampling
temperature	RBR Solo T	101197	180m	high frequency sampling
temperature	RBR Solo T	100320	190m	high frequency sampling
temperature	RBR Solo T	72132	199m	
temperature/ conductivity/ pressure	Seabird 37 SM	2528	200m	w/ pressure

Depressor weights were added along the suspended wire and chain assembly to keep the drag elements vertical and to reduce snap loading on the subsurface instruments.

A.2 Description of conditions during the 2019 field campaign using D-BASIS and basis for DWL thresholds

The D-BASIS profilers' ability to concurrently measure the air-sea fluxes and resolve OBL at a high vertical resolution is instrumental in understanding the conditions favorable for DWLs. Meteorological measurements from the D-BASIS profilers also allow us to classify the operational period of the 2019 field campaign (Figure A.5a) into three distinct regimes. These regimes correspond to phases of the monsoon intra-seasonal variability (ISV) as the field campaign took place during the Southwest Monsoon Season in the Bay. These ISV's are characterized by active and break phases. Break phases feature clear skies, which leads to diurnal cycles in the SST and increased likelihood of DWLs. In contrast, the active phases feature steady high wind speeds, overcast conditions, high precipitation rates, leading to a suppression in the diurnal cycles of SST.

The period from 12–17 July 2019 was marked by moderate wind speeds (6.2–8.7 $\mathrm{m\,s^{-1}}$, Figure A.6a), persistent southwesterly winds associated with the Southwest Monsoon (Figure A.6b), and clear skies with peak shortwave radiation nearing $1000\mathrm{W\,m^{-2}}$ (Figure A.6e). Rainfall was absent except for a heavy rain event on 17 July (Appendix A.3, Figure A.6d). Diurnal SST amplitudes of 0.1 °C to 0.2 °C were observed, along with a 0.2 °C increase in foundational SST (Figure A.7a,b). These conditions suggest that the sampled region of the Bay was in a break phase of the ISV. However, the upper 30 m of the ocean remained relatively well mixed, and no signatures of DWL formation were observed (Figure A.7c, A.8b,d,e).

A drop of 4°C in air temperature is observed across the three D-BASIS profilers on 17 July (Figure A.6c). This is also followed by very high precipitation rate of 80 $\mathrm{mm\,h^{-1}}$ (Figure A.6d). These conditions indicate an atmospheric cold pool event (de Szoeke et al., 2017; Simoes-Sousa et al., 2022), which is followed by calm conditions with night-time cooling and diurnal warming on the next day. The net rainfall due to this cold pool event is about

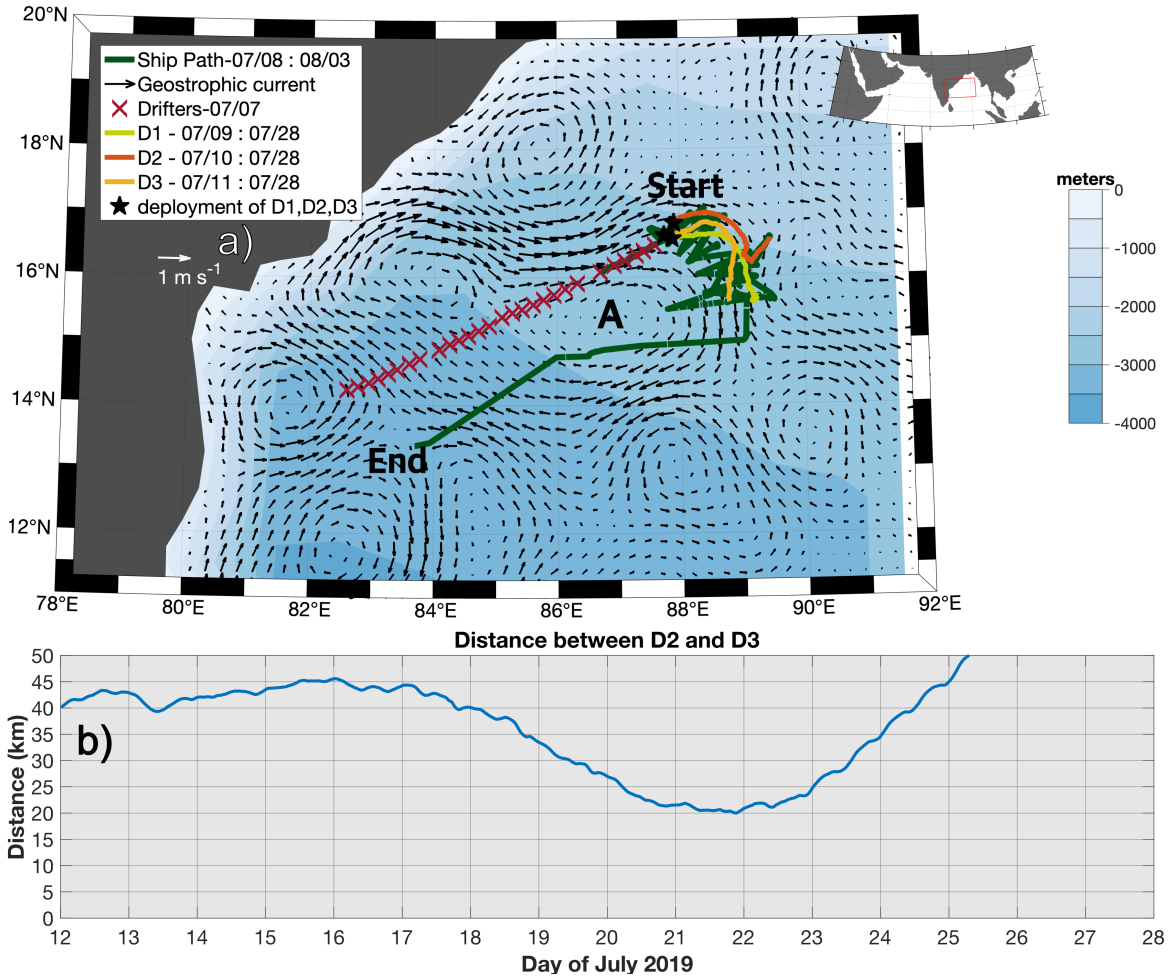

Figure A.5: (a) Map of the Bay of Bengal displaying various assets used for sampling during the MISO-BoB Intensive Observational Period (IOP) in 2019. The legend provides information about the deployment dates and positions of drifters. It also includes deployment positions, paths, deployment dates, and recovery dates for the D-BASIS profilers (D1, D2, D3). The map also illustrates the ship's route and sampling dates. The background colors represent the bathymetry of the Bay, while the background arrows depict geostrophic currents averaged over a ten-day period from 15-24 July 2019. The letter A indicates the anticyclonic eddy along which the drifters moved. (b) Time Series of separation distance between D2 and D3 profilers between 12 July to 27 July 2019. Time series is shown in local time (IST).

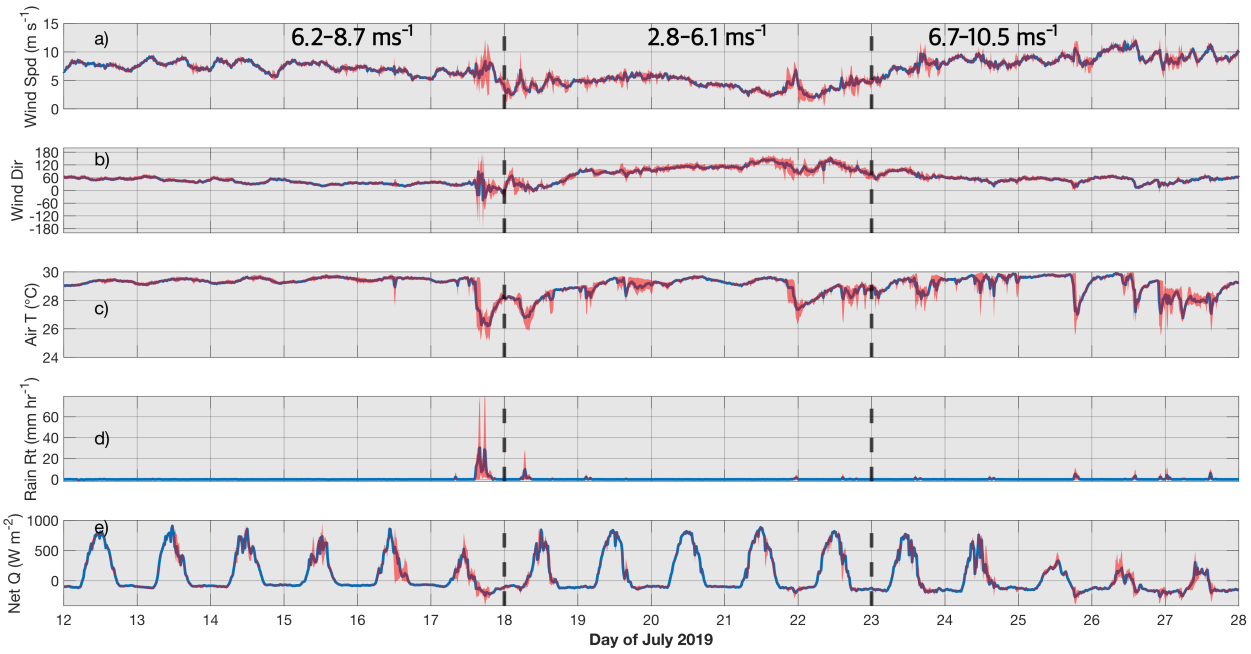

Figure A.6: Mean of Meteorological measurements from the three D-BASIS and averaged to 15-minute intervals in blue while the range between the three D-BASIS is indicated in red shaded area. (a) Wind speeds, (b) wind direction (0^o indicates southerly winds whereas -90^o angle indicates easterly winds), (c) air temperature near the air-sea interface (2.65 m), (d) precipitation rate and (e) Net Heat Flux from 12 July to 27 July 2019. The 10^{th} and 90^{th} percentile values of wind speeds for each of the three periods from D-BASIS buoys are reported on panel a). The black dashed vertical lines in panels a–e are used to separate different periods described in Appendix A.2. All time series are shown in local time (IST).

75 mm and 101 mm at D2 and D3 respectively. Such events freshen the upper ocean and create rain lenses (Moulin et al., 2021; Iyer and Drushka, 2021).

During the period of 18-22 July 2019, wind speeds ranged from 2.8–6.1 $\mathrm{m\,s^{-1}}$ (Figure A.6a), predominantly from the west and northwest direction (which is uncharacteristic as the winds are typically south-westerly during the monsoons in the Bay, Figure A.6b). Clear sky conditions with peak SWR of nearly 1000 $\mathrm{W\,m^{-2}}$ persisted during this period (Figure A.6e). The diurnal SST amplitudes during this period are 0.5 °C to 0.8 °C (or even

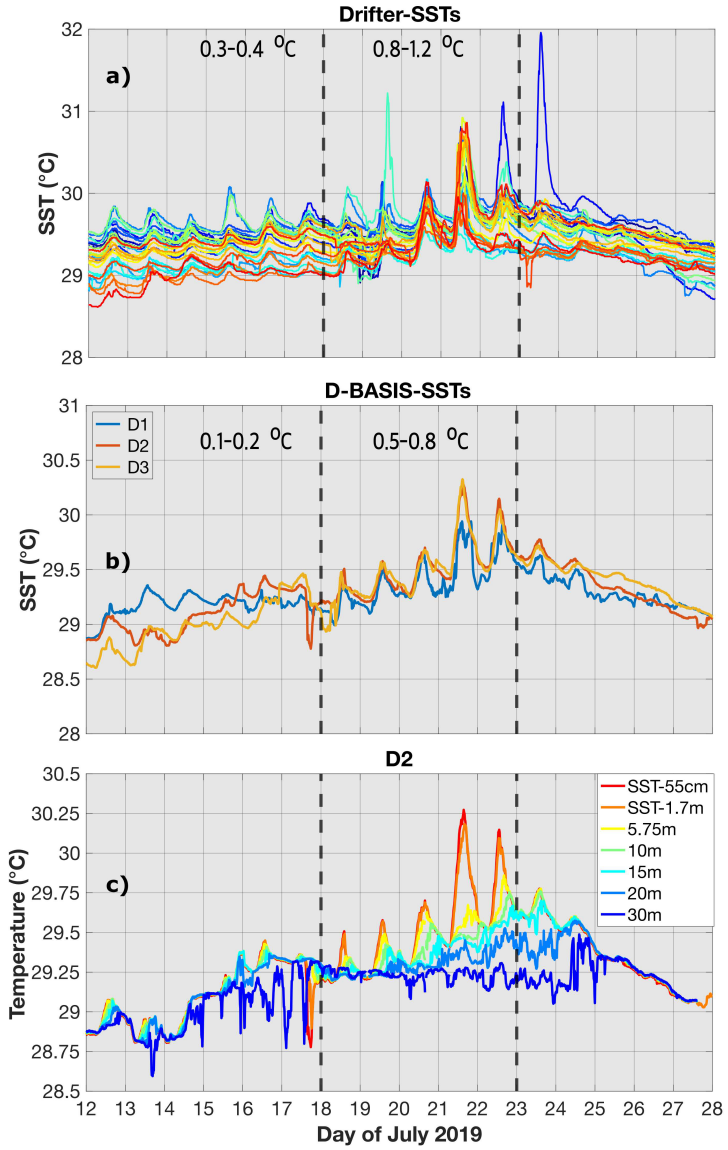

Figure A.7: Time series of SSTs as measured from (a) drifters at 0.2 m depth, (b) D-BASIS at 0.55 m and (c) temperatures measured at various depths using D2 from 12 July to 27 July 2019. The typical diurnal cycles of SSTs for the periods where the diurnal cycles are prominent is reported on panels (a) and (b). The black dashed vertical lines in panels (a)–(c) are used to separate different periods described in Appendix A.2. All time series are shown in local time (IST).

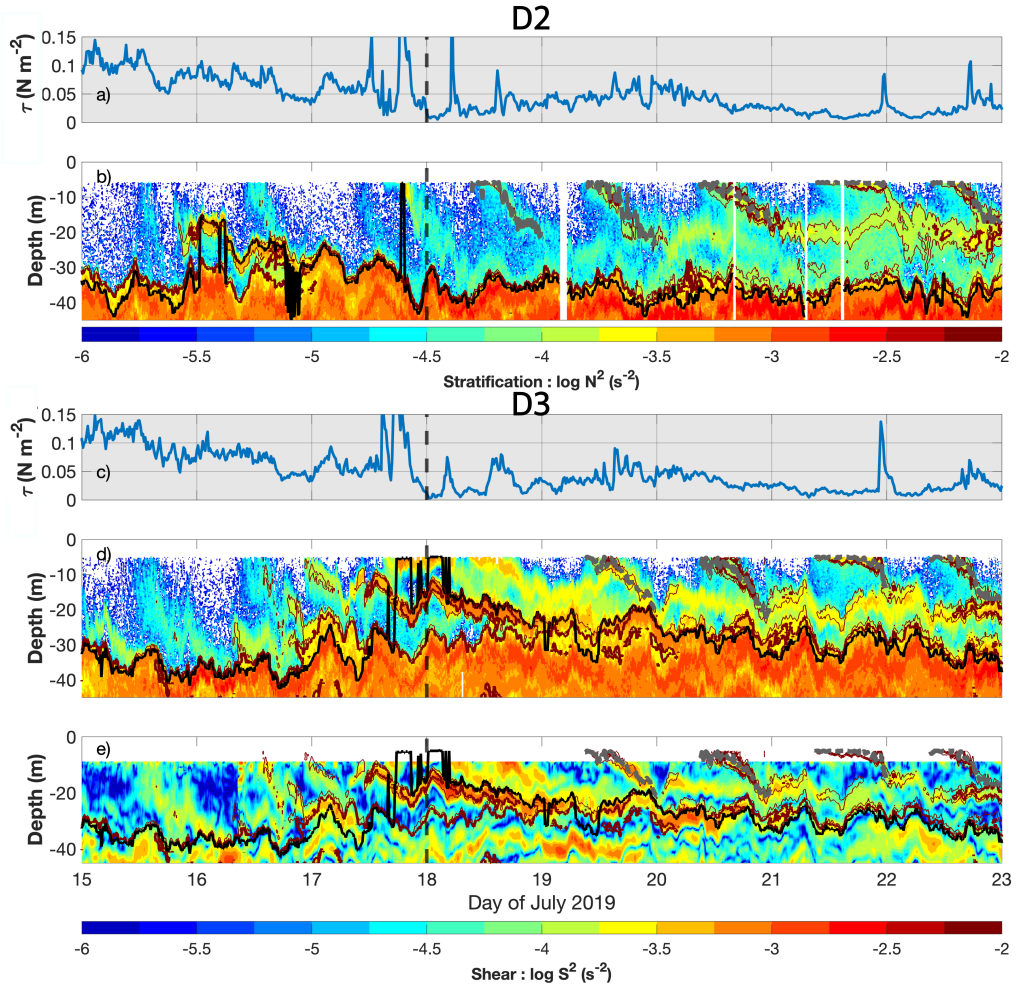

Figure A.8: (a) Wind stress from D2. (b) Stratification in logarithmic scale from D2 during 18 July to 22 July 2019. Panels (c), (d) are similar to panels (a), (b) respectively but for D3. (e) Shear in logarithmic scale calculated from D3. Shear measurements from D2 are missing due to the loss of its ADCP. The thick brown contours in panels (b), (d), (e) indicate the 0.04 °C m^{-1} temperature gradient while the thin brown contour indicates the 0.02 °C m^{-1} gradient. The gray dashed lines in panels (b), (d) and (e) indicate the DWL depth. The thick black lines in panels (b), (c), (e) indicate the upper pycnocline depth (based on the maximum N^2 below the typical DWL depth). The black dashed vertical lines in panels (a)–(e) indicate the beginning of the DWL period during the 2019 field campaign (see Appendix A.2). All time series are shown in local time (IST).

more in some cases), with an increase of 0.25 °C in the foundational SST (Figure A.7a,b). These conditions indicate that the sampled part of the Bay was still in the break phase. However, the upper 30 m of the ocean exhibited strong stratification and shear along with enhanced temperature gradients, which are signatures consistent with the presence of DWLs. (Figure A.7c, A.8b,d,e, Hughes et al. 2020a).

During the remainder of the operational cruise period (23-28 July 2019), the wind speeds increased nearly two-fold from the previous period (6.7-10.5 $\mathrm{m\,s^{-1}}$, Figure A.6a) with the wind direction returning to the typical southwest monsoon pattern (Figure A.6b). This period was also marked with steady rainfall at times (Figure A.6d) and persistent overcast skies (with peak SWR of nearly 500 $\mathrm{W\,m^{-2}}$, Figure A.6e). As a result, the diurnal cycles in SST are suppressed and the foundational temperature gradually cools (Figure A.7a,b). These conditions indicate that the sampled part of the Bay was in the active phase, with no possibility of DWLs due to lack of clear skies.

Based on the wind speeds observed during this field campaign, we define DWL-favorable conditions in the Bay as wind speeds below 6 $\mathrm{m\,s^{-1}}$ (at 3 m height). This limit is close to 7.6 $\mathrm{m\,s^{-1}}$ (at 10 m height) defined for the wind speed limits for DWL formation in Equatorial Indian Ocean (Thompson et al., 2019). In addition, we use a peak SWR threshold of 750 $\mathrm{W\,m^{-2}}$ or greater to detect clear skies for DWL conditions (based on theoretical SWR calculations in Renner et al. 2019).

A.3 Evolution of upper ocean structure before and after the 17 July 2019 cold-pool event

The cold pool event on 17 July 2019 triggered heavy rainfall, leading to the formation of freshwater lens. However, the variability in stratification in the sampling region is not solely controlled by this intense precipitation event. The FastCTD measurements from the ship showed significant gradients in stratification in the East-West direction even before the

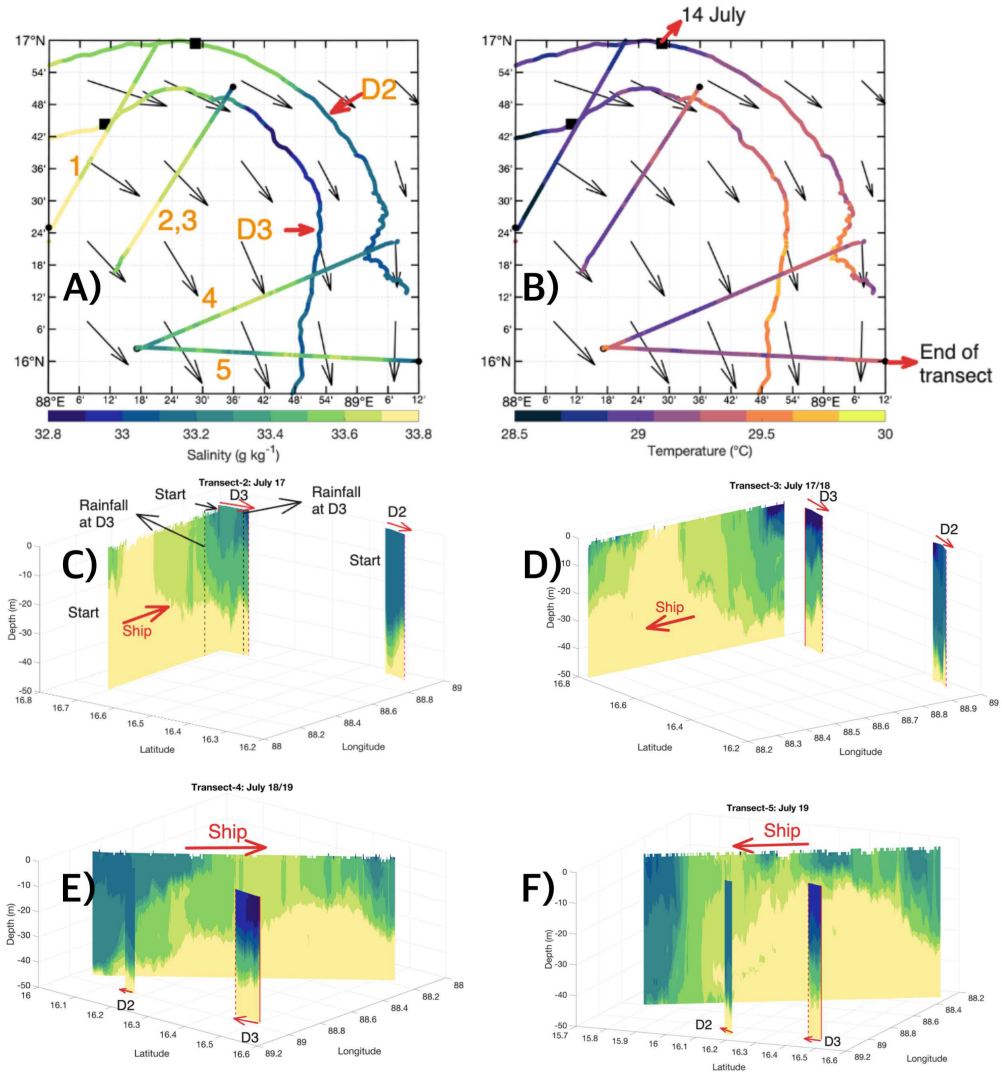

Figure A.9: (a) Surface salinity and (b) surface temperature observed from various ship transects, D2, and D3 during the 2019 field campaign. The black arrows indicate geostrophic currents averaged over the ten-day period from 15–24 July 2019. The start and end dates, along with the extents of each transect, are listed in Table A.3. Black squares mark the positions of D2 and D3 on 14 July 2019, while black circles indicate the endpoints of each ship transect. (c), (d), (e), and (f) indicate 3-D plots of the salinity from ship transects 2, 3, 4, 5, as well as sections sampled from D2 and D3 during the same time, respectively (the color bar for these panels is the same as panel-(a)).

Table A.3: Information about ship transects during the 2019 Field Campaign as shown in Figure A.9. The times are reported as local time (UTC + 5.5 hours)

Transect	Date and Time Start	Date and Time End	Location Start	Location End
1	14 Jul 04:30	14 Jul 18:30	17.07°N, 88.4°E	16.35°N, 87.98°E
2	17 Jul 05:45	17 Jul 17:10	16.27°N, 88.2°E	16.88°N, 88.55°E
3	17 Jul 18:20	18 Jul 04:25	16.88°N, 88.55°E	16.27°N, 88.2°E
4	18 Jul 18:15	19 Jul 07:50	16.38°N, 89.13°E	16.05°N, 88.28°E
5	19 Jul 07:50	19 Jul 20:05	16.05°N, 88.28°E	16°N, 89.23°E

rainfall event (Transect-1, Figure A.9a,b). Transect-2 cuts across the D3 path on 17 July 2019 such that the end of the ship transect (post-rainfall) overlaps with the start of D3 (pre-rainfall; Figure A.9c). Similarity in the salinity structure between the two sources indicates that the shallow stratification existed before the cold pool event. Ship transects conducted on 19 July reveal greater spatial variability in upper ocean salinity structure compared to earlier transects, likely influenced by both the cold pool event and pre-existing mesoscale-structured stratification. (Figure A.9e,f).

Focusing on the cold pool event, both ship and D-BASIS profilers (D2, D3) detected rain lens formation during Transect-3 (a repeat of Transect-2; Figure A.9d, Figure 2.8c,f). The lens at D3 persisted longer that D2 due to stronger upper-ocean stratification at D3, consistent with observations from the tropical Pacific (Iyer and Drushka, 2021). Between 17–18 July, near-surface salinity at D3 fluctuated even in the absence of recorded rainfall (Figure 2.8f, Figure A.6d), likely due to advection of nearby freshwater lens. IMERG imagery shows rainfall near D3 on 18 July at 03:00 (Figure A.10c), not captured by in-situ rain gauges. Temperature fluctuations at D3 between 07:00 and 09:00 on 18 July (Figure 2.8e) further suggest D3 drifted through multiple lenses. These observations imply that lateral differences in background stratification may also result from advection of rain lens (similar to the movement of rain lenses as gravity current propagation in Moulin et al. 2021).

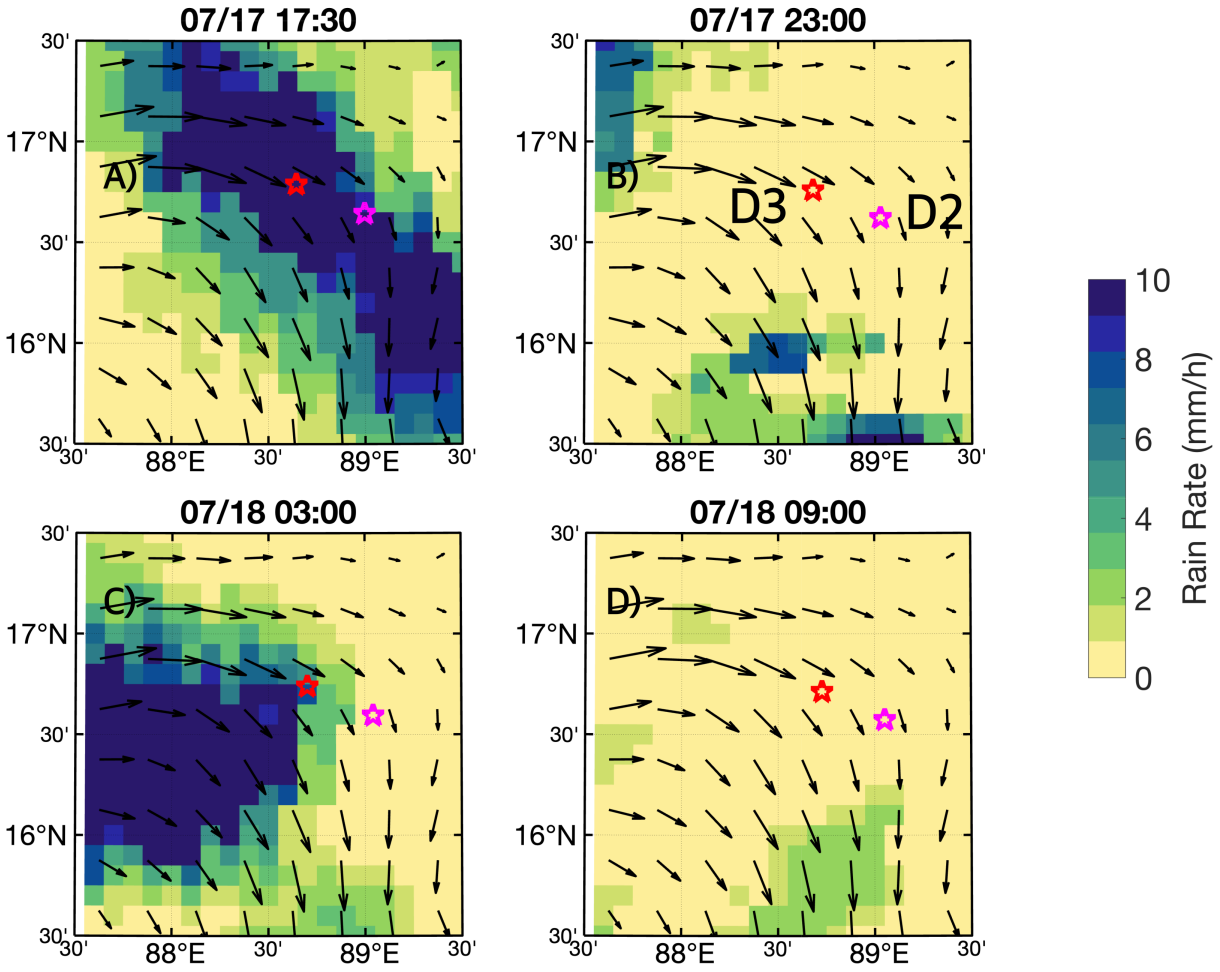

Figure A.10: Rainfall rates from IMERG at four different times (see subplot title for the time) on 17 and 18 July 2019 (Local Time). The magenta and red stars indicate the position of D2 and D3 respectively at the time of the snapshot from IMERG. The rainfall event in (a) is captured at D2 and D3 (Figure A.6d), while the rainfall around D3 in (c) is not captured in the in-situ measurements.

A.4 Verification of 1-D physics during DWL evolution on 19 July at D3 with shallow salinity stratification

To verify that the DWL evolution at D3 on 19 July, in the presence of strong pre-existing salinity stratification, can be considered one-dimensional, we compare the different terms of

the heat budget (modified from McPhaden and Hayes 1991) using observations from D3 and ship-based FastCTD profiles as follows:

$$\underbrace{\frac{\partial T}{\partial t}}_{\text{a)}} + \underbrace{v.\nabla T}_{\text{b)}} + \underbrace{w\frac{\partial T}{\partial z}}_{\text{c)}} = \underbrace{\frac{Q}{\rho_o c_p H}}_{\text{d)}} \tag{A.1}$$

where v is the horizontal velocity within the mixed layer from D3, T is the temperature, H is the mixed layer depth and w is the vertical velocity. Q represents the net surface heat flux at D3 while ρ, c_p indicate the density and specific heat capacity of water (assumed as 3991 $\mathrm{J\,kg^{-1}\,K^{-1}}$) respectively. Terms a–d correspond to: (a) the temperature tendency, (b) advection by the mean horizontal flow, (c) entrainment from below the mixed layer, and (d) surface heat flux within the mixed layer. The horizontal gradients in temperature is inferred from a nearby FastCTD sections (Figure A.5). Since direct measurements of vertical velocity are challenging, we restrict the comparison in Equation A.1 to terms (a), (b) and (d).

A simple comparison reveals that the contribution of mesoscale advective term to the temperature tendency, inferred from temperature gradients between D3 and FastCTD, is negligible throughout the DWL evolution (Figure A.11). The surface heat flux mostly explains the changes in temperature tendency. The occasional abrupt variations in the temperature tendency term (term (a) in Equation A.1) suggest the presence of internal wave/tide action. Otherwise, the temperature tendency remains predominantly one-dimensional, even in the presence of enhanced pre-existing salinity stratification.

A.5 Salinity stratification effects on TKE budget during DWL evolution

Prior studies (e.g., Hughes et al., 2021) have highlighted that as the net heat flux decreases in tropical regions about 15:00 to 17:00 hours, the shear due to the trapping of the momentum fluxes overpowers the stratification. This situation leads to marginal instability ($Ri < 0.25$

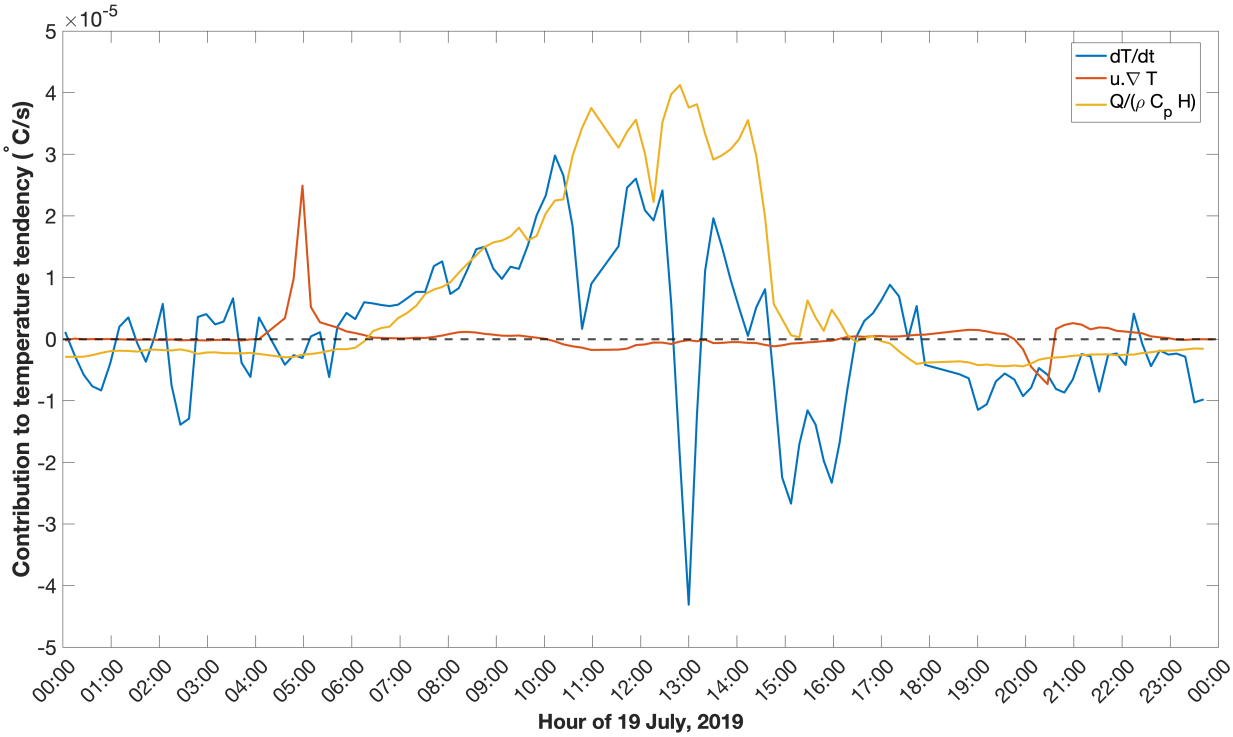

Figure A.11: Comparison of terms (a), (b) and (d) in Equation A.1 (blue, red and yellow lines respectively) as a function of time on 19 July 2019 based on observations from D3 and FastCTD.

where Ri is the Richardson number and is defined as the ratio of local stratification (N^2) and shear squared (S^2) at the base of the DWL. This condition causes the DWL to deepen. Because Ri can be noisy in practice, studies also use reduced shear term (S^2-$4N^2$), which becomes positive under marginally unstable conditions as a more robust indicator.

Model simulations of the DWL deepening at D2 and D3 on 19 July 2019 (Figure 2.9) reveal the presence of such marginal instability, consistent with findings of Hughes et al. (2021) (Figure A.12). However, the presence of enhanced stratification below the region of marginal instability in the D3 simulations introduces an additional source of stability (Figure A.12b). This enhanced stratification below the DWL slows its deepening, effectively

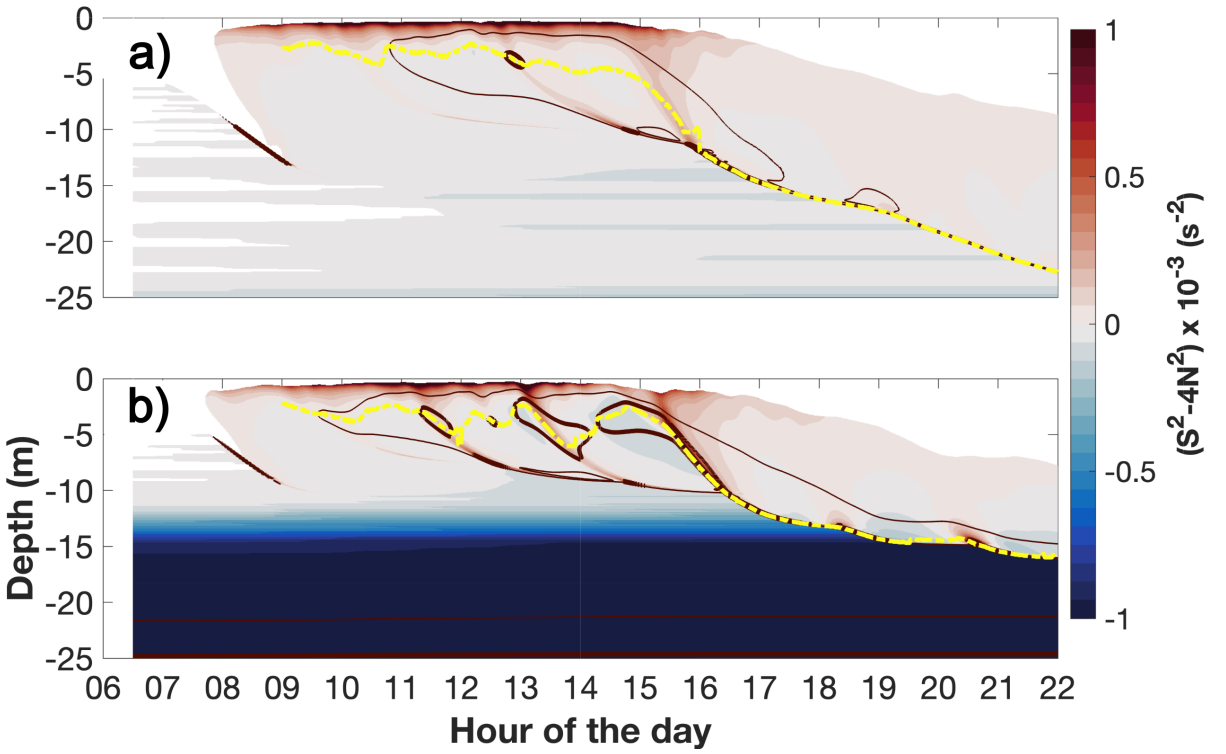

Figure A.12: (a) The reduced shear (S^2-4N^2) analyzed through GOTM simulations using initial and forcing conditions from D2 on 19 July 2019. The yellow dashed line indicates the DWL depth. (b) The same as (a) but for D3.

trapping it at comparatively shallower depths (Figure A.12b) as observed in our measurements (Figure 2.9d).

We next diagnose the impact of enhanced background stratification on the various terms in the Turbulent Kinetic Energy (TKE) budget. The TKE equation (ignoring the flux divergence term, e.g., equation 1 of Nilsson et al. 2016) is as follows:

$$\underbrace{\frac{D}{Dt}\overline{\left(\frac{1}{2}u_i'^2\right)}}_{\text{Time derivative of TKE}} = \underbrace{-\overline{u_i'u_j'}\frac{\partial u_i'}{\partial x_j}}_{\text{Shear Production (P)}} + \underbrace{\overline{w'b'}}_{\text{Buoyancy production (G)}} - \underbrace{\epsilon}_{\text{Dissipation}} \tag{A.2}$$

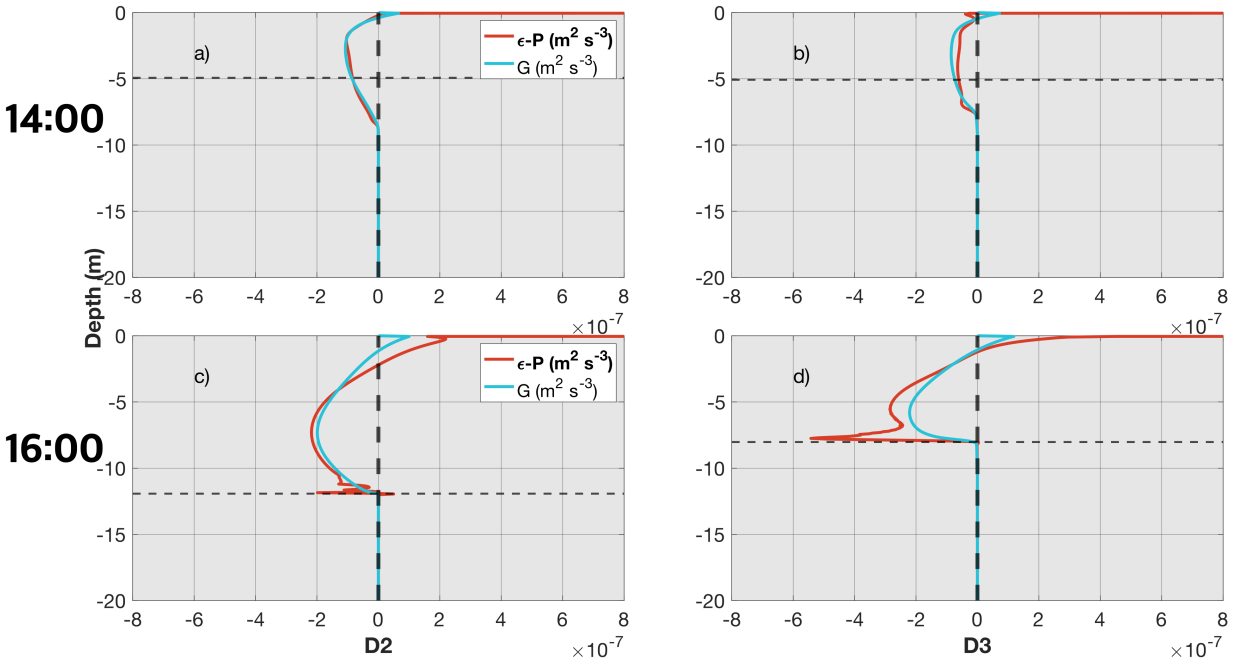

Figure A.13: Comparison of dissipation (ϵ) - shear production (P) and buoyancy production (G) profiles from GOTM simulations (see equation A.2 for more details) for (a) D2 and (b) D3 at 14:00 hours on 19 July 2019. (c) and (d) are the same as (a) and (b) for 16:00 hours. The horizontal dashed lines indicate the respective DWL depth from simulations.

As mentioned earlier, prior to the shear overpowering the stratification within the DWL, we observe that the TKE production terms balances the TKE dissipation term in both D2 and D3 simulations (Figure A.13a,b). However, once the shear begins to overpower the stratification within the DWL (e.g., at 16:00 hours, Hughes et al. 2021), the TKE production and dissipation terms are no longer balanced at the base of the DWL (Figure A.13c,d). The shear production term overpowers the dissipation in both the D2 and D3 simulations. However, the magnitude of the shear production term is 2.5 times higher at D3 due to the presence of background stratification, as greater shear production is required to overcome the stratification and deepen the DWL.

Appendix B Additional Material for Chapter 3

B.1 Deriving the temperature tendency equation and Q_{cross}

To investigate the role of salinity stratification on SST warming, we derive the temperature tendency equation within the mixed layer following Echols and Riser (2020), assuming temperature and velocity are uniform over the mixed-layer depth.

$$\underbrace{\frac{\partial T}{\partial t}}_{\text{a)}} + \underbrace{v.\nabla T}_{\text{b)}} + \underbrace{\frac{(T_{ML} - T_{-H})w_e}{H}}_{\text{c)}} = \underbrace{\frac{(F(H).Q_{SWR} - Q_{cool})}{\rho_o c_p H}}_{\text{d)}} \tag{B.1}$$

where v is the horizontal velocity within the mixed layer, T_{ML} is the temperature within the mixed layer, T_{-H} is the temperature just below the base of the mixed layer, H is the mixed layer depth and w_e is the entrainment velocity. $F(H)$ represents the fraction of shortwave radiation trapped within an effective MLD of H (dependent on the optical properties of water). Q_{SWR} and Q_{cool} represent the shortwave and cooling components of heat flux respectively. ρ, c_p indicate the density and specific heat capacity of water (assumed as 3991 $\mathrm{J\,kg^{-1}\,K^{-1}}$). Terms a–d represent, respectively: (a) the temperature tendency, (b) advection by the mean horizontal flow, (c) entrainment from below the mixed layer, and (d) surface heat flux within the mixed layer.

Since direct measurements of entrainment velocity are difficult, we estimate the entrainment velocity (w_e) derived from McPhaden and Hayes 1991:

$$w_e = \frac{2m(\frac{\rho_a C_D}{\rho_o})^{3/2}|U|^3}{-g(\frac{\rho}{\rho_o})H} \tag{B.2}$$

where m is an efficiency factor of entrainment (typically 0.4), ρ is the density jump across

the mixed layer and g is acceleration due to gravity. ρ_a, C_D and U are the air density, drag coefficient, and wind velocity, respectively.

We assume a purely one-dimensional budget, so term (b) is omitted. Using temperature and density jumps from our simulations indicates that the vertical entrainment term (c) is an order of magnitude smaller than the surface heat flux contribution (d) to the temperature tendency, and can therefore be neglected. As a result, we obtain:

$$\frac{\partial T}{\partial t} = \frac{(F(H).Q_{SWR} - Q_{cool})}{\rho_o c_p H} \tag{B.3}$$

Integrating both sides with respect to time yields equation B.4 (or equation 3.1 in main text),

$$\Delta T_f = \frac{\int (F(H).Q_{SWR} - Q_{cool})dt}{\rho c_p H} \tag{B.4}$$

The integral in equation 3.1 can be expressed using daily mean (overbar) quantities for SWR (Q_{SWR}) and cooling heat fluxes (Q_{cool}), as shown in equation 3.2 of the main text:

$$\Delta T_f^{str} - \Delta T_f^{unstr} = \frac{F(H_{str}).\overline{Q_{SWR}} - \overline{Q_{cool}}}{\rho c_p H_{str}} - \frac{F(H_{unstr}).\overline{Q_{SWR}} - \overline{Q_{cool}}}{\rho c_p H_{unstr}} \tag{B.5}$$

We assume that the heat fluxes are identical in both the non-salinity-stratified (labeled "unstr") and salinity-stratified scenarios (labeled "str"). The H_{str} and H_{unstr} represent the effective depths controlled by the shallow salinity-stratification and deeper temperature-stratification/wind mixing respectively. Setting equation B.5 to zero yields the condition $\Delta T_f^{str} = \Delta T_f^{unstr}$:

$$\frac{F(H_{str}).\overline{Q_{SWR}} - \overline{Q_{cool}}}{\rho c_p H_{str}} = \frac{F(H_{unstr}).\overline{Q_{SWR}} - \overline{Q_{cool}}}{\rho c_p H_{unstr}} \tag{B.6}$$

We can then express $\overline{Q_{cool}}$ as follows (equation 3.3 of the main text):

$$\overline{Q_{cool}} = \left[\frac{F(H_{str}).H_{unstr} - F(H_{unstr}).H_{str}}{H_{unstr} - H_{str}}\right]\overline{Q_{SWR}} \tag{B.7}$$

Using the expression for $\overline{Q_{cool}}$ in equation B.7, we derive an expression for $\overline{Q_{net}}$ for the case where $\Delta T_f^{str} = \Delta T_f^{unstr}$. We define this value as Q_{cross} as follows:

$$Q_{cross} = \overline{Q_{SWR}} - \overline{Q_{cool}}(eqn.\ B.7) \tag{B.8}$$

This results in:

$$Q_{cross} = \overline{Q_{SWR}}[1 - \left[\frac{F(H_{str}).H_{unstr} - F(H_{unstr}).H_{str}}{H_{unstr} - H_{str}}\right]] \tag{B.9}$$

Defining H^* as the ratio between H_{unstr} and H_{str} to simplify equation B.9 leads to equation B.10 (also equation 3.4 in the main text):

$$Q_{cross} = \left[\frac{H^*[1 - F(H_{str})] - [1 - F(H_{unstr})]}{H^* - 1}\right]\overline{Q_{SWR}} \tag{B.10}$$

Appendix C Additional Material for Chapter 4

C.1 Restratification timescales associated with different individual processes and their combination

To quantify the contribution of lateral processes such as Ekman Buoyancy Fluxes (EBFs) and mixed layer eddies to wake recovery, we use the recovery timescale scalings derived by Haney et al. (2012) and for surface forcing case, by both Price (1981) and Haney et al. (2012).

The restratification timescale due to surface fluxes according to Haney et al. (2012) is,

$$\mathrm{T}_{sf} = \frac{\rho_o c_p H_{out}}{C_{sst}} \tag{C.1}$$

where H_{out} is the mixed layer depth of the regions surrounding the wake and C_{sst} is the linear perturbation factor that represents the reduced ocean to atmosphere heat flux due to colder SSTs in the wake. Based on our observations of heat fluxes within and around the wake, C_{sst} is 46.8 ± 10.7 $\mathrm{W\,m^{-2}\,^{\circ}C}$.

The restratification timescale by solar fluxes as per Price (1981) is given by:

$$\mathrm{T}_{sf_{Price81}} = c\ \frac{\tau}{C_{sst}\sqrt{Q_n}} \tag{C.2}$$

where τ is the wind stress and Q_n is the peak noon time shortwave radiation. The constant c is defined based on known similarity and physical constants as:

$$c = \frac{C_D \rho_o c_p^{3/2}}{\sqrt{g \rho_o \alpha / P_Q}} \tag{C.3}$$

where C_D is a similarity constant which assumes a value of 1.2, α is the thermal expansion

coefficient (3.27×10^{-4} °C^{-1}), g is the acceleration due to gravity (9.81 m s^{-2}) and P_Q is the half the duration of positive heat flux (nearly 5 hours in this area).

Additionally, the recovery timescale due to EBFs is (equation-7 of Haney et al. 2012),

$$\mathrm{T}_{ebf} = \frac{2L_f f H_{out}}{u_*^2 cos\theta} \tag{C.4}$$

where $2L_f$ is the width of the wake, f is the coriolis frequency and $u_*^2\ cos\theta$ is the crossfront component of friction velocity.

A timescale associated with the recovery process from the mixed layer eddies is (Haney et al. 2012):

$$\mathrm{T}_{eddy} = \frac{0.2}{C_e g \alpha} \frac{L_f^2 f}{H_{eddy}(T_{out} - T_{wake})} \tag{C.5}$$

where C_e is the efficiency coefficient (Fox-Kemper et al., 2008), H_{eddy} is the depth over which eddies act ($H_{eddy} \approx \frac{1}{2}[H_{wake} + H_{out}]$, where H_{wake} is the approximate depth of the wake), T_{out} and T_{wake} are the temperatures surrounding and within the wake respectively.

Using the observed parameters from this section (as referred from Table C.1), the recovery timescales associated to surface forcing (T_{sf}), EBFs (T_{ebf}) and mixed layer eddies (T_{eddy}) are found to be 29.6 ± 7, 25.4 ± 6 and 38.4 ± 8 days respectively, i.e. EBFs have a slightly faster recovery rate than the other two mechanisms. The recovery timescales by surface fluxes as per Price (1981) ($\mathrm{T}_{sf_{Price81}}$) is found to be 18 ± 4 days.

So far, the processes were considered in isolation. Next, we investigate the combined action of some of these processes. The recovery timescale due to a combination of EBFs and surface forcing is given by (equations-23 and 24 in Haney et al. 2012),

$$\mathrm{T}_{sf+ebf} = \frac{\rho_o c_p H_{out}}{C_{sst+ebf}} \tag{C.6}$$

where

$$C_{sst+ebf} = C_{sst} + \frac{u_*^2 cos\theta \rho_o c_p}{f L_f} \tag{C.7}$$

The factor of 2 in equation-C.7 is dropped (when compared to equation-C.4) under the assumption that EBFs would only restratify half of the wake width on the western edge (L_f), since the eastern edge undergoes destratification. The scaling of the recovery timescale due to the combined action of EBFs and surface forcing in equation-C.6 yields an estimate of 9 ± 2 days. Additionally, we estimate the recovery timescales due to the combination of all the processes (surface forcing, EBFs and mixed layer eddies) using a similar approach:

$$\mathrm{T}_{sf+ebf+eddy} = \frac{\rho_o c_p H_{out}}{C_{sst+ebf+eddy}} \tag{C.8}$$

where

$$C_{sst+ebf} = C_{sst} + \frac{u_*^2 cos\theta \rho_o c_p}{f L_f} + \frac{C_e g \alpha H_{eddy} (T_{out} - T_{wake}) \rho_o c_p H_{out}}{0.2 L_f^2 f} \tag{C.9}$$

This results in a recovery timescale of 7 ± 1 days due to the combined influence of all the above processes. The scaling arguments highlight that presence of lateral processes like EBFs (on the western edge of the wake) and mixed layer eddies, contributing to a faster recovery of the wake. These processes although may interact non-linearly, which needs further numerical investigation.

C.2 Unique structure of the wake

As mentioned in the main text, a comparison of satellite SST maps between 11-19 June reveals a thinning and warming trend of the wake. The wake's western edge moves eastward under the influence of Ekman flow (due to the upfront orientation with winds), while the eastern edge remains nearly stationary due to the downfront orientation (Figure C.4c-f), thereby causing the wake thinning. Additionally, high-resolution infrared Level-2 (L-2) SST

images highlight the complex structure of the wake, showing a region of warm water surrounding two cold water zones, each with temperatures around 27.4°C (Figure C.4b). This structure gives the appearance of two narrow filaments, which could be misleading without in-situ observations or high-resolution salinity data.

A comparison of L-2 satellite measurements with in-situ measurements reveals a similar temperature structure (Figure C.4g). However, the warm core area is associated with elevated salinity (Figure C.4h), indicating that the warm core is also part of the cyclone wake. The warming of the wake's core is hypothesized to be driven by diurnal warming, as both VIIRS-NPP satellite measurements and in-situ measurements are conducted during the daytime. To evaluate this hypothesis, we use the diurnal warm-layer correction model (Fairall et al., 1996a; Prytherch et al., 2013) incorporated in the COARE algorithm (Fairall et al., 1996b), applying observed parameters such as heat fluxes and wind stress during the sampling period on 17 June (the sampling period for section S2-W to S2-E). Our calculations indicate that the core of the wake remains warm even after accounting for diurnal warming effects (which is found to be around 0.1-0.15°C, Figure C.8). This finding is further confirmed with nighttime SST measurements from the Advanced Very High Resolution Radiometer (AVHRR) on NOAA's polar-orbiting satellites (Figure C.7b,c, Casey et al. 2010), which reveal a similar wake structure during nighttime conditions.

This suggests the wake has a distinctive structure, with a warm, salty core shielded by cooler waters, surrounded by warmer, fresher waters (Figure C.1). As a result, the density at the core of the wake is dominated by salinity and is partially compensated due to the warming of the core of the wake. This unique structure is challenging to capture using coarser satellite measurements. However, nighttime SST measurements taken on 18 June and later show that this unique structure of the wake has disappeared, with a single cold

wake now surrounded by warmer surface waters, consistent with subsequent in-situ sampling (Figure C.7c).

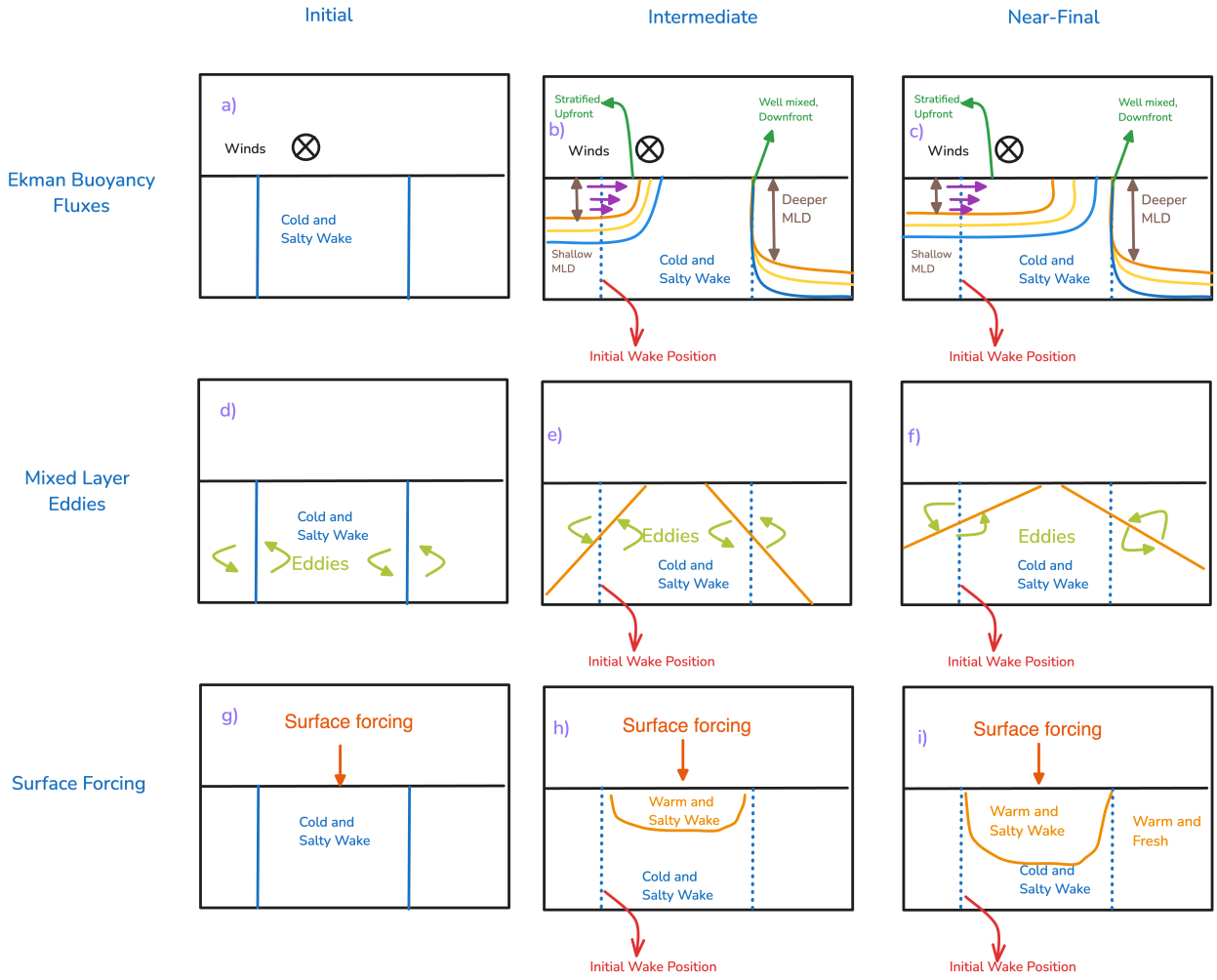

Figure C.1: Schematic illustrating snapshots of wake evolution at different stages: (a) initial, (b) intermediate, and (c) near-final recovery timescales, assuming only Ekman Buoyancy Fluxes (EBFs) drive wake evolution. Panels (d)-(f) and (g)-(i) depict the same stages for wake evolution influenced by Mixed Layer Eddies (MLEs) and surface forcing, respectively.

Table C.1: Observed and estimated parameters from the section and estimated values.

Parameter	**Value**
ρ_o	$1022.7\ \mathrm{kg\,m^{-3}}$
c_p	$3991.9\ \mathrm{J\,kg^{-1}\,K^{-1}}$
H_{out}	28.3 ± 4 m
$u_*^2 \cos\theta$	$5.97 \pm 1.2 \times 10^{-5}\ \mathrm{m^2\,s^{-2}}$
H_{wake} (estimated from nearby ARGO floats)	70 m
T_{wake}	28.3°C
T_{out}	29.4°C
Initial Width (from AMSR-2, Figure C.4c)	150 ± 20 km

Table C.2: Coordinates of survey waypoints on Figure 4.2 and 4.4.

Location	**Latitude (°N)**	**Longitude (°E)**
S2-C	12.07	66.87
S2-S	11.6	66.87
S2-E	12.07	67.34
S2-W	12.07	66.4
S3-E1	11.7	67.1
S3-W2	11.89	66.6
S3-E2	11.89	67.1
S3-E3	12.07	67.1
S3-W3	12.07	66.6
S3-W4	12.23	66.6
S3-E4	12.23	67.1
S3-E5	12.42	67.1
S3-W5	12.42	66.6

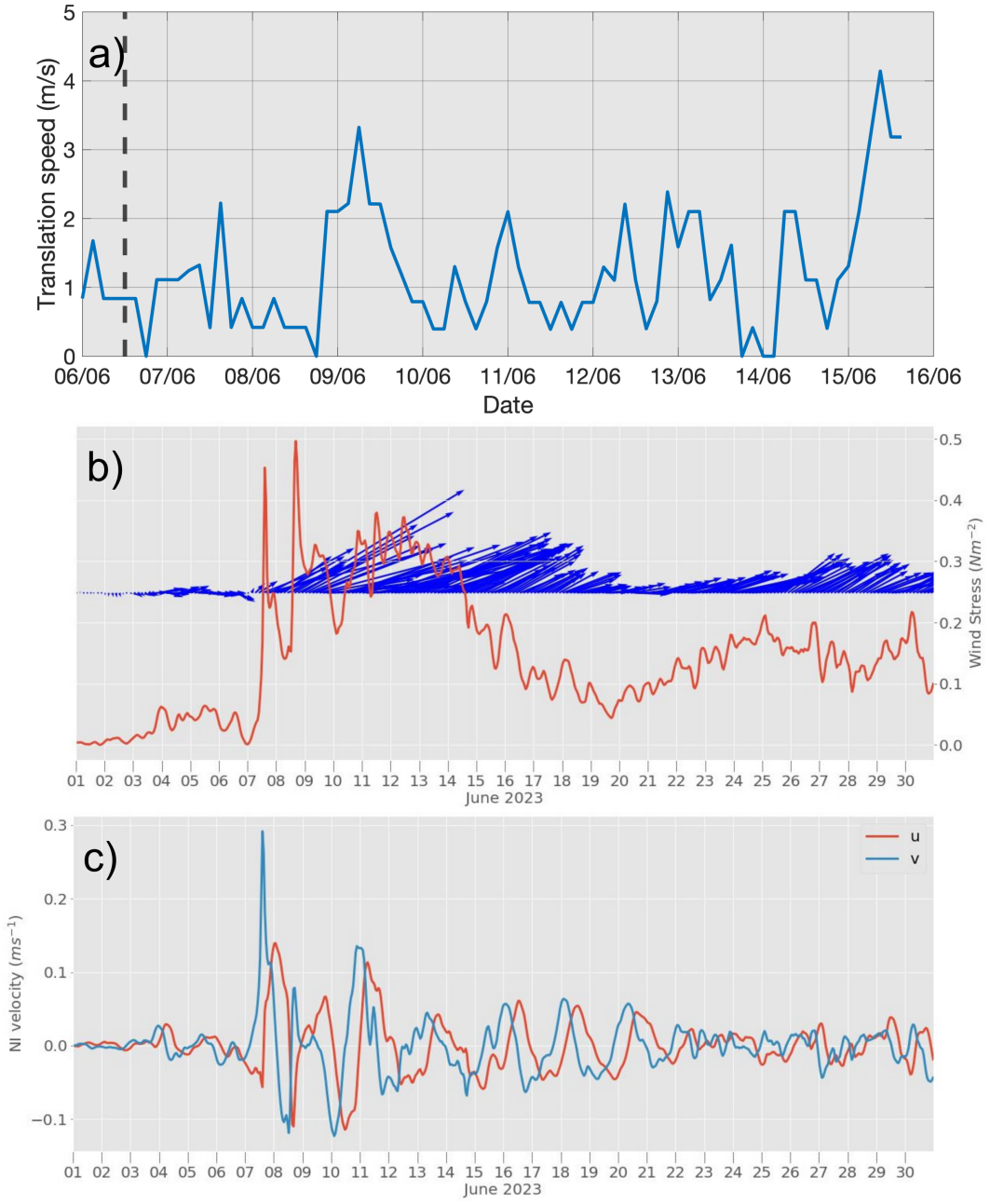

Figure C.2: (a) Translation Speed of cyclone Biparjoy. The dashed vertical line indicates the passage of the cyclone over the ship-survey area. Typical translation speeds of 4 $\mathrm{m\,s^{-1}}$ or lesser is defined as a "slow-moving cyclone" (Price, 1981). (b) Time series of wind stress vectors (in blue) and corresponding magnitudes (in red) during June 2023 from MERRA-2 reanalysis product (Global Modeling and Assimilation Office (GMAO), 2015) (c) Resulting currents from the slab model using the wind stress vectors in panel (b) from (Pollard and Millard, 1970) during June 2023. [NOTE: Panel-(a) and (b), (c) have different time axis limits.]

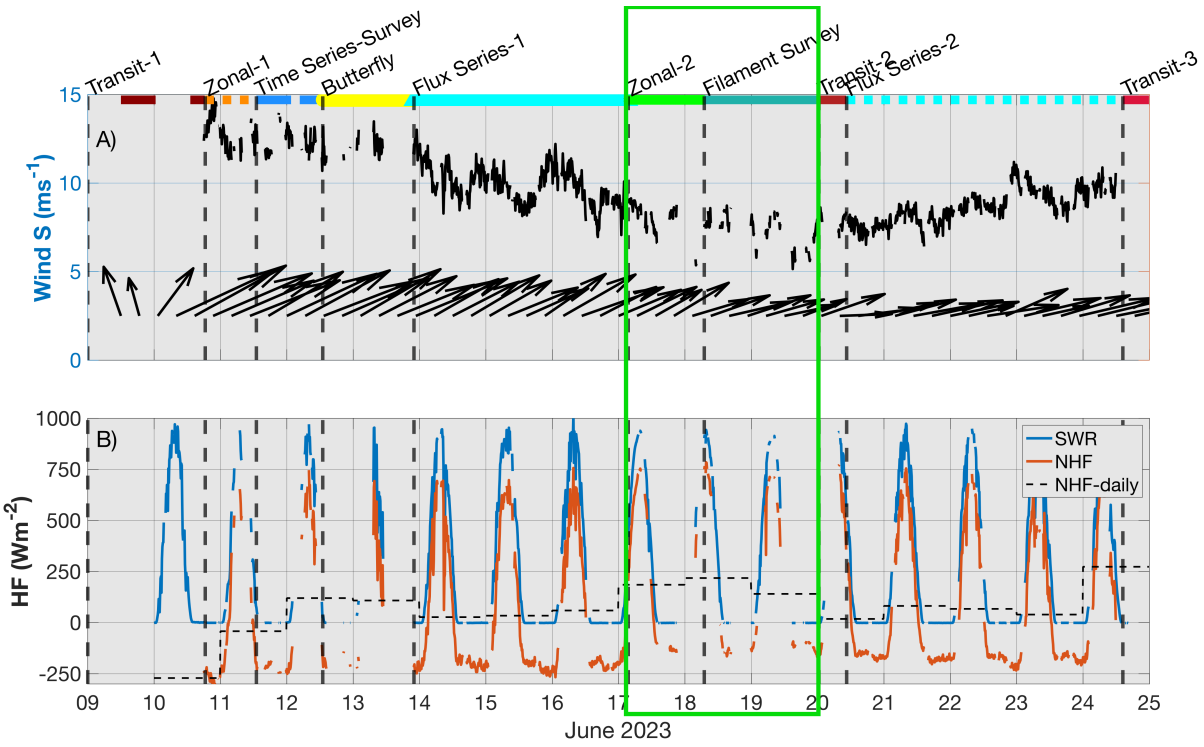

Figure C.3: Time-series of (A) wind speed magnitude and direction, (B) shortwave radiation (blue), net heat (red) and daily averaged net heat fluxes (broken line) during EKAMSAT Pilot Cruise (field campaign described in this study) in June 2023. The time series was divided based on sections shown in Figure C.5, with the major focus of the paper on Zonal-2 and Filament survey sections (i.e. within green box).

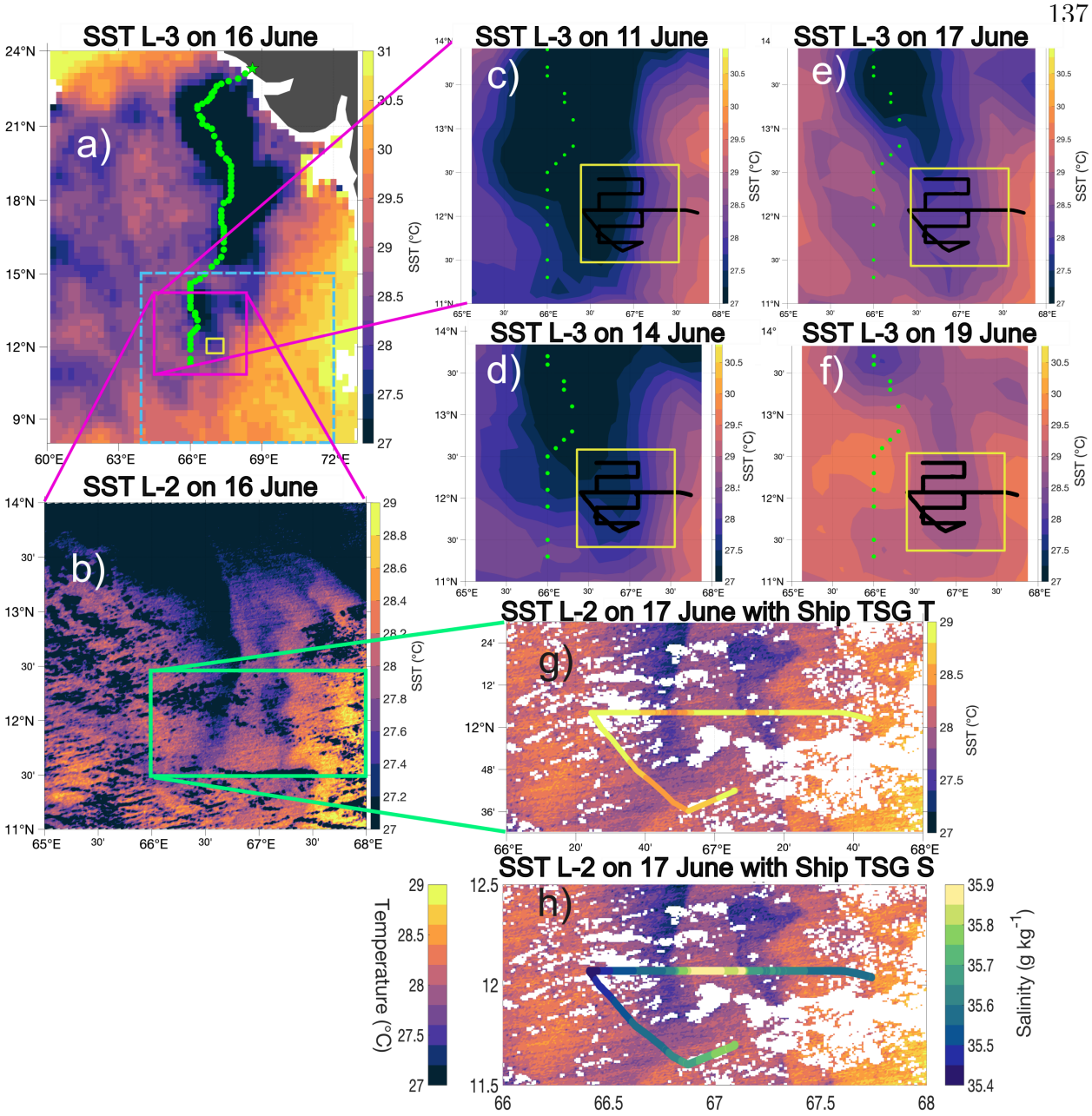

Figure C.4: (a) SST from AMSR-2 on 16 June 2023. The green dots indicate the path of the cyclone Biparjoy (as obtained from IMD 2023). (b) SST from MODIS Aqua L-2 product on 16 June 2023 over the solid magenta box in (a). SST from AMSR-2 over the same box is shown for (c) 11 June, (d) 14 June, (e) 17 June, and (f) 19 June 2023, respectively. Ship tracks are indicated by black lines in panels (c)-(f). (g) SST from VIIRS-NPP over the green box highlighted in (b), with in-situ SST data overlaid. (h) Same as (g) but with in-situ Sea Surface Salinity (SSS) overlaid on the satellite SST. The yellow box indicates the area around ship operations in panels (a), (c)-(f). Panels (a), (b), (c), (f) are also shown in Figure 4.1

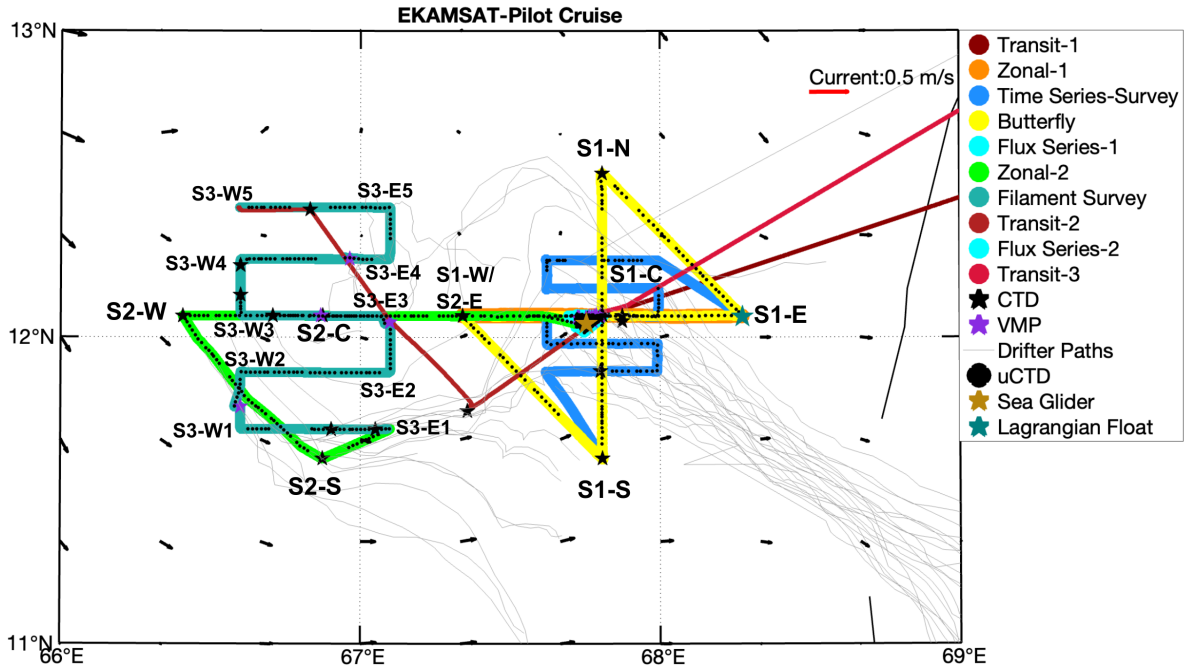

Figure C.5: Map of the Arabian Sea showing different ship sections sampled and assets employed during EKAMSAT pilot cruise (field campaign described in this study) in June 2023. The background arrows are the currents averaged over a five-day period from 17-22 June 2023 as derived from OSCAR current product (Dohan, 2021).

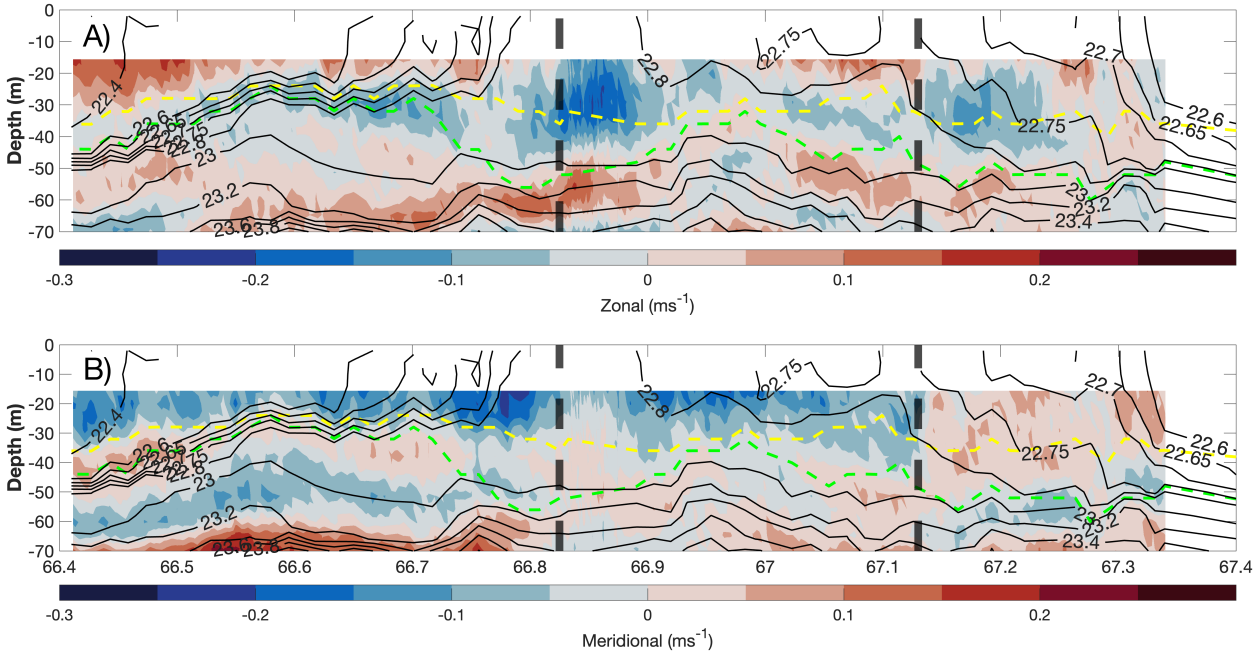

Figure C.6: Vertical sections of (a) zonal velocity and (b) meridional velocity between S2-E and S2-W after removing the effects due to background flow by subtracting the depth-averaged velocities below the mixed layer depth. Black contours in each panel indicate the isopycnals. The yellow line indicates the MLD, while the green line indicates the ILD. Vertical black dashed lines indicate section dividers based on change in meridional velocity.

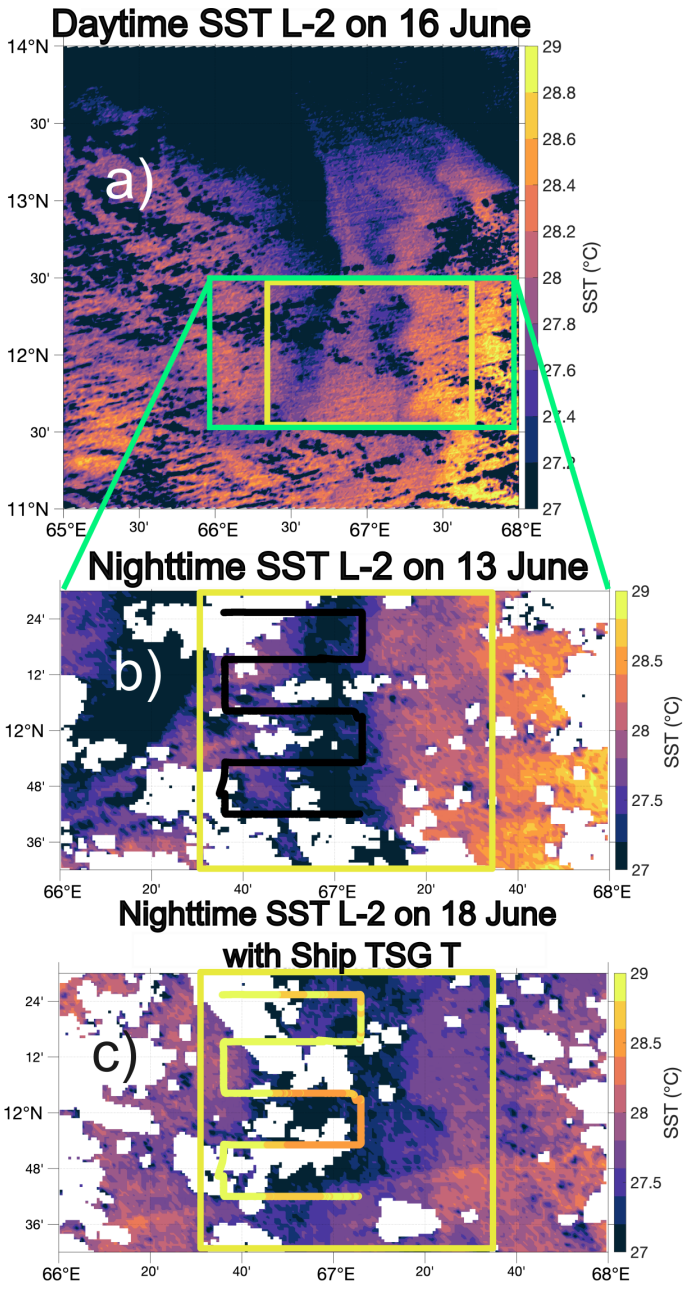

Figure C.7: (a) SST from MODIS Aqua L-2 product on 16 June 2023. This image was obtained during the daytime. (b) and (c) SST from Advanced Very High Resolution Radiometer (AVHRR) during the nightime over the green box shown in (a) for 13 June and 18 June respectively. Ship tracks are indicated by black lines in panel (b). In-situ Temperature data from ship's TSG is overlaid on panel (c). The yellow box indicates the area around ship operations. Panel (a) is also shown in Figure 4.1.

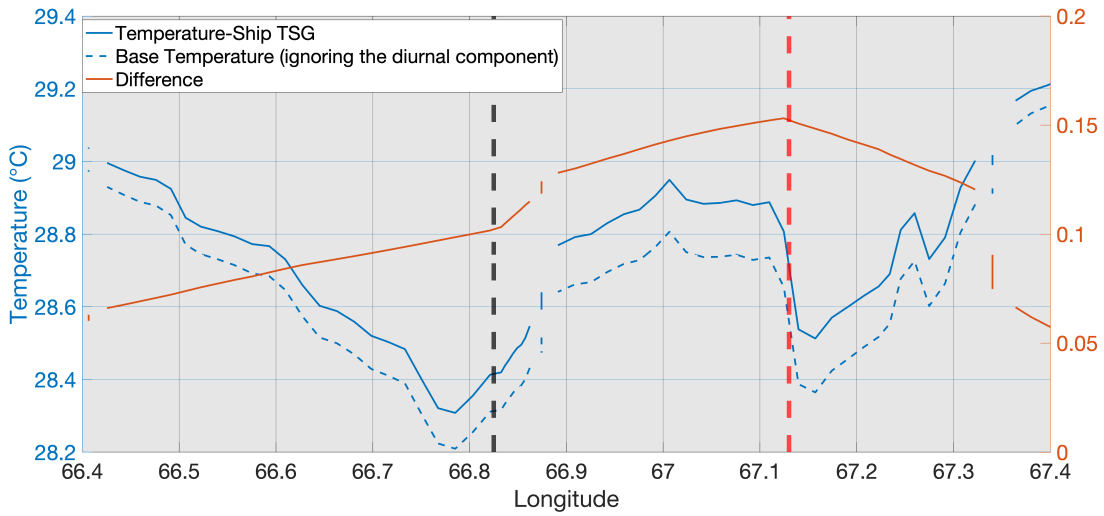

Figure C.8: Temperature from the ship's TSG between S2-E and S2-W (solid blue line), base temperature with diurnal variability removed (dashed blue line), and diurnal component (red line). Base and TSG temperatures refer to the left axis limits, while the diurnal component refers to the right.

Appendix D Additional Research

In addition to the specific research detailed in the preceding chapters, my time as a member of Dr. Tandon's diverse research group provided unparalleled opportunities for well-rounded scientific development and fostered extensive engagement with the broader scientific community locally, regionally and internationally.

D.1 Mentoring

One of the most rewarding aspects of my time as a PhD student in the Tandon Lab has been the opportunity to engage in research mentorship with both undergraduate and graduate students, while recognizing that one of the educator's primary roles is to advise and support students. I had the privilege of mentoring three undergraduate students and one graduate student from the Mechanical Engineering and Physics departments, many of whom were encountering oceanography and air-sea interactions for the first time. Guiding them through each stage of the research process, from advising on coding and shaping research questions to supporting data analysis and communicating results, was both a challenge and a joy. It was especially gratifying to witness how quickly they developed essential skills and confidence, reaffirming my belief in the transformative power of focused mentorship. These experiences especially deepened my commitment to mentoring those from marginalized communities and to making science education more inclusive and accessible. Helping students navigate scientific challenges also sharpened my ability to break down complex ideas and adapt my communication style for diverse audiences, skills that continue to shape my approach as both a scientist and a mentor.

Below are the students that I mentored during my PhD tenure:

Debarshi Sarkar

Debarshi is a PhD student in Engineering and Applied Sciences at UMass Dartmouth since Fall 2023. Debarshi is currently working with me and Prof. Tandon on analyzing the OMNI mooring records (maintained by NIOT, India) in Arabian Sea and comparing measured and derived air-sea interaction parameters with re-analysis products like MERRA-2, ERA-5 etc for his first chapter. See more in the section on collaboration (Page 131 of this dissertation).

Nicholas Monroe

B.S (Honors) in Mechanical Engineering

Honors Thesis: Biases in the Modeled Air-Sea Interaction During the Year 2017-18 in the Arabian Sea

Abstract: Within the study of Monsoons, use of computer models to predict the variables that relate to the state of the atmosphere and ocean (e.g. sea surface temperature and heat fluxes) is important to weather forecasting. These variables are calculated using different methods and algorithms and hence discrepancies could exist between observations and various model outputs. Considering the non-linearity of the system, small errors in such outputs could lead to different outcomes in terms of monsoon prediction. In this study, we investigate the annual patterns of these variables collected in the Arabian Sea from October 2017 to September 2018 and describe four different seasons: transition period, northeast monsoon, spring, and the southwest monsoon. The transition period corresponds to the period of September 16 – October 31, northeast monsoon season to the dates of November 1 – February 15, Spring season to February 16 – May 21, and Southwest monsoon to May 22 – September 15. The southwest and the northeast monsoons are usually characterized with strong winds of 8 $\mathrm{m\,s^{-1}}$ and extended periods of heating and cooling (also called the break and active phases), with tropical cyclones commonly observed during the northeast monsoon period. Spring period is marked by periods of clear skies and consistent ocean and atmo-

sphere warming by about 3 °C, while the transition period serves as a shift between the two types of monsoons. We further describe the biases between the model outputs (MERRA-2 from NASA and ERA-5 from Copernicus-an EU program) and the observations collected from a mooring in the Arabian Sea, with large biases existing during the monsoon periods. Correction of these biases in model outputs will lead to better predictions of monsoons, thus protecting human life and reducing economic loss.

Viktoriya Balabanova

B.S in Physics & UMassD-WHOI Blue Economy Internship program

Project: Investigation of the Validity of the Geostrophic Balance in the North Atlantic Ocean

Abstract: At global scales, ocean circulation plays an important role in transporting heat from the equator to the poles, thereby regulating weather patterns on Earth. Ocean currents accelerate due to wind, pressure gradients, and the rotation of the Earth (also known as the Coriolis force). At time scales much longer than a day, there is often a balance between the pressure gradient and the Coriolis forces, which is called the geostrophic balance. This balance accurately approximates ocean currents on a larger scale and hence this study focuses on validating this balance in the North Atlantic Ocean. We obtain geostrophic ocean currents by inferring pressure gradients from sea surface height, which are measured using satellite altimetry, and compare it with the in-situ measured ocean currents during the SPURS oceanographic expedition. The power of cloud computing, applied to large datasets, is used to test the geostrophic balance. Failure of this theory would point towards the importance of small-scale geostrophic or divergent flows (ageostrophic currents), as satellite altimetry has a limited spatial and temporal resolution of 25 km and 1 day, respectively. These smaller-scale processes may play a disproportionately large role in heat transport and air-sea circulation. The recently launched Surface Water and Ocean Topography (SWOT)

satellite aims to help see surface height at a spatial resolution of 1 km, thus offering a window to understanding the smaller-scale flows.

Ersen'S Joseph

B.S in Mechanical Engineering & UMassD-WHOI Blue Economy Internship program

Project: Studying the Ocean Surface Variables using Satellite imagery and Numerical Modeling

Abstract: The oceans are very important to monitor for phenomenon related to short-term weather (e.g. storms) to long term climate. Though important, in-situ ocean observations are hard to make, and are often complemented by satellite observations. In this work we study the ocean surface variables such as Sea Surface Temperature (SST), Sea Surface Salinity (SSS), Chlorophyll using satellite observations and to put the in-situ observations in context. In the first part of this study, we developed an ocean particle tracking numerical model using MATLAB. This model uses ocean currents measured from satellite altimetry as input to follow particles in the ocean, based on the forward Euler method integrations. To verify the performance of our model, we compare the numerical simulations of the particle motion to actual particle motion in the ocean. Our results highlight the importance of winds and other transient currents in the particle motion in the ocean. In the second part of this study, we use cloud computing tools to obtain high-resolution satellite imagery of above-mentioned variables. We are working to detect regions of high near-surface variations in such variables, called ocean fronts. These ocean fronts are important for ocean dynamics as well as ecosystem. We will detect these regions of significant gradients and compare them to field measurements obtained from various campaigns e.g. Monsoon Intra-Seasonal Oscillations in the Bay of Bengal (MISO-BoB).

D.2 Collaborations

My involvement in several large-scale, multi-institutional research initiatives, supported by Dr. Tandon's grant-funded projects, provided extensive opportunities for collaboration with researchers across oceanography and atmospheric sciences. These projects, spanning the USA and India, often required coordinated efforts, fostering a unique platform for interdisciplinary exchange. Participating in associated field campaigns, both at sea and through shore-side support, allowed me to work directly with scientists from diverse backgrounds. These collaborations underscored the importance of teamwork in addressing complex problems. Working within such diverse teams as well as co-ordinating the waves working group as a part of EKAMSAT research initiative honed my skills in clear communication, adaptability, and shared responsibility, shaping my current approach to research. Listed below are papers/research material of which I am part of:

- Sarkar, D., **Kerhalkar, S.** & Tandon, A.(in prep). *Assessing Air-Sea Heat Flux Biases in Reanalyses Products over the Arabian Sea Using OMNI Moorings*, Journal of Climate.

- Pham, H.T., Sarkar, S., Tandon, A., & **Kerhalkar, S.** (in prep). *How do the interactions between winds, heat fluxes and frontal currents / jets affect the vertical and cross-front thermal transport in the Dense Water Filament?*

D.3 Sea-going experience

Over the course of my PhD, I spent a total of 97 days at sea, participating in fieldwork for both projects I was directly involved in and others where I volunteered to gain additional experience. Beyond the collaborative environment these opportunities provided, fieldwork offered valuable exposure to the practical aspects of oceanographic research, including hands-on experience with state-of-the-art observational technologies used to study the ocean and

atmosphere. These experiences provided insights that cannot be gained in a classroom, deepening my understanding of air-sea interactions. Being in the field also strengthened my intuition for forming scientific hypotheses, while the ocean itself often offered clarity and comfort during periods of personal or academic challenge. Collectively, these experiences have shaped my perspective as a researcher and reaffirmed my commitment to oceanography. Outlined below are the fieldwork experiences undertaken during my PhD tenure.

- **Enhancing Knowledge of the Arabian Sea Marine environment through Science and Advanced Training Intensive Observational Period (EKAMSAT-ASTraL IOP)**

  Bay of Bengal, R/V Thomas G. Thompson, May–June 2024 (29 days)

  Chief Scientist: Dr. Leah Johnson (University of Washington)

  Funding agency: Office of Naval Research

  Responsibilities: Fast-CTD watch team, WaMoS data processing, Coordinating the waves working group.

- **Enhancing Knowledge of the Arabian Sea Marine environment through Science and Advanced Training (EKAMSAT-ASTraL) Pilot Cruise**

  Arabian Sea, R/V Roger Revelle, June 2023 (17 days)

  Chief Scientist: Dr. Craig Lee (University of Washington)

  Funding agency: Office of Naval Research

  Responsibilities: uCTD watch team, Processed ship MET, TSG, and WaMoS data.

- **Oxygen Deficient Zone Study**

  Eastern Tropical North Pacific, R/V Sally Ride, December 2020 (21 days)

  Chief Scientist: Prof. Mark Altabet (UMass Dartmouth)

  Funding agency: National Science Foundation

Responsibilities: Water sampling, CTD deployment and processing, Remote sensing–based shore-side support for N-loss studies witin Oxygen Deficient and Minimum Zones.

- **Monsoon Intraseasonal Oscillations in the Bay of Bengal Intensive Observational Period (MISO-BoB IOP)**

  Bay of Bengal, R/V Sally Ride, July–August 2019 (28 days)

  Chief Scientist: Dr. Emily Shroyer (Oregon State University)

  Funding agency: Office of Naval Research

  Responsibilities: Fast-CTD deployment, watch, and recovery.

- **Training Cruise – Introduction to Physical Oceanography**

  Buzzards Bay, R/V Lucky Lady, October 2019 (1 day)

  Chief Scientists: Profs. Miles Sundermeyer, Geoff Cowles (UMass Dartmouth)

  Responsibilities: Hands-on training in CTD deployment and water sampling.

Bibliography

Babin, S., J. Carton, T. Dickey, and J. Wiggert, 2004: Satellite evidence of hurricane-induced phytoplankton blooms in an oceanic desert. *Journal of Geophysical Research: Oceans*, **109 (C3)**.

Balaguru, K., P. Chang, R. Saravanan, L. R. Leung, Z. Xu, M. Li, and J.-S. Hsieh, 2012: Ocean barrier layers' effect on tropical cyclone intensification. *Proceedings of the National Academy of Sciences*, **109 (36)**, 14 343–14 347, https://doi.org/10.1073/pnas.1201364109.

Beal, L. M., and Coauthors, 2020: A road map to IndOOS-2: Better observations of the rapidly warming Indian Ocean. *Bulletin of the American Meteorological Society*, **101 (11)**, E1891–E1913, https://doi.org/10.1175/BAMS-D-19-0209.1.

Bellenger, H., and J. P. Duvel, 2009: An analysis of tropical ocean diurnal warm layers. *Journal of Climate*, **22 (13)**, 3629–3646, https://doi.org/10.1175/2008JCLI2598.1.

Bellenger, H., Y. N. Takayabu, T. Ushiyama, and K. Yoneyama, 2010: Role of diurnal warm layers in the diurnal cycle of convection over the tropical Indian Ocean during MISMO. *Monthly Weather Review*, **138 (6)**, 2426–2433, https://doi.org/10.1175/2010MWR3249.1.

Bernie, D. J., S. J. Woolnough, J. M. Slingo, and E. Guilyardi, 2005: Modeling diurnal and intraseasonal variability of the ocean mixed layer. *Journal of Climate*, **18 (8)**, 1190–1202, https://doi.org/10.1175/JCLI3319.1.

Bhardwaj, P., D. R. Pattanaik, and O. Singh, 2019: Tropical cyclone activity over Bay of Bengal in relation to El Niño-Southern Oscillation. *International Journal of Climatology*, **39 (14)**, 5452–5469, https://doi.org/10.1002/joc.6165.

Bhat, G. S., 2002: Near-surface variations and surface fluxes over the northern Bay of Bengal

during the 1999 Indian summer monsoon. *Journal of Geophysical Research Atmospheres*, **107 (17)**, ACL 6–1–ACL 6–19, https://doi.org/10.1029/2001JD000382.

Bogdanoff, A. S., 2017: Physics of diurnal warm layers: Turbulence, internal waves, and lateral mixing. Massachusetts Institute of Technology.

Brannigan, L., D. P. Marshall, A. Naveira-Garabato, and A. G. Nurser, 2015: The seasonal cycle of submesoscale flows. *Ocean Modelling*, **92**, 69–84.

Brown, M. E., V. Escobar, S. Moran, D. Entekhabi, P. E. O'Neill, E. G. Njoku, B. Doorn, and J. K. Entin, 2013: NASA's Soil Moisture Active Passive (SMAP) mission and opportunities for applications users. *Bulletin of the American Meteorological Society*, https://doi.org/10.1175/BAMS-D-11-00049.1.

Buckley, J. M., B. Mingels, and A. Tandon, 2020: The impact of lateral advection on SST and SSS in the northern Bay of Bengal during 2015. *Deep Sea Research Part II: Topical Studies in Oceanography*, **172**, 104 653, https://doi.org/10.1016/j.dsr2.2019.104653.

Burchard, H., and K. Bolding, 2001: Comparative analysis of four second-moment turbulence closure models for the oceanic mixed layer. *Journal of Physical Oceanography*, **31 (8)**, 1943–1968, https://doi.org/10.1175/1520-0485(2001)031<1943:CAOFSM>2.0.CO;2.

Burchard, H., K. Bolding, T. P. Rippeth, A. Stips, J. H. Simpson, and J. Sündermann, 2002: Microstructure of turbulence in the northern North Sea: A comparative study of observations and model simulations. *Journal of Sea Research*, **47 (3)**, 223–238, https://doi.org/https://doi.org/10.1016/S1385-1101(02)00126-0.

Burchard, H., K. Bolding, and M. R. Villarreal, 1999: *GOTM, a general ocean turbulence model: Theory, implementation and test cases*. Space Applications Institute.

Canuto, V. M., A. Howard, Y. Cheng, and M. S. Dubovikov, 2001: Ocean turbulence. Part I: One-point closure model—Momentum and heat vertical diffusivities. *Journal of Physical Oceanography*, **31 (6)**, 1413–1426.

Cao, C., F. J. De Luccia, X. Xiong, R. Wolfe, and F. Weng, 2013: Early on-orbit performance of the visible infrared imaging radiometer suite onboard the Suomi National Polar-Orbiting Partnership (S-NPP) satellite. *IEEE Transactions on Geoscience and Remote Sensing*, **52 (2)**, 1142–1156.

Casey, K. S., T. B. Brandon, P. Cornillon, and R. Evans, 2010: The past, present, and future of the AVHRR Pathfinder SST program. *Oceanography from space: Revisited*, 273–287.

Centurioni, L., A. Horányi, C. Cardinali, E. Charpentier, and R. Lumpkin, 2017: A global ocean observing system for measuring sea level atmospheric pressure: Effects and impacts on numerical weather prediction. *Bulletin of the American Meteorological Society*, **98 (2)**, 231–238.

Centurioni, L. R., 2017: Drifter technology and impacts for sea surface temperature, sea-level pressure, and ocean circulation studies. *Observing the oceans in real time*, Springer, 37–57.

Chattopadhyay, R., S. A. Rao, C. T. Sabeerali, G. George, D. N. Rao, A. Dhakate, and K. Salunke, 2016: Large-scale teleconnection patterns of Indian summer monsoon as revealed by CFSv2 retrospective seasonal forecast runs. *International Journal of Climatology*, **36 (9)**, 3297–3313, https://doi.org/10.1002/joc.4556.

Chaudhuri, D., D. Sengupta, E. D'Asaro, and S. Shivaprasad, 2021: Trapping of wind momentum in a salinity-stratified ocean. *Journal of Geophysical Research: Oceans*, **126 (12)**, e2021JC017 770, https://doi.org/10.1029/2021JC017770.

Clayson, C. A., and A. S. Bogdanoff, 2013: The effect of diurnal sea surface temperature warming on climatological air–sea fluxes. *Journal of Climate*, **26 (8)**, 2546–2556.

Clayson, C. A., and D. Weitlich, 2007: Variability of tropical diurnal sea surface temperature. *Journal of Climate*, https://doi.org/10.1175/JCLI3999.1.

Cornillon, P., L. Stramma, and J. F. Price, 1987: Satellite measurements of sea surface cooling during hurricane Gloria. *Nature*, **326 (6111)**, 373–375.

D'Asaro, E. A., 2003: The ocean boundary layer below hurricane Dennis. *Journal of Physical Oceanography*, **33 (3)**, 561–579.

D'Asaro, E. A., B. Sanford, P. P. Niiler, and E. J. Terrill, 2007: Cold wake of hurricane Frances. *Geophysical Research Letters*, **34 (15)**.

Dauhajre, D. P., and J. C. McWilliams, 2018: Diurnal evolution of submesoscale front and filament circulations. *Journal of Physical Oceanography*, **48 (10)**, 2343–2361.

de Szoeke, S. P., T. Marke, and W. A. Brewer, 2021: Diurnal ocean surface warming drives convective turbulence and clouds in the atmosphere. *Geophysical Research Letters*, **48 (4)**, e2020GL091 299.

de Szoeke, S. P., E. D. Skyllingstad, P. Zuidema, and A. S. Chandra, 2017: Cold pools and their influence on the tropical marine boundary layer. *Journal of the Atmospheric Sciences*, **74 (4)**, 1149–1168, https://doi.org/10.1175/JAS-D-16-0264.1.

DeMott, C. A., N. P. Klingaman, and S. J. Woolnough, 2015: Atmosphere-ocean coupled processes in the Madden-Julian oscillation. *Reviews of Geophysics*, **53 (4)**, 1099–1154, https://doi.org/10.1002/2014RG000478.

Dewey, R. K., and J. N. Moum, 1990: Enhancement of fronts by vertical mixing. *Journal of Geophysical Research*, **95 (C6)**, 9433, https://doi.org/10.1029/jc095ic06p09433.

Dobbelaere, T., A. Dekens, A. Saint-Amand, L. Alaerts, D. M. Holstein, and E. Hanert, 2024: Hurricanes enhance coral connectivity but also superspread coral diseases. *Global Change Biology*, **30 (6)**, 1–16, https://doi.org/10.1111/gcb.17382.

Dohan, K., 2021: Ocean Surface Current Analyses Real-time (OSCAR) surface currents - near real time 0.25 Degree (version 2.0). NASA Physical Oceanography Distributed Active Archive Center, https://doi.org/10.5067/OSCAR-25N20.

Donlon, C., and Coauthors, 2007: The global ocean data assimilation experiment high-resolution sea surface temperature pilot project. *Bulletin of the American Meteorological Society*, **88 (8)**, 1197–1214.

Drushka, K., W. E. Asher, B. Ward, and K. Walesby, 2016: Understanding the formation and evolution of rain-formed fresh lenses at the ocean surface. *Journal of Geophysical Research: Oceans*, **121 (4)**, 2673–2689.

D'Asaro, E., C. Lee, L. Rainville, R. Harcourt, and L. Thomas, 2011: Enhanced turbulence and energy dissipation at ocean fronts. *science*, **332 (6027)**, 318–322.

Echols, R., and S. C. Riser, 2020: The impact of barrier layers on arabian sea surface temperature variability. *Geophysical Research Letters*, **47 (3)**, e2019GL085 290, https://doi.org/10.1029/2019GL085290.

Emanuel, K., 2001: Contribution of tropical cyclones to meridional heat transport by the oceans. *Journal of Geophysical Research: Atmospheres*, **106 (D14)**, 14 771–14 781.

Emanuel, K., 2003: Tropical cyclones. *Annual review of earth and planetary sciences*, **31 (1)**, 75–104.

Entekhabi, D., and Coauthors, 2014: SMAP handbook–soil moisture active passive: Mapping soil moisture and freeze/thaw from space. *Jet Propulsion Lab., California Inst. Technol., Pasadena, Calif.*

Essink, S., V. Hormann, L. R. Centurioni, and A. Mahadevan, 2019: Can we detect submesoscale motions in drifter pair dispersion? *Journal of Physical Oceanography*, **49 (9)**, 2237–2254.

Evan, A. T., and S. J. Camargo, 2011: A climatology of Arabian Sea cyclonic storms. *Journal of climate*, **24 (1)**, 140–158.

Fairall, C. W., E. F. Bradley, J. S. Godfrey, G. A. Wick, J. B. Edson, and G. S. Young, 1996a: Cool-skin and warm-layer effects on sea surface temperature. *Journal of Geophysical Research: Oceans*, **101 (C1)**, 1295–1308, https://doi.org/10.1029/95JC03190.

Fairall, C. W., E. F. Bradley, J. E. Hare, A. A. Grachev, and J. B. Edson, 2003: Bulk parameterization of air-sea fluxes: Updates and verification for the COARE algorithm. *Journal of Climate*, **16 (4)**, 571–591, https://doi.org/10.1175/1520-0442(2003)016<0571:BPOASF>2.0.CO;2.

Fairall, C. W., E. F. Bradley, D. P. Rogers, J. B. Edson, and G. S. Young, 1996b: Bulk parameterization of air-sea fluxes for tropical ocean-global atmosphere coupled-ocean atmosphere response experiment. *Journal of Geophysical Research: Oceans*, **101 (C2)**, 3747–3764, https://doi.org/10.1029/95JC03205.

Ferrari, R., and C. Wunsch, 2009: Ocean circulation kinetic energy: Reservoirs, sources, and sinks. *Annual Review of Fluid Mechanics*, **41 (1)**, 253–282.

Fox-Kemper, B., R. Ferrari, and R. Hallberg, 2008: Parameterization of mixed layer eddies. Part I: Theory and diagnosis. *Journal of Physical Oceanography*, **38 (6)**, 1145–1165.

Gadgil, S., 2003: The Indian monsoon and its variability. *Annual Review of Earth and Planetary Sciences*, **31 (1998)**, 429–467, https://doi.org/10.1146/annurev.earth.31.100901.141251.

Gadgil, S., 2018: The monsoon system: Land–sea breeze or the ITCZ? *Journal of Earth System Science*, **127 (1)**, 1, https://doi.org/10.1007/s12040-017-0916-x.

Gadgil, S., and S. Gadgil, 2006: The Indian monsoon, GDP and agriculture. *Economic and Political Weekly*, **41 (47)**, 4887–4895.

Gentemann, C. L., P. J. Minnett, P. Le Borgne, and C. J. Merchant, 2008: Multi-satellite measurements of large diurnal warming events. *Geophysical Research Letters*, **35 (22)**.

Gentemann, C. L., P. J. Minnett, and B. Ward, 2009: Profiles of ocean surface heating (POSH): A new model of upper ocean diurnal warming. *Journal of Geophysical Research: Oceans*, **114 (C7)**, https://doi.org/https://doi.org/10.1029/2008JC004825.

Global Modeling and Assimilation Office (GMAO), 2015: MERRA-2 tavg1_2d_lnd_nx: 2d,1-Hourly,Time-Averaged,Single-Level,Assimilation,Land Surface Diagnostics V5.12.4. Published: Greenbelt, MD, USA, Goddard Earth Sciences Data and Information Services Center (GES DISC), https://doi.org/10.5067/RKPHT8KC1Y1T.

Goswami, B. N., S. A. Rao, D. Sengupta, and S. Chakravorty, 2016: Monsoons to mixing in the Bay of Bengal. *Oceanography*, **29 (2)**, 18–27.

Gutiérrez Brizuela, N., M. H. Alford, S.-P. Xie, J. Sprintall, G. Voet, S. J. Warner, K. Hughes, and J. N. Moum, 2023: Prolonged thermocline warming by near-inertial internal waves in the wakes of tropical cyclones. *Proceedings of the National Academy of Sciences*, **120 (26)**, e2301664 120.

Haine, T. W., and J. Marshall, 1998: Gravitational, symmetric, and baroclinic instability of the ocean mixed layer. *Journal of physical oceanography*, **28 (4)**, 634–658.

Halley, E., 1686: An historical account of the trade winds, and monsoons, observable in the seas between and near the Tropicks, with an attempt to assign the physical cause of the said winds. *Philosophical Transactions of the Royal Society of London*, **16 (183)**, 153–168, https://doi.org/10.1098/rstl.1686.0026.

Haney, S., and Coauthors, 2012: Hurricane wake restratification rates of one-, two- and three-dimensional processes. *Journal of Marine Research*, **70 (6)**, 824–850, https://doi.org/10.1357/002224012806770937.

Hormann, V., L. R. Centurioni, and A. L. Gordon, 2019: Freshwater export pathways from the Bay of Bengal. *Deep-Sea Research Part II: Topical Studies in Oceanography*, **168 (September)**, 104 645, https://doi.org/10.1016/j.dsr2.2019.104645.

Hormann, V., L. R. Centurioni, A. Mahadevan, S. Essink, E. A. D'Asaro, and B. P. Kumar, 2016: Variability of near-surface circulation and sea surface salinity observed from Lagrangian drifters in the northern Bay of Bengal during the waning 2015 southwest monsoon. *Oceanography*, **29 (2)**, 124–133.

Huffman, G. J., D. T. Bolvin, D. Braithwaite, K. Hsu, R. Joyce, P. Xie, and S.-H. Yoo, 2015: NASA global precipitation measurement (GPM) integrated multi-satellite retrievals for GPM (IMERG). *Algorithm theoretical basis document (ATBD) version*, **4 (26)**, 30.

Hughes, K. G., J. N. Moum, and E. L. Shroyer, 2020a: Evolution of the velocity structure in the diurnal warm layer. *Journal of Physical Oceanography*, **50 (3)**, 615–631, https://doi.org/10.1175/JPO-D-19-0207.1.

Hughes, K. G., J. N. Moum, and E. L. Shroyer, 2020b: Heat transport through diurnal warm layers. *Journal of Physical Oceanography*, **50 (10)**, 2885–2905, https://doi.org/10.1175/JPO-D-20-0079.1.

Hughes, K. G., J. N. Moum, E. L. Shroyer, and W. D. Smyth, 2021: Stratified shear instabilities in diurnal warm layers. *Journal of Physical Oceanography*, https://doi.org/10.1175/jpo-d-20-0300.1.

Imberger, J., 1985: The diurnal mixed layer. *Limnology and oceanography*, **30 (4)**, 737–770.

IMD, 2023: Extremely severe cyclonic storm "BIPARJOY" over the ARABIAN Sea (6^{th}-19^{th} June, 2023): A report. India Meteorological Department, New Delhi.

Iyer, S., and K. Drushka, 2021: The influence of preexisting stratification and tropical rain modes on the mixed layer salinity response to rainfall. *Journal of Geophysical Research: Oceans*, **126 (10)**, 1–18, https://doi.org/10.1029/2021JC017574.

Jaeger, G. S., and A. Mahadevan, 2018: Submesoscale-selective compensation of fronts in a salinity-stratified ocean. *Science Advances*, **4 (2)**, 1–9, https://doi.org/10.1126/sciadv.1701504.

Jarugula, S., D. Sengupta, E. Shroyer, and F. Papa, 2024: Mixing of rain and river water in the Bay of Bengal from basin-scale freshwater balance. *Geophysical Research Letters*, **51 (3)**, e2023GL106 451, https://doi.org/10.1029/2023GL106451.

Johnson, L., B. Fox-Kemper, Q. Li, H. T. Pham, and S. Sarkar, 2023: A finite-time ensemble method for mixed layer model comparison. *Journal of Physical Oceanography*.

Johnson, L., C. M. Lee, E. A. D'Asaro, L. Thomas, and A. Shcherbina, 2020a: Restratification at a California Current upwelling front. Part I: Observations. *Journal of Physical Oceanography*, https://doi.org/10.1175/JPO-D-19-0203.1.

Johnson, L., C. M. Lee, E. A. D'Asaro, J. O. Wenegrat, and L. N. Thomas, 2020b: Restratification at a California Current upwelling front. Part II: Dynamics. *Journal of Physical Oceanography*, **50 (5)**, 1473–1487, https://doi.org/10.1175/JPO-D-19-0204.1.

Johnston, T. S., D. L. Rudnick, N. Brizuela, and J. N. Moum, 2020: Advection by the North Equatorial Current of a cold wake due to multiple typhoons in the western Pacific: Measurements from a profiling float array. *Journal of Geophysical Research: Oceans*, **125 (4)**, e2019JC015 534.

Johnston, T. S., S. Wang, C.-Y. Lee, J. N. Moum, D. L. Rudnick, and A. Sobel, 2021: Near-inertial wave propagation in the wake of Super Typhoon Mangkhut: Measurements from a profiling float array. *Journal of Geophysical Research: Oceans*, **126 (2)**, e2020JC016 749.

Joseph, K. J., A. Tandon, R. Venkatesan, J. T. Farrar, and R. A. Weller, 2022: Longwave radiation corrections for the OMNI buoy network. *Journal of Atmospheric and Oceanic Technology*, **39 (2)**, 271–282, https://doi.org/10.1175/JTECH-D-21-0069.1.

Karnauskas, K. B., L. Zhang, and K. A. Emanuel, 2021: The feedback of cold wakes on tropical cyclones. *Geophysical Research Letters*, **48 (7)**, e2020GL091 676.

Kerhalkar, S., A. Kannad, A. Kinsella, A. Tandon, J. Sprintall, and C. M. Lee, 2025: Monsoon-Frontal interactions drive cyclone Biparjoy's wake recovery in the Arabian Sea. *Geophysical Research Letters*, **52 (4)**, https://doi.org/10.1029/2024GL112413.

Kerhalkar, S., and Coauthors, In Review: Modulation of diurnal SST and diurnal warm layer variability by salinity-driven stratification in the Bay of Bengal. *Journal of physical oceanography*.

Kikuchi, K., and B. Wang, 2010: Formation of tropical cyclones in the northern Indian Ocean associated with two types of tropical intraseasonal oscillation modes. *Journal of*

the Meteorological Society of Japan. Ser. II, **88 (3)**, 475–496, https://doi.org/10.2151/jmsj.2010-313.

Kondo, J., Y. Sasano, and T. Ishii, 1979: On wind-driven current and temperature profiles with diurnal period in the oceanic planetary boundary layer. *Journal of Physical Oceanography*, **9 (2)**, 360–372.

Krishnamurti, T. N., P. Ardanuy, Y. Ramanathan, and R. Pasch, 1981: On the onset vortex of the summer monsoon. *Monthly Weather Review*, **109 (2)**, 344–363.

Krishnamurti, T. N., A. Chakraborty, R. Krishnamurti, W. K. Dewar, and C. A. Clayson, 2007: Passage of intraseasonal waves in the subsurface oceans. *Geophysical Research Letters*, **34 (14)**, 1–5, https://doi.org/10.1029/2007GL030496.

Kunze, E., 1990: The evolution of salt fingers in inertial wave shear. *Journal of Marine Research*, **48 (3)**.

Lau, W. K. M., and D. E. Waliser, 2007: *Intraseasonal variability in the atmosphere-ocean climate system*. Springer-Praxis books in environmental sciences, Springer Praxis Publishing, Berlin Chichester.

Levitus, S., 1983: Climatological atlas of the world ocean. *Eos, Transactions American Geophysical Union*, **64 (49)**, 962–963.

Lin, H., G. Brunet, and J. Derome, 2009: An observed connection between the North Atlantic Oscillation and the Madden–Julian Oscillation. *Journal of Climate*, **22 (2)**, 364–380, https://doi.org/10.1175/2008JCLI2515.1.

Lotliker, A. A., M. M. Omand, A. J. Lucas, S. R. Laney, A. Mahadevan, and M. Ravichandran, 2016: Penetrative radiative flux in the Bay of Bengal. *Oceanography*, **29 (2)**, 214–221.

Lucas, A. J., and Coauthors, 2014: Mixing to monsoons: Air–sea interactions in the Bay of Bengal. *Eos, Transactions American Geophysical Union*, **95 (30)**, 269–270, https://doi.org/10.1002/2014EO300001.

MacKinnon, J. A., and Coauthors, 2021: A warm jet in a cold ocean. *Nature Communications*, **12 (1)**, https://doi.org/10.1038/s41467-021-22505-5.

Mahadevan, A., G. S. Jaeger, M. Freilich, M. M. Omand, E. L. Shroyer, and D. Sengupta, 2016: Freshwater in the Bay of Bengal. *Oceanography*, **29 (2)**, 72–81.

Mahadevan, A., A. Tandon, and R. Ferrari, 2010: Rapid changes in mixed layer stratification driven by submesoscale instabilities and winds. *Journal of Geophysical Research: Oceans*, **115 (C3)**.

Marullo, S., P. J. Minnett, R. Santoleri, and M. Tonani, 2016: The diurnal cycle of sea-surface temperature and estimation of the heat budget of the Mediterranean Sea. *Journal of Geophysical Research: Oceans*, **121 (11)**, 8351–8367.

Maze, G., and K. Balem, 2020: argopy: A python library for Argo ocean data analysis. *Journal of Open Source Software*, **5 (53)**, 2425, https://doi.org/10.21105/joss.02425.

McKie, T., A. J. Lucas, and J. MacKinnon, 2024: Submesoscale dynamics in the Bay of Bengal: Inversions and instabilities. *Journal of Geophysical Research: Oceans*, **129 (3)**, e2023JC020 563, https://doi.org/10.1029/2023JC020563.

McPhaden, M. J., and S. P. Hayes, 1991: On the variability of winds, sea surface temperature, and surface layer heat content in the western equatorial Pacific. *Journal of Geophysical Research: Oceans*, **96 (S01)**, 3331–3342.

Mei, W., and C. Pasquero, 2012: Restratification of the upper ocean after the passage of a tropical cyclone: A numerical study. *Journal of physical oceanography*, **42 (9)**, 1377–1401.

Mellor, G. L., and T. Yamada, 1982: Development of a turbulence closure model for geophysical fluid problems. *Reviews of Geophysics*, **20 (4)**, 851–875.

Merchant, C. J., M. J. Filipiak, P. Le Borgne, H. Roquet, E. Autret, J. F. Piollé, and S. Lavender, 2008: Diurnal warm-layer events in the western Mediterranean and European shelf seas. *Geophysical Research Letters*, **35 (4)**, 2–5, https://doi.org/10.1029/2007GL033071.

Monterey, G. I., and S. Levitus, 1997: Seasonal variability of mixed layer depth for the world ocean.

Moulin, A. J., J. N. Moum, E. L. Shroyer, and M. Hoecker-Martínez, 2021: Freshwater lens fronts propagating as buoyant gravity currents in the equatorial Indian Ocean. *Journal of Geophysical Research: Oceans*, **126 (8)**, 1–14, https://doi.org/10.1029/2021JC017186.

Mrvaljevic, R. K., and Coauthors, 2013: Observations of the cold wake of Typhoon Fanapi (2010). *Geophysical Research Letters*, **40 (2)**, 316–321, https://doi.org/10.1029/2012GL054282.

NASA Goddard Space Flight Center, O. B. P. G., 2018: Moderate-resolution Imaging Spectroradiometer (MODIS) aqua ocean color data. NASA OB.DAAC, type: dataset, https://doi.org/10.5067/AQUA/MODIS/L2/OC/2018.

National Academies of Sciences, Engineering, and Medicine, 2016: *Next Generation Earth System Prediction: Strategies for Subseasonal to Seasonal Forecasts*. The National Academies Press, Washington, DC, https://doi.org/10.17226/21873.

Nie, J., W. R. Boos, and Z. Kuang, 2010: Observational evaluation of a convective quasi-equilibrium view of monsoons. *Journal of Climate*, **23 (16)**, 4416–4428, https://doi.org/10.1175/2010JCLI3505.1.

Niiler, P. P., A. S. Sybrandy, K. Bi, P. M. Poulain, and D. Bitterman, 1995: Measurements of the water-following capability of holey-sock and TRISTAR drifters. *Deep Sea Research Part I: Oceanographic Research Papers*, **42 (11)**, 1951–1964, https://doi.org/https://doi.org/10.1016/0967-0637(95)00076-3.

Nilsson, E., M. Lothon, F. Lohou, E. Pardyjak, O. Hartogensis, and C. Darbieu, 2016: Turbulence kinetic energy budget during the afternoon transition–Part 2: A simple TKE model. *Atmospheric Chemistry and Physics*, **16 (14)**, 8873–8898.

Nuijens, L., and Coauthors, 2024: The Air-Sea Interaction (ASI) submesoscale: physics and impact. *Lorentz Workshop*.

Ohlmann, J. C., 2003: Ocean radiant heating in climate models. *Journal of Climate*, **16 (9)**, 1337–1351, https://doi.org/10.1175/1520-0442-16.9.1337.

Pargaonkar, S. M., S. K. Mallick, B. K. Kalita, and P. N. Vinayachandran, 2025: Submesoscale processes associated with the East India Coastal Current. *Journal of Geophysical Research: Oceans*, **130 (2)**, e2023JC020 451, https://doi.org/10.1029/2023JC020451.

Pasquero, C., and K. Emanuel, 2008: Tropical cyclones and transient upper-ocean warming. *Journal of Climate*, **21 (1)**, 149–162.

Paulson, C. A., and J. J. Simpson, 1977: Irradiance measurements in the upper ocean. *Journal of Physical Oceanography*, **7 (6)**, 952–956, https://doi.org/10.1175/1520-0485(1977)007<0952:IMITUO>2.0.CO;2.

Phillips, H. E., and Coauthors, 2021: Progress in understanding of Indian Ocean circulation, variability, air–sea exchange, and impacts on biogeochemistry. *Ocean Science*, **17 (6)**, 1677–1751, https://doi.org/10.5194/os-17-1677-2021.

Pimentel, S., K. Haines, and N. K. Nichols, 2008: Modeling the diurnal variability of sea surface temperatures. *Journal of Geophysical Research: Oceans*, **113 (C11)**.

Pimentel, S., W.-H. Tse, H. Xu, D. Denaxa, E. Jansen, G. Korres, I. Mirouze, and A. Storto, 2019: Modeling the near-surface diurnal cycle of sea surface temperature in the Mediterranean sea. *Journal of Geophysical Research: Oceans*, **124 (1)**, 171–183, https://doi.org/10.1029/2018JC014289.

Pinkel, R., 2012: Velocity imprecision in finite-beamwidth shipboard Doppler sonar: A first-generation correction algorithm. *Journal of Atmospheric and Oceanic Technology*, **29 (10)**, 1569–1580.

Pinkel, R., M. A. Goldin, J. A. Smith, O. M. Sun, A. A. Aja, M. N. Bui, and T. Hughen, 2011: The Wirewalker: a vertically profiling instrument carrier powered by ocean waves. *Journal of Atmospheric and Oceanic Technology*, **28 (3)**, 426–435, https://doi.org/10.1175/2010JTECHO805.1.

Pollard, R. T., and R. Millard, 1970: Comparison between observed and simulated wind-generated inertial oscillations. *Deep Sea Research and Oceanographic Abstracts*, Elsevier, Vol. 17, 813–821, issue: 4.

Pradhan, M., S. A. Rao, A. Bhattacharya, and S. Balasubramanian, 2022: Improvements in diurnal cycle and its impact on seasonal mean by incorporating COARE flux algorithm in CFS. *Frontiers in Climate*, **3 (February)**, 1–21, https://doi.org/10.3389/fclim.2021.792980.

Prakash, K. R., V. Pant, T. V. S. Udaya Bhaskar, and N. Chandra, 2022: What made the sustained intensification of tropical cyclone Fani in the Bay of Bengal? an investigation

using coupled atmosphere–ocean model. *Atmosphere*, **13 (4)**, 535, https://doi.org/10.3390/atmos13040535.

Price, J. F., 1981: Upper ocean response to a hurricane. *Journal of Physical Oceanography*, **11 (2)**, 153–175.

Price, J. F., J. Morzel, and P. P. Niiler, 2008: Warming of SST in the cool wake of a moving hurricane. *Journal of Geophysical Research: Oceans*, **113 (7)**, 1–19, https://doi.org/10.1029/2007JC004393.

Price, J. F., R. A. Weller, and R. Pinkel, 1986: Diurnal cycling: observations and models of the upper ocean response to diurnal heating, cooling, and wind mixing. *Journal of Geophysical Research: Oceans*, **91 (C7)**, 8411–8427, https://doi.org/10.1029/JC091iC07p08411.

Prytherch, J., J. T. Farrar, and R. A. Weller, 2013: Moored surface buoy observations of the diurnal warm layer. *Journal of Geophysical Research: Oceans*, **118 (9)**, 4553–4569, https://doi.org/10.1002/jgrc.20360.

Rainville, L., C. M. Lee, K. Arulananthan, S. U. Jinadasa, H. J. Fernando, W. N. Priyadarshani, and H. Wijesekera, 2022: Water mass exchanges between the Bay of Bengal and Arabian Sea from multiyear sampling with autonomous gliders. *Journal of Physical Oceanography*, **52 (10)**, 2377–2396, https://doi.org/10.1175/JPO-D-21-0279.1.

Ramachandran, S., and A. Tandon, 2020: Generation of submesoscale temperature inversions below salinity fronts in the Bay of Bengal. *Journal of Geophysical Research: Oceans*, **125 (12)**, https://doi.org/10.1029/2020JC016278.

Ramachandran, S., and Coauthors, 2018: Submesoscale processes at shallow salinity fronts in

the Bay of Bengal: Observations during the winter monsoon. *Journal of Physical Oceanography*, **48 (3)**, 479–509, https://doi.org/10.1175/JPO-D-16-0283.1.

Ramu, D. A., and Coauthors, 2016: Indian summer monsoon rainfall simulation and prediction skill in the CFSv2 coupled model: Impact of atmospheric horizontal resolution. *Journal of Geophysical Research: Atmospheres*, **121 (5)**, 2205–2221, https://doi.org/https://doi.org/10.1002/2015JD024629.

Ranganathan, S., R. A. Weller, R. Venkatesan, A. Tandon, M. Arul Muthiah, and M. Mohapatra, 2024: Performance of moored real-time ocean observations during cyclones in the Bay of Bengal. *Marine Technology Society Journal*, **58 (3)**, 56–69.

Rao, R. R., M. S. Girish Kumar, M. Ravichandran, A. R. Rao, V. V. Gopalakrishna, and P. Thadathil, 2010: Interannual variability of Kelvin wave propagation in the wave guides of the equatorial Indian Ocean, the coastal Bay of Bengal and the southeastern Arabian Sea during 1993-2006. *Deep-Sea Research Part I: Oceanographic Research Papers*, **57 (1)**, 1–13, https://doi.org/10.1016/j.dsr.2009.10.008.

Rao, R. R., V. Jitendra, M. S. GirishKumar, M. Ravichandran, and S. S. Ramakrishna, 2015: Interannual variability of the Arabian Sea warm pool: observations and governing mechanisms. *Climate Dynamics*, **44 (7-8)**, 2119–2136, https://doi.org/10.1007/s00382-014-2243-0.

Rao, R. R., and R. Sivakumar, 1999: On the possible mechanisms of the evolution of a mini-warm pool during the pre-summer monsoon season and the genesis of onset vortex in the South-Eastern Arabian Sea. *Quarterly Journal of the Royal Meteorological Society*, **125 (555)**, 787–809, https://doi.org/10.1002/qj.49712555503.

Rao, R. R., and R. Sivakumar, 2003: Seasonal variability of sea surface salinity and salt

budget of the mixed layer of the north Indian Ocean. *Journal of Geophysical Research: Oceans*, **108 (C1)**, 9–14, https://doi.org/https://doi.org/10.1029/2001JC000907.

Ray, K., R. Giri, S. Ray, A. Dimri, and M. Rajeevan, 2021: An assessment of long-term changes in mortalities due to extreme weather events in India: A study of 50 years' data, 1970–2019. *Weather and Climate Extremes*, **32**, 100 315, https://doi.org/10.1016/j.wace.2021.100315.

Renner, M., M. Wild, M. Schwarz, and A. Kleidon, 2019: Estimating shortwave clear-sky fluxes from hourly global radiation records by quantile regression. *Earth and Space Science*, **6 (8)**, 1532–1546, https://doi.org/10.1029/2019EA000686.

Reynolds, R. W., T. M. Smith, C. Liu, D. B. Chelton, K. S. Casey, and M. G. Schlax, 2007: Daily high-resolution-blended analyses for sea surface temperature. *Journal of climate*, **20 (22)**, 5473–5496.

Roemmich, D., and Coauthors, 2009: The Argo program: Observing the Global Ocean with profiling floats. *Oceanography*, **22 (2)**, 34–43.

Rudnick, D. L., and R. A. Weller, 1993: The heat budget in the North Atlantic subtropical frontal zone. *Journal of Geophysical Research: Oceans*, **98 (C4)**, 6883–6893, https://doi.org/10.1029/92JC02885.

Sanabia, E. R., and S. R. Jayne, 2020: Ocean observations under two major hurricanes: evolution of the response across the storm wakes. *AGU Advances*, **1 (3)**, 1–15, https://doi.org/10.1029/2019av000161.

Schlosser, T. L., A. J. Lucas, M. Omand, and J. T. Farrar, 2022: Monsoons , plumes , and blooms : intraseasonal variability in the subsurface chlorophyll maximum in the Bay of Bengal.

Schmitt, M., H. Pham, S. Sarkar, K. Klingbeil, and L. Umlauf, 2024: Diurnal warm layers in the ocean: Energetics, nondimensional scaling, and parameterization. *Journal of Physical Oceanography*, **54 (4)**, 1037–1055.

Schneider, T., T. Bischoff, and G. H. Haug, 2014: Migrations and dynamics of the intertropical convergence zone. *Nature*, **513 (7516)**, 45–53, https://doi.org/10.1038/nature13636.

Seager, R., S. E. Zebiak, and M. A. Cane, 1988: A model of the tropical Pacific sea surface temperature climatology. *Journal of Geophysical Research: Oceans*, **93 (C2)**, 1265–1280, https://doi.org/10.1029/JC093iC02p01265.

Sengupta, D., G. N. Bharath Raj, M. Ravichandran, J. Sree Lekha, and F. Papa, 2016: Near-surface salinity and stratification in the north Bay of Bengal from moored observations. *Geophysical Research Letters*, **43 (9)**, 4448–4456, https://doi.org/https://doi.org/10.1002/2016GL068339.

Sengupta, D., G. N. Bharath Raj, and S. S. C. Shenoi, 2006: Surface freshwater from Bay of Bengal runoff and Indonesian Throughflow in the tropical Indian Ocean. *Geophysical Research Letters*, **33 (22)**, https://doi.org/https://doi.org/10.1029/2006GL027573.

Sengupta, D., S. R. Parampil, G. S. Bhat, V. S. N. Murty, V. Ramesh Babu, T. Sudhakar, K. Premkumar, and Y. Pradhan, 2008: Warm pool thermodynamics from the Arabian Sea Monsoon Experiment (ARMEX). *Journal of Geophysical Research: Oceans*, **113 (C10)**, https://doi.org/10.1029/2007JC004623.

Sengupta, D., and M. Ravichandran, 2001: Oscillations of Bay of Bengal sea surface temperature during the 1998 Summer Monsoon. *Geophysical Research Letters*, **28 (10)**, 2033–2036, https://doi.org/https://doi.org/10.1029/2000GL012548.

Sengupta, D., P. K. Ray, and G. S. Bhat, 2002: Spring warming of the Eastern Arabian Sea and Bay of Bengal from buoy data. *Geophysical Research Letters*, **29 (15)**, 24–1–24–4, https://doi.org/10.1029/2002GL015340.

Seo, H., A. C. Subramanian, A. J. Miller, and N. R. Cavanaugh, 2014: Coupled impacts of the diurnal cycle of sea surface temperature on the Madden–Julian oscillation. *Journal of Climate*, **27 (22)**, 8422–8443.

Seo, H., and Coauthors, 2023: Ocean mesoscale and frontal-scale ocean–atmosphere interactions and influence on large-scale climate: a review. *Journal of Climate*, **36 (7)**, 1981–2013.

Shcherbina, A. Y., E. A. D'Asaro, and R. R. Harcourt, 2019: Rain and Sun create slippery layers in the Eastern Pacific fresh pool. *Oceanography (Washington, DC)*, **32 (2)**, 98.

Shcherbina, A. Y., and Coauthors, 2015: The LatMix summer campaign: Submesoscale stirring in the upper ocean. *Bulletin of the American Meteorological Society*, **96 (8)**, 1257–1279.

Shenoi, S. S. C., N. Nasnodkar, G. Rajesh, K. J. Joseph, I. Suresh, and A. M. Almeida, 2009: On the diurnal ranges of Sea Surface Temperature (SST) in the north Indian Ocean. *Journal of Earth System Science*, **118 (5)**, 483.

Shenoi, S. S. C., D. Shankar, and S. R. Shetye, 2002: Differences in heat budgets of the near-surface Arabian Sea and Bay of Bengal: Implications for the summer monsoon. *Journal of Geophysical Research: Oceans*, **107 (C6)**, 5–14, https://doi.org/10.1029/2000JC000679.

Shroyer, E. L., D. L. Rudnick, J. T. Farrar, B. Lim, S. K. Venayagamoorthy, L. C. St. Laurent, A. Garanaik, and J. N. Moum, 2016: Modification of upper-ocean temperature struc-

ture by subsurface mixing in the presence of strong salinity stratification. *Oceanography*, **29 (2)**, 62–71.

Shroyer, E. L., and Coauthors, 2021: Bay of Bengal intraseasonal oscillations and the 2018 monsoon onset. *Bulletin of the American Meteorological Society*, 1–44, https://doi.org/10.1175/bams-d-20-0113.1.

Sijikumar, S., and K. Rajeev, 2012: Role of the Arabian Sea warm pool on the precipitation characteristics during the monsoon onset period. *Journal of Climate*, https://doi.org/10.1175/JCLI-D-11-00286.1.

Simoes-Sousa, I. T., A. Tandon, J. Buckley, D. Sengupta, E. Shroyer, and S. P. de Szoeke, 2022: Atmospheric cold pools in the Bay of Bengal. *Journal of the Atmospheric Sciences*.

Skyllingstad, E. D., D. Vickers, L. Mahrt, and R. Samelson, 2007: Effects of mesoscale sea-surface temperature fronts on the marine atmospheric boundary layer. *Boundary-Layer Meteorology*, **123 (2)**, 219–237, https://doi.org/10.1007/s10546-006-9127-8.

Smith, T. A., J. K. Jolliff, N. D. Walker, and S. Anderson, 2019: Biophysical submesoscale processes in the wake of hurricane Ivan: Simulations and satellite observations. *Journal of Marine Science and Engineering*, **7 (11)**, 378.

Sobel, A. H., E. D. Maloney, G. Bellon, and D. M. Frierson, 2008: The role of surface heat fluxes in tropical intraseasonal oscillations. *Nature Geoscience*, **1 (10)**, 653–657, https://doi.org/10.1038/ngeo312.

Soloviev, A., and R. Lukas, 1997: Observation of large diurnal warming events in the near-surface layer of the western equatorial Pacific warm pool. *Deep Sea Research Part I: Oceanographic Research Papers*, **44 (6)**, 1055–1076, https://doi.org/https://doi.org/10.1016/S0967-0637(96)00124-0.

Soloviev, A., and R. Lukas, 2006: *The Near-Surface Layer of the Ocean Structure, Dynamics and Applications*. Publication Title: PoLAR.

Song, X., X. Xie, B. Qiu, H. Cao, S. P. Xie, Z. Chen, and W. Yu, 2022: Air-sea latent heat flux anomalies induced by oceanic submesoscale processes: An observational case study. *Frontiers in Marine Science*, **9 (March)**, 1–12, https://doi.org/10.3389/fmars.2022.850207.

Song, Y., X. Yang, Y. Bao, F. Qiao, and Z. Song, 2024: Role of strong sea surface temperature diurnal variation in triggering the summer monsoon onset over the Bay of Bengal in a climate model. *Geophysical Research Letters*, **51 (15)**, e2023GL108 015.

Sprintall, J., and M. Tomczak, 1992: Evidence of the barrier layer in the surface layer of the tropics. *Journal of Geophysical Research: Oceans*, **97 (C5)**, 7305–7316, https://doi.org/10.1029/92JC00407.

Sree Lekha, J., J. M. Buckley, A. Tandon, and D. Sengupta, 2018: Subseasonal dispersal of freshwater in the northern Bay of Bengal in the 2013 summer monsoon season. *Journal of Geophysical Research: Oceans*, **123 (9)**, 6330–6348.

Sree Lekha, J., A. J. Lucas, J. Sukhatme, J. K. Joseph, M. Ravichandran, N. Suresh Kumar, J. T. Farrar, and D. Sengupta, 2020: Quasi-biweekly mode of the Asian summer monsoon revealed in Bay of Bengal surface observations. *Journal of Geophysical Research: Oceans*, **125 (12)**, e2020JC016 271.

Stan, C., D. M. Straus, J. S. Frederiksen, H. Lin, E. D. Maloney, and C. Schumacher, 2017: Review of Tropical-Extratropical teleconnections on intraseasonal time scales. *Reviews of Geophysics*, **55 (4)**, 902–937, https://doi.org/10.1002/2016RG000538.

Stramma, L., P. Cornillon, and J. F. Price, 1986: Satellite observations of sea surface cooling by hurricanes. *Journal of Geophysical Research: Oceans*, **91 (C4)**, 5031–5035.

Stuart-Menteth, A. C., I. S. Robinson, and P. G. Challenor, 2003: A global study of diurnal warming using satellite-derived sea surface temperature. *Journal of Geophysical Research: Oceans*, **108 (C5)**, https://doi.org/10.1029/2002JC001534.

Stuart-Menteth, A. C., I. S. Robinson, R. A. Weller, and C. J. Donlon, 2005: Sensitivity of the diurnal warm layer to meteorological fluctuations part 1: observations. *Journal of Atmospheric and Ocean Science*, **10 (3)**, 193–208.

Sullivan, P. P., J. C. McWilliams, and E. G. Patton, 2025: An investigation of coupled atmospheric and oceanic boundary layers using large-eddy simulation. *Journal of the Atmospheric Sciences*, **82 (4)**, 829–846.

Sullivan, P. P., J. C. McWilliams, J. C. Weil, E. G. Patton, and H. J. S. Fernando, 2020: Marine boundary layers above heterogeneous SST: Across-front winds. *Journal of the Atmospheric Sciences*, https://doi.org/10.1175/JAS-D-20-0062.1.

Sullivan, P. P., J. C. McWilliams, J. C. Weil, E. G. Patton, and H. J. S. Fernando, 2021: Marine Boundary Layers above Heterogeneous SST: Alongfront Winds. *Journal of the Atmospheric Sciences*, https://doi.org/10.1175/JAS-D-21-0072.1.

Sun, C., A. Zhang, B. Jin, X. Wang, X. Zhang, and L. Zhang, 2022: Seasonal variability of eddy kinetic energy in the north Indian Ocean. *Frontiers in Marine Science*, **9**, https://doi.org/10.3389/fmars.2022.1032699.

Sutherland, G., L. Marié, G. Reverdin, K. H. Christensen, G. Broström, and B. Ward, 2016: Enhanced turbulence associated with the diurnal jet in the ocean surface boundary

layer. *Journal of Physical Oceanography*, **46 (10)**, 3051–3067, https://doi.org/10.1175/JPO-D-15-0172.1.

Tandon, A., and C. Garrett, 1994: Mixed layer restratification due to a horizontal density gradient. *Journal of Physical Oceanography*, **24 (6)**, 1419–1424.

Thangaprakash, V. P., K. Suprit, N. S. Kumar, and D. Chaudhuri, 2016: What controls seasonal evolution of sea surface temperature in the Bay of Bengal? Mixed layer heat budget analysis using moored buoy observations. *Oceanography*, **29 (2)**, 202–213, https://doi.org/10.5670/oceanog.2016.52.

Thomas, L. N., and C. M. Lee, 2005: Intensification of ocean fronts by down-front winds. *Journal of Physical Oceanography*, **35 (6)**, 1086–1102.

Thomas, L. N., A. Tandon, and A. Mahadevan, 2008: Submesoscale processes and dynamics. *Ocean modeling in an Eddying Regime*, **177**, 17–38.

Thompson, E. J., J. N. Moum, C. W. Fairall, and S. A. Rutledge, 2019: Wind limits on rain layers and diurnal warm layers. *Journal of Geophysical Research: Oceans*, **124 (2)**, 897–924, https://doi.org/10.1029/2018JC014130.

Venkatesan, R., V. Shamji, G. Latha, S. Mathew, R. Rao, A. Muthiah, and M. Atmanand, 2013: In situ ocean subsurface time-series measurements from OMNI buoy network in the Bay of Bengal. *Current Science*, 1166–1177.

Venkatesan, R., A. Tandon, D. Sengupta, and K. N. Navaneeth, 2018: *Recent Trends in Ocean Observations*. https://doi.org/10.1007/978-3-319-66493-4_1.

Venkatesan, R., N. Vedachalam, and G. Vengatesan, 2021: Quantification of ocean-atmosphere energy exchange during super cyclone Amphan in the Bay of Bengal using

Indian Ocean moored observatories. *Dynamics of Atmospheres and Oceans*, **94**, 101 210, https://doi.org/10.1016/j.dynatmoce.2021.101210.

Vinayachandran, P. N., and R. S. Nanjundiah, 2009: Indian Ocean sea surface salinity variations in a coupled model. *Climate dynamics*, **33**, 245–263.

Vinayachandran, P. N., D. Shankar, J. Kurian, F. Durand, and S. S. Shenoi, 2007: Arabian Sea mini warm pool and the monsoon onset vortex. *Current Science*, **93 (2)**, 203–214.

Vinayachandran, P. N., and S. R. Shetye, 1991: The warm pool in the Indian Ocean. *Proceedings of the Indian Academy of Sciences - Earth and Planetary Sciences*, **100 (2)**, 165–175, https://doi.org/10.1007/BF02839431.

Vincent, E. M., M. Lengaigne, G. Madec, J. Vialard, G. Samson, N. C. Jourdain, C. E. Menkes, and S. Jullien, 2012: Processes setting the characteristics of sea surface cooling induced by tropical cyclones. *Journal of Geophysical Research: Oceans*, **117 (C2)**.

Webster, P. J., C. A. Clayson, and J. A. Curry, 1996: Clouds, radiation, and the diurnal cycle of sea surface temperature in the tropical Western Pacific. *Journal of Climate*, **9 (8)**, 1712–1730.

Weller, R. A., M. F. Baumgartner, S. A. Josey, A. S. Fischer, and J. C. Kindle, 1998: Atmospheric forcing in the Arabian Sea during 1994–1995: Observations and comparisons with climatology and models. *Deep Sea Research Part II: Topical Studies in Oceanography*, **45 (10)**, 1961–1999, https://doi.org/10.1016/S0967-0645(98)00060-5.

Weller, R. A., J. T. Farrar, H. Seo, C. Prend, D. Sengupta, J. S. Lekha, M. Ravichandran, and R. Venkatesen, 2019: Moored observations of the surface meteorology and air–sea fluxes in the northern Bay of Bengal in 2015. *Journal of Climate*, https://doi.org/10.1175/JCLI-D-18-0413.1.

Weller, R. A., A. S. Fischer, D. L. Rudnick, C. C. Eriksen, T. D. Dickey, J. Marra, C. Fox, and R. Leben, 2002: Moored observations of upper-ocean response to the monsoons in the Arabian Sea during 1994–1995. *Deep Sea Research Part II: Topical Studies in Oceanography*, **49 (12)**, 2195–2230, https://doi.org/10.1016/S0967-0645(02)00035-8.

Weller, R. A., and Coauthors, 2016: Air-sea interaction in the Bay of Bengal. *Oceanography*, **29 (2)**, 28–37.

Wentz, F. J., T. Meissner, C. Gentemann, K. Hilburn, and J. Scott, 2014a: Remote sensing systems GCOM-W1 AMSR2 3-day environmental suite on 0.25° grid, version 08.2. Remote Sensing Systems, Santa Rosa, CA.

Wentz, F. J., T. Meissner, C. Gentemann, K. A. Hilburn, and J. Scott, 2014b: Remote sensing systems GCOM-W1 AMSR2 daily environmental suite on 0.25° grid, version 8.2. Place: Santa Rosa, CA Medium: Remote Sensing Systems.

Wijesekera, H. W., and Coauthors, 2016: ASIRI: An ocean–atmosphere initiative for Bay of Bengal. *Bulletin of the American Meteorological Society*, **97 (10)**, 1859–1884, https://doi.org/10.1175/BAMS-D-14-00197.1.

Witte, C. R., A. Subramaniam, and C. J. Zappa, 2024: An improved bio-physical parameterization for ocean radiant heating in conditions of near-surface stratification. *Journal of Geophysical Research: Oceans*, **129 (11)**, e2024JC021 049, https://doi.org/10.1029/2024JC021049.

Yablonsky, R. M., and I. Ginis, 2009: Limitation of one-dimensional ocean models for coupled hurricane–ocean model forecasts. *Monthly Weather Review*, **137 (12)**, 4410–4419.

Yi, Z., C. Qiu, D. Wang, Z. Cai, J. Yu, and J. Shi, 2024: Submesoscale kinetic energy induced

by vertical buoyancy fluxes during the tropical cyclone Haitang. *Journal of Geophysical Research: Oceans*, **129 (7)**, e2023JC020 494.

Yuan, X., X. Yu, and Z. Su, 2020: Seasonal and interannual variabilities of the barrier layer thickness in the tropical Indian Ocean. *Ocean Science*, **16 (5)**, 1285–1296, https://doi.org/10.5194/os-16-1285-2020.

Zhang, C., H. H. Hendon, W. S. Kessler, and A. J. Rosati, 2001: A workshop on the MJO and ENSO. *Bulletin of the American Meteorological Society*, **82 (5)**, 971–976.

Zheng, B., A. J. Lucas, R. Pinkel, and A. Le Boyer, 2022: Fine-scale velocity measurement on the Wirewalker wave-powered profiler. *Journal of Atmospheric and Oceanic Technology*, **39 (2)**, 133–147.

Zhou, L., R. Murtugudde, D. Chen, and Y. Tang, 2017: A central Indian Ocean mode and heavy precipitation during the Indian summer Monsoon. *Journal of Climate*, **30 (6)**, 2055–2067, https://doi.org/10.1175/JCLI-D-16-0347.1.